Doktorarbeit

Growth and Characterization of Single Molecular Wires on Metal Surfaces

Matthias Koch

June 2013

Im Fachbereich Physik der Freien Universität Berlin eingereichte Dissertation

Disputation: 15.07.2013

This work was started in May 2009 and finished in June 2013 in the group of Priv.-Doz. Dr. Leonhard Grill at the Department of Physical Chemistry of the Fritz-Haber-Institut der Max-Planck-Gesellschaft.

Berlin, June 2013

Erstgutachter: Priv.-Doz. Dr. Leonhard Grill
Zweitgutachterin: Prof. Dr. Katharina Franke

Abstract

Molecular wires will be an essential part in future nanotechnology as they are necessary to connect the functional molecules. In this thesis the growth and characterization of molecular wires are investigated by scanning tunneling microscopy. The bottom-up approach "on-surface polymerization" was used to fabricate the moleculare wires. Two types of molecular wires are investigated in this thesis: porphyrin tapes and graphene nanoribbons. Steric hindrance limits the polymerization of the porphyrin-based molecules and the trapezoid-shaped molecules so that only very short or fragmented chains are observed. Furthermore, the influence of the surface was studied in regard to the polymerization process. In contrast to Au(111), on Cu(111) 2,11-dibromohexabenzocoronene dehalogenate at room temperature, and molecular chains emerge. The higher catalytic activity of Cu(111) reduces the dehalogenation temperature. These chains are linked by a metal-ligand bond and are not covalently bound as it is observed on Au(111). On Cu(111) copper adatoms are available at room temperature. The surface can also be used to suppress the growth of polymerized species. On Au(111) the polymerization of 2,3-dibromoanthracene leads to dimers and trimers, whereas on Au(100) only dimers are produced.

One aspect of this thesis is the study of the conductance and the electronic properties of graphene nanoribbons, which are polymerized from 10,10'-dibromo-9,9'-bianthryl building blocks. Scanning tunneling spectroscopy is used to investigate the electronic structure, and the highest occupied (HOMO) as well as the lowest unoccupied molecular orbital (LUMO) are found to be delocalized along the armchair edges of the ribbon. The HOMO-LUMO gap amounts to 2.8 eV in agreement with expectations. At the short zigzag edges a localized Tamm state is detected, which is only observed for defect-free termini. To measure the conductance the molecule is lifted from the surface by the tip while the current is recorded. The role of the molecular orbitals on the charge transport is investigated by recording length-dependent conductance spectra for electron energies in the range of +1.8 and -2.4 eV. Independent of the electron energies the measured current decays exponentially with the tip height. If the electron energy coincides with the molecular orbitals the inverse decay length of the ribbon drops from $\sim$0.45 Å^{-1} in the HOMO-LUMO gap to $\sim$0.10 Å^{-1} which points to an improved conductance. Furthermore, molecular vibrations of a single graphene nanoribbon in pulling geometry are observed by inelastic electron tunneling spectroscopy, and, amongst others, the D mode and the G mode are detected. When the ribbon geometry is changed from planar to bent no shift in the energy of the molecular vibrations is detected.

In the last part of this thesis the required force is studied to lift a molecular chain from the surface. Long polyfluorene chains are fabricated and pulled from the surface with an atomic force microscope tip while the frequency shift signal is recorded. In contrast to the conductance experiments, the frequency shift does not decay as a function of the tip height. The polyfluorene chains are lifted stepwise from the surface, and the main contribution in the frequency shift signal results from the fluorene unit lifted up next. In agreement with expectations a maximum attractive force between the molecule and the surface of -0.5 nN is determined.

Kurzzusammenfassung

Molekulare Drähte sind essentielle Bauteile in zukünftiger Nanotechnologie, da diese die funktionalen Einheiten, sprich die Moleküle, verbinden. In dieser Arbeit wird das Wachstum und die Charakterisierung von molekularen Drähten mit Hilfe eines Rastertunnelmikroskops untersucht. Die Drähte wurden nach dem "Bottom-Up"-Ansatz "On-Surface Polymerization" auf der Oberfläche synthetisiert mit dem Fokus auf Porphyrinketten und Graphenstreifen. Die sterische Abstoßung zwischen den Molekülen ist dabei eine große Herausforderung für die Oberflächen-assistierte Polymerisierung. Für einige der untersuchten molekularen Bausteine von Porphyrinketten und Graphendrähten wurde das Wachstum durch die sterische Abstoßung beschränkt, sodass entweder nur sehr kurze oder stark fragmentierte Ketten auf der Oberfläche gefunden wurden. Des Weiteren wurde der Einfluß der Oberfläche auf die Polymerisierung untersucht. Durch das Verwenden der Cu(111)- anstelle der Au(111)-Oberfläche entfällt der benötigte Heizschritt für die Aktivierung der 2,11-dibromohexabenzocoronene, ein Hinweis für eine erhöhte katalytische Aktivität. Während auf Cu(111) die einzelnen Elemente der Kette über ein Kupfer-Adatom gebunden sind, befinden sich auf der Au(111) Oberfläche kovalent gebundene Ketten. Auf Cu(111) diffundieren Kupfer-Adatome bei Raumtemperatur. Auch die Art des Wachstums lässt sich durch die Wahl der Oberfläche beinflussen: 2,3-dibromoanthracene polymerisiert auf Au(111) zu Dimeren und Trimeren, wobei auf Au(100) keine Trimere auftreten.

Außerdem wurde die elektronische Struktur und die Leitfähigkeit von Graphendrähten untersucht, die auf 10,10'-dibromo-9,9'-bianthryl basieren. Mit Hilfe von Rastertunnelspektroskopie konnten das höchste besetzte (HOMO) und das niedrigste unbesetzte Molekülorbital (LUMO) aufgelöst werden, wobei beobachtet wurde, dass diese entlang des Drahtes delokalisiert sind. Das "HOMO-LUMO gap" stimmt mit den Werten aus der Literatur überein. Der Tamm-Zustand ist an den kurzen Enden mit Zickzack-Struktur lokalisiert, verschwindet allerdings bereits bei geringfügigen Änderungen der chemischen Struktur der Enden. Die Leitfähigkeit eines Moleküls wurde gemessen, indem es mit der Spitze kontaktiert wird, um es dann von der Oberfläche zu ziehen, dabei wird der Strom aufgezeichnet. Um die Rolle der molekularen Orbitale im Ladungstransport zu untersuchen, wird die Elektronenenergie zwischen +1.8 und -2.4 eV variiert. Unabhängig von der Elektronenenergie wird ein exponentieller Abfall des Stroms festgestellt, jedoch verringert sich dieser von $\sim$0.45 $Å^{-1}$ zu $\sim$0.10 $Å^{-1}$ (d.h. verbesserte Leitfähigkeit), wenn die Energie der Elektronen höher als die der molekularen Orbitale ist. Außerdem wurden intramolukulare Schwingungen (unter anderem die D-Mode und die G-Mode) in der Schwingungsstruktur eines einzelnen freischwebenden Graphendrahts detektiert. Dabei wurde kein Einfluss der Struktur des Drahts auf seine Schwingungsenergie festgestellt.

Abschließend wurde die Kraft bestimmt, die benötigt wird, um eine molekulare Kette von der Oberfläche zu ziehen. Dafür wurden Polyfluorenketten mit der Spitze eines Rasterkraftmikroskops von der Oberfläche gehoben, während die Verschiebung der Resonanzfrequenz aufgezeichnet wurde. Das Messsignal nimmt, im Gegensatz zum Tunnelstrom, nicht mit dem Abstand zwischen Spitze und Probe ab, weist aber ebenso ein periodisches Muster auf. Daraus ließ sich in Übereinstimmung mit den Erwartungen eine attraktive Kraft von maximal -0.5 nN bestimmen.

Contents

List of Figures

List of Tables

Abbreviations

STM scanning tunneling microscope
AFM atomic force microscope
LDOS local density of states
STS scanning tunneling spectroscopy
GNR graphene nanoribbon
CNT carbon nanotube
HOMO highest occupied molecular orbital
LUMO lowest unoccupied molecular orbital
MCBJ mechanically controllable break junction
SWNT single wall carbon nanotube
UHV ultra-high vacuum
SAM self-assembled monolayer
DT n-dodecanethiol
DPEBT 4,4'-di(phenylene-ethynylene)-benzothioacetate
ML monolayer
ONI oligonaphtalenefluoreneimine
OPI oligophenyleneimine
CVD chemical vapour deposition
FET field effect transistor
MOSFET metal-oxide-semiconductor field-effect transistor
DBDA 10,10'-dibromo-9,9'-bianthryl
HBC hexa-peri-hexabenzocoronene
RT room temperature
tdBA 2,3-dibromoanthracene
SEM scanning electron microscopy
DBTF dibromoterfluorene
dBP dibromo-diphenylporphyrin
DBA 9,10-dibromo-anthracene
DBDP dibromo-tetraphenyl-bisporphyrin
TB-dBP dibromo-bis(3,5-tert-butylphenyl)porphyrin
QMS quadropol mass spectrometer
LEED low-energy-electron-diffraction
AD analog-to-digital
DA digital-to-analog
fcc face-centered cubic
hcp hexagonal closed-packed
TPP 1,4-Bis(4-bromophenyl)-2,3,6,11-tetraphenyltriphenylene

TB-TPP 1,4-Bis(4-bromophenyl)-2,3-bis(4-tert-butylphenyl)-6,11-diphenyltriphenylene
TPO 5,14-dibromotribenzo[ef,hi,o]triphenyleno[11,12,1,2-uvabc]ovalene

Chapter 1

Introduction

According to Moore's law, the number of electronic devices on a computer chip doubles every 36 months [1]. A 22 nanometer manufacturing process is the basis for the current (2013) fabrication of microprocessors by Intel, the world's number one in semiconductor chips. For further down-scaling of semiconductor transistors the short channel effects, e.g., impaired drain-current saturation, gate leakage current or drain-induced barrier lowering, will rise in importance and, thereby, will limit the minimum size of the transistor in the future [2]. A possible solution might be delivered by molecular electronics. In a pioneer work Arieh Aviram and Mark Ratner suggested the use of a single molecule as a rectifier [3], which was experimentally demonstrated by the group of Metzger [4]. Nowadays other functional units such as switches and transistors were realized by single molecules [5, 6, 7]. A famous molecular switch is azobenzene, which exists in two conformations: *trans* and *cis*. In a solution the *trans* to *cis* and *cis* to *trans* isomerization can be triggered by illumination with a laser at a wavelength of 366 nm and 436 nm, respectively [8]. Illumination experiments on the Au(111) surface proved the reversible switching of 3,3',5,5'-tetra-tert-butyl-azobenzene between the *trans* and *cis* isomer [9]. Together with the functional units the wires connecting the single molecules need to shrink. Instead of conventional wires, molecular chains connect the functional units.

Graphene nanoribbons, stripes of graphene, are promising candidates for this application because of the high carrier mobility of graphene. An additional advantage is the tuneability of the electronic properties of a graphene nanoribbon by its chemical structure [10]. Changing the width of the ribbon allows the control of the band gap which is proportional to the reciprocal width of the ribbon [11]. For certain edge structures of the graphene nanoribbon a localized electronic state appears [12]. As a result, industrial application requires a fabrication technique of graphene nanoribbons which guarantees a well-defined width and edge structure. This is difficult to achieve for top-down approaches like etching and lithography. With these techniques there is a lack of control over the edge structure as an edge roughness of 5 nm was reported [13]. In the present thesis the bottom-up approach on-surface polymerization is studied for the fabrication of graphene nanoribbons.
On-surface polymerization is based on molecular building blocks which are equipped with halogen atoms [14]. The bond energy of the halogen atoms is lower compared to the other bonds of the molecule, and its bond breaks first at an elevated temperature. At the former positions of the dissociated halogen atoms reactive sites are created, and other activated molecules can covalently link. This process combined with molecular self-assembly permits

the growth of molecular structures on the surface. The architecture of these molecular networks is defined by the design of the molecular building block, and the resulting structure is fabricated on the surface. An essential aspect of on-surface polymerization is the reduction of the steric repulsion between the molecular building blocks, which limits the polymerization. This might be achieved by additional side groups, like tert-butyl groups, which decouple the molecules from the surface. However, the surface is more than only a template for the polymerization process. With the choice of the substrate the resulting structure can be tuned. In the on-surface polymerization the catalytic reactivity, the binding energy and the corrugation, amongst others, are crucial for the synthesis. For example, the average chain length might be tuned by using surfaces where the molecules have different adsorption energies, which changes their diffusion barrier of the molecules. For the three (111) surfaces of gold, silver and copper different coupling probabilities between the molecules were reported leading to different shapes of the molecular networks [15]. Therefore, the influence of the surface on the growth needs to be investigated. In this thesis the substrates Au(111), Au(100) and Cu(111) were used. While Au(111) is known for its inert nature Cu(111) is more active.

Scanning tunneling microscopy is a versatile technique for the investigation of molecular structures. Its capabilities for imaging surfaces and molecules on a subnanometer resolution are ideal for the characterization of the different stages of the growth. The atomic precision of the tip also facilitates the manipulation of the fabricated structure, e.g., the bond between the building blocks in a molecular wire can be tested by lateral manipulation. Even more important for the characterization of molecular wires is the measurement of the conductance and the electronic structure of a molecular wire. Scanning tunneling spectroscopy is, therefore, a powerful technique which can be used for mapping the local density of states of a single molecule. The conductance of single molecules was measured by vertical manipulation [16]. A single molecular chain was lifted from the surface while the current was recorded as a function of the tip height. The electrons only travel through the lifted part of the molecular wire as the metal substrate is a much better conductor. With increasing tip height the length of the lifted part of the molecule increases, which corresponds to a longer effective transport path of the electrons. By repeating the pulling experiment for different bias voltages the role of the molecular orbitals in the charge transport may be investigated and, thereby, also the charge transport mechanism. However, for an insight into the charge transport the electronic structure such as the molecular orbitals needs to be observed first.

The aim of this work is the growth and characterization of molecular wires. On-surface polymerization was used for the fabrication of molecular wires which were later investigated by scanning tunneling microscopy. The present thesis can be divided into two parts: The first part treats the growth of molecular chains and the influence of the substrate on the resulting products (Chapter 5), the second part discusses the electronic and vibrational structure of graphene nanoribbons based on 10,10'-dibromo-9,9'-bianthryl (Chapter 6).

Apart from graphene nanoribbons, porphyrin tapes were investigated (Chapter 5.1). The highest occupied molecular orbital of the fully conjugated porphyrin tape is supposed to shift to a higher energy with the increasing length of the molecular chain, while an electronic excitation with an energy of 0.43 eV was reported [17]. For comparison, alkane chains have a gap between the highest occupied and the lowest unoccupied molecular orbital of $\sim$9 eV [18]. In general, a gap between the highest occupied and the lowest

unoccupied molecular orbital smaller than 1 eV is considered as very low [19]. The growth of graphene nanoribbons was approached by two different kinds of molecular building blocks: trapezoid-shaped building blocks and anthracene-based building blocks. These are discussed in chapter 5.3.1 and 5.3.2, respectively.

The role of the surface was studied by depositing the same molecule onto different substrates (Chapter 5.2). 2,11-dibromohexabenzocoronene was studied on Au(111) and Cu(111), both exhibit different catalytic reactivities (Chapter 5.2.1).
2,3-dibromoanthracene and 10,10'-dibromo-9,9'-bianthryl were deposited onto Au(111) and Au(100). Au(100) reconstructs into parallel corrugations which appear every 14.4 Å [20]. The spacing between these atomic rows on the Au(100) surface is much smaller than the periodicity of the herringbone reconstruction on the Au(111) surface. The hcp region and the fcc region of the herringbone reconstruction have a width of 25 Å and 38 Å, respectively [21]. The narrower reconstruction of the Au(100) might influence the polymerization (Chapter 5.2.2 and 5.3.2).

The electronic structure of graphene nanoribbons fabricated by 10,10'-dibromo-9,9'-bianthryl molecular building blocks on Au(111) is discussed in chapter 6.1. In the following chapter 6.2 the conductance of single graphene nanoribbons is studied with and without defects. In chapter 6.3 the vibrational structure of a planar graphene nanoribbon and of a graphene nanoribbon in pulling geometry is presented.

Finally, in chapter 7 the atomic force microscopy results of polyfluorene chains are shown.

Chapter 2

Scanning Tunneling Microscopy

Before the invention of the STM spectroscopic techniques, that obtain information in the reciprocal space, dominated surface science. These techniques are mainly based on diffraction and scattering and are only sensitive to periodic structures up to ∼100 Å, which is the limit of the finite coherence of the electron beam [22]. There were only few real space techniques with sub-nm resolution. One of these real space techniques is scanning electron microscopy (SEM). In SEM a heavily focused electron beam with an energy up to 30 keV scans the surface. The secondary electrons of the surface are detected to produce the image of the sample. The resolution of SEM depends on the spot size of the electron beam and is in the order of 10 Å [22]. However, a commercially available SEM setup with an electron beam energy of 200 keV achieves a resolution as low as 1.4 Å [23]. Drawbacks of the SEM are the required vacuum and the need of a conducting structure.

In 1982 G. Binnig and H. Rohrer invented the STM, a non-destructive real space technique. It had a large impact on further developments in surface science. In 1982 the monoatomic steps of the $CaIrSn_4$ and the Au(110) surface were for the first time imaged with STM [24]. The real-space observation and the explanation of the structure of the Si(111)(7x7) surface in 1983 was the breakthrough for STM (Fig. 2.1a) [25]. A few years later the surface state on Si(111)(7x7) was measured by scanning tunneling spectroscopy (STS) [26]. STS obtained by to the first derivative of the current, which is proportional to the local density of states (LDOS) of the sample (see chapter 2.5 for more details). If the molecules were decoupled from the substrate by an insulation layer of NaCl even the molecular orbitals have been imaged by STS [27, 28]. The sensitivity of the tip can be tuned by the structure of its apex. For example, picking up a CO molecule with the STM tip leads to tunneling through the degenerated π_x and π_y orbitals of the CO molecule [28]. This increases the p-wave contributions on the tunneling current and simultaneously improves the resolution in a controlled manner.

As conventional STM imaging is not sensitive to the chemical structure of different molecules with a similar size, C_2H_2, C_2D_2 and C_2HD can have the same appearance in STM imaging [32]. With inelastic tunneling spectroscopy it is possible to detect the vibrational modes of the molecule [32]. Three different molecules, C_2H_2, C_2D_2 and C_2HD, were identified by their vibrational peaks in the second derivative of the current. The C-H stretch vibration lies at higher energies than the C-D stretch vibration. Therefore, vibrational spectroscopy means to obtain chemical sensitivity with STM. To image the vibrations of single molecules

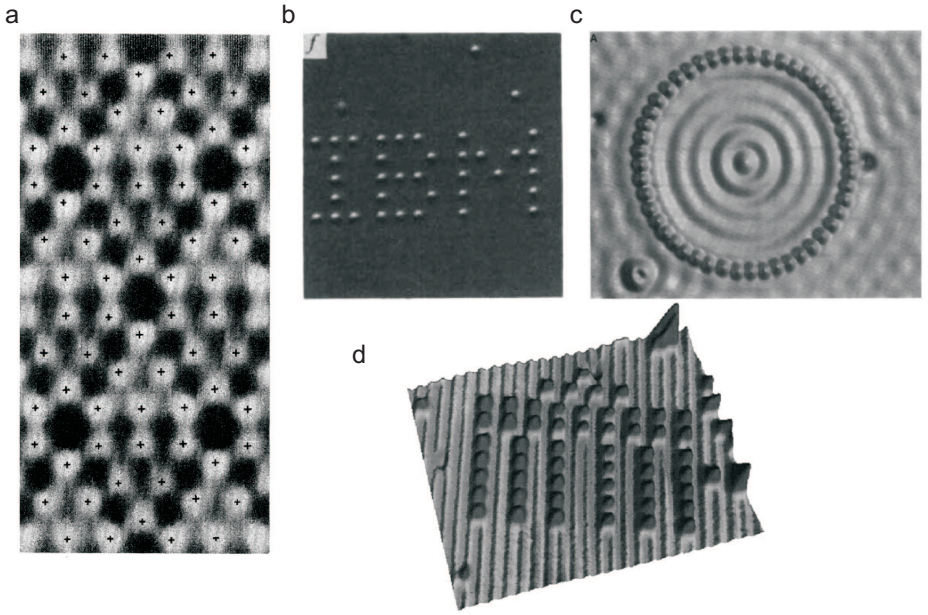

Figure 2.1: **a**, Topview of the 7×7 reconstruction on Si(111). Reprinted figure with permission from [25]. Copyright 2013 by the American Physical Society. **b**, IBM written with single Xenon atoms on Ni(110). Reprinted by permission from Macmillan Publishers Ltd: Nature [29], copyright 2013. **c**, Positioning Iron atoms on Cu(111). From [30]. Reprinted with permission from AAAS. **d**, Brandenburger Gate build by CO on Cu(211). Form [31]. Copyright 2013. The Japan Society of Applied Physics.

the STM head and the sample were cooled to liquid helium temperature (∼5 K). At this temperature the motion of most atoms and molecules is frozen [29]. With the tip of the STM, which can be moved with Ångström precision, single atoms can also be manipulated in a controlled manner. Examples of the controlled arrangement of single atoms to artificial structures are shown in figures 2.1b, c and d [29, 30]. Moreover, the interaction between STM tip and molecule is even strong and precise enough to break or create bonds inside a molecule [33, 34]. In the group of K.-H. Rieder (Freie Universität Berlin) the Ullmann reaction was studied on the Cu(111) surface with two benzene molecules each connected to one iodine atom [33]. A voltage pulse applied to the STM tip was used to break the iodine-phenyl bond. The reactive sides of both molecules were brought into contact by lateral manipulation and then a covalent bond between the two benzene molecules was formed by a further voltage pulse.
A low temperature STM cannot only be used to characterize molecules by imaging and spectroscopy. The atomically precise positioning system of the STM tip allows the fabrication of artificial structures and the activation of chemical reactions on the surface. Therefore, scanning tunneling microscopy is a powerful technique for the investigation of nanostructures.

2.1 Principles of Scanning Tunneling Microscopy

The setup of the STM consists of the sample and an atomically sharp tip attached to a piezo crystal. The magnitude of the current between tip and sample (a bias voltage is

applied between sample and tip) reflects the sample surface (see below). To record an STM image the surface is scanned by the tip and at each point the current and the elongation of the piezo, i.e. the tip-sample distance, are recorded. To image the atomic corrugation of a surface controlling the motion of the STM tip in *xyz* direction with high precision is essential for the experiment. In case of the flat Au(111) surface the atomic corrugation is at maximum 1 Å [35]. The tip mounted to a piezo crystal can be moved in any direction with a sensitivity of about 2 Å/V [36] which results in a desired precision of 0.1 Å vertically and 1.0 Å laterally [37]. The tip-sample distance amounts to a few Ångström and the electrons tunnel through the controllable vacuum barrier in between. The electron has to overcome a potential barrier U, the vacuum gap. If the electron energy is lower than the potential barrier the probability for the electron to travel across the barrier decays exponentially with its width. When a bias voltage V is applied to the sample only the electronic states which lie between the Fermi energy E_F and $E_F + V$ contribute to the tunneling current. Depending on the polarity the electrons tunnel from the tip to the sample or vice versa. This is illustrated in Fig. 2.2. Therefore, the tunneling current I depends exponentially on the tip-sample distance z and is approximated by:

$$I = \exp^{-2z\kappa} \tag{2.1}$$

$$\kappa = \sqrt{\frac{2m}{\hbar^2}(U - V)} \tag{2.2}$$

$\hbar$ is the Planck's constant, V is the energy of the tunneling electron, m is their mass and U is the potential in the barrier. The probability for an electron to cross the vacuum barrier decreases exponentially with the tip-sample distance z. For U-$V \sim 1$ eV, $m \sim$ MeV$/c^2$ (c is the speed of light) and $\hbar \sim$ eVs $\kappa \sim 10^{10}$ a change of 1 Å in tip-sample distance corresponds to a change of one order of magnitude in the tunneling current. This relation makes the tunneling current and, thereby, scanning tunneling microscopy extremely sensitive to small changes of the surface curvature.
To obtain atomic resolution the amplitudes of mechanical vibrations have to be damped down to less than one Ångström [22]. The mechanical noise can be divided into three different frequency regimes, which depend on the duration of the STM image and the image-resolution. For example, if the duration of an STM image lasts 3 min the image frequency is 0.005 Hz. In case of an image resolution of 256×256 points the duration of one point is 0.002 sec, which corresponds to a frequency of 364 Hz. The noise with a frequency lower than 0.005 Hz is considered as low frequency noise. The low frequency noise causes a curved background in the STM image, which can be eliminated to a great extent in the image analysis. The high frequency noise above 364 Hz is averaged and does not contribute to the STM image. The noise between the low frequency noise and the high frequency noise has to be damped by the isolation system of the STM.

To take an STM image two different modes are used: the constant-current mode and the constant-height mode. In the constant-current mode the current and bias voltage is kept fixed during the whole image. To compensate the surface curvature the tip-sample distance is adjusted by the feedback loop for each point until the chosen current is reached. An STM image taken in the constant-current mode shows the elongation of the tip piezo necessary to maintain the current.
A different mode is constant-height imaging. For this operation mode bias and the vertical

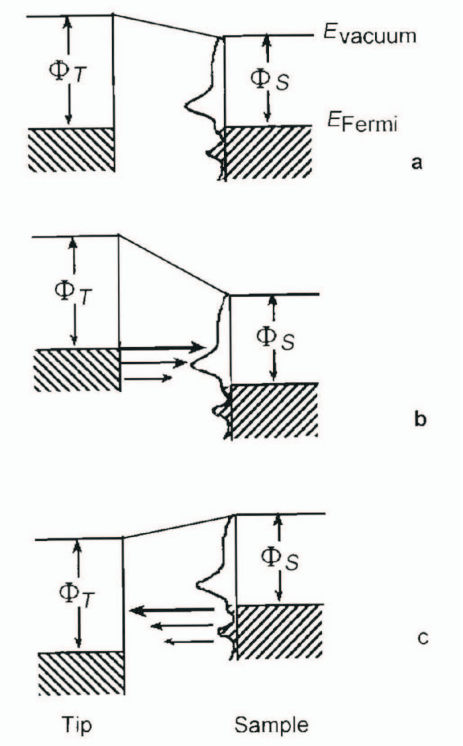

Figure 2.2: Energy levels contributing to the tunneling current. Φ_T and Φ_S are the work functions of the tip and the sample, respectively. **a**, Zero bias: no current. **b**, Positive sample bias: Occupied tip states tunnel into unoccupied sample states. **c**, Negative sample bias: Occupied sample states tunnel into unoccupied tip states. From [37]. This material is reproduced with permission of John Wiley & Sons, Inc.

tip position are kept at fixed values during the whole image. The feedback loop, which readjusts the tip-sample distance to keep the current constant, is open, i.e., deactivated. Due to changes in the topographic structure and/or the LDOS of the surface a variation in the intensity of the tunneling current is detected. In case of an image in constant-current mode, the current channel is constant and the piezo height is displayed. For the constant-height mode the current channel is displayed and the piezo height is constant.

Nevertheless, STM images mislead to be interpreted as topographic images, in particular, STM images taken in the constant-current mode where the current is translated into a height information. But the height profile of measured by the tip does not have to be the same as the surface curvature. This is, e.g., the case for metal surfaces with LDOS distributions that are spatially uniform. In reality, the contrast in an STM image is the convolution of the local electronic structure of the surface and of the tip [37].

2.2 Square Barrier Problem

The square barrier problem is basic in quantum mechanics. It describes an incoming particle whose kinetic energy E_I is not sufficient to overcome a potential barrier U_0. In a classical world the particle would reflect at the potential barrier and a transmission through

the barrier would be forbidden. A quantum mechanical particle with an energy lower than the barrier tunnels through the barrier with a certain probability. The probability for transmission depends exponentially on the barrier width.

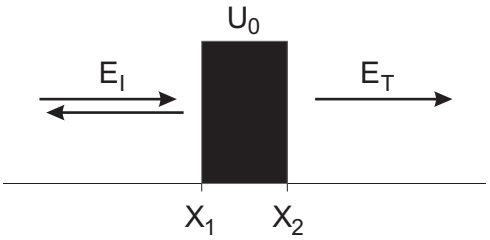

Figure 2.3: Incoming particle with an energy E_I which is lower than the barrier U_0. E_T is the energy of the transmitted particle.

To calculate this problem the area is divided it into three different regions (Fig. 2.3):

- Region I: Left side of the barrier
- Region II: The barrier
- Region III: Right side of the barrier

In region I two wave functions are defined, one for the incoming free particle and one for the reflected particle at the potential barrier.

$$\psi_I = \exp^{ik_0 x} \tag{2.3}$$

$$\psi_R = A \exp^{-ik_0 x} \tag{2.4}$$

The Schrödinger equation of a free particle is:

$$-\frac{\hbar^2}{2m}\frac{d^2\psi_I}{d^2x} = E\psi_I \tag{2.5}$$

A similar equation with an additional potential for the barrier is used for region II:

$$\psi_b = B \exp^{ikx} + C \exp^{-ikx} \tag{2.6}$$

$$-\frac{\hbar^2}{2m}\frac{d^2\psi_b}{d^2x} + U_0\psi_b = E\psi_b \tag{2.7}$$

In region III only the outgoing wave function is a solution of the Schrödinger equation.

$$\psi_T = D \exp^{ik_0 x} \tag{2.8}$$

$$-\frac{\hbar^2}{2m}\frac{d^2\psi_I}{d^2x} = E\psi_I \tag{2.9}$$

The transmission probability T and reflection probability R are defined as

$$T = j_T/j_I \tag{2.10}$$
$$R = j_R/j_I \tag{2.11}$$

The current density of the incoming, reflected and transmitted electrons are

$$j_I = -i\frac{\hbar}{2m} = (\overline{\psi_I}\frac{d\psi_I}{dx} - \psi_I\frac{d\overline{\psi_I}}{dx}) = \hbar k/m \tag{2.12}$$

$$j_R = -i\frac{\hbar}{2m} = (\overline{\psi_R}\frac{d\psi_R}{dx} - \psi_R\frac{d\overline{\psi_R}}{dx} = -\hbar k/m|A|^2 \tag{2.13}$$

$$j_T = -i\frac{\hbar}{2m} = (\overline{\psi_T}\frac{d\psi_T}{dx} - \psi_T\frac{d\overline{\psi_T}}{dx} = \hbar k/m|D|^2 \tag{2.14}$$

The wave function is continuously differentiable (which means $\psi_I(x_0) = \psi_b(x_0)$, $\psi_b(x_1) = \psi_T(x_1)$, $\psi_I'(x_0) = \psi_b'(x_0)$ and $\psi_b'(x_1) = \psi_T'(x_1)$), which allows the calculation of the coefficients A and D. This leads to a transmission probability of:

$$T = |D|^2 \sim \exp^{-2\sqrt{\frac{2m}{\hbar^2}(U_0-E)}x} \tag{2.15}$$

This dependence was already discussed in the previous section of this chapter. The transmission probability of the electrons through a barrier decays exponentially with the width x of the barrier and the square root of the effective barrier height $\sqrt{(U_0 - E)}$. The square barrier problem demonstrates the exponential decay of the tunneling current. However, it neither includes the shape of the potential barrier nor the electronic structure of the tip or the surface. To treat the tunneling current precisely a more sophisticated approach is required.

2.3 Bardeen Approach

The Bardeen Ansatz [38] treats the problem of electron tunneling between two metals through an insulating barrier. In light of STM one of the metals is the tip and the other one is the sample. In this section and the next the statements on the approaches of Bardeen [38], Tersoff, Hamann [39] and Chen [40] are based on the ideas of Wesloski and Gottlieb [41].

The Bardeen theory makes the following assumptions:

1. The electron-electron interaction can be ignored.
2. The occupation probabilities for the tip and sample are independent of each other and do not change despite the tunneling.
3. The tip and sample are both in electrochemical equilibrium so that the Fermi-Dirac distribution describes the occupation probabilities.
4. The tunneling is weak enough that the first-order approximation is sufficient.
5. The tip and sample states are nearly orthogonal.

These assumptions form the basis for the further discussion. According to assumptions 2 and 3, the occupied states of the tip and the sample can be described by a chemical potential μ and the Fermi-Dirac function. This is valid because the influence of the tunneling electrons is vanishingly small on the density of the states of tip and sample. Assumption 4 and 5 are essential to neglect several terms and simplify the calculations hereafter. Most important for getting started is the first assumption, which allows to treat the electrons with a single electron Hamiltonian.

$$H\psi = -\frac{\hbar^2}{2m}\Delta\psi(r) + V(r)\psi(r) \tag{2.16}$$

At t=0 both metals are infinitely far away and the system is described by a time independent Hamiltonian. For the sake of simplicity only the one-dimensional case is discussed. The wave functions of the tip and the sample oscillate in the metal blocks and exponen-

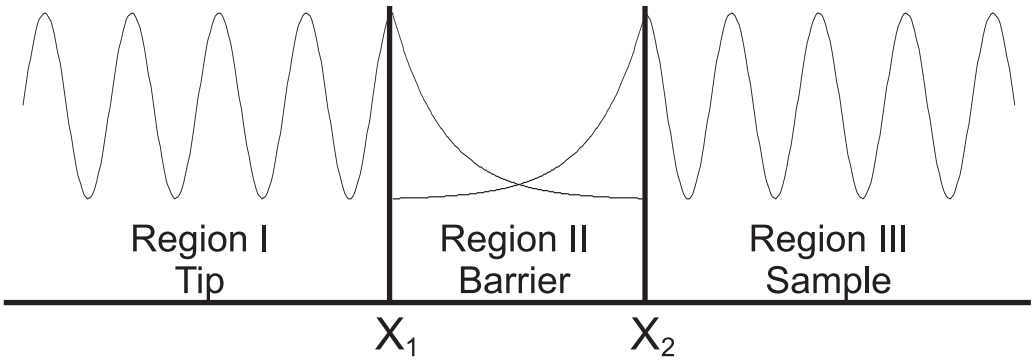

Figure 2.4: The two wave functions from the metals decay into the barrier.

tially decay in the vacuum barrier. This is illustrated in Fig.2.4. The eigenstates of tip and sample are:

$$H_S\psi = E_S\psi \tag{2.17}$$
$$H_T\phi_k = E_{T,k}\phi \tag{2.18}$$

Bardeen divided the problem into three different areas: the tip (area I), the barrier (area II) and the sample (area III). The tip potential $V_T(r)$ is equal $V(r)$ in area I and II and zero in area III. While the sample potential $V_S(r)$ equals $V(r)$ in area II and III, $V_S(r)$ is zero in area I:

$$H_S\psi = -\frac{\hbar^2}{2m}\Delta\psi(r) + V_S(r)\psi(r) \tag{2.19}$$
$$H_T\psi = -\frac{\hbar^2}{2m}\Delta\psi(r) + V_T(r)\psi(r) \tag{2.20}$$

and

$$V_T(r) = \begin{cases} V(r) & r \leq X_2 \\ 0 & r > X_2 \end{cases} \tag{2.21}$$

$$V_S(r) = \begin{cases} V(r) & r \geq X_1 \\ 0 & r < X_1 \end{cases} \tag{2.22}$$

Tunneling can be considered as a weak perturbance. The time evolution of the sample state ψ is close to $\exp^{-itE_S/\hbar}\psi$, which describes the case of the tip infinitely far away from the sample. Therefore, the tunneling can be approximated by the coefficients $a_k(t)$:

$$\psi(t) = \exp^{-itE_S/\hbar}\psi + \sum_k a_k(t)\phi_k \tag{2.23}$$

To calculate the coefficients $a_k(t)$ 2.23 is used together with the Schrödinger equation 2.24

$$-i\hbar\frac{\partial}{\partial t}\psi(\vec{r},t) = H\psi(\vec{r},t) \tag{2.24}$$

which is multiplied by $\langle\phi_j|$

$$-i\hbar\frac{d}{dt}a_j(t) = \exp^{-itE_S/\hbar}\langle\phi_j|H - H_S|\psi\rangle + E_{T,j}a_j(t) + \sum_k a_k(t)\langle\phi_j|H - H_T|\phi_k\rangle \tag{2.25}$$

Based on assumption 4 all coefficients $a_k(t)$ stay small (~ 0) and $a_j(t)$ should sufficiently solve the differential equation for $a_j(0)$=0

$$|a_j(t)|^2 = \frac{4sin^2(t(E_{T,j} - E_S)/2\hbar)}{(E_{T,j} - E_S)^2}|\langle\phi_j|H - H_S|\psi\rangle|^2 \tag{2.26}$$

Equation 2.23 is used to calculate the transition probability $|\langle\phi_j|\psi(t)\rangle|^2$

$$\langle\phi_j|\psi(t)\rangle = a_j(t) + \langle\phi_j|\psi\rangle \exp^{-itE_S/\hbar} \tag{2.27}$$

As $\langle\phi_j|$ and $|\psi\rangle$ are nearly orthogonal the transition probability for one electron is $|a_j(t)|^2$. The rate at which an electron initially scatters from a sample state to a tip state is

$$\begin{aligned}\frac{d}{dt}\sum_k |a_k(t)|^2 = \frac{d}{dt}\sum_k \frac{4sin^2(t(E_{T,k} - E_S)/2\hbar)}{(E_{T,k} - E_S)^2}|\langle\phi_k|H - H_S|\psi\rangle|^2 \\ = 4\frac{d}{dt}\sum_k P_t(E_{T,k} - E_S)M^2(\phi_k, \psi)\end{aligned} \tag{2.28}$$

where

$$M^2(\phi, \psi) = |\langle\phi|H - H_S|\psi\rangle|^2 \tag{2.29}$$

$$P_t(x) = \frac{sin^2(tx/2\hbar)}{x^2} \tag{2.30}$$

The sum over the tip states can be simplified by Fermi's Golden Rule. Since $P_t(x)$ has its main contribution around $x = 0$, which is equivalent to $E_{T,k} \approx E_S$. The sum can be converted into an integral with respect to the energy in the range of $|E_{T,k} - E_S| < 2\hbar/t$. This means the transition rate is approximated by

$$\begin{aligned}\frac{d}{dt}\sum_k |a_j(t)|^2 \approx \frac{d}{dt}4[M^2(\psi)\rho_T(E_S)\int_{-\infty}^{+\infty} P_t(E)dE] = \\ \frac{d}{dt}4[M^2(\psi)\rho_T(E_S)\frac{\pi t}{2\hbar}]\end{aligned} \tag{2.31}$$

where $M^2(\psi) = \frac{1}{N_{E_S}}\sum_{k:|E_{T,k}-E_S|<2\hbar/t} M^2(\phi_k, \psi)$, N_{E_S} is the number of tip states in the interval $|E_{T,k} - E_S| < 2\hbar/t$ and $\rho_T(E)$ describes the local density of states of the tip.

The way Bardeen chose the potentials $V_T(r)$ and $V_S(r)$ the matrix elements for the sample state ψ_n can be approximated. The integral of H-H_T with respect to the tip area is zero:

$$
\begin{aligned}
0 &= \int_{Tip+Barrier} \psi_n(\vec{r})(H - H_T)\overline{\phi_j(\vec{r})}d\vec{r} \qquad (2.32)\\
&= \int_{Tip+Barrier} \psi_n(\vec{r})H\overline{\phi_j(\vec{r})}dr - E_{T,j}\int_{Tip+Barrier} \psi_n(\vec{r})\overline{\phi_j(\vec{r})}d\vec{r}\\
&= -\frac{\hbar^2}{2m}\int_{Tip+Barrier} \psi_n(\vec{r})\Delta\overline{\phi_j(\vec{r})}d\vec{r} + \int_{Tip+Barrier} \psi_n(\vec{r})V(\vec{r})\overline{\phi_j(\vec{r})}d\vec{r}\\
&\quad -E_{T,j}\int_{Tip+Barrier} \psi_n(\vec{r})\overline{\phi_j(\vec{r})}d\vec{r}
\end{aligned}
$$

The integral of the matrix elements $M = \langle\phi_j|H - H_S|\psi\rangle$ is zero on the sample side, so that the integration area is reduced to the area of the tip and the barrier:

$$
\begin{aligned}
&\langle\phi_j|H - H_S|\psi_n\rangle =\\
&-\frac{\hbar^2}{2m}\int_{Tip+Barrier} \overline{\phi_j(\vec{r})}\Delta\psi_n(\vec{r})d\vec{r} + \int_{Tip+Barrier} \overline{\phi_j(\vec{r})}V(r)\psi_n(\vec{r})d\vec{r} \qquad (2.33)\\
&\quad -E_{S,n}\int_{Tip+Barrier} \overline{\phi_j(\vec{r})}\psi_n(\vec{r})d\vec{r}
\end{aligned}
$$

Subtracting equation 2.32 results in

$$
\begin{aligned}
&\langle\phi_j|H - H_S|\psi_n\rangle =\\
&\int_{Tip+Barrier} \overline{\phi_j(\vec{r})}(-\frac{\hbar^2}{2m}\Delta\psi_n(\vec{r}) - E_{S,n}\psi_n(\vec{r}))d\vec{r} \qquad (2.34)\\
&-\int_{Tip+Barrier} \psi_n(\vec{r})(-\frac{\hbar^2}{2m}\Delta\overline{\phi_j(\vec{r})} - E_{T,j}\overline{\phi_j(\vec{r})})d\vec{r}
\end{aligned}
$$

As $E_{T,j} \approx E_{S,n}$ equation 2.34 simplifies to

$$
\begin{aligned}
&\langle\phi_j|H - H_S|\psi_n\rangle \approx \qquad (2.35)\\
&-\frac{\hbar^2}{2m}\int_{Tip+Barrier} (\overline{\phi_j(\vec{r})}\Delta\psi_n(\vec{r}) - \psi_n(\vec{r})\Delta\overline{\phi_j(\vec{r})})d\vec{r},
\end{aligned}
$$

which reduces to a surface integral after applying the Gauss's theorem.

$$
\begin{aligned}
&\langle\phi_j|H - H_S|\psi_n\rangle =\\
&-\frac{\hbar^2}{2m}\int_{Tip+Barrier} \nabla(\overline{\phi_j(\vec{r})}\nabla\psi_n(\vec{r}) - \psi_n(\vec{r})\nabla\overline{\phi_j(\vec{r})})d\vec{r} \approx \qquad (2.36)\\
&\quad -\frac{\hbar^2}{2m}\int_{Barrier} (\overline{\psi_n(\vec{r})}\nabla\phi_j(\vec{r}) - \phi_j(\vec{r})\nabla\overline{\psi_n(\vec{r})})d\vec{n}
\end{aligned}
$$

Instead of integrating over the whole tip and barrier region, solving the surface integral of the barrier is enough.

2.4 Tersoff Hamann Approach

In the previous section the Bardeen approach was discussed. Tersoff and Hamann combined his Ansatz with a s-wave like tip state [39]. Thereby, the tip is modeled by a radial symmetric wavefunction. To calculate the current all the electrons are summed up which tunnel from the tip to the sample and vice versa. The electrons, which are fermions, must tunnel from an occupied tip (sample) state into an unoccupied sample (tip) state. Combining the Fermi-Dirac function f(E), which gives the average number of particles with energy E, with the transition rate 2.31 from a tip state ϕ_j to a sample state ψ_n, results in the tunneling current:

$$I = \frac{2\pi e}{\hbar} \sum_n [f(E_n)(1 - f(E_n + eU)) - (1 - f(E_n))f(E_n + eU)]|M(\psi_n)|^2 \rho_{tip}(E_n) \quad (2.37)$$

U is the bias voltage applied to the sample. In the limit of low temperature the Fermi-Dirac functions behaves like a step-function, which is 1 for $E_n \leq E_F$ and 0 for $E_n > E_F$. E_F is the Fermi energy of the system. The sign of the bias voltage U defines the sign of the current. In case of a positive voltage the current is:

$$I = \frac{2\pi e}{\hbar} \sum_{n:E_F - E_n < eU} |M(\psi_n)|^2 \rho_{tip}(E_n) \quad (2.38)$$

To model the tip states the Tersoff-Hamman Ansatz assumes a spherically symmetric shape and approximates the tip states by:

$$\phi_j(r) \approx A_j \exp^{-k_j r} / r, \quad (2.39)$$

which satisfies the Schrödinger equation in vacuum for $k_j = \sqrt{2mE_j}/\hbar$:

$$-\frac{\hbar}{2m}\phi_j = E_j \phi_j \quad (2.40)$$

ϕ_j facilitates the calculation of the matrix elements $M_{j,n}$, as J. Chen showed first [40]

$$-\frac{\hbar^2}{2m}\Delta\phi_j(\vec{r}) - E_j(\vec{r})\phi_j = -\frac{\hbar^2}{2m} 4\pi\delta(\vec{r}) \quad (2.41)$$

The location of the tip is $\vec{r} = \vec{0}$. The matrix elements are

$$\begin{aligned}\langle\phi_j|H-H_S|\psi_n\rangle \approx -\overline{A_j}\int_{Tip}\psi_n(-\frac{\hbar^2}{2m}\Delta\phi_j(\vec{r})-E_j\phi_j(\vec{r}))d\vec{r}= \\ -\overline{A_j}\int_T\psi_n(\vec{r})\frac{\hbar^2}{2m}4\pi\delta(\vec{r})d\vec{r}= \\ -\frac{\hbar^2}{m}2\pi\overline{A_j}\psi_n(0)\end{aligned} \tag{2.42}$$

Finally, the tunneling current is calculated by the equation 2.38:

$$\begin{aligned}I=\frac{2\pi e}{\hbar}(\frac{\hbar^2}{m}2\pi A)^2\sum_{n:E_F-E_n<eU}|\psi_n(\vec{0})|^2\rho_{tip}(E_n)= \\ (E_T-E_S)\frac{eh^3}{m^2}A^2\rho_{tip}(E_F)\rho_{sam}(E_F)\end{aligned} \tag{2.43}$$

The tunneling current is proportional to the LDOS of the sample and tip states. Regardless of the demonstrative correlation many approximations have been used to achieve it. This equation is only valid for a small bias and a low temperature. This approximation does not apply for large bias voltages necessary for STS [41] which will be discussed in the following section. Another drawback is the spherical tip structure in the Tersoff Hamann theory. Atomic resolution cannot be explained by a spherical tip, which has been shown by Chen [40]. The Tersoff-Hamman approach adequately explains the contours of the superstructures with a large periodicity, e.g., Au(110) with periodicities of 8.15 and 12.23 Å [42]. For a calculated STM image of a metal surface with a fundamental periodicity of 2 Å atomic resolution is achieved only for a tip-sample distance which corresponds to the mechanical contact. Calculated STM images with a realistic tip-sample distance show corrugation amplitudes which are too small to be detected experimentally [42]. Chen proposes a d_z-like state which predominantly contributes to the tunneling current [42].

2.5 Scanning Tunneling Spectroscopy

STS is a spectroscopic technique of STM and sensitive to the electronic states of the sample. In the constant-current mode the bias voltage and the current are maintained while taking an STM image. Only the position of the tip is changed to scan the surface. In STS it is vice versa. The feedback loop is open and the lateral position of the tip as well as the tip sample distance are kept fixed while recording a spectrum. The dependence of the current on the bias voltage, which is the free parameter, is studied in a STS spectrum. The last equation in the previous section 2.43 shows the proportionality of the current to the LDOS of tip and sample. Assuming that the tip states are constant the current is proportional to the LDOS of the sample. However, this assumption is only valid for low temperatures, small bias voltages close to the Fermi energy and a metallic tip with a flat LDOS [41]. To measure the electronic structure of, e.g., a molecular state, this relation is

no longer valid. In STS the derivative of the current is used to be sensitive to the LDOS of the surface or molecule. To extract the derivative from the current, the bias voltage is modulated by a small sinusoidal signal (typically by 10-20 mV) and the respective current signal is extracted by the lock-in amplifier. The Taylor series of the tunneling current with a modulated bias $U_0 + U_m \sin(\omega t)$ is

$$I(U_0 + U_m sin(\omega t)) = I(U_0) + \frac{dI}{dU}(U_0) U_m sin(\omega t) + \frac{1}{2}\frac{d^2I}{dU^2}(U_0) U_m^2 sin^2(\omega t) + ... \quad (2.44)$$

In the case of STS the lock-in amplifier obtains the signal with a $\sin(\omega t)$ shape, thus the first derivative. For a better physical understanding of the meaning of the first derivative of the current, the derivative is calculated by equation 2.38. In this case the sum can be written as an integral where the average value of $\mathrm{M}(\psi_n)$ replaces the matrix elements $\mathrm{M}(E)$ for all ψ_n with energy E. No approximation for the tip has been used so far.

$$I = \frac{4\pi e}{\hbar} \int_0^{eV} \rho_S(E_F + E) \rho_T(E_F + E - eV) |M(E_F + E)|^2 dE \quad (2.45)$$

This results in

$$\begin{aligned} \frac{dI}{dE}(V) &= \frac{2\pi e}{\hbar} \rho_S(E_F + eV) \rho_T(E_F) |M(E_F)|^2 \\ &+ \frac{2\pi e}{\hbar} \int_0^{eV} \rho_S(E_F + E) \frac{d\rho_T(E_F + E - eV)}{dV} |M(E_F + E)|^2 dE \\ &+ \frac{2\pi e}{\hbar} \int_0^{eV} \rho_S(E_F + E) \rho_T(E_F + E - eV) \frac{d|M(E_F + E)|^2}{dV} dE \end{aligned} \quad (2.46)$$

Assuming that the change of the tip's LDOS ρ_T and of the transfer matrix elements $\mathrm{M}(E)$ is small both integrals vanish:

$$\frac{dI}{dV}(V) \approx \frac{2\pi e}{\hbar} \rho_S(E_F + eV) \rho_T(E_F) |M(E_F)|^2 dE \quad (2.47)$$

The signal related to the electronic states of the tip or of the sample/molecule cannot be distinguished in STS. The electronic states of the molecule are observed but also the electronic states of the tip. Therefore, to probe only the LDOS of a surface or of a molecule a metallic STM tip is required with a constant LDOS in the energy range of interest. It is essential for spectroscopic experiments to confirm the metallic state of the tip as preparation for the actual experiments, e.g., by comparing the shape of a surface state in the STS spectrum to the literature. This check can prove a constant distribution of $\rho_T(E)$ and should be done before and after each measurement to guarantee a stable tip. For this thesis STS has only been performed on Au(111), which has a surface state at -0.52 eV [21]. The results of M.F. Crommie and co-workers [21] on the surface state of Au(111) are shown in Fig. 2.5.

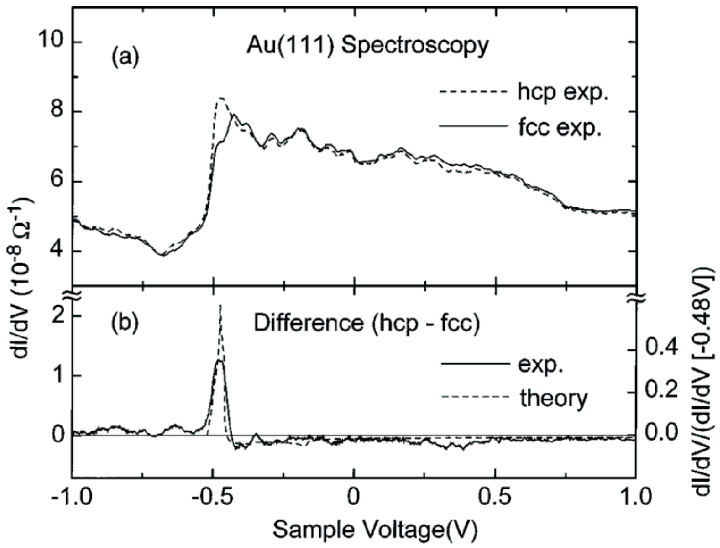

Figure 2.5: **a**, $\mathrm{d}I/\mathrm{d}V$ spectra taken with the tip positioned over the fcc and the hcp region of the herringbone reconstruction. **b**, Difference between the two spectra in **a**. Reprinted figure with permission from [21]. Copyright 2013 by the American Physical Society.

So far only spectroscopy with a fixed tip position was discussed. A related technique is $\mathrm{d}I/\mathrm{d}V$ mapping. Therefore, a constant-current image and simultaneously the $\mathrm{d}I/\mathrm{d}V$ signal is recorded. Similar to a $\mathrm{d}I/\mathrm{d}V$ spectrum the bias voltage is modulated by a sinusoidal signal with a small amplitude, while the lock-in amplifier extracts the first derivative of the current. If the frequency of the modulation signal is lower than the cut-off frequency the feedback loop adjusts the z-height to keep the current constant. Therefore, the modulation signal must be higher than the cut-off frequency of the feedback loop to exclude an interference with the z-signal. In a $\mathrm{d}I/\mathrm{d}V$ spectrum the bias is ramped through a certain energy window. In case of a $\mathrm{d}I/\mathrm{d}V$ map the constant tunneling voltage, which is modulated with the sinusoidal signal, is maintained during a $\mathrm{d}I/\mathrm{d}V$ map. Therefore, the LDOS at this energy is mapped.

2.6 Vibrations

So far only elastic scattering was discussed. The first derivative of the current is proportional to the LDOS. A peak, which is observed in the $\mathrm{d}I/\mathrm{d}V$ signal (so in the LDOS), creates a step in the current. For vibrational spectroscopy the lock-in amplifier extracts the second derivative of the current, which is modulated by $\sin^2(\omega t)$. $\sin^2(\omega t)$ is proportional to $\sin(2\ \omega t)$, hence the lock-in is sensitive to the double modulation frequency.

In contrast to optical methods, in tunneling spectroscopy there are no selection rules for the detection of vibrational states [44]. Inelastic scattering occurs because of the interaction of the electron with the molecular dipoles, which creates an electronic or vibrational excitation $h\nu$. The electron loses part of its energy. If the energy of the electrons, thus the applied bias, is too small the inelastic channel is closed. If the electron energy is larger than $h\nu$

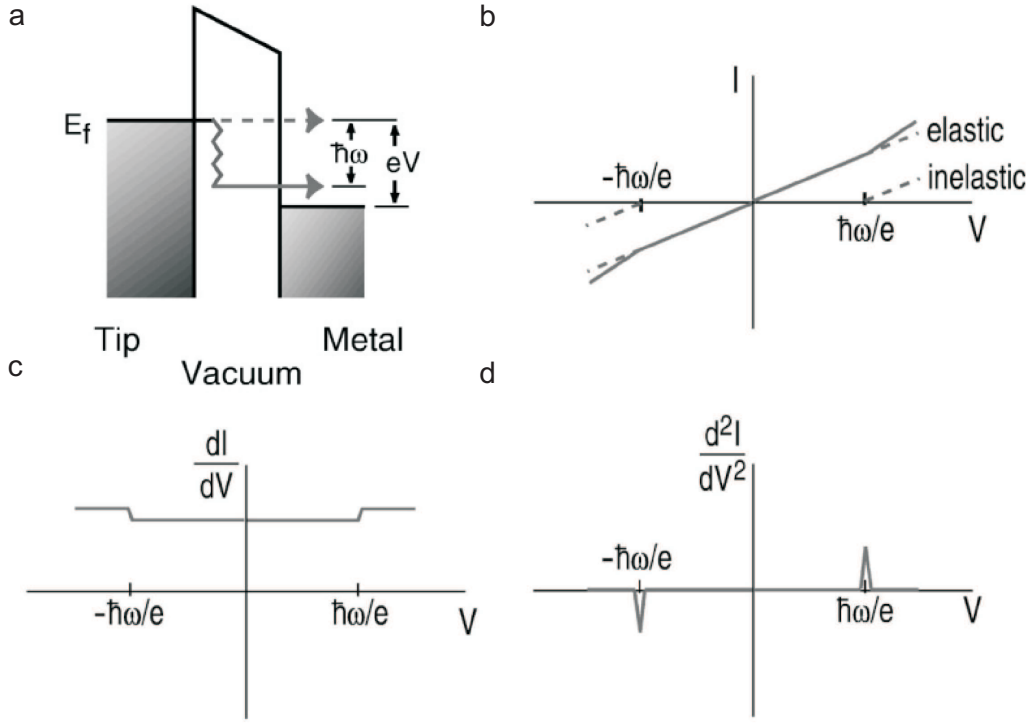

Figure 2.6: **a**, Schematic representation of inelastic tunneling spectroscopy. **b**, Change in tunneling current **c**, $\mathrm{d}I/\mathrm{d}V$ and **d**, $\mathrm{d}^2I/\mathrm{d}V^2$ signal because of an inelastic excitation. Reprinted with permission from [43]. Copyright 2013, AIP Publishing LLC.

an additional transport channel opens and the slope of the current increases. This change in the slope is equal to a step in the $\mathrm{d}I/\mathrm{d}V$ signal and a peak in the $\mathrm{d}^2I/\mathrm{d}V^2$ signal (see Fig. 2.6).

W. Ho reported a famous example of vibrational spectroscopy [32]: Three single molecules, C_2H_2, C_2D_2 and C_2HD, were identified by their vibrational peaks. The energy of the C-H stretch lies at higher energies than the C-D stretch. Vibrational spectroscopy gives a chemical sensitivity to STM. It is important to note that in conventional STM imaging the three species look the same.

2.7 Manipulation

As mentioned in the introduction, STM is about more than only imaging surfaces, atoms or molecules. Most of the atomic and molecular motion is frozen when operating the STM at a low temperature. To induce some movement an external trigger is necessary: the STM tip. The interaction between tip and atom (or molecule) is used to cause a controlled motion of the atom. Decreasing the gap between tip and surface increases the strength of the interaction. Depending on the balance between attractive or repulsive forces the manipulation is called pulling or pushing, respectively. The difference between these two types of manipulations becomes visible in the tunneling current [45]. During the lateral

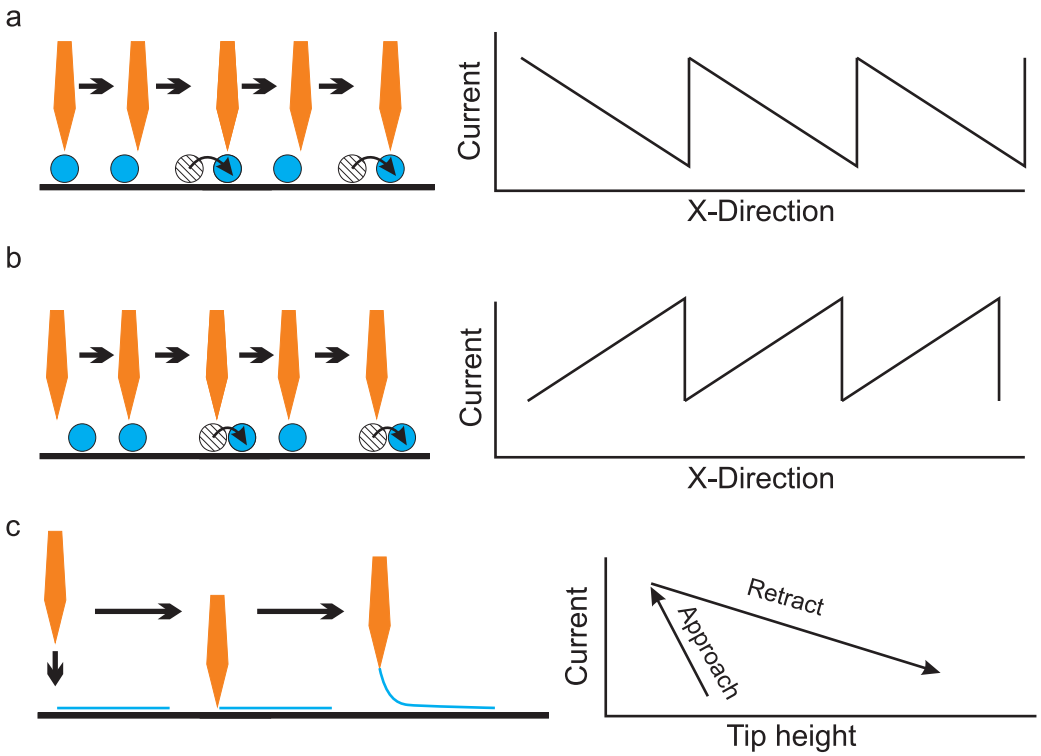

Figure 2.7: Schematic representation of lateral constant-height manipulation: **a**, pulling and **b**, pushing an atom. **c**, Schematic representation of vertical pulling manipulation.

manipulation the tip height is kept constant. In case of pulling, the sawtooth pattern begins at the center of the atom. Moving the tip away in x-direction leads to a continuous decrease in the tunneling current. As soon as the attractive forces between tip and atom are strong enough the atom hops in x-direction below the tip, displayed as a jump in the current (see Fig. 2.7a). The repulsive forces act in the opposite way: The tip is moved in x-direction to the center of the atom while the current increases as the tip approximates the center of the atom. At the same time the repulsive forces rise and a sudden drop in the current is detected. The atom jumps away from the tip to the next adsorption side (Fig. 2.7b).

However, instead of changing the lateral tip position along the surface, manipulation is also possible perpendicular to the surface. This type of manipulation is called vertical manipulation. The most common vertical manipulation is "tip sharpening" (at least on noble metals), which is nothing else than approaching the tip in a controlled manner to the surface until they are in contact. Depending on the strength of the "tip-sharpening" (the bias voltage and the z-displacement) small to large changes of the tip shape are induced.

Doing a more gentle vertical manipulation allows a controlled modification of the tip structure. Instead of indenting it into the bare metal surface, the tip is approached towards a CO-molecule. At a certain point the CO molecule is lifted from the surface and attached to the tip [28]. The CO molecule at the tip is now the last molecule the electrons pass when a positive bias is applied to the sample. The tunneling occurs through the degenerated π_x and π_y orbitals of the CO molecule which results in the increase of the p-wave contributions while the resolution is simultaneously improved in a controlled manner [28].

These types of experiments demonstrate how the chemical nature of the tip apex can be controlled.

This idea can also be adapted to larger molecules, even to molecular chains, if the bond between tip and molecule is strong enough. Retracting the tip peels the molecular chain from the surface while at the same time the current is recorded [16]. Tip and surface, thereby, act as electrodes. A change in the slope during approach and retraction is an indication that a bond is successfully established between tip and molecule. This is illustrated in Fig. 2.7c. Length-dependent conductance measurements of a single molecular wire can be performed because the metal surface usually conducts better than the molecule: The electrons pass only through the lifted part of the molecule and escape into the substrate as soon as possible [16].

Chapter 3

Background

The experimental part of this thesis can be divided into the growth and characterization of molecular wires. The successful fabrication of a molecular wire is a prerequisite for further experiments. For the characterization of a molecular chain by low temperature STM its conductance as well as the electronic and vibrational states of the molecule were studied. The deposition of the molecules onto a substrate in ultra-high vacuum (UHV) is required for a preparation without contaminants which would perturb the single molecule measurements. The evaporation temperature typically increases with the molecular weight. For large molecules the deposition temperature might be too high to use conventional evaporation techniques so that a defect-free preparation cannot be guaranteed. High evaporation temperatures may lead to the decomposition of the molecule. Instead of depositing the complete wire, on-surface polymerization was used, which is described in section 3.4. The advantage of this procedure is that the weight of the molecules shrinks as part of the synthesis is performed on the surface. On-surface polymerization is based on molecular building blocks which define the final structure of the chain. After activation, i.e. dehalogenation, the molecular building blocks become reactive and link covalently with each other on the surface. Thereby, the molecular weight during the evaporation does no longer depend on the length of the desired molecular wire. Summing up, on-surface polymerization enables chain fabrication on the surface and smaller precursor molecules are required and deposited.

For the first part of this thesis the STM was used mainly for imaging the different stages of the deposition experiments to grow a molecular wire. In the second part the spectroscopic capabilities and manipulation capabilities of the STM were exploited in order to characterize the molecules. The determination of its electronic properties is essential for the insight into the conductance of a molecular wire. Depending on the electron energy a different conductance of the molecular wire is expected since different electronic states participate in the electron transport. In addition, the delocalization of the molecular orbitals, such as the highest occupied molecular orbital (HOMO) and the lowest unoccupied molecular orbital (LUMO), has to be considered which may lead to an improved electron transport within a molecule. Tunneling occurs for electrons with energies in the HOMO-LUMO gap E_G, and pseudo-ballistic transport might become important for electron energies which match the molecular orbitals depending on the electron delocalization within the molecule. Therefore, for understanding the conduction mechanism, the electronic structure has to be studied. Despite of the electronic properties of the molecule, the

length of the molecular wire is essential for the success of the experiment. An impressive example has been performed by Wang et al. [46] who accomplished the growth of a single wall carbon nanotube (SWNT) up to 18.5 cm with a diameter between 1 nm and 2.7 nm.

3.1 Molecular Wires

According to Ohm's law, the current passing through a macroscopic metallic wire is proportional to the applied voltage. The constant of proportionality is the conductance

$$G = \sigma \frac{S}{d} \tag{3.1}$$

where σ is the conductivity of the wire, d denotes its length and S is its cross section. This rule is no longer valid for nanodevices where three length scales of the molecular system become important [47]:

- the length of the molecule,
- the phase coherence length and
- the mean free path of the electrons.

The phase coherence length describes the average distance that an electron can travel within the molecule up to which the electron wave function is conserved. Inelastic scattering events with other electrons, phonons or magnetic impurities cause the dephasing of the electron wave function. If the phase coherence length is larger than the size of the molecule the phase of the electron wave function is preserved during the transport through the molecule. In other words, inelastic scattering does not occur while the electron passes through the molecule. The mean free path measures the average distance between two elastic collisions. If the mean free path is much shorter than the molecule the transport can be considered as diffusive. In the other extreme case the length of the wire is shorter than the mean free path with the result that ballistic transport occurs. Scattering is limited to the boundaries of the molecular wire and the momentum of the electron can be approximated as constant [47]. The remaining resistance of a ballistic wire results from the interface between the electrodes and the wire [47].

In the regime of coherent transport through a molecular wire four conduction mechanisms are important (see table 3.1). The voltage dependence and the temperature dependence of the current give an indication which mechanism for charge transport dominates the conductance [48]. If the current is insensitive to the temperature the conduction mechanism is direct tunneling or Fowler-Nordheim tunneling. In the low voltage regime, where the potential barrier is higher than the electron energy, direct tunneling describes the electron transport. In the high voltage regime Fowler-Nordheim tunneling occurs. The applied voltage, thus the electron energy, is much larger than the average barrier height, and the Fermi level of one electrode is shifted below the conduction band of the other electrode. No electrons can tunnel through the barrier from this electrode as there are no empty states available at the other side. On the other hand, electrons from the other electrode

Conduction mechanism	Characteristic behavior	Temperature dependence	Voltage dependence
Direct tunneling	$J \sim V exp(-\frac{2d}{\hbar}\sqrt{2m\Phi})$	none	$J \sim V$
Fowler-Nordheim	$J \sim V^2 exp(-\frac{4d\sqrt{2m}\Phi^{3/2})}{3q\hbar V})$	none	$ln(\frac{J}{V^2}) \sim \frac{1}{V})$
Thermionic emission	$J \sim T^2 exp(-\frac{\Phi - q\sqrt{qV/4\pi\epsilon d}}{kT})$	$ln(\frac{J}{T^2}) \sim \frac{1}{T}$	$ln(J) \sim V^{1/2}$
Hopping conduction	$J \sim V exp(-\frac{\Phi}{kT})$	$ln(\frac{J}{V}) \sim \frac{1}{T}$	$J \sim V$

Table 3.1: Relationship of the current density J, temperature T and voltage V. Φ is the barrier height. d is the barrier length. From reference [48].

can tunnel into any state because at this energy none of the states are occupied [49]. This is similar to field emission. The difference between direct tunneling and Fowler-Nordheim tunneling becomes obvious in their voltage dependence (see table 3.1) [47].

The two other conduction mechanisms, hopping conduction and thermionic emission, depend on the temperature. The electrons for the hopping conduction are strongly localized inside the molecular wire. The probability for hopping between two points increases exponentially as a function of the temperature. Therefore, hopping conductance can be considered as a thermally activated process. Different from tunneling, the current does not decay exponentially with the length of the molecular wire but linearly with its length [47]. Thermionic emission is strongly temperature-dependent and occurs when the electrons are excited over the potential barrier. The temperature dependence becomes obvious when the potential barrier is relatively small [47]. At low bias voltages and at a low temperature direct tunneling dominates the charge transport through a molecular wire. Characteristic for tunneling is the exponential decay of the current with the molecular length d.

$$I = I_0 e^{-\beta d} \tag{3.2}$$

The inverse decay length β can be used as a benchmark criterium to compare the conductance of different molecular chains. β depends on the position of the HOMO, the LUMO, the HOMO-LUMO gap of the molecule, the energy of the tunneling electrons as well as their effective mass m. For organic molecules β is in the range of 0.2 [50] to 0.9 $Å^{-1}$ [51, 48]. For comparison, β of a vacuum junction is ~2.5 $Å^{-1}$ in an STM setup [52]. The conductance of alkane chains does not depend on the temperature, and their current-voltage curves exhibit a characteristic shape. Together with the exponential decay of the current as a function of the molecular length this leads to the conclusion that direct tunneling is the transport mechanism. The inverse decay length β of an alkane chain is ~0.7-0.9 $Å^{-1}$ [51, 48], which corresponds to its large HOMO-LUMO gap E_g of ~9 eV [18].

Reducing E_g also improves the conductance. For instance, a higher current is measured for oligo-thiophene with four thiophene rings than for oligo-thiophene with three rings. Thus, a higher current is measured for the longer chain, which is equivalent to a larger effective transport path of the electrons. This is surprising, in particular, if tunneling is the transport mechanism and the current decays exponentially with the length of the molecular chain. By adding a thiophene ring to the molecular wire the HOMO moves closer to the Fermi energy which improves the conductance of the molecule despite its slightly increased length [53]. Similar results are observed for fully conjugated porphyrin chains. Elongation

of a porphyrin chain expands the π-electronic system and shifts the position of the HOMO to higher energies [17]. However, apart from a decrease of β, a transition from tunneling to hopping has been reported when the length of the molecular chain is extended [54, 55, 56]. The conductance improves in both cases, regarding the shift of the HOMO as well as the transition of the charge transport mechanism from tunneling to hopping. The temperature dependence of the current indicates the different causes for the higher conductance.

For conjugated oligophenyleneimine (OPI) and oligonaphtalenefluoreneimine (ONI) wires the transport mechanism changes with their length from direct tunneling to hopping [55, 56]. For up to four units long OPI molecules direct tunneling dominates the charge transport: the current is temperature-independent and decays exponentially with the molecular length d. From five units long wires onwards the current increases with the temperature, and the length dependence of the current for direct tunneling is much weaker than expected. Thermally activated hopping occurs through the long conjugated part of the OPI wire.

Not only the HOMO-LUMO gap changes the conductance, also the conjugation of a molecular wire has a large influence [57, 58]. This has been tested by synthesizing slightly different molecules that alter the twist angle Φ of the phenyl rings [57]. An increase of the twist angle to 88° results in a drop of the conductance from $\sim 10^{-3}$ G_0 to $\sim 10^{-5}$ G_0. A relation of $\cos^2(\Phi)$ is found between the twist angle and the conductance because the conjugation vanishes [57]. G_0 is the quantum of conductance.

The quantum of conductance describes the maximum conductance which can be reached via one transition channel with degenerated spins (the factor 2) [59]

$$G_0 = \frac{2e^2}{h} \tag{3.3}$$

e is the electron charge and h is Planck's constant. Rolf Landauer assumed that due to the phase coherence of direct tunneling inelastic scattering takes place only inside the electrodes [60]. Within the molecule no energy dissipation of the electron occurs and the transport through a molecular wire is approximated by elastic scattering. The conductance of a molecular wire can be related to the transmission and to the reflection probabilities. The maximum value of the conductance per transition channel is G_0. In case of a molecule with N channels, the total conductance is made up of the sum of all channels:

$$G = G_0 \sum_{n=0}^{N} T_n \tag{3.4}$$

T_n is the transmission probability of the nth channel. Experimentally, a step-like behavior was found in the conductance for metallic single atom contacts between two electrodes of the same material [61, 62, 63]. While the junction is elongated, atomic rearrangement occurs and the conductance decreases in multiple steps of the quantum conductance G_0. At bias voltages that match the energy of a molecular orbital resonant tunneling occurs. For a homonuclear diatomic molecule theory shows that the transmission behaves like a pure Landauer channel [64]. The transmission probability is unity for resonant tunneling which leads to a conductance of one G_0.

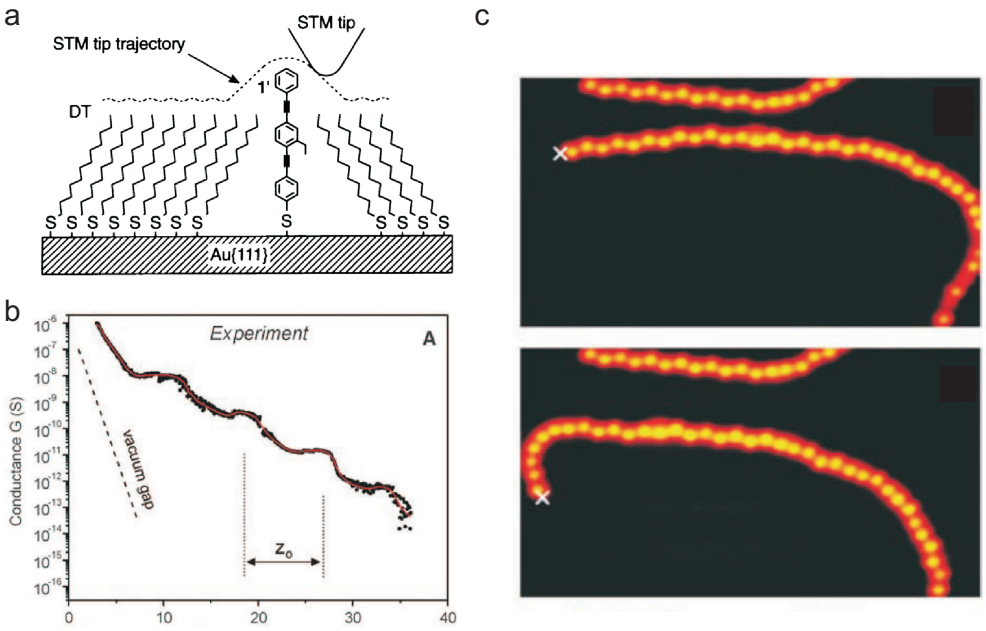

Figure 3.1: **a**, Measuring the current through DPEBT molecules by STM imaging. From [65]. Reprinted with permission from AAAS. **b**, Conductance curve of a polyfluorene wire pulled up by an STM tip. From [16]. Reprinted with permission from AAAS. **c**,**d**, 25.4x13.7 nm^2 STM images of a single and isolated DBTF chain **c** before and **d** after the pulling experiment. From [16]. Reprinted with permission from AAAS.

A central challenge in the field of molecular conductance is the means to measure the current flowing through a molecule. In the macroscopic world two electrodes are attached to the opposite sides of the wire, and the current is detected depending on the applied bias. Contacting a single molecule with a size of a few nm with two electrodes is challenging. First of all, moving the electrodes in Ångström precision cannot be taken for granted. In many experimental setups the surface is used as one of the two electrodes. The other electrode can be the tip of an STM but the bond between molecule and tip remains undefined. In several techniques discussed below the molecules are not even characterized before the conductance experiments. Therefore, the condition of the molecules in the junction is undefined and the measured current might correspond to an intact as well as to a defected molecule.

One of the first experiments on molecular conductance has been conducted 1996 by the group of P. Weiss [65]. They measured the conductance of a self-assembled monolayer (SAM) of n-dodecanethiol (DT) together with DPEBT. Due to the poor conductance of the DT molecules they were used to isolate the DPEBT molecules, which are bound through a sulfur atom to the surface. At a coverage of a full monolayer (ML) the DPEBT molecules align perpendicular to the surface. To study the conductance STM images of the surface were taken as shown in Fig. 3.1a. The apparent height difference measured by STM between the DPEBT molecules and the surrounding DT molecules is 7 Å. This is in good agreement with the calculated length of DPEBT, which is 21.3 Å in total and 7.3 Å higher than the length of the DT ML (if they grow perpendicular to the surface). A drawback of this method is that the molecules are not isolated and that there is no chemical bond between the STM tip and the molecule. By fixing the tip position on top

of the molecule and approaching it towards the molecule the transparency of a single C_{60} molecule was observed [66]. The C_{60} molecule was compressed by the tip but molecule and tip did not form a chemical bond.

A widespread technique to measure the conductance of single molecules is mechanically controllable break junction (MCBJ). Fig. 3.2a sketches the experimental setup, which consists of a lithographically etched wire, a bending beam and a piezo driven rod. The etched wire has a constriction with a width of ∼100 nm. The wire is mounted onto the bending beam and the piezo-driven rod together with two supports deform the beam in a controlled manner. Approaching the rod from below bends the beam, and the attached wire elongates until the size of the constriction reduces to a few atoms. Finally, the wire breaks into two electrodes. By mechanically controlling the distortion of the beam the distance between the two electrodes is varied. The gap between the two wires can be tuned in the sub Ångström regime with typical motion speeds of 10 nm/s to 10 μm/s [47]. There are several advantages which make MCBJ a popular technique. First of all, MCBJ is an easy setup without the necessity of UHV. This allows one to study the conductance of molecules in solution or in a high pressure regime. A huge quantity of data can be recorded by the automatic repetition of the formation and the controlled break of the junction. Using MCBJ the conductance of a really small wire, probably as small as a single benzene unit attached with two thiol endgroups to the electrodes, was studied by Reed et al. in 1997 [67]. The experimental setup is shown in Fig. 3.2c. The experiments were conducted at room temperature (RT) and the resistance was 22.2 MΩ, which is equivalent to a conductance of 0.0058 G_0.

The type of contact between molecule and electrodes has a large influence on the conductance. Often anchor groups are used to form a strong bond between the molecule and the electrodes, particularly in break junction experiments. In case of butyl chains terminated with amines (NH_2), dimethyl phosphines (PMe_2), and methyl sulfides (SMe) the measured inverse decay length β is 1.02±0.02 Å, 0.93±0.02 Å and 0.89±0.04 Å, respectively [68]. Due to the anchor groups the HOMO and LUMO align slightly different to the Fermi level of the electrodes, and a variation in the conductance is observed.

Tao et al. modified the MCBJ approach to the STM break junction approach [69]. The STM tip moves repeatedly into and out of contact with the substrate in solution containing the molecules of interest. Without molecules the previously discussed integer steps of G_0 in the conductance of metallic contacts are reproduced [61, 62, 63]. An example of the conductance of atom sized sodium contacts is shown in Fig. 3.2b. When adding molecules to the solution each approach of the STM tip forms a new junction between the tip and the molecules, this leads to a high statistic. However, there are also some major disadvantages of MCBJ. Amongst the most important is the lack of information about the junction formed between molecule and electrode as well as the inability to determine the amount of molecules inside the junction. Further, it is impossible to know if the molecules inside the junction are defect-free, twisted or if the conductance experiment itself causes damages inside the molecules. The conductance of an isolated single molecule can differ from that of a molecule in a SAM [70]. Whereas contacting one or many molecules in the SAM configuration with a top electrode is expected to scale linearly with the number of molecules in the junction [70, 71]. No coherent transport is expected as the molecules are connected through the electrodes where inelastic scattering occurs according to the assumptions by Landauer [60]. The conductance of a single and isolated molecule is thereby different from

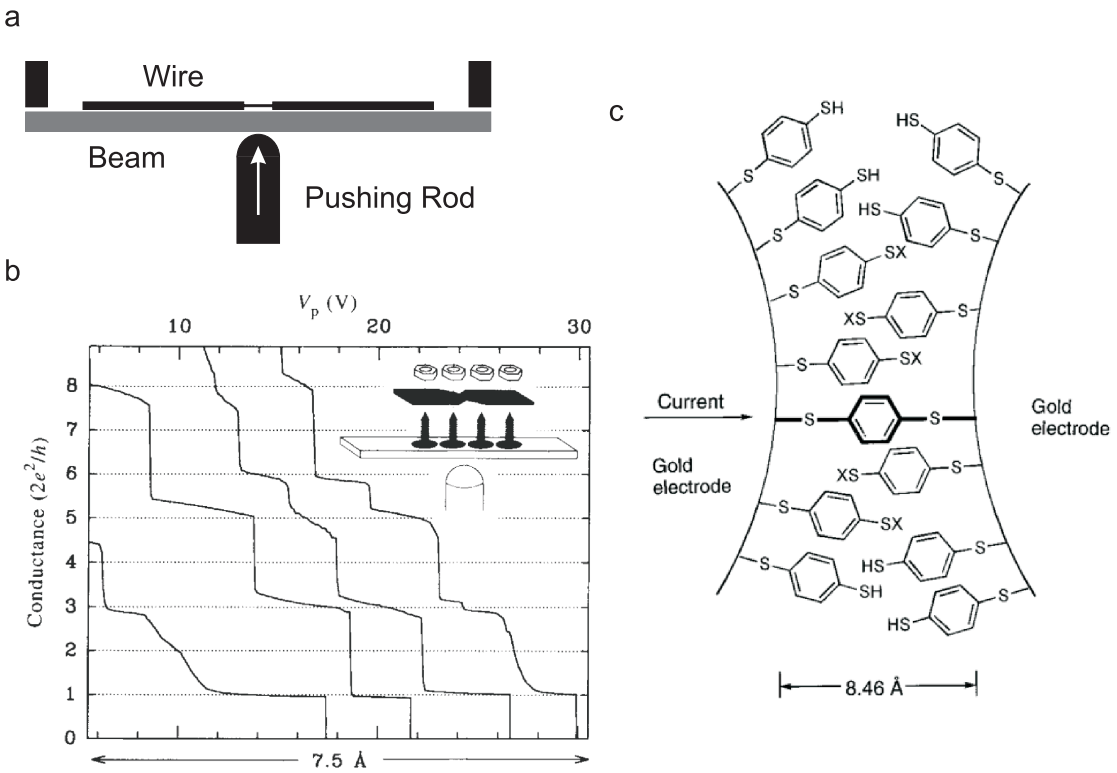

Figure 3.2: **a**, Experimental setup of a mechanically controllable break junction. **b**, Measured conductance of atom sized sodium contacts by a mechanically controllable break junction. Reprinted by permission from Macmillan Publishers Ltd: Nature [62], copyright 2013. **c**, Schematic representation of a benzene-1,4-dithialate SAM conductance measurement by a mechanically controllable break junction. From [67]. Reprinted with permission from AAAS.

the conductance of only one connected molecule inside the SAM [70]. If coherent transport occurs the characteristic conductance of a molecule with two parallel backbones is more than twice than the conductance with a single backbone [72].

A different approach is vertical manipulation, or pulling, with the STM tip at low temperatures [73, 16]. Low temperatures are necessary to freeze the motion of the molecules. With conventional STM the single molecule is imaged before and after the pulling experiment to characterize the molecular wire (see Fig. 3.1c). Approaching the tip to the terminus of the molecular wire end can cause the formation of a strong bond between tip apex and molecule. The bond can be strong enough to lift the molecular chain from the surface by retracting the tip. While the tip moves up, the current passing through the molecule is detected. The STM tip and the sample are the electrodes. This technique paves the way to continuous length-dependent conductance measurements of a single molecule. For instance a single chain of polyfluorene has been lifted from the Au(111) substrate. Exponential decay and characteristic oscillations of the length of a single fluorene have been observed in the current (Fig3.1b) [16]. Unlike the MCBJ or STM break junction approaches the number of molecules inside the junction is well defined. In such an experiment a single molecule contact is ensured and (depending on the coverage) interactions between neighboring molecules can be neglected. Before and after a pulling experiment the molecules

can be characterized.

3.2 Graphene

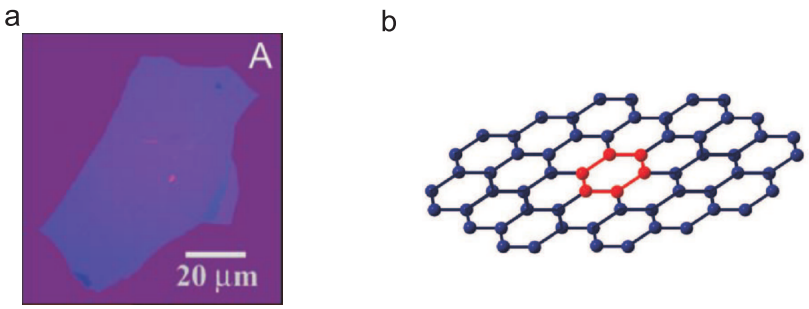

Figure 3.3: **a**, Single graphene flake on an oxidized silicon sample. From [74]. Reprinted with permission from AAAS. **b**, Sketch of the chemical structure of graphene. From [75]. This material is reproduced with permission of John Wiley & Sons, Inc.

Graphene, a single atomic plane of graphite, fascinates scientists worldwide [76, 77]. It consists of sp^2-hypridized carbon atoms which arrange in a honeycomb lattice (see Fig. 3.3b). Their nearest neighbor distance is ∼1.42 Å[10]. In 2004 single layers of graphene were fabricated by mechanical exfoliation with an adhesive tape [74, 78], and A.K. Geim and K.S. Novoselov have been rewarded for this discovery with the Nobel Prize in 2010. Nonetheless, the fabrication of high quality graphene is not straightforward. The highest quality of graphene is still obtained by cleaving but most of the cleaved flakes have a limited size and are 20 to 100 graphene layers thick, thus graphite. Single layers of graphene are difficult to detect [77]. Fig. 3.3a shows an oxidized Si wafer with a single graphene flake, which becomes visible in an optical microscope by a change in the color of the substrate due to an interference effect [78]. Industrial applications demand the fabrication of large graphene sheets of a guaranteed quality.

There are different approaches to produce graphene. One attempt to grow graphene is based on chemical vapour deposition (CVD) at UHV conditions. Metal substrates like Ir(111) [79], Ru(0001) [80, 81] or Ni(111) [82] are exposed to hydrocarbon, while heated at temperatures in the range of 600 to 1400 K. A drawback of these methods is the small size of the graphene flakes and the lack of thickness control. Not only graphene monolayers but also multilayers are produced [83]. The size of the graphene sheet can be increased by using a flexible copper foil as template. A huge graphene film of 30 inches, which is predominantly composed of monolayers, has been produced by CVD on such a copper foil (Fig 3.4) [84]. The copper foil is heated homogeneously to 730 K for 30 min while it is exposed to a gas mixture of CH_4 and H_2. After rapidly cooling the sample (10 K/s) a thermal release tape is attached to the copper foil. The copper foil is etched off and the graphene film can be transferred to any kind of surface. These sheets are used as transparent electrodes with a sheet resistance of ∼125 Ω/sheet [84].

Raman spectroscopy is a versatile and non-destructive method for the characterization of the graphene flake [85] as it enables, e.g., to distinguish a multilayer of graphene sheets (graphite) from a single graphene flake [86]. In Raman spectra, particularly, two features are intensive: the G mode at ∼1580 cm^{-1} and the 2D mode at ∼2700 cm^{-1} (Fig. 3.5a).

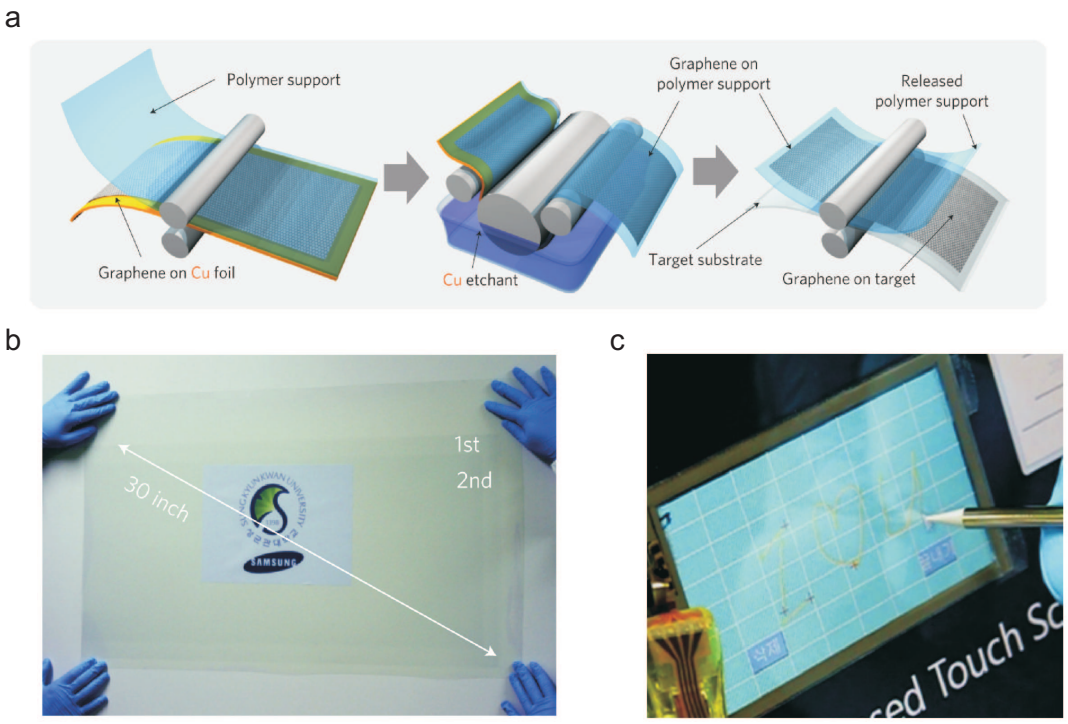

Figure 3.4: **a**, Sketched fabrication process of a graphene film. **b**, Ultra large graphene film transferred on a polyethylene terephthalate sheet. **c**, Graphene based touchscreen panel. Reprinted by permission from Macmillan Publishers Ltd: Nature Nanotechnology [84], copyright 2013.

Depending on the amount of layers of the graphene sample the peak of the 2D mode shifts to higher wavenumbers. For more than five layers of graphene the Raman spectrum is close to the one of bulk graphite (Fig. 3.5b). The D mode, which is located at 1350 cm^{-1}, belongs to the breathing vibration of the phenyl rings; it needs activation by defects and its intensity is a fingerprint for the quality of the sample [85]. Additionally, the D band can be used to analyze the edge structure of the graphene flake. Fig. 3.6a shows the armchair and the zigzag edge structure, which is discussed in more detail in the next section. D band scattering is forbidden for edges with a zigzag structure. Therefore, the D band can be used to distinguish zigzag edges from armchair edges in the graphene sample [85]. The G band related to the C-C stretching, helps to identify the doping level, the strain and even the bending of the graphene flake just to mention a few [85].

The interest in graphene is motivated scientifically and technologically. Due to the massless propagation of the electrons through the graphene flake they mimic relativistic particles and are described by the Dirac equation instead of the Schrödinger equation. The electrons lose their mass at the Dirac points, and their carrier mobility can be as high as 100,000 $cm^2V^{-1}s^{-1}$. The transmission coefficient of a relativistic particle tunneling through a potential barrier should become unity if the barrier increases to infinity. This behavior, the so called Klein paradox, has been proven through the magnetic field dependence of the conductance oscillations of a graphene heterostructure [87]. Moreover the appearance of the quantum Hall effect in Graphene does not require liquid helium temperature [88, 89]. This makes graphene an interesting material for easily probing many different effects.

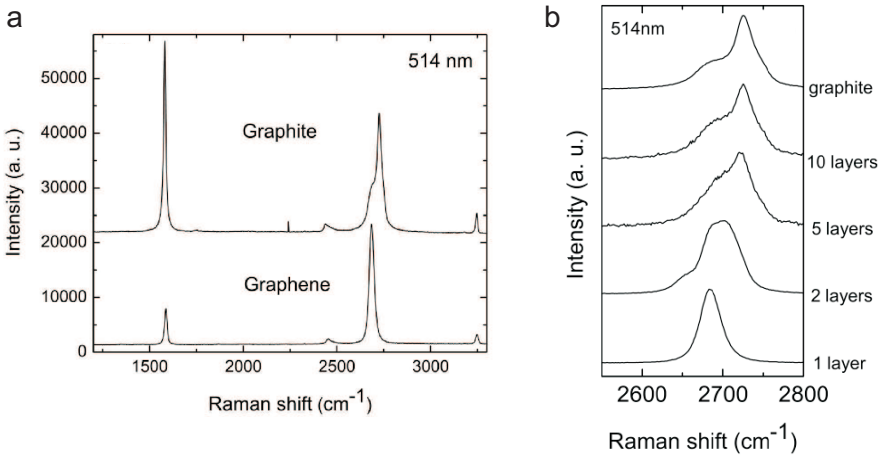

Figure 3.5: **a**, Comparison of Raman spectra of bulk graphite and graphene. Reprinted figure with permission from [86]. Copyright 2013 by the American Physical Society. **b**, Change in the Raman spectrum with the number of graphene layers. Reprinted figure with permission from [86]. Copyright 2013 by the American Physical Society.

Graphene flakes have a vanishing band gap at the Dirac points. So, graphene is neither a semiconductor nor a metal. The high carrier mobility makes it promising for the use as a molecular wire in future molecular electronics. However, to achieve high carrier mobilities high quality samples are essential, which are obtained through mechanical exfoliation [90]. However, the defect rate and the number of graphene layers up to now is difficult to control in CVD grown graphene samples. An initial application could be the use of a graphene sheet as a transparent electrode [90]. For industrial purposes it can replace transparent indium tin oxide electrodes which are used in touchscreens and solar cells [84, 91]. Recently a sensor built of graphene to detect single NO_2 and NH_3 molecules was demonstrated [92].

Another industrial application for graphene is the field effect transistor (FET). A FET consists of a source and a drain connected via a channel and a gate. It is unipolar and behaves like a voltage-controlled resistance. A widespread version of an FET is the Si metal-oxide-semiconductor field-effect transistor (MOSFET) [22]. The substrate is positively doped silicon with two highly negatively doped regions. Graphene-based FETs have been produced by several groups [93, 94, 95]. A CVD fabricated FET device with a 40 nm short channel reaches a cut-off frequency of 155 GHz, the frequency at which the current gain becomes unity [95]. This is still low compared to transistors based on semiconductors [96]. As graphene has a zero band gap the I_{On}/I_{Off} ratio is small [95]. A narrow stripe of graphene, a GNR ,has a finite band gap, which leads hopefully to larger I_{On}/I_{Off} ratios.

3.3 Graphene Nanoribbons

A GNR is a thin stripe cut out of a larger graphene flake (Fig. 3.6a). Due to the high carrier mobility of graphene GNRs are promising candidates for molecular wires in future nanoelectronics. An additional advantage of GNRs is the tuneability of their electronic properties. Apart from doping, the electronic structure of a GNR can be controlled by its width and its edge structure [10]. For example, reducing the width of a GNR increases the band gap (Fig. 3.6c) [11].

Depending on the edge structure two different types of GNRs exist: armchair GNRs and zigzag GNRs (Fig. 3.6a). Although the difference lies only in the shape of their edges, this difference has an enormous influence on the electronic properties of a GNR. In case of zigzag edges an edge state has been predicted theoretically [12] and recently observed experimentally with STM [97]. This state is localized at the zigzag edge of a GNR and appears in the LDOS as a sharp peak close to the Fermi energy. The highest valence band and the lowest conductance band degenerate at $k{=}\pi$. The increasing width of the zigzag GNR leads to two nearly flat bands with k between $\frac{2}{3}\pi$ and π (Fig 3.6b). This band structure is attributed to the edge state and does not exist for GNRs with armchair edges.

Both types of GNRs, armchair and zigzag, have a band gap which increases with the decrease of their width. Depending on the number m of carbon atoms perpendicular to the direction of the armchair GNR there are three sub-families of armchair GNR: $m = 3n$, $m = 3n+1$ or $m = 3n+2$ where n is an integer (Fig. 3.7). The size of the band gap varies with respect to the classification of the sub-family (Fig. 3.6d). The $m = 3n + 2$ family has the smallest band gap followed by the $m = 3n$ and the $m = 3n + 1$ armchair GNR (Fig. 3.6d) [98]. These sub-families exist only for the armchair GNRs but not for the zigzag GNRs and can be explained by Clar's theory [99]. The $m = 3m+2$ family has delocalized double bonds along the armchair edges (Fig. 3.7c and f) while the other two sub-families $m = 3n$ and $m = 3n+1$ have a benzoid (Fig. 3.7a and d) or a Kekule character (Fig. 3.7b and e), respectively. No periodic behavior with respect to the width was found for zigzag GNRs [99].

The edge structure is crucial for the electronic properties of a GNR. Studying the electronic properties or the conductance requires well defined edges to exclude disturbances caused by mixed zigzag and armchair edge structures or by defects. Guaranteeing smooth edges is difficult for most of the top-down approaches to produce GNRs, e.g., the STM based lithography [100]. This technique uses an STM tip to cut a graphene flake into pieces, whereby the tip moves at a speed of 2.0 nm/s and a bias voltage of 2.4 V is applied. By the predefined tip path the resulting structure made of graphene is determined. Etching is another technique to produce GNRs. An etch mask made of Si [101] or Al [13] nanowires protects part of the graphene flake. The shape and the width of the mask defines the structure after the etch process. The width of an etched GNR is approximately 20 nm [13, 101]. Subsequent narrowing to a width as small as ∼5 nm can be achieved by exposing the etched GNRs to a gas mixture of O_2 and NH_3/Ar [13]. Nevertheless, the edge roughness before the narrowing has been reported to be as large as ∼5 nm [13].

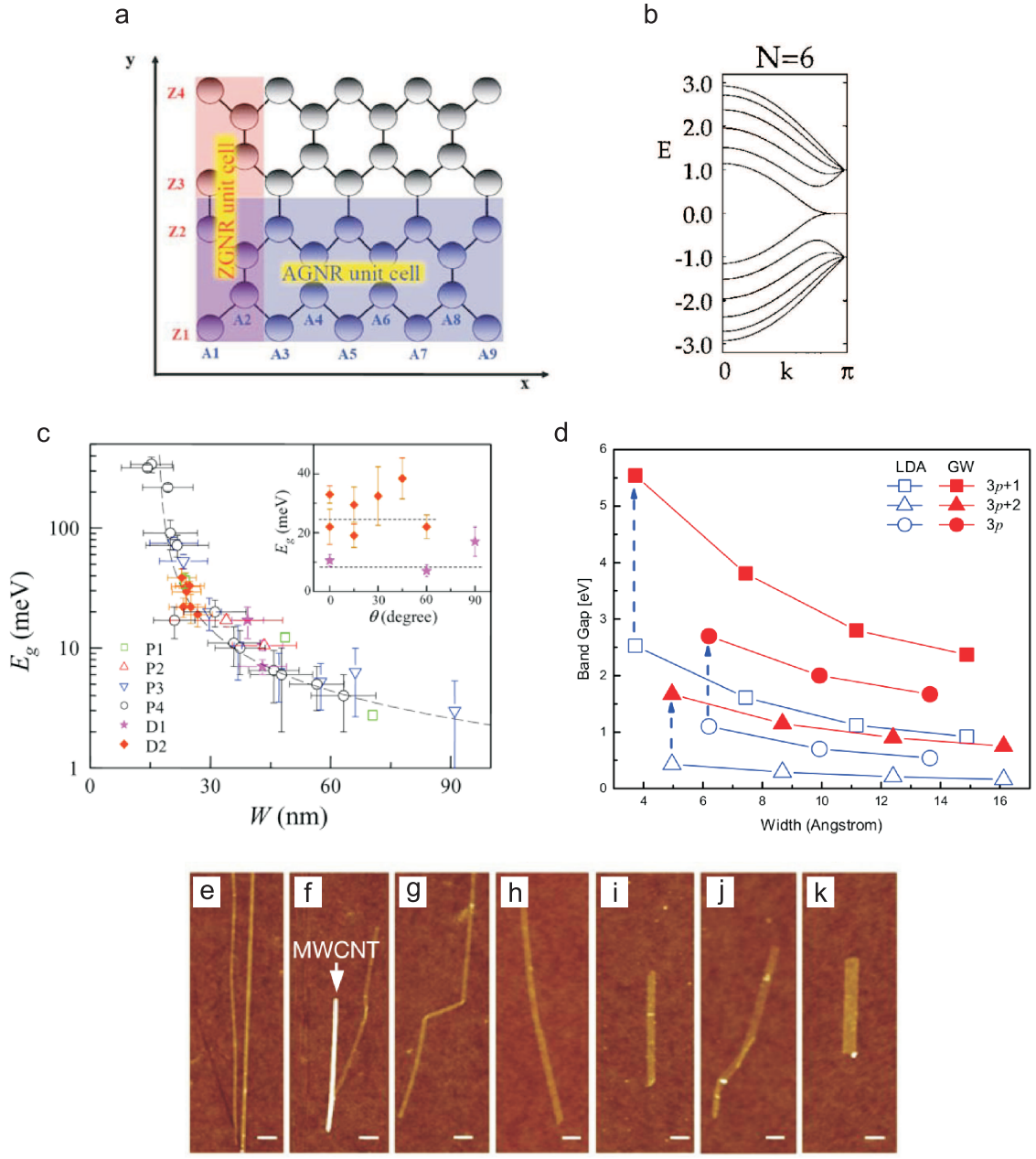

Figure 3.6: **a**, Schematic model of a GNR. "Z" and "A" indices specify the width of a zigzag and an armchair GNR, respectively. Reproduced from [10] with permission of The Royal Society of Chemistry. **b**, Calculated band structure of N=6 zigzag ribbon. Reprinted figure with permission from [12]. Copyright 2013 by the American Physical Society. **c**, Band gap vs. width of six different devices. Reprinted figure with permission from [11]. Copyright 2013 by the American Physical Society. **d**, Band gap of armchair GNRs depending on their width. Reprinted figure with permission from [98]. Copyright 2013 by the American Physical Society. **e-k**, AFM images of different GNRs produced by etched multi walled CNTs. Scale bars: 100 nm. Reprinted by permission from Macmillan Publishers Ltd: Nature [102], copyright 2013.

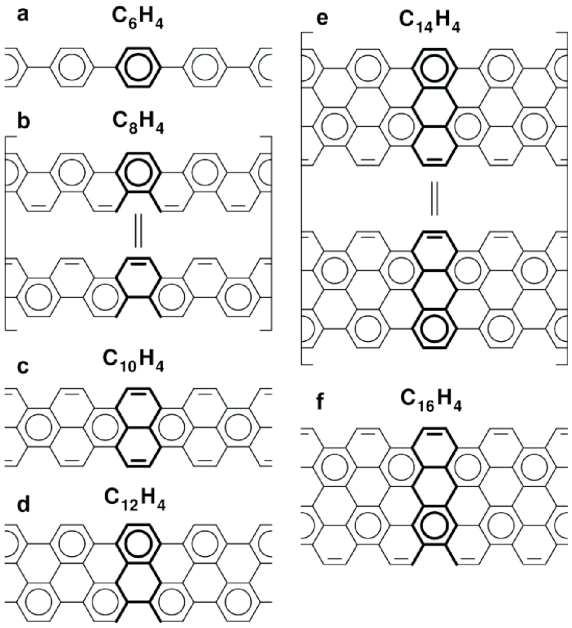

Figure 3.7: Clar representation of an armchair GNR with increasing width. **a**,**d**, belong to the 3n sub-family, **b**,**e** to the 3n+1 sub-family and **c**,**f** to the 3n+2 sub-family. Reprinted from [99], Copyright 2013, with permission from Elsevier.

A different attempt to fabricate GNRs uses multi-walled carbon nanotube (CNT). A poly(methyl methacry-late) layer protects the CNT while etching the sample with Ar plasma. After the etching and removing of the protection layer single GNRs are produced with a width of 10 to 20 nm (Fig. 3.6e-k) [102]. The smaller ratio I_D/I_G of the Raman intensities of the D and the G bands indicates a higher quality compared to lithographic patterned GNRs. However, controlling the edge structure is complicated for top-down approaches. One possibility to improve the quality of the edges is Joule-heating; Applying a bias voltage of 1.6 V to a graphitic nanoribbon leads to a rearrangement of the edges [103]. Zigzag edges, which have an electronic state close to the Fermi energy, are preferred because of their higher conductance due to this state. The current mainly flows along the zigzag edge, while a contact between a zigzag edge and a non-zigzag edge or, in general, a point defect, reduces the current flow and acts as a resistor [103]. Therefore, the carbon atoms at the edges vaporize, which leads to a reconstruction into a zigzag or an armchair structure [103].

A bottom-up approach to grow $N = 7$ armchair GNR has been reported by the group of Fasel [104]. 10,10'-dibromo-9,9'-bianthryl (DBDA) molecules are connected and cyclodehydrogenated on the surface through on-surface polymerization, which automatically leads to a well-defined width and edge structure. This approach is applied in chapter 5.3.2.2 and discussed in more detail in the next section.

The relation between the width of a GNR and its band gap has experimentally been observed by lithographically patterned GNRs out of a graphene flake [11]. The band gap E_g of several GNRs, which are a few μm long and 10 to 100 nm wide, was recorded. The following equation was used to fit the relation between the band gap of the GNR and its width W [11]:

$$E_g = \frac{\alpha}{W - W^*} \tag{3.5}$$

$\alpha = 0.2$ eV nm and W^*=16 nm. These experiments prove that the band gap can be tuned by the ribbon width, which is in good agreement with theory. Calculations predict an inverse relation of the band gap on the width. However, the calculated band gap depends on the precise edge structure as discussed before.

The length-dependent conductance of a single GNR with a width below 20 nm has been measured on a SiO_2 sample [105]. One end of the GNR is still connected to a graphitic flake, which is connected to the gold electrode. The conducting atomic force microscope (AFM) tip, which is brought into close contact with the GNR, is the second electrode. By varying the position of the tip, length-dependent conductance experiments are possible. The disadvantage of this method is the uncertainty in the tip-GNR contact as the contact can change during the experiment. Furthermore, the undefined width strongly changes along the GNR. This makes the interpretation of the measured resistance complicated.

In general, for all experiments mentioned above the edge structure and width of the GNRs is not well defined. A promising approach to grow molecular networks is the bottom-up solution on surface polymerization, which is discussed in the next section.

3.4 On-Surface Polymerization

For conventional evaporation techniques the investigation of large molecules like molecular wires is complicated in UHV. The vaporization temperature typically increases with the weight of the molecule. Depending on their size a high temperature may be required for vaporization. If the evaporation temperature is too high a defect-free preparation cannot be guaranteed, and the molecule starts to decompose inside the crucible of the evaporator.

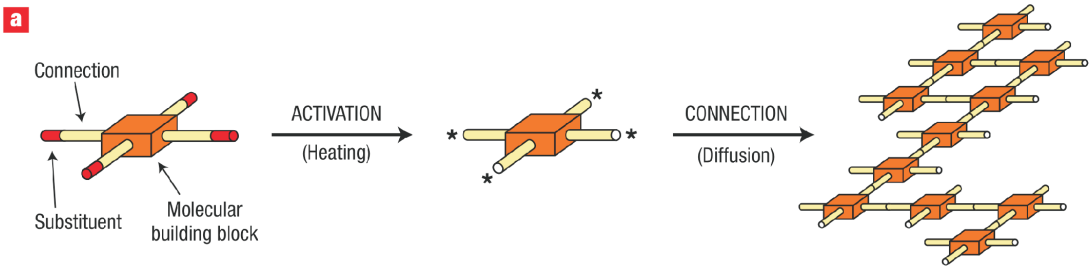

Figure 3.8: Schematic representation of on-surface polymerization. Reprinted by permission from Macmillan Publishers Ltd: Nature Nanotechnology [14], copyright 2013.

A different approach is on-surface polymerization. Instead of depositing the complete molecule, smaller building blocks are evaporated. The characteristic feature of these molecular building blocks is a predefined bond, which is designed to cleave at elevated temperatures while the remaining molecule stays intact. The predetermined breaking point is realized through a halogen atom whose bond energy is lower than all other bond energies of the molecule. A C-C and C=C bond have an average bond energy of 83 kcal/mol

and 146 kcal/mol, respectively, whereas the C-Br and C-I bonds have energies of only 68 kcal/mol and 51 kcal/mol, respectively [106]. For comparison the C-H has a bond energy of 99 kcal/mol [106]. The molecular building blocks are equipped with bromines which will be discussed in the experimental part of this work. The dehalogenated molecule, in the following nominated as activated, can be considered to be a surface-stabilized radical. The basic idea of on-surface polymerization is to combine molecular self-assembly with the Ullmann reaction on a surface. In the pioneering study in the group of Rieder, the Ullmann reaction was executed with two iodobenzenes molecules adsorbed on the Cu(111) surface [33]. Applying voltage pulses with the STM tip activates both molecules, thus dehalogenates them. At the former position of the iodine a free dangling bond is left and a surface-stabilized radical is created. During the next step lateral STM manipulation pushes both activated molecules together. A final voltage pulse triggers a bond formation and couples them covalently. The two benzenes are covalently linked to a larger biphenyl molecule which has been created on the surface.

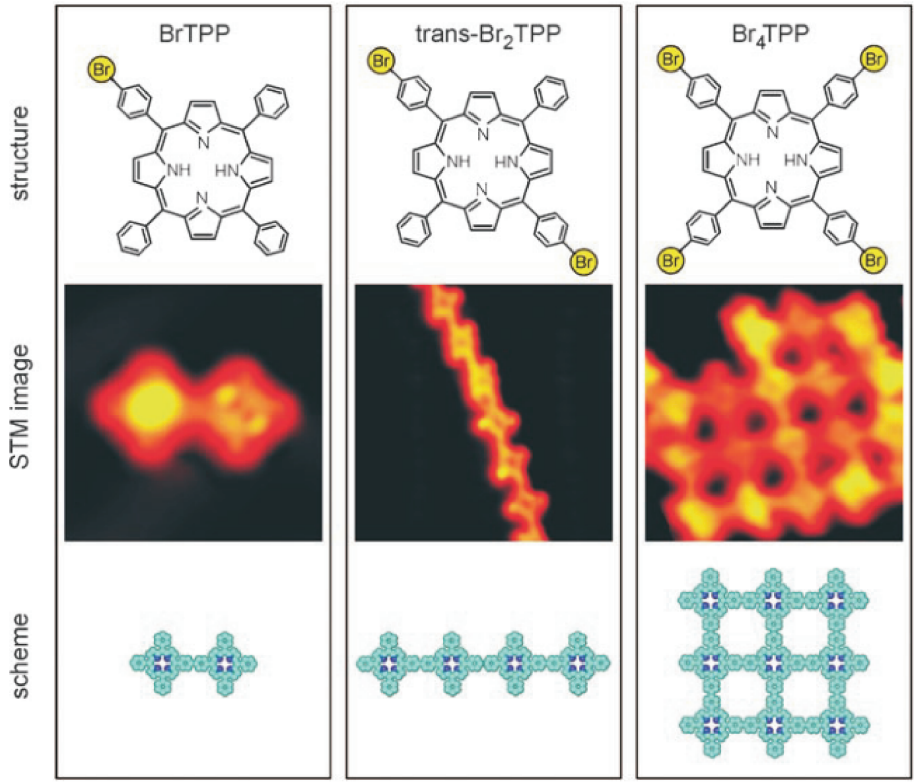

Figure 3.9: 1D and 2D structures formed via on-surface polymerization [14]. Depending on the number of bromine atoms dimers, chains or two-dimensional networks are created. Reprinted by permission from Macmillan Publishers Ltd: Nature Nanotechnology [14], copyright 2013.

To utilize the Ullmann reaction in molecular self-organization an automatic activation is necessary (Fig. 3.8). There are several approaches to trigger the activation of the molecular building blocks. Preactivated molecules are deposited by increasing the evaporation temperature [14]. The activation of the molecules occurs in the crucible of the doser. Heating the substrate to a certain temperature also leads to the activation of the molecules [14]. In case of molecular building blocks equipped with bromines, the activation on Au(111)

starts at ∼370 K [107]. Efficient bromine dissociation requires a heating step to 520 K [107, 14, 16, 108]. Using a more reactive substrate like Cu(111), which catalytizes reactions, lowers the activation temperature for bromine below RT [109]. No subsequent heating of the surface is necessary. This procedure is useful for fragile molecules which dissociate before the activation takes place and thus do not allow sample heating.

Depending on the design of the molecular building block in particular concerning the position of the halogens, the resulting structure can be defined. In case of a precursor molecule with two halogens in *trans*-position, molecular wires are formed [14, 16, 104]. When adding four halogens two-dimensional networks grow (Fig. 3.9) [14, 108]. If the molecular building block is equipped with halogens, which dissociate at different energies, a stepwise growth is possible. Even the combination of two different molecular species, like porphyrins and DBTF molecules, has been demonstrated [108].

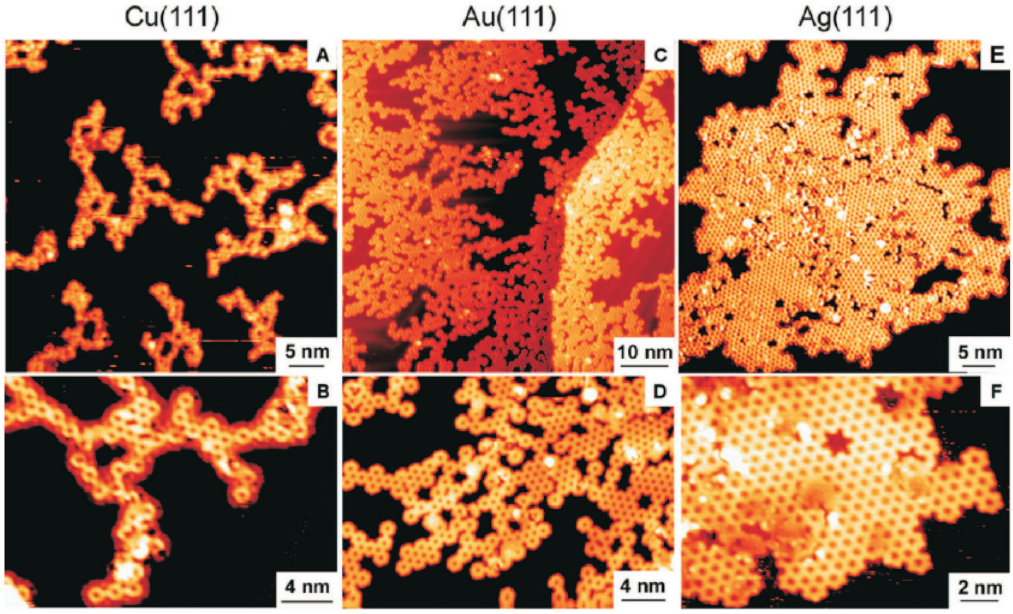

Figure 3.10: STM images of polyphenylene networks on Cu(111), Au(111) and Ag(111). Reprinted with permission from [15]. Copyright 2013 American Chemical Society.

Beside the design of the molecular building blocks, the substrate defines the resulting structure of the network. Instead of covalent bonds, metal-coordination bonds are sometimes formed on Cu(111) surfaces [109]. Also the alignment along certain surface reconstructions is used to influence the out-coming network [108]. A study on Cu(111), Ag(111) and Au(111) suggests a different coupling probability for each surface [15]. A comparison with Monte Carlo simulations shows lower coupling probabilities, which leads to more closed networks while a higher coupling probability and a lower mobility lead to branched network structures (Fig. 3.10) [15].

Recently, the growth of GNRs with smooth edges and a well-defined width has been reported [104]. The precursor molecule is DBDA equipped with two bromine atoms in *para* position. Annealing the Au(111) substrate to 470 K activates the molecules, and anthracene oligomers are created. These molecular chains are not GNRs yet: For dehydrogenation and subsequent cyclization a further heating step to 670 K is required because

the C-H bond has a higher bond energy of ∼99 kcal/mol [106]. In Raman spectroscopy the G and D modes are clearly observed [104, 110]. This will be discussed in more detail in the result section 5.3.2.2.

Chapter 4

Experimental Details

4.1 The Scanning Tunneling Microscope and the Ultra-High Vacuum Setup

The low temperature scanning tunneling microscope (STM) used in this thesis consists of the preparation chamber and the STM chamber. Both are separated by a gate-valve (see Fig. 4.1). Four pneumatically damped feet (Newport) decouple the UHV system from the floor in order to reduce vibrational noise.

The preparation chamber consists of a manipulator (VAB), a sputter gun, an evaporator, a low-energy-electron-diffraction (LEED) (Omicron), a quadropol mass spectrometer (QMS) (Balzers QMA200) and an ion gauge. The STM chamber contains the STM head, a liquid nitrogen and a liquid helium cryostat. The manipulator accesses both chambers and can be used to transfer the sample in and out of the STM head. Depending on the experiment the manipulator is not only used for the transfer but also to position the sample in front of the evaporator, the sputter-gun, the QMS or the LEED. Furthermore, with the heating and cooling mechanism of the manipulator the sample temperature is controlled.

The commercially available Kentax evaporator has four crucibles, which can be heated independently of each other. A shutter in front of the crucibles controls the flux of the molecules. Depending on the position of the shutter molecules of one, two, or three crucibles can simultaneously be deposited while the molecular flux is detected by a quartz crystal microbalance.

A turbo molecular pumped load-lock chamber is attached via a gate-valve to the preparation chamber. This has the advantage that samples can be transferred into the UHV system without breaking the vacuum of the STM and the preparation chamber. A sample storage exists in the preparation chamber to keep two additional samples in the UHV.

The base pressure of the STM and the preparation chamber is $1x10^{-9}$ mbar. A turbo molecular pump (Pfeifer) and a scroll pump (Edwards) evacuate the load-lock and the main chamber. As the vibronic noise of the turbo molecular pump interferes with the STM measurements it must be switched off to achieve a high STM image quality. An ion getter pump in the preparation chamber is used to maintain the base pressure during the STM experiments.

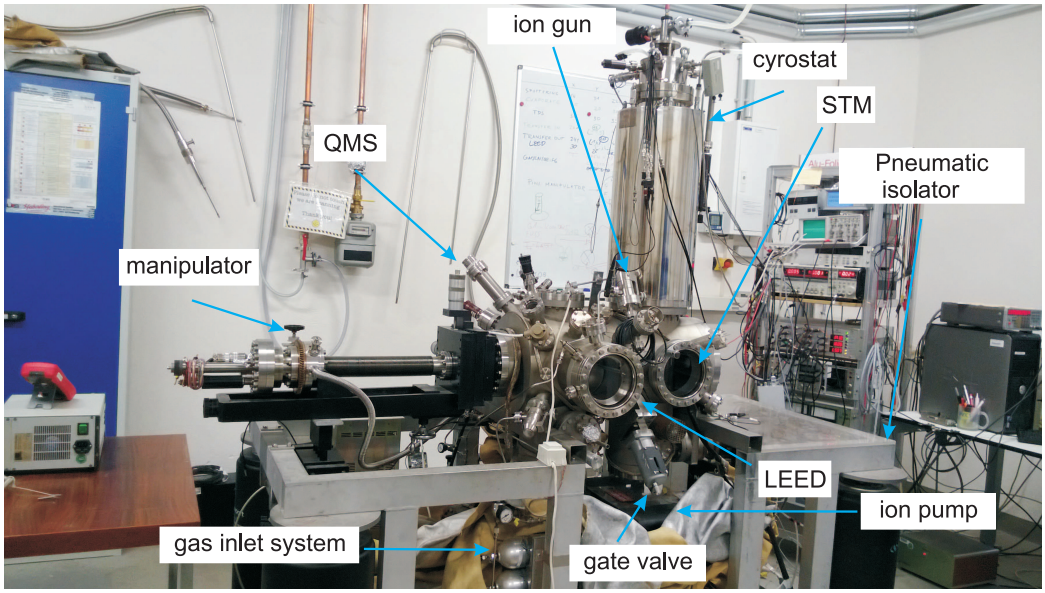

Figure 4.1: Picture of the used low temperature STM.

In the STM chamber a liquid nitrogen and a liquid helium bath Cryovac cryostat are mounted. These are sketched in Fig. 4.3. The modified version of the Createc low temperature STM is attached by three springs to the helium cryostat, which allows to operate the STM at ∼10 K. Fig 4.2 shows the used STM head. To achieve temperatures as low as ∼10 K the STM head is surrounded by two radiation shields. The outer shield is cooled with liquid nitrogen and the inner one with liquid helium. To cool down the STM head as well as for sample transfers a clamping mechanism presses the STM head against the inner radiation shield, which is at liquid helium temperature. Three springs, which are mounted on the helium cryostat, decouple the STM head electrically as well as vibrationally from the remaining chamber during the measurements. Additionally, three magnets are attached to the inner radiation shield and the STM head in order to improve the isolation by an eddy current damping setup.

The STM head is based on the principle of the Besocke type STM [111] and was constructed by G. Meyer [112]. Four piezos drive the STM: three outer piezos and the main piezo, which is connected to the STM tip. The three outer piezos are responsible for the coarse motion. The main piezo with the STM tip is attached to an angled disc. The moment of inertia of this angled disc is exploited to move the tip up and down in a slip-stick motion. Depending on the settings the three outer piezos or the main piezo are used to scan the surface, and the bias voltage is applied to the sample. The tunneling current was amplified by two commercial devices: a Femto DLPCA-200 preamplifier for the vibrational spectroscopy and the defect conductance measurements as well as a Balzers EP112 pre-amplifier for the remaining experiments.

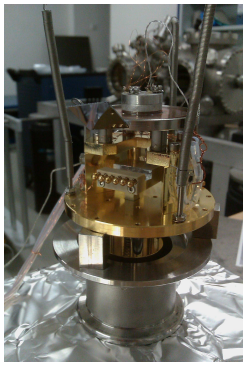

Figure 4.2: Picture of the Createc STM head.

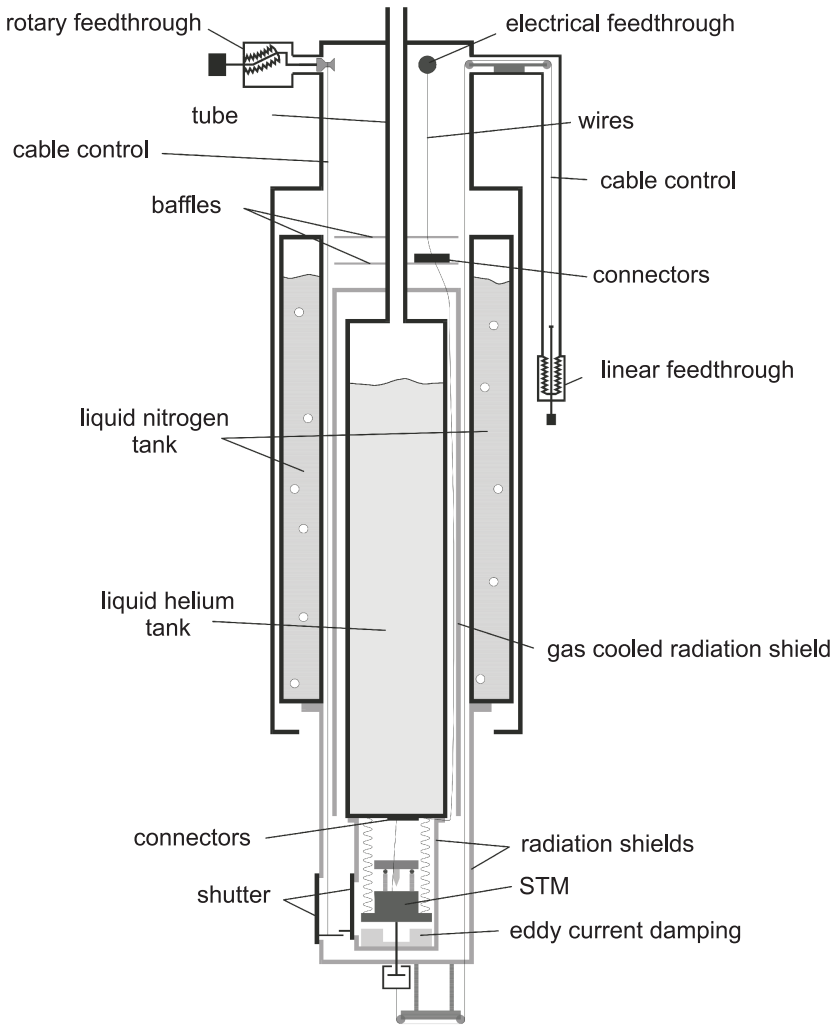

Figure 4.3: Sketch of the bath cryostats and the STM setup. From [113].

The STM electronics consists of a digital signal processor unit connected to a personal computer, which runs the commercial software (Createc). The digital signal processor unit controls the analog-to-digital (AD) and the digital-to-analog (DA) converter as well as the tip height by the P/I feedback loop, which keeps the tunneling current constant. An AD converter translates the amplified tunneling current and together with the P/I feedback loop the piezo-voltage necessary for the tip height is calculated. The new voltage value is transferred by a DA converter to the high-voltage amplifier connected to the piezos. The desired bias voltage is also translated by the DA converter and applied to the sample. An additional AD converter channel for incoming signals is available, which can be used for the signal of the lock-in amplifier.

To calibrate the measured images, the lattice constants of Cu(111), Au(111) and Au(100) surfaces are used that are obtained by imaging these surfaces with atomic resolution. All images in this thesis are recorded in the constant-current mode. To measure the $\mathrm{d}I/\mathrm{d}V$ ($\mathrm{d}I^2/\mathrm{d}V^2$) signal the bias voltage was modulated by a 610 Hz signal with 20 mV (8 mV).

The gas phase calculations were performed by HyperChem 8.0.8 (Hypercube Inc.).

4.2 Au(111), Au(100) and Cu(111) Surfaces

Three different substrates have been used for the experiments to study the influence of the reconstruction and the catalytic activity of the surface on the growth of molecular chains.

Among the three surfaces the Cu(111) surface is the catalytically most reactive surface. The energy required to remove copper atoms from step edges is lower than on Au(111) [114]. Therefore, copper adatoms are available in a large number at room temperature [115]. Beside the copper adatoms, the reactivity of a surface depends on the degree of the filling of the antibonding d states and the overlap between the interacting atoms or molecules with the d states of the metal [116]. To understand why Au is more noble than Cu, the latter is important, since the filling of the d states is similar. The orthogonalization energy of the adsorbate s and metal d states increases with the square of the coupling matrix element between the s and the d states. The orthogonalization energy cost increases for Au compared to Cu, which makes Au more noble and Cu more reactive [116].

4.2.1 Au(111) and Au(100)

The noble metal gold is rather inert, and thus exhibits a low catalytic activity is expected. The crystal structure of gold is face-centered cubic (fcc) with a lattice constant of a = 4.08 Å [117]. The distance to its nearest neighbors is $a/\sqrt{2}$=2.88 Å, and the height of a step edge is $a/\sqrt{3}$=2.36 Å.

The hexagonal structure of the Au(111) surface does not extend over large scales. Instead, the Au(111) surface reconstructs at room temperature in a (22x$\sqrt{3}$) overlayer structure known as herringbone reconstruction (see Fig. 4.4c). The herringbone reconstruction develops because 23 atoms of the top layer are placed on top of 22 atoms of the second layer [120]. A pattern of fcc and hcp areas appears with a periodicity of 63 Å. The fcc and hcp areas are separated by ridges [120] caused by the bridge atoms between the fcc and hcp stacking. The hcp regions are narrower than the fcc regions, which have a width of 25 Å and 38 Å, respectively [21]. On the clean Au(111) surface a Shockley-like surface state appears at -0.52 eV [21]. This surface state is important for the $\mathrm{d}I/\mathrm{d}V$ spectroscopy and can be used to confirm the metallic nature of the STM tip, because tip with a constant LDOS in the energy range of interest is required.

The Au(100) surface reconstructs quasihexagonal in parallel corrugations which appear every 14.4 Å [20]. This is a multiple of five atom rows of 2.88 Å distance. The top layer is compressed along this direction by 4 % compared to the bulk structure. Local-density theory calculations supports a (5x20) reconstruction with a maximum corrugation of 0.65 Å (see Fig. 4.4a) [118] and a step edge height of $a/2$ = 2.04 Å.

4.2.2 Cu(111)

The copper crystal has a fcc structure with a lattice constant of a = 3.61 Å [117]. This leads to a step height of $a/\sqrt{3}$=2.08 Å with a nearest neighbor distance of $a/\sqrt{2}$=2.55 Å. The Cu(111) surface exhibits an fcc stacking and the unit cell of the Cu(111) surface is hexagonal. The Cu(111) surface also exhibits a Shockley like surface state with a band

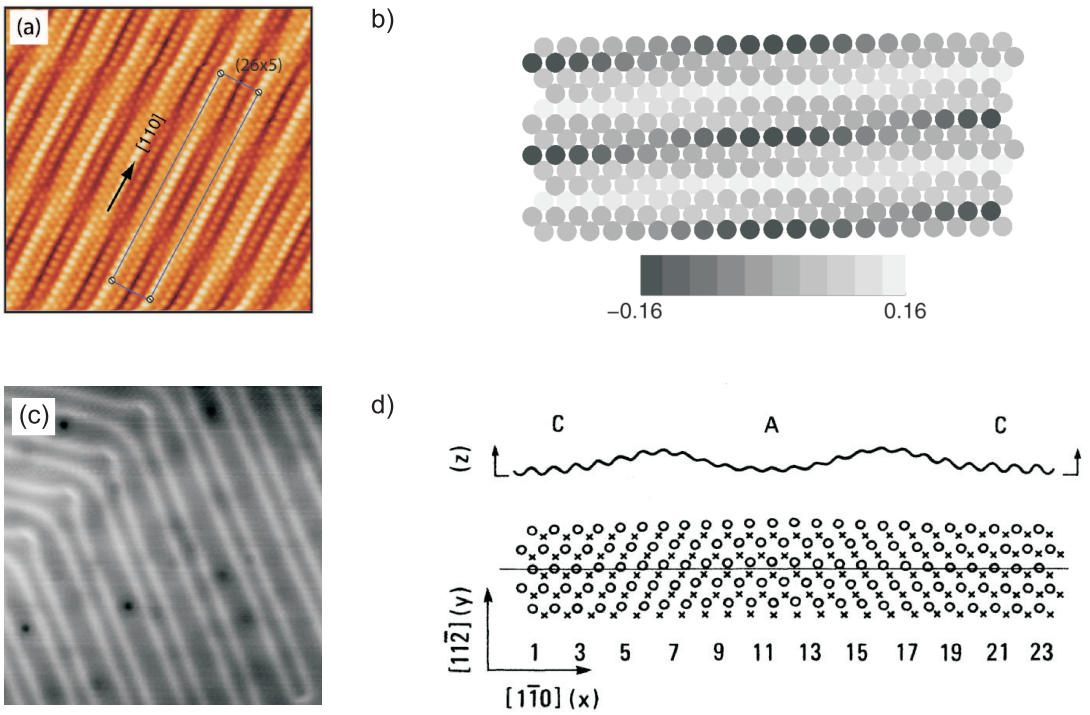

Figure 4.4: **a**, 10x10 nm^2 STM image of the Au(100) surface. Reprinted figure with permission from [20]. Copyright 2013 by the American Physical Society. **b**, Top view of the hexagonal layer of the Au(100)-(5x20) reconstruction: The gray scale indicates the z-position of the atoms relative to the average z-position of the plane. Reprinted figure with permission from [118]. Copyright 2013 by the American Physical Society. **c**, 40x40 nm^2 STM image of the Au(111) surface. **d**, Model for the (22x$\sqrt{3}$) reconstruction of the Au(111) surface: A and C mark the regions of hcp and fcc stacking, respectively. Open circles denote atoms from the top layer and crosses the positions of the atoms in the second layer. Reprinted figure with permission from [119]. Copyright 2013 by the American Physical Society.

edge energy of −450 eV [121]. In case of Cu(111) the energy required to remove an atom from a step is lower compared to Au(111) [114] and copper adatoms are available at room temperature [115].

4.3 Sample Preparation

Before the deposition of the molecules the sample was cleaned. The cleaning of the substrate can be divided into sputtering and the annealing. For the sputtering ionized neon atoms are accelerated towards the substrate to remove the top layers of the surface. During sputtering the partial pressure of the neon gas was ∼1x10^{-5} mbar, while the kinetic energy of the neon atoms was 1.5 keV for Au(111) as well as Au(100) and 1.3 keV for Cu(111). After sputtering the sample is annealed for 10 minutes at temperatures between 670 and 770 K. After cooling the samples to RT the molecules were evaporated onto the surface. All these steps occurred under UHV conditions.

Molecule	Evaporation temperature	Shown in figure
dibromo-diphenylporphyrin	460 K	Fig. 4.5a
dibromo-tetraphenyl-bisporphyrin	620 K	Fig. 4.5b
dibromo-bis(3,5-tert-butylphenyl)porphyrin	500 K	Fig. 4.5c
2,3-dibromoanthracene	400 K	Fig. 4.5d
9,10-dibromo-anthracene	380 K	Fig. 4.5e
10,10'-dibromo-9,9'-bianthryl	420 K	Fig. 4.5f
2,11-dibromohexabenzocoronene	600 K	Fig. 4.5g
5,14-dibromotribenzo[ef,hi,o]triphenyleno[11,12,1,2-uvabc]ovalene	700 K	Fig. 4.5h
1,4-Bis(4-bromophenyl)-2,3,6,11-tetraphenyltriphenylene	500 K	Fig. 4.5i
1,4-Bis(4-bromophenyl)-2,3-bis(4-tert-butylphenyl)-6,11-diphenyltriphenylene	500 K	Fig. 4.5j
dibromoterfluorene	390 K	Fig. 4.5k

Table 4.1: Evaporation temperatures of the investigated molecules (leading to rates of about 0.1 to 1.0 ML/min).

4.4 Molecules

In this thesis four different species of precursor molecules were studied for the fabrication of molecular chains. Two of the species should polymerize to GNRs (Fig. 4.5d-f and g-j), one species to polyfluorene (Fig. 4.5k) and the other one to fully conjugated porphyrin tapes (Fig. 4.5a-c).

Fig. 4.5a-c shows the porphyrin based building blocks that were synthesized in the group of S. Hecht (Humboldt Universität zu Berlin, Institut für Organische Chemie).

The anthracene building blocks differ in the position of the attached bromines. Two building blocks, the anthracene monomer and the dimer, have bromine atoms in *trans* position (Fig. 4.5e and f). 9,10-dibromo-anthracene was purchased from Sigma-Aldrich GmbH and 10,10'-dibromo-9,9'-bianthryl from Ruiyuan Group. The bromine atoms of 2,3-dibromoanthracene are attached at the outer phenyl ring (Fig. 4.5d). The molecule was synthesized in the group of S. Hecht (Humboldt Universität zu Berlin, Institut für Organische Chemie).

The trapezoid-shaped building blocks (Fig. 4.5h-j), the 2,11-dibromohexabenzocoronene (Fig. 4.5g) and the dibromoterfluorene (DBTF) (Fig. 4.5k) were also synthesized in the group of S. Hecht (Humboldt Universität zu Berlin, Institut für Organische Chemie). The molecular compounds of 2,11-dibromohexabenzocoronene (diBr-HBC) also contain triBr-HBC, monoBr-HBC and HBC without bromine atoms after the chemical synthesis (S. Hecht and co-workers, Humboldt Universität zu Berlin).

The evaporation temperatures are listed in table 4.4.

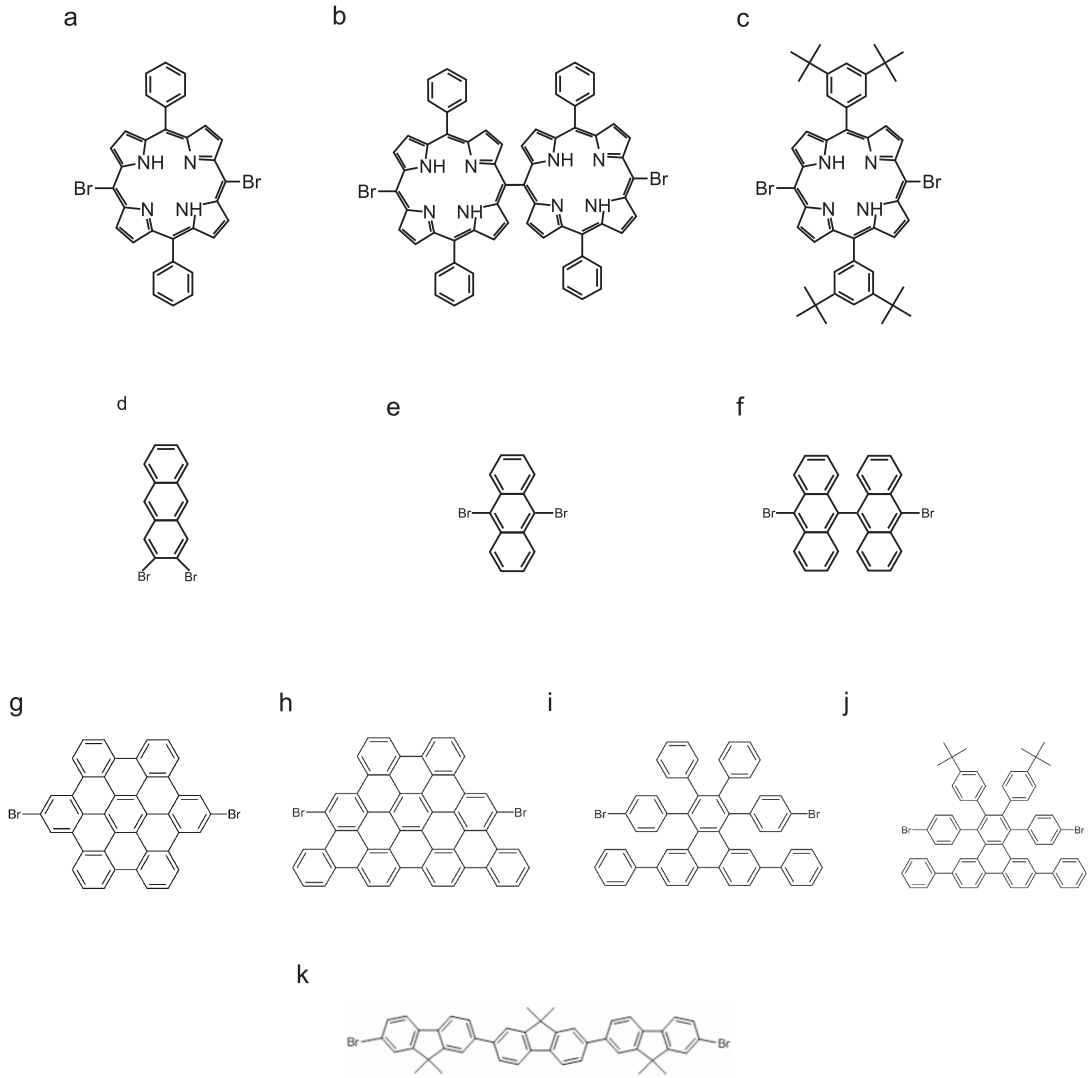

Figure 4.5: Porphyrin tapes: **a**, dibromo-diphenylporphyrin **b**, dibromo-tetraphenyl-bisporphyrin **c**, dibromo-bis(3,5-tert-butylphenyl)porphyrin. Anthracene based molecules: **d** 2,3-dibromoanthracene **e**, 9,10-dibromo-anthracene **f**, 10,10'-dibromo-9,9'-bianthryl. The trapezoid shaped molecules: **g**, 2,11-dibromohexabenzocoronene **h** 5,14-dibromotribenzo[ef,hi,o]triphenyleno[11,12,1,2-uvabc]ovalene **i**, 1,4-Bis(4-bromophenyl)-2,3,6,11-tetraphenyltriphenylene **j**, 1,4-Bis(4-bromophenyl)-2,3-bis(4-tert-butylphenyl)-6,11-diphenyltriphenylene. **k**, dibromoterfluorene

Chapter 5

Growth of Molecular Nanostructures

The fabrication of molecular wires is challenging for top-down approaches like lithography and etching [100, 101, 13] as well as for bottom-up approaches like on-surface polymerization. The top-down approaches struggle with the edge-structure and the width of the molecular wire. An edge roughness of ∼5 nm was reported for graphene nanoribbons (GNRs) [13], which results in a not well-defined width and chemical structure of the ribbon edges. Bottom-up approaches like on-surface synthesis allow the formation of extended conjugated electronic systems. Moreover, they lead to atomically defined edges which are required for charge transport studies as structural defects, especially for GNRs, have been predicted to modify the electronic structure [122, 98] and to reduce the conductance. The choice of the molecular building block is crucial because steric hindrance can block the polymerization. Steric repulsion between the precursor molecules is one of the major challenges of on-surface synthesis. It might stop the molecules from linking or even cause the dissociation of parts of the molecular wires.

Chapter 5.1 discusses several porphyrin-based precursor molecules which are supposed to link covalently to long fully conjugated porphyrin tapes. The HOMO-LUMO gap becomes smaller with the length of the tape and, therefore, the conductance of the tape should also improve with its length [17].

The role of the substrate in on-surface polymerization is the topic of the next chapter 5.2 where hexa-peri-hexabenzocoronene molecules equipped with two bromines were deposited on Au(111) and Cu(111). Cu(111) is known to have a higher catalytic activity than Au(111) [123]. Steering the alignment of the 2,3-dibromoanthracene (tdBA) precursor molecules through the reconstruction of the Au(111) and Au(100) substrate is studied in chapter 5.2.2.

Finally, in chapter 5.3 the growth of GNRs for two different types of molecules is investigated: trapezoid-shaped building blocks and anthracene-based molecules [104].

5.1 Growth of Porphyrin Tapes

A benchmark criterium of a molecular wire is its conductance. Needless to say that for a molecular wire higher values of conductance are preferred. As mentioned in the introduction there are several approaches to improve the conductance (see chapter 3.1). Designing a molecular chain with a small HOMO-LUMO gap is one attempt for a good conducting wire. The HOMO of a fully conjugated porphyrin tape shifts to a higher energy with the increasing length of the molecular chain (see Fig. 5.1a) [17]. 2900 nm is the longest absorption band of a porphyrin tape with a length of 19 porphyrin-units. The 2900 nm absorption band corresponds to a transition energy of 0.43 eV, which is extremely low [19]. For comparison, alkane chains have a HOMO-LUMO gap of ∼9 eV [18] and a large inverse decay length β of ∼0.7-0.9 Å^{-1} [51, 48]. In general, a HOMO-LUMO gap below 1 eV is considered as very low [19].

STM break junction was used to determine the inverse decay length by measuring the conductance of synthesized oligo-porphyrin wires which consist of one to three porphyrin-units [124]. Even for not planarized oligo-porphyrin wires the inverse decay length of the tunneling current is as small as β=0.040±0.006 Å^{-1}. The inverse decay length would probably even decrease further if the porphyrin wire was fully conjugated as it is the case for the porphyrin tapes [17].

The idea of this section is to grow fully conjugated porphyrin tapes on the surface. To avoid problems of fragmentation due to the sublimation temperature the on-surface polymerization technique was used (see chapter 3.4). For the synthesis of these porphyrin wires on the Au(111) surface several molecular building blocks were studied.

5.1.1 Dibromo-diphenylporphyrin

The dibromo-diphenylporphyrin (dBP) molecules were deposited on the clean Au(111) surface at RT. Fig. 5.1b shows the chemical structure of dBP. The evaporation temperature of the molecules was 460 K. After cooling the substrate to low temperatures (∼10 K) the dBP molecules were found in large islands (Fig. 5.1c) which is an evidence of the mobility of dBP molecules on Au(111) at RT. The close-packed structure of these islands complicates the identification of a single dBP molecule in an STM image. Partially isolated dBP molecules arrange in a less strict pattern at the border of the islands enabling the detection of the shape of a single molecule. The sketched porphyrins in Fig. 5.1c indicate a dBP molecule near an island as well as a dBP molecule inside an island.

The porphyrins are not dehalogenated yet as the bromines are still attached. This is reasonable as the evaporation temperature of dBP (460 K) is below the reported deposition temperature of activated tetra(4-bromophenyl)porphyrins. Bromine bonds were reported to dissociate from porphyrins during deposition at an evaporation temperature above 590 K [14]. Fig. 5.1c shows an STM image of an island of dBP molecules. The appearance of 9,10-dibromo-anthracene (DBA) is similar to dBP in STM images (see chapter 5.3.2.1). Both molecules are equipped with bromines at opposite sides. In STM images of DBA the bromines are assigned to the sharp protrusions (see Fig. 5.27b). The small lobes at the opposite sides of the porphyrin core, which are indicated by the red arrow in Fig. 5.1c, are assigned to bromine atoms. The apparent height of these protrusions is 1.3±0.1 Å for a

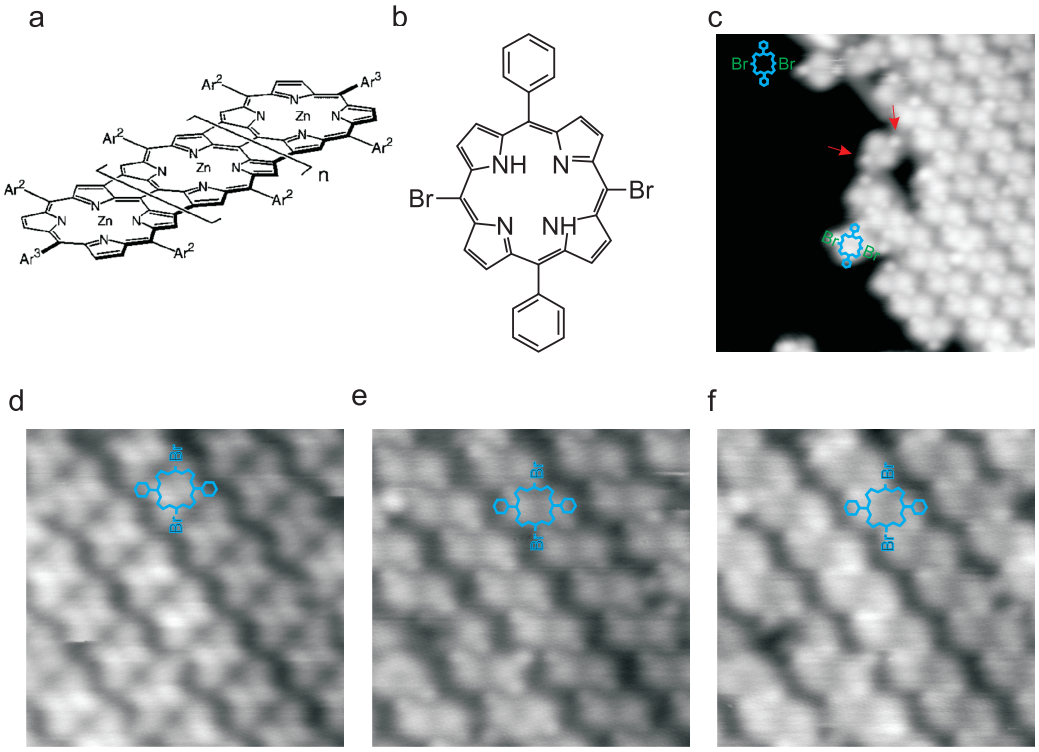

Figure 5.1: **a**, Chemical structure of the porphyrin tapes. From [17]. **b**, Chemical structure of the dBP molecule. **c**, 13x13 nm^2 STM image of a dBP island on Au(111) deposited at RT. The blue outline indicates the shape of a single molecule. The red arrows denote the position of the bromines. **d**,**e**,**f** 15x15 nm^2 STM images of a dBP island at different bias voltages: **d** 2 V, **e** 1 V, and **f** -2 V.

bias voltage between 0.05 and 1 V. This coincides with the reported height of bromines attached to porphyrins [108]. The appearance of dBP molecules in STM images depends on the applied bias. If the bias voltage is higher than 2 V (Fig. 5.1d) the dBP molecules have a cross-like shape and the features in the STM image assigned to the bromine atoms are no longer that sharp. For smaller or negative bias values the bromine atoms look like sharp protrusions and the two phenyl rings look broad (Fig. 5.1e and f). This effect was reproduced with different STM tips and is related to the electronic structure of the molecules.

Heating the sample to 470 K changes the appearance of the dBP molecules. The porphyrin core with the two phenyl rings lead to a characteristic shape, which is no longer bias dependent in the range of -1.5 to +1.5 V (Fig. 5.2c). Although the molecules are dehalogenated the dBP molecules do not connect to chains but arrange in islands (Fig. 5.2a). In contrast to previously reported polymerization of porphyrins, the bromine atoms are directly attached to the porphyrin core and not separated by a phenyl ring [14, 108]. The missing phenyl ring probably causes a higher steric repulsion which has to be overcome by the molecular building blocks in order to link covalently. To trigger a linking between the precursor molecules the temperature of the second heating step was increased to 670 K.

After heating the sample to 670 K the dBP molecules lie isolated instead of forming islands (Fig. 5.2b). At a temperature of ∼670 K dehydrogenation for several molecules on

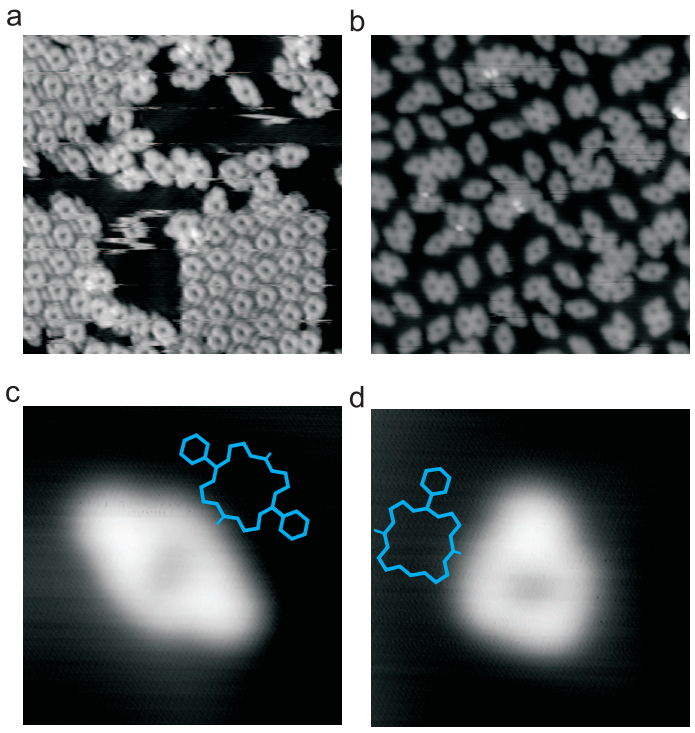

Figure 5.2: **a**, 15x15 nm^2 STM image of dBP islands on Au(111) after heating the substrate to 520 K. **b**, 80x80 nm^2 STM image of dBP after heating the substrate to 670 K. **c**,**d**, 3x3 nm^2 STM images of **c** a complete dBP and **d** a fragmented molecule. The blue outlines indicate the chemical structure.

Au(111) has been observed [125, 126, 104]. Probably the hydrogens dissociate and the remaining molecules become negatively charged. This could explain the repulsive nature of the molecules, which suppresses the typically preferred arrangement in islands as it reduces the total energy. Next to single dBP molecules, fragments of dBP appear after heating the sample to 670 K (Fig. 5.2d). In total, about 5 % of the molecules are fragmented after the second heating step. The full width at half maximum of a dBP molecule along the phenyl rings decreases from 2.03±0.5 nm for the intact molecule (Fig. 5.2c) to 1.65±0.04 nm for the fragmented dBP. The size of a phenyl ring in gas phase calculations is 0.39 nm, which points to the dissociation of one phenyl ring (see sketch in Fig. 5.2d).

Beside single molecules also short chains of dBP molecules are found. The bond between these chains could not be cleaved by lateral constant-current manipulation with a tunneling resistance of 327 kΩ which points to a covalent bond. Fig. 5.3 shows STM images before the lateral manipulation, b, and after, c. The manipulation path of the tip is indicated by the red arrow in Fig. 5.3b. It was even possible to pull a dBP chain from the surface with the STM tip and measure the current up to a tip-sample distance of ∼40 Å. Fig. 5.3d shows the molecule which was lifted form the surface by the STM tip. After a bond is formed between STM tip and molecule the tip was retracted while the current was recorded (Fig. 5.3e). This technique is explained in greater detail in chapter 6. Fig. **??**e shows the recorded current spectrum, the arrows indicate the direction of the vertical tip movements. On first glance the slope is different when comparing the current during the approach (without a molecule in the junction) to the current while the tip is retracted (with a molecule in the junction). The current falls of less steep with a molecule inside the junction. However,

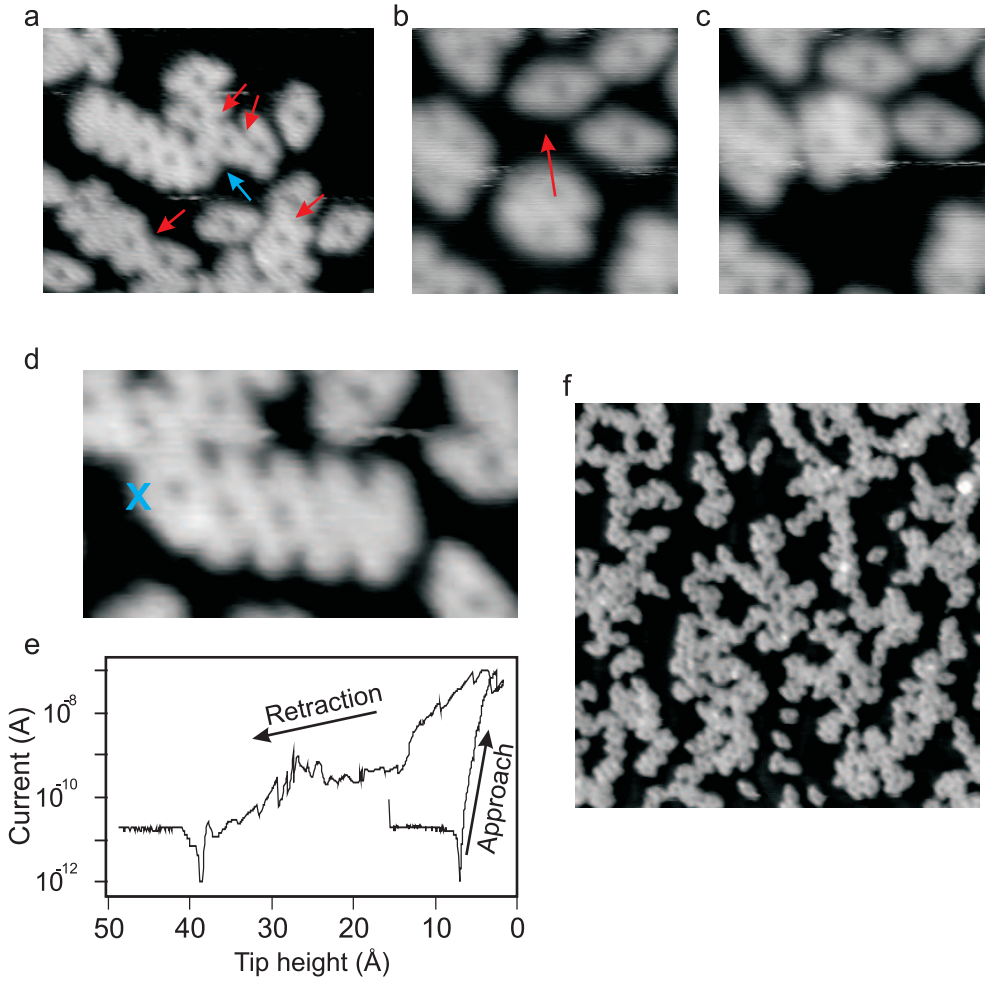

Figure 5.3: **a**, 10x8 nm^2 STM image of a defected porphyrin chain on Au(111) after heating the substrate to 670 K. The red and blue arrows indicate the positions of defects. **b**,**c**, 6x6 nm^2 STM images **b** before and **c** after the lateral constant-current manipulation (52 nA, 17 mV). The manipulation path is denoted by the red arrow. **d**, 7x4 nm^2 STM image of a porphyrin chain which was pulled up by the STM tip. The current spectrum is shown in **e** and the blue cross indicates the position of the tip. **f**, 35x35 nm^2 STM images of dBP chains on Au(111) after heating the substrate to 700 K.

the spectrum in Fig. 5.3e has many jumps, which are probably due to reorientation of the molecule in the junction. It has also been reported that the angle between the porphyrin units has a large influence on the conductance [57]. The drawback with these structures is that the bond between the porphyrin units is not well defined and occurs at random (see Fig. 5.3a). Thus, heating the substrate to 670 K leads to partial dehydrogenation [126, 110, 104] and additional active sites for linking are created [126, 110]. The arrows in Fig. 5.3a point to bonds which emerge in an uncontrolled manner. For example the bond highlighted by the blue arrow probably is between the reactive site of one porphyrin and the fragmented phenyl ring of the other porphyrin. Increasing the heating temperature further to 690 K results in even longer chains but at the same time in a higher defect rate (Fig. 5.3f).

5.1.2 Dibromo-tetraphenyl-bisporphyrin

For the growth of GNRs with anthracene based precursor molecules the decisive factor is the number of anthracenes in the monomer (see chapter 5.3.2.2). Anthracene dimers successfully link to GNRs [104] whereas anthracene monomers do not polymerize. The steric repulsion between the anthracene monomers seems to suppress the polymerization. The anthracene units in the dimer are rotated with respect to each other. This reduces the repulsive interaction between the molecular building blocks (for more details see chapter 5.3.2). A similar approach was applied to the fabrication of the porphyrin tapes by using porphyrin dimers as precursor molecules (see Fig. 5.4a for the chemical structure). The dibromo-tetraphenyl-bisporphyrin (DBDP) molecules were deposited on the clean Au(111) sample at RT. Due to the high evaporation temperature of 620 K caused by the large molecular weight the molecules were probably activated during the preparation. In case of tetra(4-bromophenyl)porphyrins an activation of the molecules occurred during the deposition at an evaporation temperature of 590 K [14].

The appearance of the DBDP molecules in STM images is similar to the dehalogenated dBP molecules confirming the dissociation of the bromine atoms (Figures 5.4b and c). Although the molecules were already activated they prefer to lie isolated on the surface without any observed chains. This stands in contrast to the results on dBP where the molecules self assemble into islands but also there no polymerization occurred. For dBP a heating step to 670 K and probably a partial dehydrogenation is necessary to make the molecules repulsive. The high evaporation temperature of DBDP could also cause dehydrogenation beside the dehalogenation during the deposition. This could explain the repulsive nature of the DBDP molecules.

Since the molecules were already activated the surface was heated directly to 670 K. This should trigger the polymerization and the cyclodehydrogenation of the porphyrins in one step. This leads to the appearance of a few short porphyrin chains consisting of three units (Fig. 5.4d and f). However, since dimers are used as precursor molecules only chains with an even number of units should occur. Only 1 % of the molecular chains are trimers and most of them are dimers (51 %). The high temperature during the second heating step leads also to defected structures (12 %) which look similar to the defected chains made of dBP molecules (compare Fig. 5.4e to Fig. 5.3a). Aside from short chains molecules are detected (36 %) which look identical to the dBP after being activated (compare Fig. 5.4f to Fig. 5.2c). These probably are a side effect of the dissociation of the dimers which gives a further indication that the original DBDP molecules have already been dissociated into two porphyrin units. These units do not polymerize as discussed in the previous chapter 5.1.1. The bond formation as well as the decomposition of the porphyrin dimers are competing processes at high temperature. The molecule-surface interaction probably causes a rather planar adsorption geometry of the precursor molecule. The angle between the porphyrin units is, therefore, too small to reduce the steric repulsion compared to the porphyrin monomers.

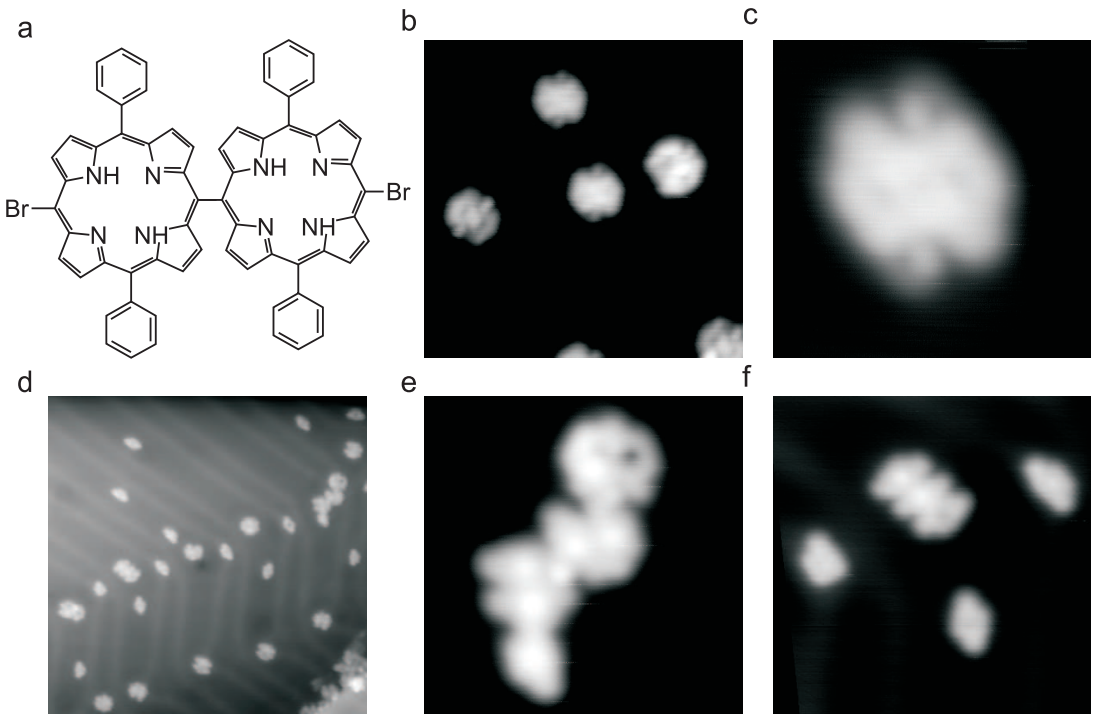

Figure 5.4: **a**, Chemical structure of DBDP. **b**, 12x12 nm^2 STM image of DBDP molecules before heating the Au(111) sample. **c**, 3.5x3.5 nm^2 STM image of a single DBDP molecule before heating the sample. **d**, 37x37 nm^2 STM images of DBDP molecules after heating the sample to 670 K. **e**, 7x7 nm^2 STM image of a defected chain after heating the sample to 670 K. **f**, 10x10 nm^2 STM image of a short chain of porphyrins after heating the sample to 670 K.

5.1.3 Dibromo-bis(3,5-tert-butylphenyl)porphyrin

Using dimers instead of monomers has not improved the polymerization (Chapter 5.1.1 and 5.1.2). The angle between the porphyrins in the precursor molecule might not be sufficiently large to reduce the repulsive interaction between the molecules. The dibromo-diphenylporphyrin was equipped with four tert-butyl groups (TB-dBP) to decouple the units in a porphyrin oligomer even further (Fig. 5.5a). Similar to the experiments discussed before, the clean Au(111) was at RT during the evaporation of TB-dBP. The temperature of the crucible was 500 K during the deposition.

The TB-dBP molecules arrange into large islands or nucleate at the kinks of the herringbone reconstruction. The tert-butyl groups appear as bright features in an STM image. Therefore, it is difficult to resolve the bromine atoms (Fig. 5.5c). Nevertheless, the TB-dBP molecules are probably not activated yet because of the low evaporation temperature (500 K). In case of tetra(4-bromophenyl)porphyrins there has been reported an activation during the deposition at an evaporation temperature of 590 K [14]. On the other hand, the butyl groups are clearly visible in STM images; They appear as two bright lobes on each side of the porphyrin (Fig. 5.5c). To identify the shape of a single molecule inside the islands is complicated. Fig. 5.5d shows a single molecule highlighted by a blue ellipse next to an island. The distance between the opposite tert-butyl groups is obviously larger than the distance between the bright lobes indicated by the red arrows inside the

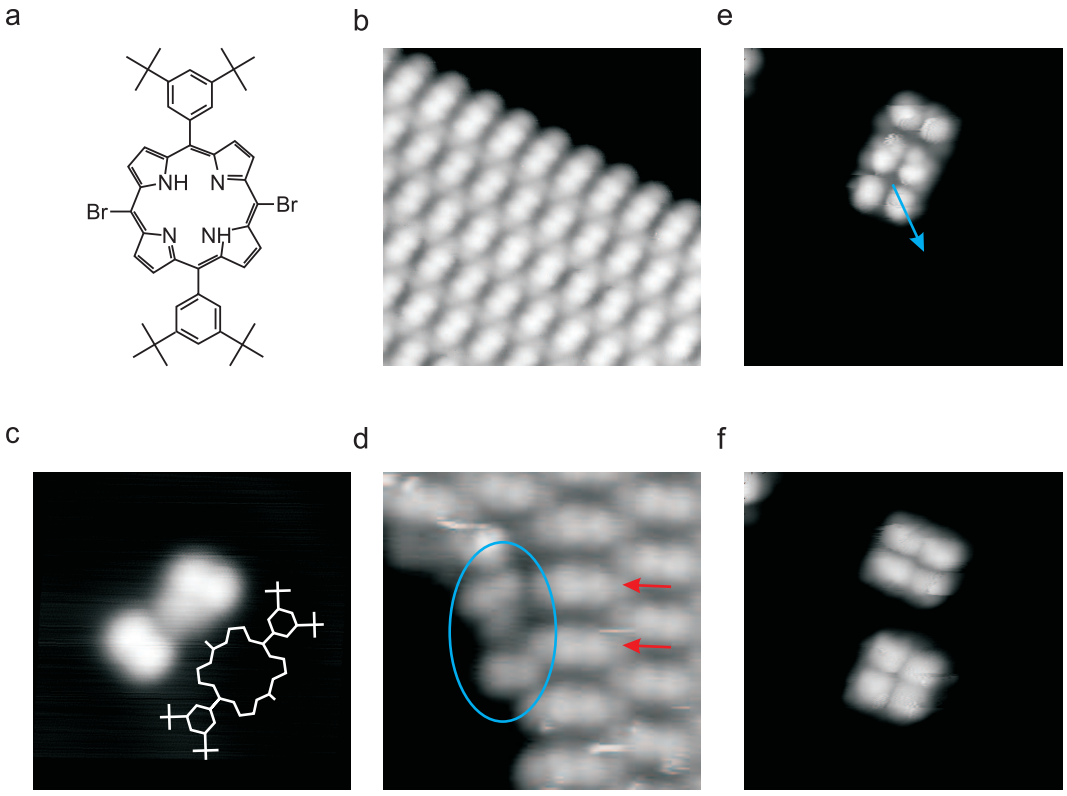

Figure 5.5: **a**, Chemical structure of TB-dBP. **b**, 10x10 nm^2 STM image on Au(111) of an island of TB-dBP molecules. **c**, 6x6 nm^2 STM image of a single TB-dBP and a sketched TB-dBP molecule. **d**, 6x6 nm^2 STM image of an island next to a single molecule which is indicated by the blue ellipse. The red arrows denote the smaller spacing between two bright lobes in an island compared to the distance between the opposite tert-butyl groups of a single porphyrin. **e**,**f**, 11x11 nm^2 STM images **e** before and **f** after lateral constant-current manipulation of a dimer (83 nA, 25 mV). These images were taken before the first heating step to 520 K. The blue arrow indicates the manipulation path.

island. Fig. 5.6b shows the line scan of a single molecule and of an island (Fig. 5.6a). The tert-butyl groups of the single molecule are denoted by a blue and an orange arrow in Fig. 5.6a whereas the red arrow points to the first lobe in the island, which is measured by the line scan. The same color code is used for the arrows in Fig. 5.6b. The peaks in the line scan denoted by the blue and the orange arrow belong to the tert-butyl groups of the single molecule, and starting from the red arrow the peaks correspond to the lobes inside the island. The apparent height of the tert-butyl groups is 0.5 Å lower than the apparent height of the features in the island. Additionally, the spacing between the features in the island is 11 Å, and the distance between the opposite tert-butyl groups of a single porphyrin is 14 Å. These differences lead to the assumption that the TB-dBP molecules in an island stack on top of each other. This is sketched in Fig. 5.7. Before heating the substrate to 520 K few isolated dimers are detected which stack up. Figures 5.5 shows STM images before e and after f lateral constant-current manipulation, and the manipulation path is indicated by the blue arrow. Two piled up dimers were separated by lateral manipulation. This provides an additional indication that the TB-dBP molecules lie on top of each other.

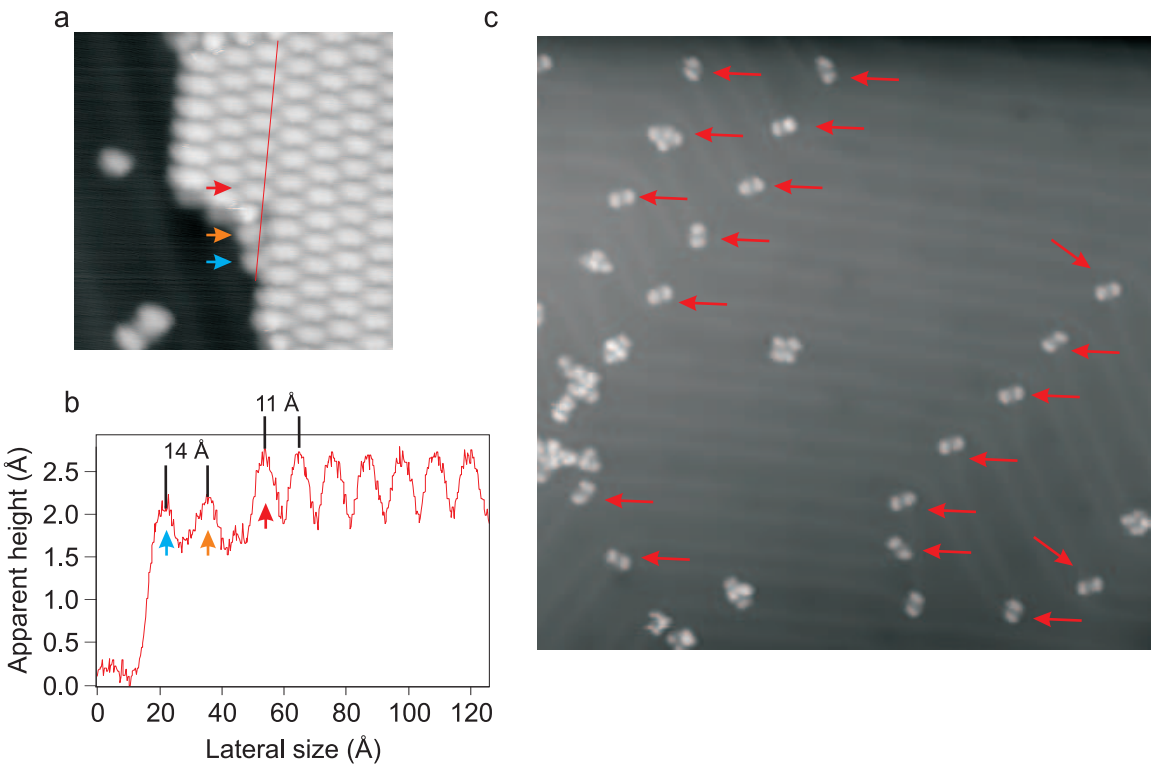

Figure 5.6: **a**, 15x15 nm^2 STM image on Au(111) of an island of TB-dBP molecules. The red line indicates the position of the line scan shown in **b**. The arrows point at the position of the peaks from the line scan **b** in the image **a**. **c**, 60x60 nm^2 STM image after heating the substrate to 520 K. Molecules located at the elbows of the herringbone reconstruction are denoted by red arrows.

After heating the sample to 520 K the islands disappeared and the coverage decreased from 0.17 ML to 0.08 ML. Most of the TB-dBP molecules are monomers, which nucleate at the kinks of the herringbone reconstruction (see red arrows in Fig. 5.6c). Roughly half of the molecules already desorbed after the first heating step, and the growth of larger chains than dimers has not been observed. Heating the surface to even higher temperatures (670 K), results in an empty surface. The four tert-butyl groups decouple the molecules from the surface, which leads to a lower desorption temperature than for dBP and DBDP, which remain on the Au(111) surface at 670 K.

5.1.4 Summary

Three different precursor molecules for the fabrication of porphyrin tapes were studied: dibromo-diphenylporphyrin (dBP), dibromo-tetraphenyl-bisporphyrin (DBDP) and dibromo-bis(3,5-tert-butylphenyl)porphyrin (TB-dBP).

Before heating the substrate the shape of the diBr-di(phenyl)Porphyrin (dBP) is bias dependent. After heating the substrate to 520 K and dehalogenating the molecules the appearance of the porphyrins in STM images changes. Heating the substrate to 520 K does not trigger the polymerization of the molecules, which instead assemble into large islands. Tempering the substrate to 670 K leads to a fragmentation of the molecules. Additionally,

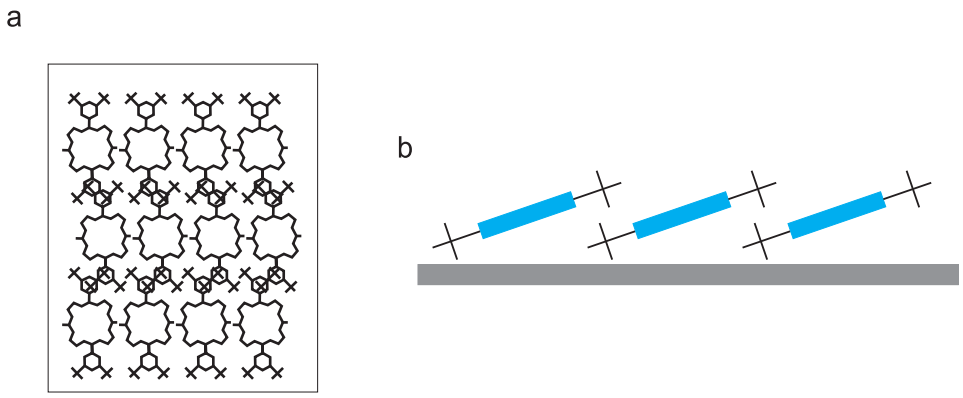

Figure 5.7: Sketch of the possible island structure from **a** top and from the **b** side.

no islands are observed and most of the molecules lie isolated. This is probably caused by a partial dehydrogenation of the molecules [125, 126, 104]. The partial dehydrogenation of the molecules also creates reactive sites at random, which allow the molecules to link in an uncontrolled manner. These defected chains are probably covalently bond since neither lateral nor vertical manipulation could separate them. Even pulling the molecules from the surface was possible.

In case of the polymerization of graphene nanoribbons (GNRs) with anthracene building blocks a successful polymerization is only observed for a dimer and not for a monomer as a precursor molecule (see chapter 5.3.2.2). The rotation of the anthracenes in the building blocks reduces the steric repulsion and enables the covalent linking to anthracene oligomers. Therefore, a dBP molecule has been synthesized by the organic chemists (S. Hecht and co-workers, Humboldt Universität zu Berlin). After heating the substrate to 670 K di(phenyl)prophyrin monomers (36 %) and short chains of three porphyrin-units (1 %) emerge. The monomers and the chains consisting of an odd number of porphyrins (the precursor molecule is a dimer) indicate that the original DBDP dissociated into monomers. The interaction between the surface and the porphyrins in the precursor molecule probably was too strong so that a planar adsorption occurred with a rather small angle between the porphyrin-units. Therefore, the strength of the steric repulsion is not reduced enough.

Porphyrins equipped with tert-butyl groups do not improve the situation. Long chains neither grow after the first heating step nor after a heating step at higher temperatures. Before heating the surface large islands of TB-dBP are observed. However, the height and the spacing of the features do not match the dimensions of a single TB-dBP which points to a stacking of the molecules. Furthermore, the experiments show that the tert-butyl groups decouple the molecules from the surface and reduce the desorption temperature of the molecules. Accordingly after the second heating step the surface is empty. Already during the first heating step to 520 K the coverage drops by ∼50 %. This is one of the limitations of the absent polymerization. Probably also the steric repulsion is another restriction for the growth of porphyrin tapes.

5.2 The Role of the Substrate on the Growth

The choice of the substrate is crucial in molecular self-assembly because the molecule-molecule interaction competes with the molecule-substrate interaction while the ratio between both interactions varies with the coverage. At a low coverage, where each molecule may lie isolated, the molecule-molecule interaction dominates the short-range interactions and the molecule-substrate interaction determines the long-range assembly of the molecules [127]. Close packed islands appear with increasing coverage, which raises the importance of the molecule-molecule interaction. At a high coverage the molecule-molecule interaction defines the short-range ordering as well as the long-range ordering [127]. The structure of the islands can be steered by the choice of the substrate as the shape of the islands is dominated by the molecule-substrate interaction. Combined with on-surface polymerization the shape of the resulting networks or chains can be controlled through the substrate [108].

In addition, the covalent linking probability between the activated molecular building blocks depends on the substrate. On Cu(111) a higher coupling probability has been reported [15], which leads to a chain-like growth of the two dimensional networks. On the contrary, the molecules link less effectively on Au(111) and densely packed islands emerge [15]. If the linking probability is high a molecular building block connects with any activated molecule which lies directly next to it. For a smaller coupling probability the building block diffuses along the island border and might bind to higher coordinated sites [15]. This automatically leads to densely packed islands.

For the synthesis of biphenyl Ullmann used iodobenzene together with copper(I)-thiophene-2-carboxylate, which contains a copper atom. The copper atoms are essential for the reaction as they act as a catalyst [128]. On the Cu(111) surface copper adatoms are available at RT due to the lower energy required to remove an atom from the step edges [114]. The Cu(111) surface is known to be catalytically more reactive than the Au(111) surface [123, 109]. The Cu(111) surface reduces the energy necessary for the dehalogenation. This is a special case of heterogeneous catalysis where catalyst (the surface) and reactant (the molecule) are in a different phase. In general, a catalyst increases the efficiency of a reaction without getting consumed in the process so that the catalyst is able to participate in many reactions [129]. In many cases the surface itself can be seen as catalytically inactive [129]. The active sides, like kink edges, step edges vacancies at the step edge or terrace and surface cluster, are considered as low-coordinated surface atoms with unsaturated valencies [130]. The adsorption strength of these defects must be strong enough to bind the reactant to improve the reaction but also has to be as low as possible to let the reactant leave after the reaction took place [129]. In case of the NO dissociation on Ru(0001) the step edges have been reported to be the active sides. Nitrogen atoms were imaged by STM moving away from the step edges [130]. In case of Cu(111) the energy required to remove an atom from a step is lower compared to Au(111) [114]. Therefore, the active sides on the Cu(111) surface, beside step edges and defects, are copper adatoms, which are available at RT [115].

5.2.1 2,11-dibromohexabenzocoronene

2,11-dibromohexabenzocoronene (diBr-HBC) (Fig. 5.8a) is a small flake of graphene equipped with two bromine atoms in *trans*-geometry. After activation a linear growth of hexa-peri-hexabenzocoronene (HBC) chains is expected. In contrast to the trapezoid-shaped molecules discussed in chapter 5.3, no steric hindrance is supposed to occur which would limit the polymerization. The linking of diBr-HBC was studied on two different noble metal surfaces: Au(111) and Cu(111). An STM study on HBCs (not equipped with bromines) observed isolated molecules on Cu(111) which cover the step edges and terraces at a low coverage [131]. Lateral dimensions of 14 Å from one corner to the opposite corner (in Fig. 5.8a along the bromine axis) and 13 Å from one side to the opposite side (in Fig. 5.8a perpendicular the bromine axis) have been reported for a single HBC [131]. In case of a high coverage above one ML it was reported that the molecules pack in HBC columns due to their large π-system [132].

After sputtering and annealing of the substrate the molecules were evaporated on the surface at RT. Afterwards the sample was cooled down to operation temperature and transferred into the STM. The molecular compounds also contain triBr-HBC, monoBr-HBC and HBC without bromine atoms after the chemical synthesis (S. Hecht and co-workers, Humboldt Universität zu Berlin).

5.2.1.1 Au(111)

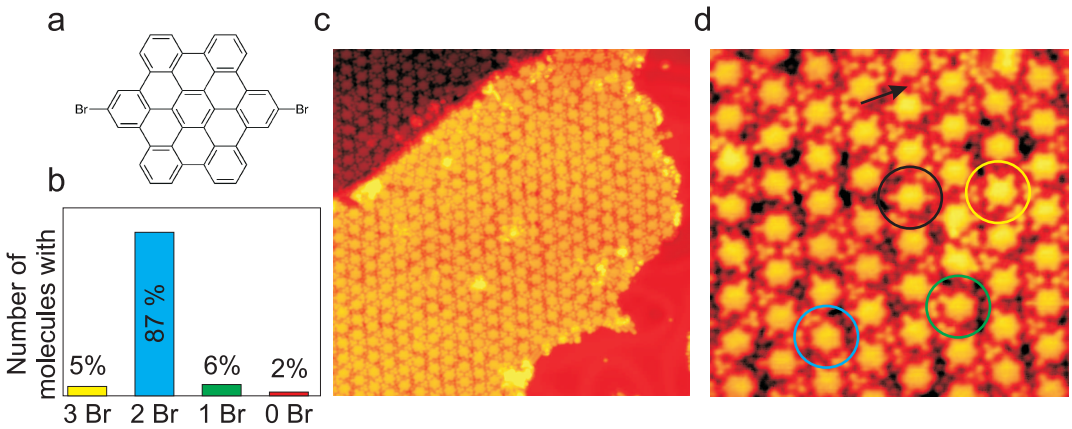

Figure 5.8: **a**, Chemical structure of HBC. **b**, Distribution of HBC species on Au(111) without a heating step. **c**, 39x38nm^2 STM image of diBr-HBC on Au(111). **d**, 13x13 nm^2 STM image of the diBr-HBC on Au(111).

Large islands of densely packed diBr-HBC appear on the Au(111) surface (Fig. 5.8c). This stands in contrast to previously reported results of HBC on Au(111) and Cu(111) where most of the molecules lie isolated from their neighbors [133, 131]. Calculations find a Coulomb repulsion between the hydrogens of HBC as the reason for the isolated molecules [133]. In the case of diBr-HBC such a behavior is not observed. The repulsive interaction between the molecules seems to be weaken if bromine atoms are attached. A single diBr-HBC is indicated by the black circle in Fig. 5.8c, which consists of the HBC core with two bright lobes next to it. The apparent height of these lobes is 1.3±0.1 Å,

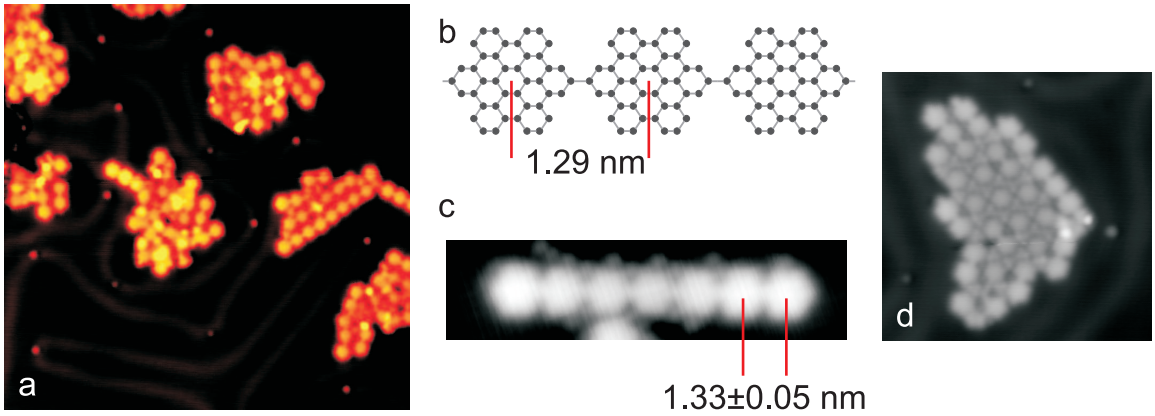

Figure 5.9: **a**, 37x37 nm^2 STM overview after heating the Au(111) to 520 K. **b**, Chemical structure of the covalently bond HBC chain. **c**, 12x3 nm^2 STM image of a HBC chain. **d** 16x16 nm^2 STM image of an island of single HBC molecules after heating the surface to 520 K.

which coincides with the observed (Chapter 5.1.1) and reported height of bromine atoms attached to porphyrins [108]. The bright lobes are, therefore, assigned to bromine atoms. The lateral full width at half maximum dimensions of diBr-HBC are 1.93±0.04 nm along the bromine axis and 1.29±0.05 nm perpendicular to it. The length perpendicular to the Br axis is in good agreement to previous results [131]. Due to the attached bromines the length along the Br axis is 0.53 nm larger than for the pure HBC [131]. Gas phase calculations find a length of 1.50 nm. This is slightly smaller as the calculations measure the length between the center of the opposite bromine atoms, whereas experimentally the full width at half maximum is observed. The presence of intact molecules is in agreement with expectations since no heating step has so far been conducted to trigger the activation.

Three more species were detected on the substrate, which are also shown in Fig. 5.8d: HBC equipped with three bromine atoms (yellow circle), one (green circle) and none (blue circle) bromine atom. In STM images the species differ in the amount of lobes attached to the HBC core. The length perpendicular to the Br axis is the same for all four species. Their abundance on the surface is 87 % of diBr-HBC, 5 % of triBr-HBC, 6 % of mono Br-HBC and 2 % of HBC (Fig. 5.8b). It is unlikely that the species with less than two bromines are completely or partially activated diBr-HBCs. So far no reports exist in the literature on the activation of molecular building blocks equipped with bromines on Au(111) at RT. Activation was found to set in at 370 K and to be completely finished at 520 K [107]. Although the HBC molecules are mobile at RT and arrange in islands no polymerization in chains was detected. This supports the assumption that mono Br-HBC and HBC, 8 % in total, are a nonreactive impurity of the diBr-HBC compounds. In contrast, the activated diBr-HBCs by bromine dissociation on the surface, polymerize to HBC chains. Between the single HBC islands small lobes fill up the space as denoted by the black arrow in Fig. 5.8d. These lobes probably are bromine atoms (see next section). Further evidence of the nonreactive character of HBC is provided through the heating of the substrate to 520 K. At this temperature most of the molecules are activated and oligomers of HBC appear. Beside chains, islands of single HBC exist (Fig. 5.9d), which point to the nonreactive species of HBC as well. These HBCs are part of the molecular powder and do not result from activation in the evaporator or on the surface.

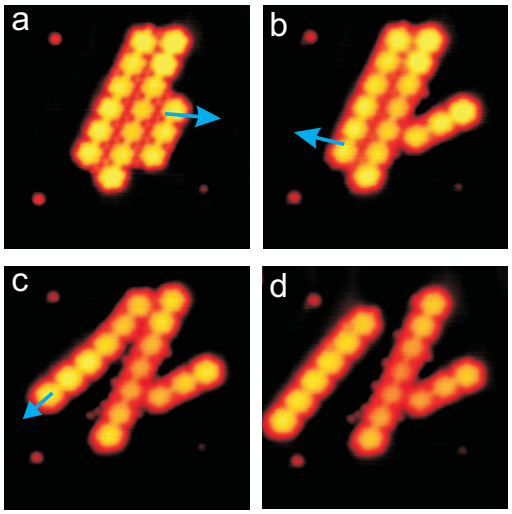

Figure 5.10: $12x12nm^2$ STM images of HBC chains on Au(111). The blue arrows indicate the tip path of the lateral constant-current manipulation (150 nA and 25 mV).

As mentioned above, chains of HBC appear after the activation (Figures 5.9a and c). The length of these chains is rather short and limited to a maximum of nine units. The HBCs, which are equipped with one bromine, act as a stopper since only one side is reactive. Such monoBr-HBCs stop the chains from growing further, but this is only one explanation for these short oligomers. 56 % of the chains consist of two or three HBC units. This is much shorter than the average length of 16 units which results from the composition of the molecular powder. 6 % of the molecules stop the growth of the HBCs equipped with two (87 %) or three bromines (5 %). The 2 % of bromines without bromines do not contribute to the molecular chains. In total 98 % of the HBCs have one bromine atom or more, and out of these 6 % are equipped only with one bromine atom. As $98/6 \approx 16$, every 16th molecule is equipped with one bromine. The diffusion barrier, which increases with the length of the chain, also limits its growth. The required tunneling resistance to manipulate a HBC chain with the STM tip is much lower compared to other molecules (discussed in detail below). This points to a stronger adsorption energy of the HBCs on Au(111) and might be explained by the extended π system of the HBC. With the stronger adsorption energy a higher diffusion barrier is expected that limits the length of the HBC chains.

The center-to-center distance of two HBCs in a chain amounts to 1.33±0.05 nm where the maximum of the line scan is attributed to the center of the HBC (see Fig. 5.9c and Fig. 5.12b and c). This is in very good agreement with gas phase calculations that predict a distance of 1.29 nm, which indicates a covalent carbon-carbon bond between the HBCs (Fig. 5.9b). To prove the covalent nature of the bond lateral constant-current manipulation was performed on a HBC chain. As explained in chapter 2.7 the tip approaches from the scanning position towards the substrate until it reaches a given setpoint of the current. During the next step the current is kept constant while the tip follows a predefined path. As setpoint a current of 150 nA and a bias voltage of 25 mV was necessary to move the molecular chain. This corresponds to a tunneling resistance of 167 kΩ which is very low compared to other manipulation experiments (For an anthracene oligomer in chapter 5.3.2.2: 850 kΩ; For a prophyrin-dimer in chapter 5.1.1: 327 kΩ). Figures 5.10a-d show images before and after each manipulation step. The manipulation path is indicated by the blue arrow. First, the small chain consisting of three units was separated from the island. Then the longer chain

was pulled away from the island and to the lower left corner of the image. Although during these manipulation experiments the STM tip was approached at the end of the chain, the complete chain followed the first HBC unit. In contrast to weakly coupled chains [109], no bond breaking was observed, which emphasizes the covalent nature of the bond between the HBC units.

5.2.1.2 Cu(111)

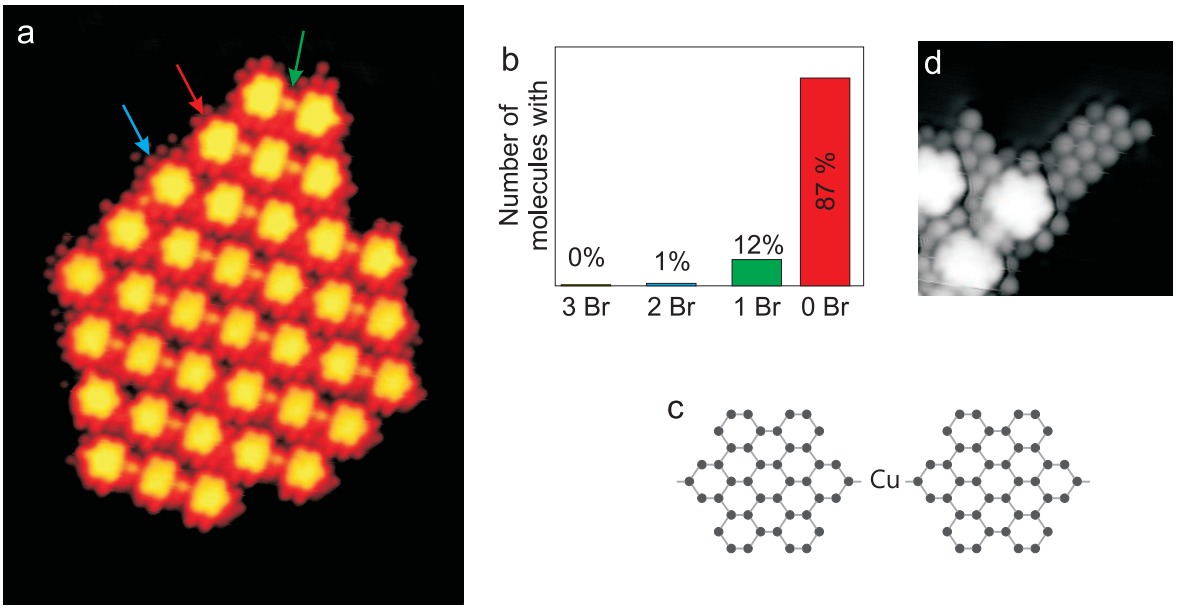

Figure 5.11: **a**, 13x17 nm^2 STM image of a HBC island on Cu(111) without heating the substrate. Blue arrow indicates a single HBC molecule. Red arrow denotes a HBC chain. Green arrow points out a protrusion between two HBCs in a chain. **b**, Distribution of HBC species on Cu(111) without heating step. **c**, Chemical structure of HBC chains on Cu(111). **d**, 5x5 nm^2 STM image on Cu(111) of the atoms surrounding the HBC islands, which are assumed to be bromines.

Similar to Au(111) the molecules are evaporated onto the clean Cu(111) surface at RT. Without heating the surface the sample is cooled down to 10 K. In contrast to the Au(111) surface, chains of HBC are observed. The activation of the molecules did not occur during the deposition because the evaporation temperature during the preparation on Cu(111) (597 K) was even lower than on Au(111) (624 K).

The copper surface is known to be catalytically more active than the gold surface. On Cu(111) copper adatoms are available at RT [115] due to the lower energy required to remove a copper atom from the step edges [114], and the bromine dissociation on Cu(111) at RT has been previously reported [109]. In agreement with these results 87 % of the HBC molecules have already lost both bromines in the present thesis. Only 12 % are partially dehalogenated and less than 1 % are fully intact. Similar to the results on Au(111) the HBC chains are surrounded by bright lobes (Fig. 5.11d). The distance between these lobes is 4.4±0.1 Å. This corresponds to the reported $(\sqrt{3} \times \sqrt{3})$R(30°)-Cl/Br overlayer on Cu(111) [134]. The nearest neighbor distance on Cu(111) is 2.55 Å [117], which leads to a

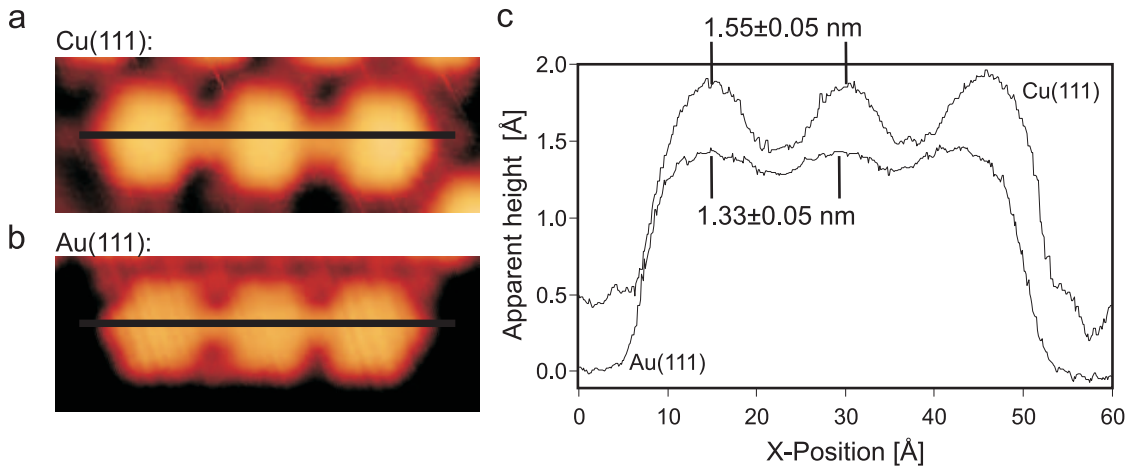

Figure 5.12: **a**,**b**, 5.5x2.0 nm^2 STM images of a HBC trimer on **a** Cu(111) and on **b** Au(111). The black lines indicate the position of the line scan shown in **c**.

reported distance of $2.55 \times \sqrt{3} = 4.41$ Å. This coincides with the measured distance of the observed lobes and supports the assumption that these are bromines.

Beside single molecules (indicated by the blue arrow in Fig 5.11a), chains of HBC are visible in Fig. 5.11a (denoted by the red arrow). As on Au(111) the chain length is rather short with a maximum length of six units. However, 33 % of the chains consist of only two units (thus dimers) and 24 % are trimers. In contrast to Au(111), a bright lobe appears between the HBC chains on Cu(111) (see green arrow in Fig. 5.11a). The distance between two HBC centers connected to a chain equals 1.55±0.05 nm (see Fig. 5.12a and c). This value is slightly larger than on Au(111), where it amounts to 1.33±0.05 nm (Fig. 5.12b and c) and, thereby, disagrees with the calculated value of 1.29 nm for a covalent bond. In contrast, the calculated distance of a metal-ligand bond, thus C-Cu-C, amounts to 1.52 nm, which matches the measured distance (1.55±0.05 nm) of a HBC chain on Cu(111). The bright lobe between the HBCs is attributed to the copper atom which is clearly visible in STM in agreement with previous studies [135, 109, 123]. In the literature it has been reported that metal-ligand bonds can be cleaved by STM manipulation [109]. Therefore, lateral manipulation experiments have been performed in

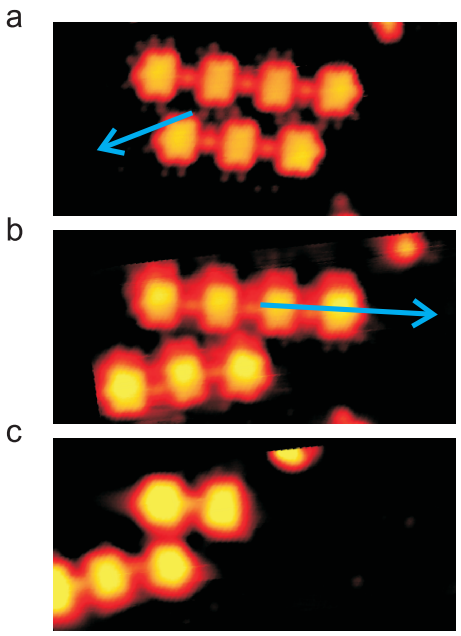

Figure 5.13: **a**,**b**,**c**, $10x5nm^2$ STM images of HBC chains on Cu(111). The blue arrows indicate the tip path in the lateral constant-current manipulation. **a**, Before the manipulation. **b**, After the first manipulation (100 nA and 25 mV). **c**, After the second manipulation (100 nA and 17 mV).

constant-current mode. Fig. 5.13 shows images before and after the manipulation with the blue arrow indicating the tip path. For the first manipulation a setpoint of 100 nA and 25 mV was used (500 kΩ) to move the three unit long chain to the left side (Fig. 5.13b). The tip-sample distance of the next manipulation was reduced by using a setpoint of 100 nA and 17 mV (170 kΩ) in order to increase the force between tip and molecule. While moving the four unit long chain to the right side the bond broke (Fig. 5.13c). Compared to the manipulation experiments on Au(111) with a tunneling resistance of 167 kΩ, which is equivalent to an even smaller tip-sample distance, no bond cleavage was observed. This provides an additional indication of two different bonding types on Cu(111) (metal-ligand bond) and Au(111) (covalent bond).

Heating the Cu(111) substrate to 450 K did not create covalently linked chains as would be expected [135]. Instead, most of the HBC molecules desorbed and an empty surface has been detected. On Au(111) a heating step to 520 K was necessary to activate the HBC molecules. On Cu(111) the activation already occurs at RT due to the higher catalytic reactivity of the Cu(111) surface [123, 109]. This is useful for molecules with dissociation or desorption temperatures below the dehalogenation temperature. A difference in the bond is observed on Au(111) and Cu(111), whereas on Au(111) the HBC chains are covalently bond on Cu(111) a slightly weaker metal coordination bond is formed. Fig. 5.14 summarizes the results on HBC.

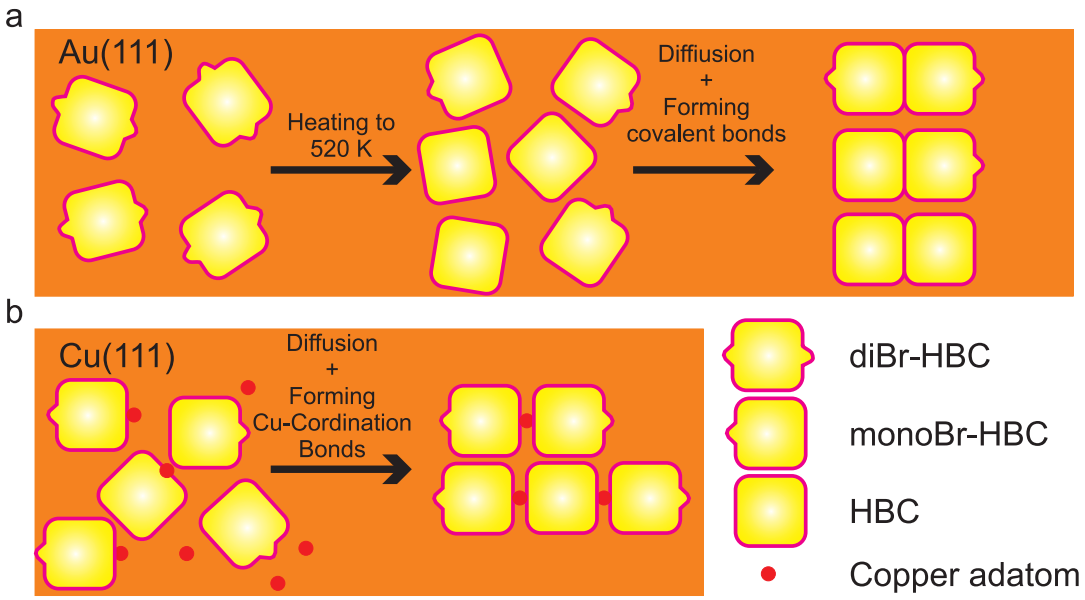

Figure 5.14: Sketch of the polymerization process on **a** Au(111) and **b** Cu(111).

5.2.2 2,3-dibromoanthracene

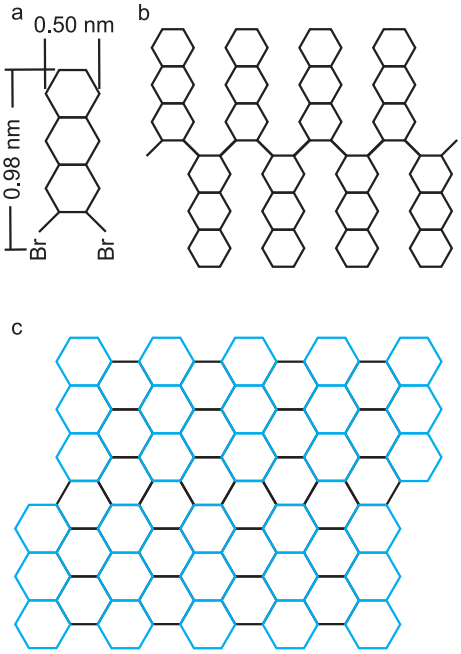

Figure 5.15: **a**, Chemical structure of tdBA. **b**,**c**, Desired structure after the **b** first heating step (activation) and **c** second heating step (dehydrogenation).

2,3-dibromoanthracene (tdBA) is an anthracene with two bromines connected at the same end of the molecule (Fig. 5.15a) and was studied as possible precursor molecule for growing GNRs [104]. The concept of the growth is sketched in figures 5.15b and c. In the first stage a tape of anthracenes is desired, which should be realized by the activation of the tdBA molecules with the first heating step (Fig. 5.15b). A second heating step is necessary to cyclodehydrogenate the oligomers to fabricate smooth and narrow GNRs with armchair edges (Fig. 5.15c). However, the polymerization of the molecules to anthracene oligomers is one of the conditions which has to be proven first.
As substrates the Au(111) and the Au(100) surfaces were used. The Au(111) surface reconstructs in the herringbone pattern with alternating fcc and hcp regions separated by ridges [35]. The hcp region and the fcc regions have a width of 25 Å and 38 Å, respectively [21]. Gas phase calculations of tdBA find a length of 10 Å and a width of 5 Å (see Fig. 5.15a). The hcp area is twice that wide and the fcc region is more than three times wider than the length of a tdBA molecule. Compared to the dimensions of the tdBA molecule, the periodicity of the herringbone reconstruction is large. On the Au(100) surface parallel corrugations appear every 14.4 Å [20], which is close to the length of the molecule.

5.2.2.1 Au(111)

The tdBA molecules (Fig. 5.15a) were deposited on the clean Au(111) surface at RT and cooled down without a heating step. The evaporation temperature was 400 K and a coverage of 1 ML was observed. The molecules are mobile at RT and assemble in large islands of parallel lying molecules which align slightly rotated to the crystal orientations

of the Au(111) surface. In Fig. 5.16a the blue and green lines denote the orientations of the molecule island and of the crystal, respectively. The angle between the three different orientations of the molecule islands is 120°, which coincides with the 120° angle between the crystal orientations of the Au(111) reconstruction [35]. Between the three different island domains boundaries appear where the molecular order is disturbed (indicated by the red arrow in Fig. 5.16a). The shape of a single molecule is identified by comparing the shape of molecules located at a boundary with the shape of molecules inside an island. In figures 5.16b and c the sketched chemical structure indicates a single tdBA molecule. Each molecule appears as a rod with two bright lobes at one terminus. The apparent height of these two bright lobes is 1.3±0.1 Å which is in agreement with the reported and measured apparent height of bromine atoms attached porphyrins and HBCs (compare with [108] and chapter 5.1.1 and 5.2.1). Therefore, the rod is assigned to the anthracene core and the two bright features belong to the bromine atoms which leads to the assumption that the activation has not occurred yet.

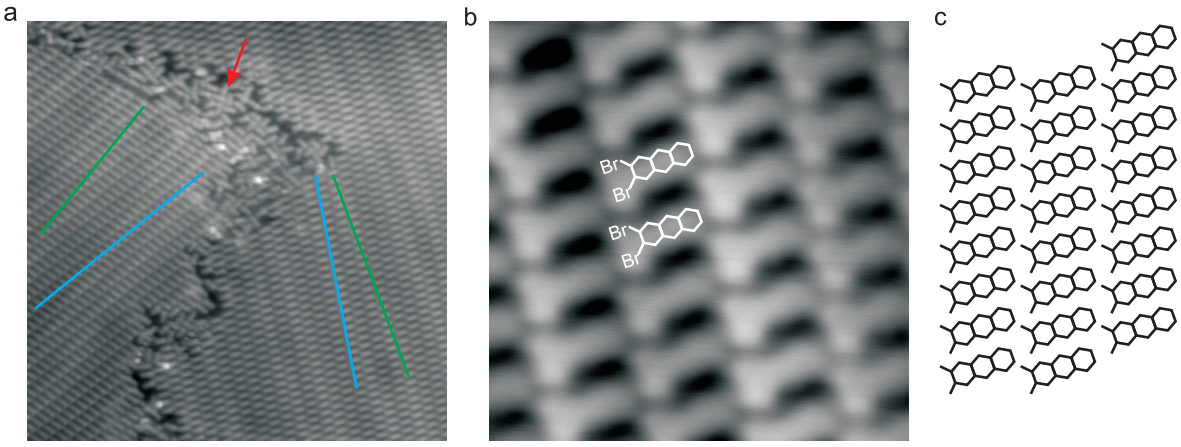

Figure 5.16: **a**, 38x38 nm^2 STM overview of tdBA on Au(111) without a heating step. The blue and green lines denote the molecule-island and crystal orientation, respectively. The red arrow indicates a domain boundary with a reduced order. **b**, 10x10 nm^2 STM image. Chemical structures indicate the adsorption geometry of the molecules. **c**, Sketched arrangement of the tdBA islands.

At the domain boundaries a few molecules lie isolated with the gold surface as a reference for the measurement of the full width at half maximum of the tdBA molecule. A length of 1.24±0.04 nm and a width of 0.49±0.04 nm was detected, whereas gas phase calculations result in a 0.98 nm long and a 0.50 nm wide tdBA (see Fig. 5.15a). The mismatch in the length probably results from different distances measured in theory and experiment. In gas phase calculations the distance between the center of the bromine and the corresponding hydrogen atom was calculated (see Fig. 5.15a), whereas in the experiments the full width at half maximum of the tdBA molecule was measured with respect to the Au(111) surface. The full width at half maximum is expected to be larger. In the islands the tdBA molecules arrange in rows of parallel molecules which are shifted to the neighboring rows (Fig. 5.16c).

The coverage dropped to 0.69 ML after heating the substrate to 520 K. The molecules are dehalogenated and the previously observed islands disappear (Fig. 5.17a). The desired tape of anthracenes did not assemble on the surface but two other species polymerized. One species are the star-shaped molecules which assemble in well ordered islands (see Fig. 5.17d). The other species appears as rods in STM images (Fig 5.17e). These rods

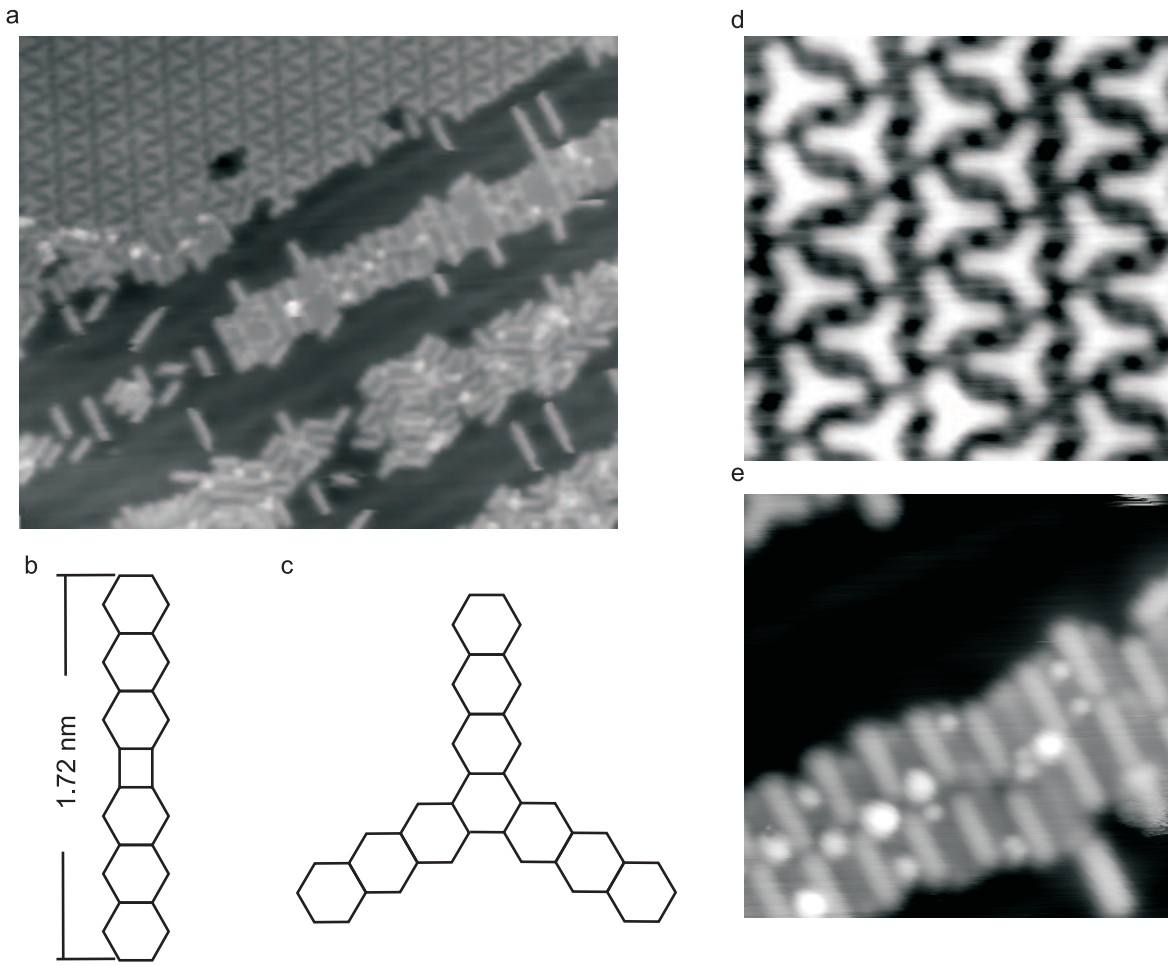

Figure 5.17: **a**, 43x43 nm^2 STM overview of tdBA on Au(111) after heating to 520 K. **b**,**c**, Assumed chemical structure of **b** the rod-shaped and **c** the star-shaped molecules. **d**, 8x8nm^2 STM image of star-shaped molecules. **e**, 10x10nm^2 STM image of rod-shaped molecules.

(1.97±0.09 nm) are larger than the single tdBA molecule (1.24±0.04 nm) and are assigned to a tdBA dimer. The length of the rod dimer is 1.97±0.09 nm, which is slightly larger than the calculated value of 1.72 nm (Fig. 5.17b). The mismatch between gas phase calculations and experiments can again be explained by the differently obtained distances. Gas phase calculations determine the distance between the center of the opposite hydrogen atoms (Fig. 5.17b), and in the experiments the full width at half maximum of the rod was measured with respect to the Au(111) surface. If the model is correct both bonds are presumably saturated which blocks further growing (see the chemical structure in Fig. 5.17b). The star-shaped molecule (Fig. 5.17d) consists of three single anthracene molecules, whereas each shares a bond with the two other anthracenes (see Fig. 5.17c for the chemical model). The ratio between stars and rods is nearly 50:50 on Au(111). In both cases, rods and stars, all bonds are saturated and neither further growth nor a change in the structure is expected which explains the limitations to these discrete sizes.

The coverage dropped to 0.40 ML after heating the substrate to an even higher temperature of 670 K. However, the molecular compounds do not change and the molecules remain

either rods or stars. The molecules of both species become repulsive as, instead of islands, single and isolated molecules are observed. After heating the porphyrin-based precursor molecules to 670 K a similar repulsive behavior arose (see chapter 5.1.1 and Fig. 5.2b). Heating the substrate to 670 K probably leads to a partial dehydrogenation of the molecules [126, 104] and, thereby, a negative charging, which makes the molecules repulsive.

5.2.2.2 Au(100)

Instead of Au(111), the Au(100) surface is used as a template for the polymerization. The parallel atomic rows of the Au(100) surface are separated by a distance of 1.44 nm [20]. This distance is smaller compared to the periodicity of the herringbone reconstruction [35], and an influence of the reconstruction on the alignment of the molecules is expected. Similar to the preparation on Au(111) the molecules were deposited on a clean Au(100) sample at RT. The evaporation temperature of 390 K was slightly lower. Immediately after finishing the evaporation the sample was cooled down and transferred into the STM. The coverage was 1 ML, and the molecules assembled into large islands. The appearance of the tdBA is similar to the results gained on Au(111) and the chemical structure is sketched in Fig. 5.18a. However, compared to Au(111), the neighboring molecules are mirrored leading to a more dense packing. The molecules are not activated yet since both bromines are clearly visible in STM images (Fig. 5.18a). The orientation of the tdBA molecules on Au(100) is promising for the growth of anthracene tapes as the neighboring molecules are mirrored. This corresponds to the sketched arrangement shown in Fig. 5.15b.

Heating the substrate to 520 K leads to the activation of the molecules and a drop in the coverage to 0.94 ML. With the dehalogenation of the molecules rods emerge (Fig. 5.18b). These rods have a similar appearance and length as the dimers formed on Au(111) (see Fig. 5.17e) and their length of 1.96±0.04 nm also corresponds to the results on Au(111) (1.97±0.09 nm). Different to Au(111), the second species, the star-shaped trimer, does

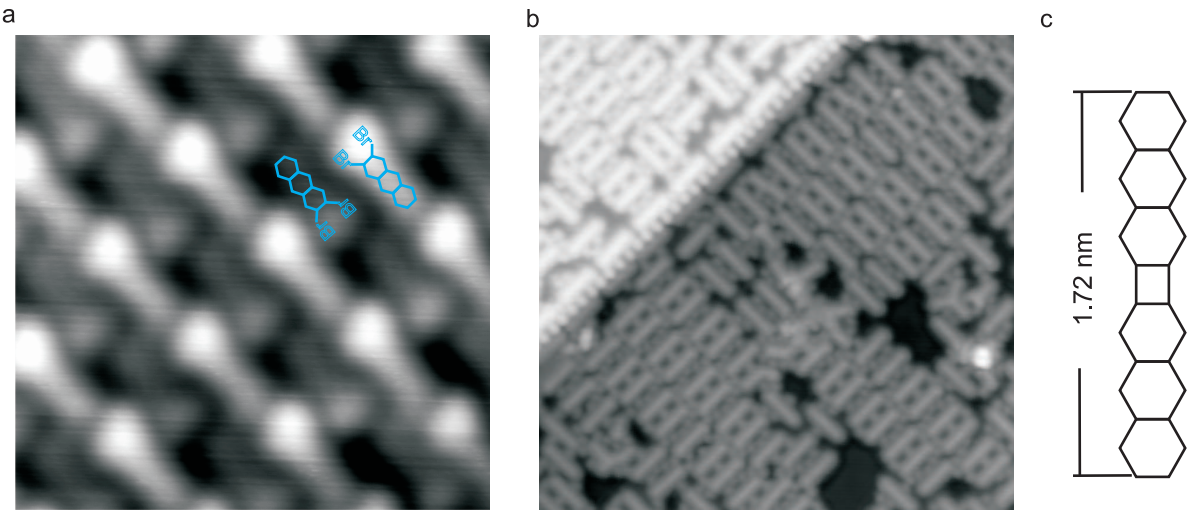

Figure 5.18: **a**, 5x5 nm^2 STM image on Au(100) of tdBA without heating the sample. Chemical structure sketches the tdBA molecules. **b**, 20x20 nm^2 STM image after heating the substrate to 520 K. **c**, Chemical structure of the rod-shaped molecules.

not occur. So, the corrugation of the Au(100) surface seems to suppress the growth of the

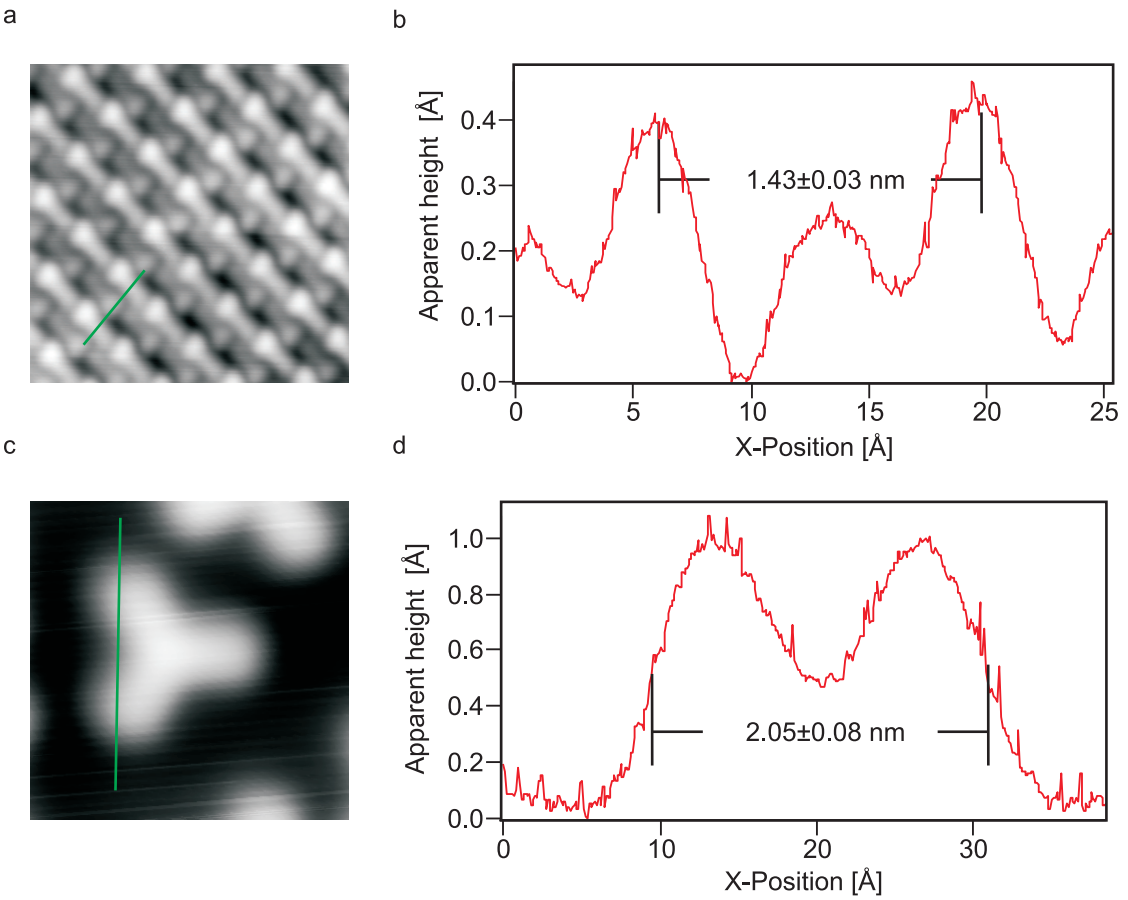

Figure 5.19: **a** 8x8 nm^2 STM image on Au(100) of tdBA without heating the sample. The green line indicates the position of the line scan shown in **b**. **c**, 4x4 nm^2 STM image on Au(111) of a star-shaped trimer. The green line indicates the position of the line scan shown in **d**.

star-shaped trimer and favors the rod-like structure. The high coverage makes the analysis of the alignment of the tdBA molecules with respect to the surface reconstruction difficult as no STM images of the pure Au(100) surface together with molecules exists.
However, there might be a relation of the bright dark pattern of the tdBA molecules, which is observed before heating the sample, to the surface reconstruction (Fig. 5.19a). The distance between two bright molecules equals 1.43±0.03 nm (see figures 5.19a and b). This coincides with the spacing of the atomic rows of the Au(100) surface, which might provide an evidence that the molecules are aligned parallel to the atomic rows. As mentioned before, beside rods, no other structures were found. The star-shaped trimers, which were observed on Au(111) after heating the substrate to 520 K (Fig. 5.17d), are suppressed in the case of Au(100). The distance between the atomic rows is 1.44 nm, which is smaller than the distance between the two anthracene of the trimer as shown by the green line in Fig. 5.19c. Therefore, the reconstruction of the Au(100) surface probably causes a preferential growth of the anthracene dimers. Although the alignment of tdBA is promising before the first heating step no traces of anthracene tapes are observed. Both bonds of the anthracenes are saturated, and heating the substrate to 670 K does not change the structures but leads to a slight decrease of the coverage to 0.5 ML.

5.2.3 Summary

Based on the results of this research the substrate has a huge influence on the final product. For both molecules, 2,11-dibromohexabenzocoronene (diBr-HBC) as well as 2,3-dibromoanthracene (tdBA), the final product depends on the chosen surface. Au(111) and Cu(111) differ in their catalytic reactivity [123, 109]. In case of diBr-HBC a polymerization occurs without heating the Cu(111) substrate. This is important for molecules with a low dissociation or desorption temperature. On Au(111) a heating step to 520 K is required for the activation and the polymerization. The distance between two neighboring HBC units in the synthesized chains on Au(111) and Cu(111) is different as the HBC oligomers on Cu(111) are slightly larger. On Au(111) a covalent bond connects the chains, whereas on Cu(111) a Cu-atom links the HBCs by a metal-ligand bond. However, on both surfaces the average chain length is very short. On Cu(111) and Au(111) 57 % and 56 % of the chains consist of two or three HBCs, respectively. On Cu(111) this might be related to the fact that the sample was not annealed for the fabrication of the chains. On Au(111) the high adsorption energy may cause a larger diffusion barrier. In case of Au(111) a very high current setpoint is required to manipulate the HBC chains with the STM tip. The tunneling resistance for lateral constant-current manipulation was 167 kΩ (for comparison see anthracene oligomer in chapter 5.3.2.2: 850 kΩ; prophyrin-dimer in chapter 5.1.1: 327 kΩ).

The islands of tdBA are similar on Au(111) and Au(100) before heating the substrate. In both cases the molecules align parallel to each other. The only difference is that the neighboring molecules are mirrored on Au(100) leading to a denser packing. Additionally, a bright dark pattern of the molecules is observed on Au(100). This pattern is probably related to the reconstruction of Au(100) as the spacing of the pattern coincides with the spacing of the reconstruction, which provides evidence that the molecules align parallel to the atomic rows of the Au(100) surface. Heating the Au(111) substrate leads to two different species: A dimer in rod-shape and a trimer with a star-shape appearance in STM images. The abundance of the dimer and the trimer is nearly the same on Au(111) after a heating step to 520 K. In case of Au(100) only one of the species is synthesized after heating the substrate to 520 K. The star-shaped trimer is probably suppressed by the surface corrugation of Au(100). The dimensions of the trimer are larger than the space between the atomic rows of the surface which could provide the explanation for the preferred growth of dimers on Au(100).

5.3 Polymerization of Graphene Nanoribbons

An obvious reason for the use of graphene-based molecular wires is the high carrier mobility of graphene itself. To achieve a carrier mobility as high as 100,000 $cm^2V^{-1}s^{-1}$ high quality graphene is required, which is obtained by mechanical exfoliation [90]. Sometimes even a special substrate like hexagonal boron nitride is necessary [136], and the transport probability directly reflects the quality of the graphene sheet [137]. By using electron beam lithography GNRs can be produced with a width down to ∼20 nm [13]. With chemical etching GNRs of a width as narrow as 5 nm are fabricated [13]. Despite all that, it is challenging to fabricate GNRs with well-defined width and edge structures using top-down techniques. Recently, an edge roughness of 5 nm has been reported [13]. The edge structure can be improved by Joule heating [103]. Applying a bias voltage above 1.6 V to graphitic nanoribbons leads to a reconstruction of the edge shape. A disordered edge structure acts like a resistance, which causes a rearrangement of the edge atoms to well-ordered armchair or zigzag edges [103].

This chapter presents several molecular building blocks for the synthesis of GNRs on the surface. This bottom-up technique automatically leads to well-defined width and edge structures of the ribbon, which can be controlled by the molecular building blocks. A successful approach of growing GNRs by using DBDA precursor molecules has been demonstrated by the group of Fasel [104], which is discussed in section 5.3.2.2.

5.3.1 Trapezoid-Shaped Building Blocks

Fig. 5.20 sketches the basic idea behind the synthesis of GNRs through trapezoid-shaped precursor molecules (5,14-dibromotribenzo[ef,hi,o]triphenyleno[11,12,1,2-uvabc]ovalene). Activating these molecules should trigger the polymerization and form an oligomer. In the second heating step the molecules are dehydrogenated and the cyclization reaction results in narrow armchair GNRs.

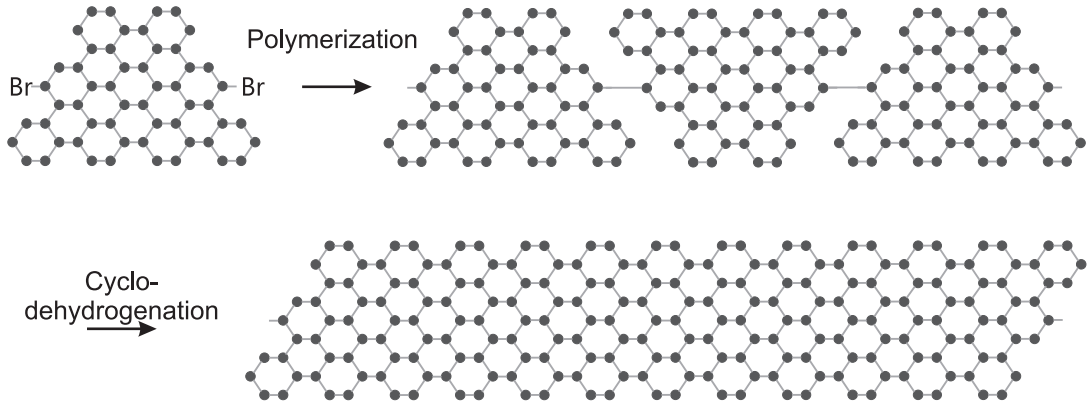

Figure 5.20: Sketched polymerization of trapezoid-shaped GNRs.

5.3.1.1 Tribenzo[ef,hi,o]triphenyleno[11,12,1,2-uvabc]ovalene

At 700 K the evaporation temperature of the 5,14-dibromotribenzo[ef,hi,o]triphenyleno[11,-12,1,2-uvabc]ovalene (TPO) molecules is extremely high and the activation is expected to happen in the doser [14]. In case of tetra(4-bromophenyl)porphyrins it has been reported that the dehalogenation occurs during the deposition at an evaporation temperature above 590 K [14]. Although the sample temperature was at RT during the deposition activated molecules were anticipated. Nevertheless, no oligomers were detected and only single trapezoid-shaped molecules are observed in STM images.

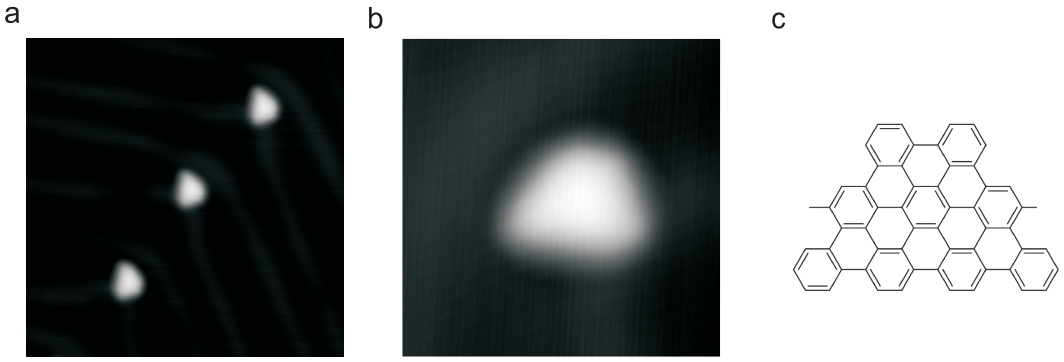

Figure 5.21: **a**, 20x20 nm^2 STM image after heating the Au(111) sample to 520 K. **b**, 5x5 nm^2 STM image of a single molecule. **c**, Chemical model of the tribenzo[ef,hi,o]triphenyleno[11,12,1,2-uvabc]ovalene molecule.

The appearance of the molecules do not change upon a heating step to 520 K. The STM images before and after the heating step give no evidence for the presence of bromine atoms. Figures 5.21a and b show completely flat and homogenous trapezoid-shaped graphene flakes. Only single molecules are detected but no chains.

After completing the experiments missing bromines are found as the main reason why the molecules are prevented from polymerizing into chains. During the organic synthesis of the molecules (S. Hecht and co-workers, Humboldt Universität zu Berlin), more precisely during the planarization of the molecules, the bromines were unintentionally removed so that a linking on the surface was impossible. The chemical model of the deposited molecule tribenzo[ef,hi,o]triphenyleno[11,12,1,2-uvabc]ovalene is shown in Fig. 5.21c. The problem in the synthetic process explains the lack of polymerization on the surface. To reduce the steric hindrance tert-butyl groups were attached to the TPO, and a not fully planarized version of the molecule was synthesized (S. Hecht and co-workers, Humboldt Universität zu Berlin).

5.3.1.2 1,4-Bis(4-bromophenyl)-2,3,6,11-tetraphenyltriphenylene

An evaporation temperature of 500 K is required for depositing the 1,4-Bis(4-bromophenyl)-2,3,6,11-tetraphenyltriphenylene (TPP) molecules onto the clean Au(111) surface (Fig. 5.22a shows the chemical model). These molecules, equipped with bromines, arrange in small islands consisting of three or four molecules (Figures 5.22b and d). Also large and well-ordered islands of TPP appear as shown in Figures 5.22c and e. In addition to the TPP

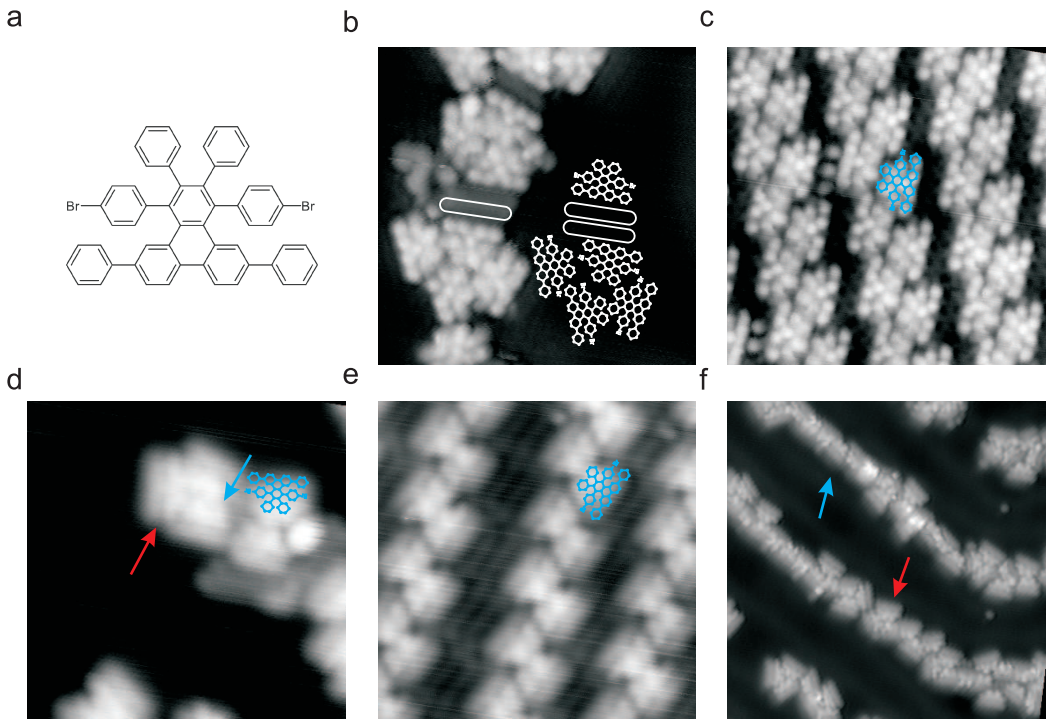

Figure 5.22: **a**, Chemical structure of the TPP molecule. **b**,**d**, 9x9 nm^2 STM images on Au(111) of small islands **b** with and **d** without a functionalized tip without heating the sample. In **d** the red and the blue arrow denote a molecular island and a bright lobe at the short side of the molecule, respectively. The island is sketched on the right side of **b**. **c**,**e**, 9x9 nm^2 STM images of large islands **c** with and **e** without a functionalized tip without heating the sample. **f**, 20x20 nm^2 STM image after heating the sample to 520 K. The red and the blue arrow indicate a molecular island and a structure which could be a molecular chain, respectively. The blue outlines indicate a single molecule in image **c**, **d** and **e**.

molecules, rod-shaped molecules are found, which separate the TPP molecules and are probably solvents (they are barely visible in Fig. 5.22c). Alkane chains show a similar appearance in STM [138] and after the first heating step the rod-shaped molecules desorb. The low desorption temperature and the characteristic shape of these rods support the interpretation that they are solvents.

With a metallic tip the molecular structure is very well resolved. A dark line appears in the middle of the molecule (denoted by the red arrow in Fig. 5.22d) and at the short top two bright lobes emerge (indicated by the blue arrow in Fig. 5.22d), which are assigned to two phenyl rings. The structure of a single molecule is highlighted in Fig. 5.22b. Functionalizing the tip, probably with a bromine, improves the resolution even further and allows to make the single phenyl rings of the molecule visible. The difference in the resolution for the small and the large islands is shown in Figures 5.22b, d and c, e, respectively.

As mentioned above, heating the substrate to 520 K leads to the desorption of the rod-shaped molecules. The coverage then decreases from 0.54 ML to 0.40 ML, which is probably caused by the desorption of the rod-shaped molecules. Most of the TPP molecules arrange into smaller islands of three or four molecules. Apart from single molecules (pointed out by the red arrow in Fig. 5.22f) a few chains are observed (indicated by the blue arrow in

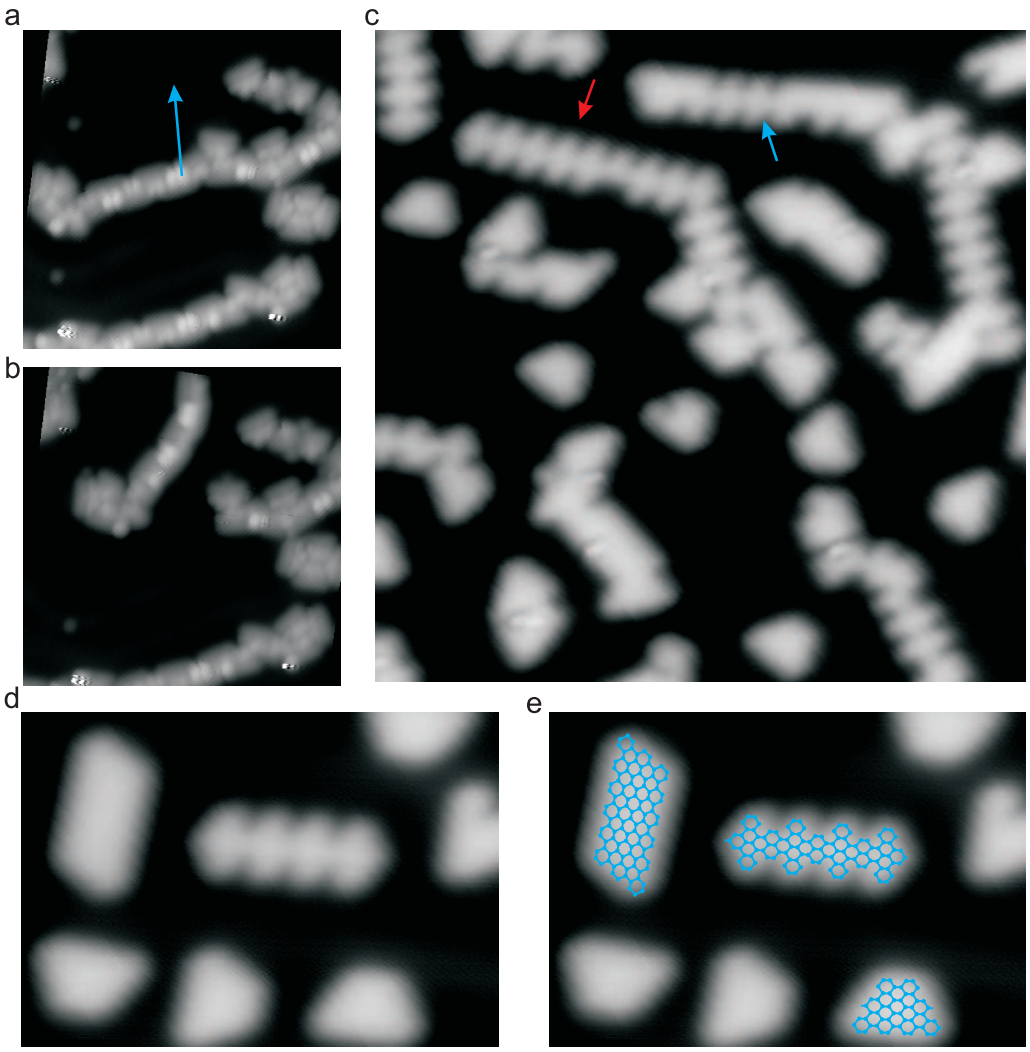

Figure 5.23: **a**,**b**, 15x15 nm^2 STM images of TPP on Au(111) after heating the sample to 520 K. **a** before and **b** after a lateral constant-current manipulation (10 nA, 0.05 V). The blue arrow indicates the manipulation pathway. **c**, 20x20 nm^2 STM image of the substrate after being heated to 670 K. **d**,**e**, 10x7 nm^2 STM overviews of the different species **d** without and **e** with chemical structure on top of the molecules.

Fig. 5.22f and Fig. 5.23a and b). These chains have two bright protrusions between the two molecules. To lower the steric repulsion the two phenyl rings at the short end may have rotated and, therefore, appear brighter in STM images. To test the bond between the molecules lateral constant-current manipulation experiments were performed with a current of 10 nA and a bias voltage of 0.05 V. This corresponds to a tunneling resistance of 500 kΩ. Figures 5.23a and b show STM images before and after manipulation with the arrow denoting the manipulation path. One end of the chain is pushed to the upper corner of the image with the tip, and the whole molecular chain follows. This indicates the presence of a covalent bond between the molecules. However, the efficiency of the polymerization is still poor: Less than 6 % of the molecules are connected to chains. To trigger a more effective polymerization the heating temperature was increased to 670 K.

After heating the substrate to 670 K single graphene flakes without internal structure as

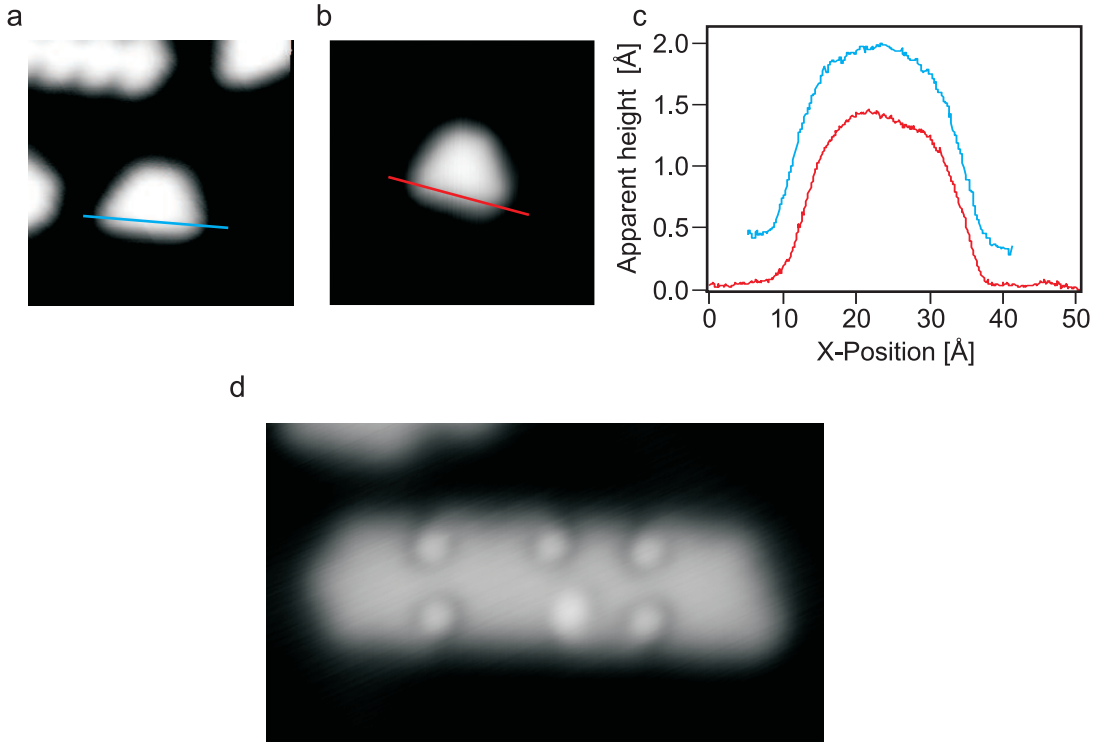

Figure 5.24: **a**, 6x6 nm^2 STM image of a unplanarized TPP molecule on Au(111) after heating the substrate to 670 K (bias voltage = 0.5 V). **b**, 6x6 nm^2 STM image of a TPO molecule on Au(111) (bias voltage = 0.5 V). **c**, Line scan of **a** and **b** as indicated by the red and the blue lines. **d**, 7x4 nm^2 STM image of the intermediate state of the chains after a heating step to 620 K.

well as zipper-shaped chains form. The single trapezoid-shaped molecules are an evidence that dehydrogenation occurred (see figures 5.23c and d). The dark line in the middle of the molecule disappeared (compare to Fig. 5.22d), and the appearance of the unplanarized trapezoid molecules (TPP) changed to the planarized trapezoids (TPO) discussed in chapter 5.3.1.2. For comparison, the length of the planarized molecule (Fig. 5.24a) is 2.13±0.09 nm, which is in good agreement with the length of trapezoids in chapter 5.3.1.2 (Fig. 5.24b and 2.12±0.08 nm). In both cases the full width at half maximum was measured (see figures 5.24a, b and c). Dimers of the TPP molecules (Figures 5.23d and e), equivalent to a short graphene nanoribbon, are very rarely detected. The cyclodehydrogenation, which should planarize the chains, competes with the dissociation of the molecules. Most of the chains are chemically changed from the desired structure sketched in Fig. 5.20. The chains are not smooth and feature-less like the trapezoid molecules. Instead, they appear as periodic bright bars which look like a zipper (denoted by the red arrow in Fig. 5.23c). A distance of 0.87±0.04 nm is measured between the two centers of each bar, which is in good agreement with the results of gas phase calculations of 0.89 nm. In Fig. 5.23c the blue arrow points out the mixed structure. The right part seems to be planarized, whereas the middle of the molecule has the characteristic zipper shape. To identify the chemical structure of the zipper-shaped molecules with STM is difficult. Fig. 5.23e shows a plausible model for the defected chains. During the polymerization the molecular chains partly decompose, which makes the formation of GNRs impossible.

A lower heating temperature of 620 K did not improve the defect rate of the molecular chains. They are partially planarized and show a pattern of protrusions (see Fig. 5.24d). These protrusions recall the intermediate states of the armchair N=7 graphene nanoribbons ([139] and chapter 5.3.2.2). The protrusions of the N=7 graphene nanoribbons are explained by phenyl rings which are not completely dehydrogenated and tilted with respect to the surface. In contrast to DBDA, a higher temperature does not lead to the planarization of the protrusions but to the partial decomposition of the chains.

In contrast to the results on DBDA-graphene nanoribbons, the dehydrogenation temperature of the TPP precursor molecules seems to be higher than the dissociation temperature of the TPP precursor molecules (see [104] and chapter 5.3.2.2). A surface which supports the dehydrogenation catalytically, e.g. Cu(111), could reduce the required temperature and serve as a template for the growth of graphene nanoribbons with these building blocks.

5.3.1.3 1,4-Bis(4-bromophenyl)-2,3-bis(4-tert-butylphenyl) -6,11-diphenyltriphenylene

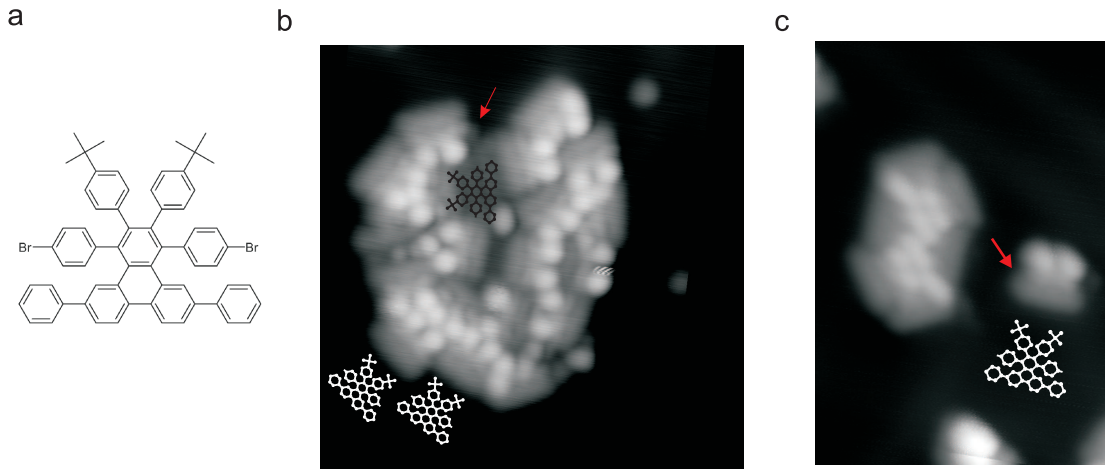

Figure 5.25: **a**, Chemical structure of the TB-TPP molecule. **b**, 13x13 nm^2 STM image of a small island before heating the substrate. **c**, 9x13 nm^2 STM image after heating the substrate to 520 K. The chemical structures in **b** and **c** sketche single molecules.

For the growth of GNRs with precursor molecules based on anthracene [104] a polymerization has only been observed for the anthracene dimer and not for the monomer (see chapter 5.3.2.2). The steric repulsion between the anthracene monomers seems to suppress the polymerization, which is reduced in case of the dimer as the anthracenes are rotated with respect to each other. To reduce steric repulsion the TPP graphene flakes were modified by two tert-butyl groups by the chemists (S. Hecht and co-workers, Humboldt Universität zu Berlin). The tert-butyl groups are attached to the short end of the graphene flake (see Fig. 5.25a). As usual the deposition of the 1,4-Bis(4-bromophenyl)-2,3-bis(4-tert-butylphenyl)-6,11-diphenyltriphenylene (TB-TPP) molecules was performed on the clean Au(111) surface at RT. The evaporation temperature is 500 K, so no activation during the deposition is expected. Similar to the TPP molecules a dark line appears in the middle of the TB-TPP molecule, which fits very well to the chemical structure. The chemical structure in Fig. 5.25b and c sketches single molecules. The molecules assemble in small islands without any chains being detected.

Comparing the shape of the molecules before and after heating the substrate to 520 K shows a reduced length of the bar in the middle of the molecule (see red arrow in Fig. 5.25b and c). This reduced length might results from the dehalogenation, which provides further evidence that the TB-TPP molecules are activated after heating the substrate to 520 K. Although the TB-TPP molecules are probably dehalogenated no oligomers are detected. For the TPP heating the substrate to 620 K was required for the planarization. However, the tert-butyl groups seem to reduce the binding energy to the surface and the TB-TPP molecules desorb after a heating step to 670 K. An empty surface was observed after the second heating step.

5.3.2 Anthracenes

The successful bottom-up growth of GNRs with DBDA molecules (Fig. 5.29) as precursors has been demonstrated by the group of R. Fasel in 2010 [104]. The basic idea of this approach is sketched in Fig. 5.26 and begins with the deposition of DBDA on Au(111) at RT. When the substrate is annealed to 470 K the molecular building blocks are activated, i.e. dehalogenated. At this elevated temperature DBDA molecules are mobile and link to anthracene oligomers. After heating the surface to 670 K the oligomers dehydrogenate and planarize leading to narrow GNRs with armchair edges. These steps are reproduced in this thesis and discussed in more detail in chapter 5.3.2.2.

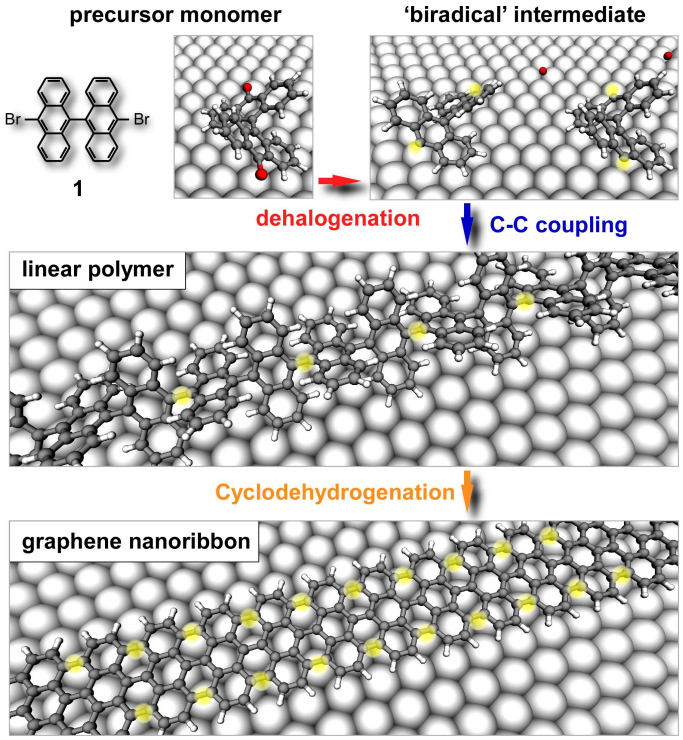

Figure 5.26: Different growth stages of DBDA on Au(111). Top: Single DBDA molecules which are dehalogenated. Middle: Polymerization of the activated DBDA molecules. Bottom: Cyclodehydrogenation of the anthracene oligomers which leads to fully conjugated GNRs. Reprinted by permission from Macmillan Publishers Ltd: Nature [104], copyright 2013.

DBA (Fig. 5.27a) was studied in chapter 5.3.2.1 as a precursor molecule for the polymerization of GNRs. It has almost the same structure as DBDA (Fig. 5.29). The difference between DBA and DBDA is that DBA is one anthracene equipped with two bromine atoms, whereas DBDA is an anthracene dimer with two bromine atoms attached. If the missing second anthracene is necessary for covalently linking the precursor molecules needs to be investigated.

5.3.2.1 9,10-dibromo-anthracene

The DBA molecules (see Fig. 5.27a for the chemical structure) are deposited at an evaporation temperature of 380 K onto the clean Au(111) sample at RT. Closed packed islands

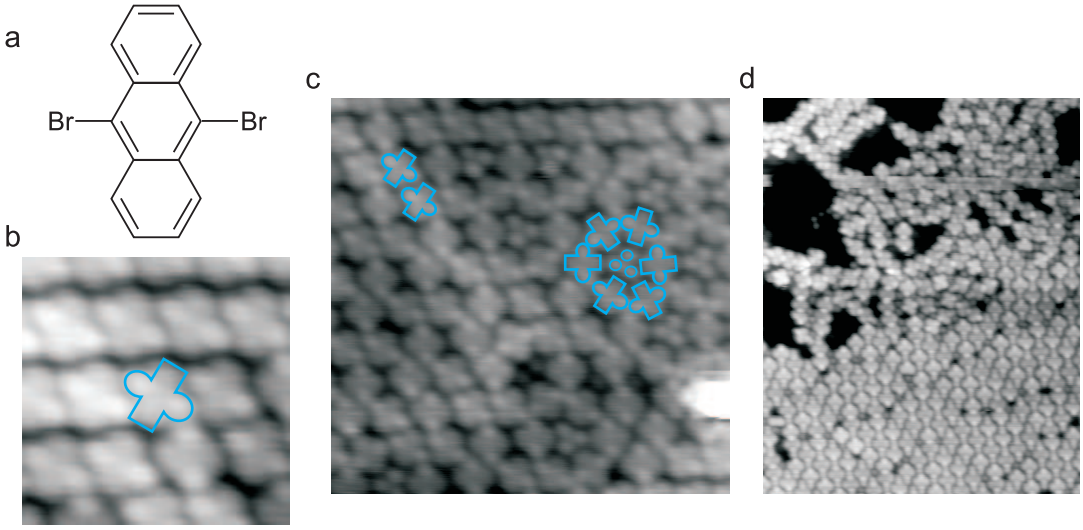

Figure 5.27: **a**, Chemical structure of the DBA molecule. **b**, 4x4 nm^2 STM image of DBA on Au(111) before heating. **c**, 10x10 nm^2 STM image of DBA. **c**, 20x25 nm^2 after heating to 470 K.

arranged with molecules, which are slightly rotated with respect to each other, cover most of the surface (see top of Fig. 5.27b). Beside the densely packed islands, there exist less dense structures with DBA molecules organized in flower-shaped cluster (Fig. 5.27c bottom). The small protrusions in the center of a DBA-flower are most likely the bromines (compare with results on HBCs of in chapter 5.2.1). The blue contour in Fig. 5.27b indicates a single DBA molecule and in Fig. 5.27c the DBA-flower is highlighted. Bromine-dehalogenation on the Au(111) surface at RT has so far not been observed in the literature where it occurs at 520 K [14, 108, 107]. The activation of the as-deposited DBA molecules is, therefore, unlikely. Hence, the molecular core is the anthracene body and the two bright lobes opposing it are the bromine atoms.

Tempering the substrate to 470 K changes the arrangement inside the islands (Fig. 5.27d). Before heating of the substrate the molecules assemble slightly rotated with respect to each other after heating the molecules align parallel to each other (Fig. 5.28a). Next to extended islands of single molecules, molecular chains can be seen (Fig. 5.28b). In a chain the distance between two anthracenes is ∼0.8 nm and a bright protrusion appears between the molecular units. This distance is in agreement with the periodicity of 0.85 nm for a covalently bond anthracene oligomer [104]. However, the appearance of these chains in STM imaging is completely different to the appearance of an anthracene oligomer. A DBA oligomer (Fig. 5.27a) and a DBDA (Fig. 5.29) oligomer have the same chemical structure and, therefore, the same appearance of a covalently bond DBA chain and a covalently bond DBDA chain (see Fig. 5.30e) is expected in STM images. As they look differently the DBA chains are probably not covalently bound. Nevertheless, lateral constant-current manipulation of DBA chains indicates a chemical bond between the molecules, which is possibly mediated by a gold atom. The gold atom connects the DBA units through a metal-ligand bond, similar to the HBC chains on Cu(111) (Chapter 5.2.1) [109]. Further evidence for the lack of a covalent bond formation is provided by the second heating step to 670 K: No GNRs emerge, the coverage drops from 0.80 to 0.26 ML and the chain-like structures disappear (Fig. 5.28c). In contrast to the results of DBA, DBDA on Au(111) polymerizes

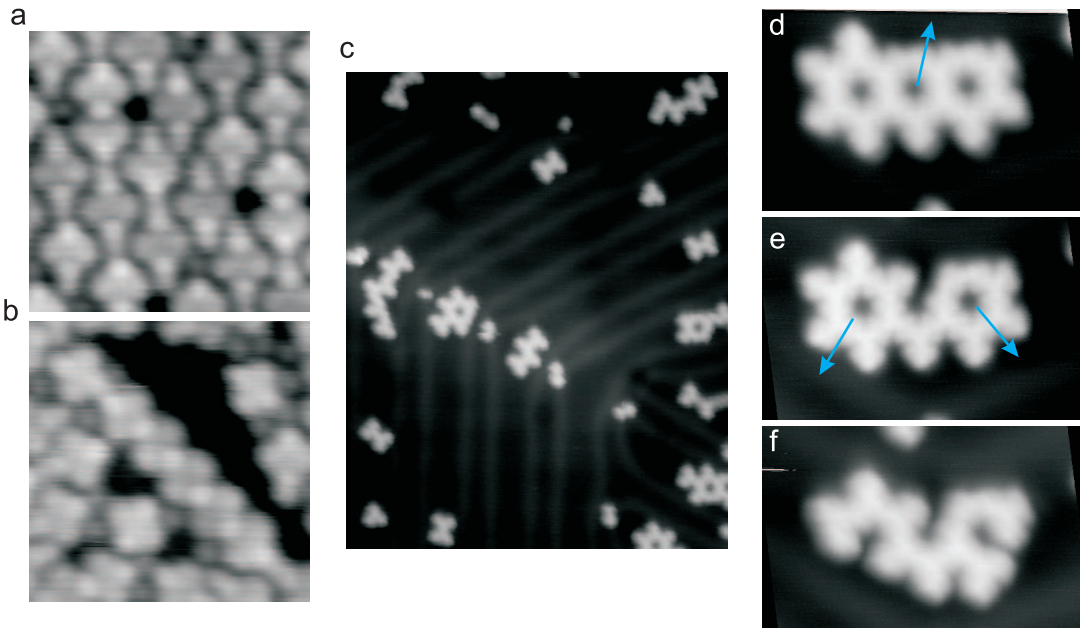

Figure 5.28: **a**, 5x5 nm^2 STM image of DBA on Au(111) after heating the sample to 470 K. **b**, 5x5 nm^2 STM image of DBA on Au(111) after heating the sample to 470 K. **c**, 40x50 nm^2 STM image of DBA on Au(111) after heating the sample to 670 K. **d**,**e**,**f**, 12.0x7.6 nm^2 STM images **d** before and **e**,**f** after lateral constant-current manipulation (80 nA, 35 mV). The manipulation path of the tip is indicated by the blue arrows.

to anthracene oligomers, which cyclodehydrogenated after heating the substrate to 670 K and narrow GNRs are fabricated. Instead, the DBA molecules assemble into star-shaped clusters (Fig. 5.28d). Using lateral manipulation single molecules are easily removed from these islands (see figures 5.28d, e, and f). The blue arrows in figures 5.28d and e indicate the tip path of the lateral manipulation. The setpoint for the lateral manipulation was a bias voltage of 0.035 V and a tunneling current of 80 nA. This provides evidence that remaining anthracenes do not link covalently. Even scanning with higher bias voltage (2.5 V) suffices to destroy the star-shaped clusters.

DBA does not polymerize to GNRs on Au(111), in contrast to DBDA. The main difference between DBA and DBDA is an additional anthracene in the molecular building block. The two anthracenes in DBDA are essential for a successful polymerization. Using a dimer as a precursor molecule allows the anthracene units to rotate with respect to each other and, thereby, to reduce the steric hindrance. Calculations find a rotation angle of 81° between the anthracenes in the oligomer (C. Joachim and F. Ample - Institute of Materials Research and Engineering, Singapore). The reduced repulsion probably results in a closer interaction between two activated DBDA molecules, so that they can link covalently.

5.3.2.2 10,10'-dibromo-9,9'-bianthryl on Au(111)

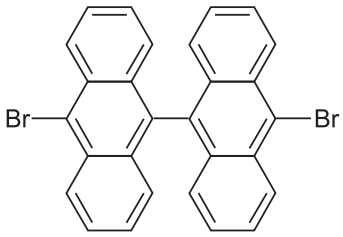

Figure 5.29: Chemical structure of the DBDA molecule.

The growth of GNRs with DBDA molecules (see Fig. 5.29) has been reported first by the group of R. Fasel in 2010 [104]. At an evaporation temperature of 420 K the molecules were deposited onto a clean Au(111) surface at RT. In the following experiments the sample is kept at 470 K during the deposition of the DBDA molecules to immediately trigger the polymerization. Directly after finishing the evaporation the sample is heated to 600 K or 670 K for cyclodehydrogenation.

Without annealing after the deposition the DBDA molecules arrange in large islands (see Figures 5.30a and d). The identification of the shape of a single molecule is difficult. From literature and calculations (C. Joachim and F. Ample - Institute of Materials Research and Engineering, Singapore) it is known that the anthracene molecules in anthracene-oligomers are rotated by 81° with respect to each other and tilted with respect to the surface [104, 140]. The upper end of an anthracene appears higher in an STM image and gives rise to bright lobes in Fig. 5.30b and e. The apparent height of these protrusions is 1.68±0.01 Å, which is higher than the apparent height of the bromines attached to HBC (see chapter 5.2.1: 1.3±0.1 Å, and attached to porphyrins (Chapter 5.1.1: 1.3±0.1 Å) [108]. The similar appearance of the DBDA and the anthracene-oligomers (compare to figures 5.30d and e) indicate that the anthracenes in the precursor molecule are rotated with respect to each other. In the STM images of as-deposited DBDA molecules (Figures 5.30a and d) the bromine atoms are not resolved and the orientation of the molecules is unclear. STM images with a functionalized tip indicate that the DBDA molecules are aligned perpendicular to the growth direction of the island (Fig. 5.30g). Accordingly, the bromines only contribute to the gray background between the anthracene lobes and the border of the island. A possible model of the packing of the DBDA molecules is highlighted in Fig. 5.30d and g.

Heating the sample to 470 K activates the DBDA molecules and stimulates the formation of anthracene oligomers (see figures 5.30b and e). Similar to the precursor molecules, each lobe corresponds to the end of an anthracene, which is rotated with respect to its neighbors and tilted against the surface [104, 140]. Theory finds a rotation angle of 81° (C. Joachim and F. Ample - Institute of Materials Research and Engineering, Singapore). Therefore, STM resolves only the lifted terminus of the anthracene. These anthracene chains are highly flexible and can be bent in nearly any direction without being damaged by lateral manipulation. Fig. 5.31 shows STM images at different stages of the lateral constant-current manipulation (20nA, 17 mV). An oligomer consists on average of 12 anthracene units (i.e. six monomers), and the longest detected chain has 24 units. Since the molecular building blocks are dimers oligomers always consist of an even number of anthracene molecules.

Heating the sample to 670 K triggers cyclodehydrogenation, which leads to a fully conjugated armchair N=7 GNR (N=7 is the number of carbon atoms along the short edge) [104]. The GNRs appear smooth with little internal structure (Fig. 5.30f), and they are stiffer than the oligomers. Neither vertical (Fig. 6.7a and b) nor lateral manipulation changes the intramolecular conformation of a GNR, which is in agreement with the properties of

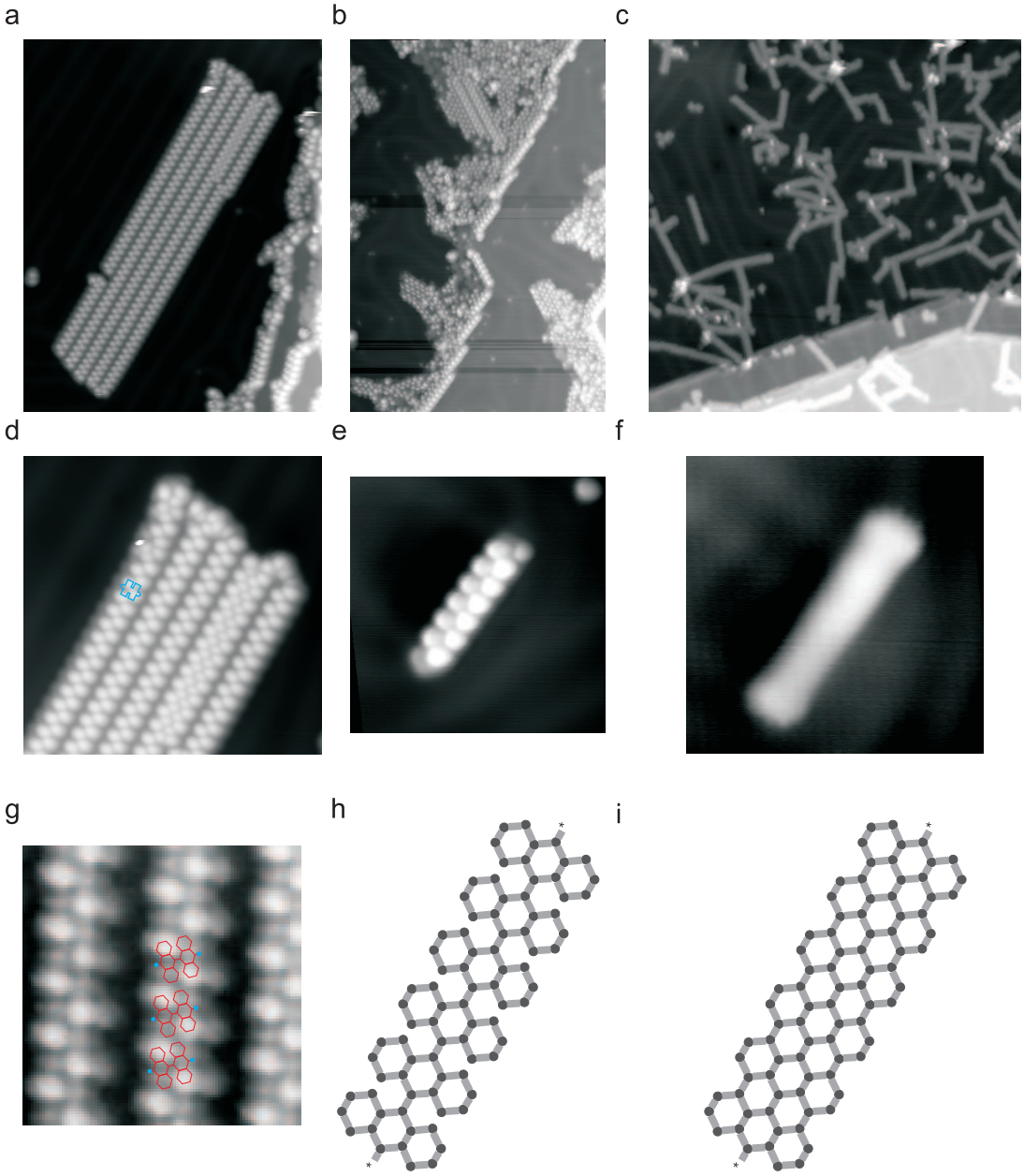

Figure 5.30: STM images of DBDA molecules before tempering **a** 40x50 nm^2, **d** 18x18 nm^2, after tempering to 520 K **b** 39x57 nm^2, **e** 10x10 nm^2 and after tempering to 670 K **c** 60x60 nm^2, **f** 10x10 nm^2. The blue contour in **d** indicates a single molecule. **g**, 8x8 nm^2 STM image of the DBDA molecules before tempering. The position of the DBDA molecules is sketched. Chemical structure of **h** the anthracene-oligomer and **i** the fully conjugated GNR.

graphene [141]. To compare the length of the GNR to the anthracene oligomers is challenging because of the high amount of branches between the GNRs (see Fig. 5.30c). These branches emerge randomly and are probably a side effect of the dehydrogenation: The long armchair edges are partially dehydrogenated, and the missing hydrogens create new active sites for bonding [126, 110]. Other activated GNRs could bind to these active sites so that T-shaped networks develop (similar results for the undefined bonds between porphyrin

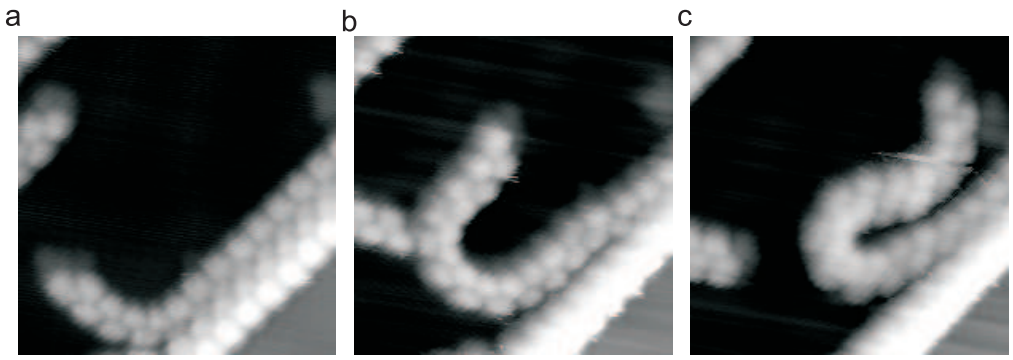

Figure 5.31: 10x10 nm^2 STM images of an anthracene oligomer which was bent. Between the images the conformation of the oligomer has been changed through lateral constant-current manipulation (20nA, 17 mV).

precursors are discussed in chapter 5.1.1). For comparison, on the Ag(111) surface after a heating step to 750 K DBDA polymerizes to GNRs with a width of N=7 to N=14 and N=21 [110], which implies parallel links between the GNRs.
Fig. 5.32 shows the length distribution of single GNRs. Gas phase calculations reveal an elongation of 0.84 nm for each additional anthracene dimer. In Fig. 5.32 accumulations at lengths of ∼4.8 nm, ∼5.6 nm, 6.4 nm (there is a double peak) and ∼7.2 nm can be seen. The experimental results suggest an elongation of ∼0.8 nm for each additional planarized anthracene dimer. This is smaller than the theoretically obtained value of 0.84 nm. A ∼5.6 nm long GNR would, therefore, consists of 14 anthracenes (i.e. 7 monomers of DBDA). So, the GNRs are, on average, slightly longer than the oligomers.

Cyclodehydrogenation reaches full efficiency around 670 K. If the sample is heated to 600 K intermediate states of partial dehydrogenated GNRs emerge (see Fig. 5.33a for an overview image) [139]. The phenyl rings, which are not completely dehydrogenated, tilt with respect to the remaining ribbon. Fig. 5.33b shows an STM image and Fig. 5.33c sketches the chemical structure. The rotated phenyl rings appear as protrusions in

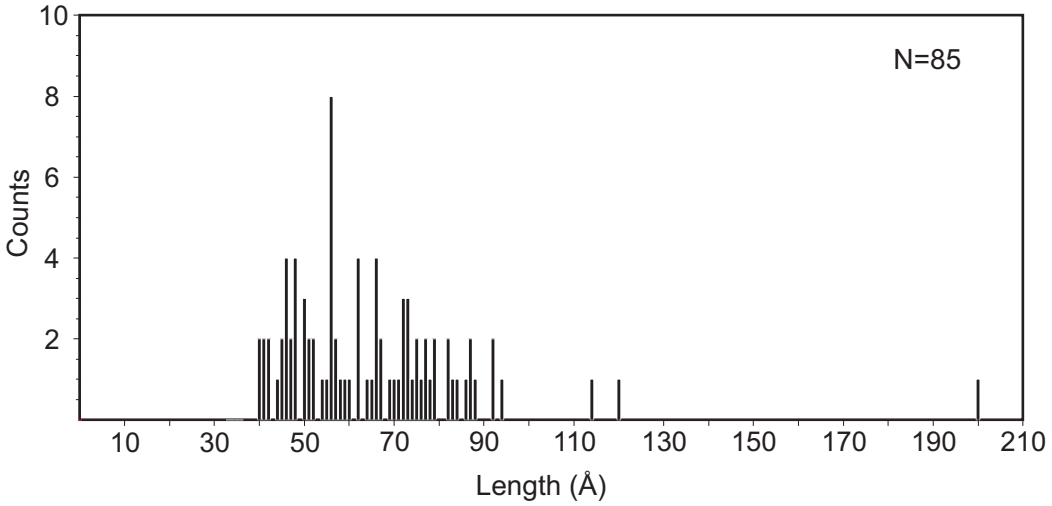

Figure 5.32: Length distribution of single GNRs on Au(111).

STM images. Applying a voltage pulse to the STM tip may trigger the cyclodehydrogenation leading to the disappearance of the bright lobe [139]. Even though most of the GNRs bond in unanticipated networks the number of single GNRs is higher compared to the sample heated to 670 K. A higher ribbon quality may probably be achieved by reducing the annealing temperature further while increasing the annealing duration.

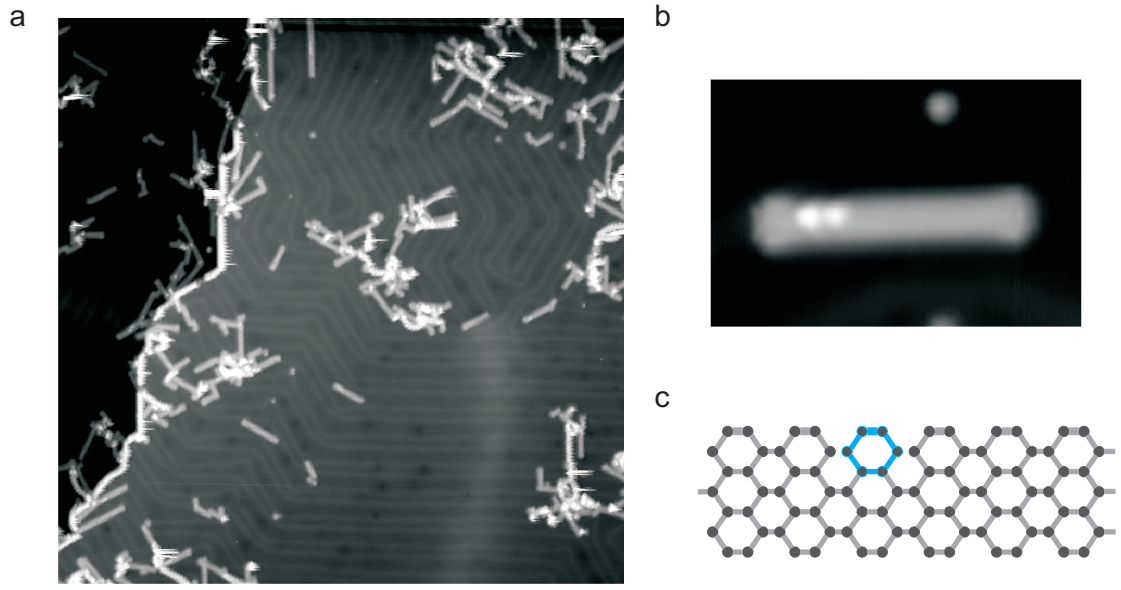

Figure 5.33: **a**, 137x137 nm^2 STM overview of the surface after heating it to 600 K. **b**, 8x12 nm^2 STM image of a partially cyclodehydrogenated GNR. **c**, Sketch of the chemical model of a partially cyclodehydrogenated GNR. The benzene ring indicated in blue appears as a protrusion in STM images.

5.3.2.3 10,10'-dibromo-9,9'-bianthryl on Au(100)

For some experimental techniques an alignment of GNRs along a certain direction on the surface is required, e.g., for spectroscopy in order to measure the electronic dispersion in the $\boldsymbol{k}$-space of the GNRs [142, 143]. The alignment might also be interesting for the transfer of the ribbons to other substrates. To study the conductance of single GNRs, the unanticipated branches between the GNRs (see Fig. 5.30c) complicate the pulling experiments discussed below. The Au(100) surface reconstructs into parallel corrugations. The distance between the atomic rows is 14.4 Å, and the reconstruction is supposed to steer the alignment of the oligomers and, thereby, also their growth [142, 108].

The sample preparation of Au(100) is similar to the preparation of the Au(111) sample. The molecules are deposited onto the clean Au(100) surface at a temperature of 470 K, which should immediately trigger the polymerization. After the evaporation the substrate is heated to 590 K in order to cyclodehydrogenate the molecules. Surprisingly, most of the DBDA molecules still exist as anthracene-dimers and only 16 % of the DBDA molecules are polymerized to anthracene oligomers or GNRs. The remaining 84 % are probably partially planarized single anthracene dimers from its appearance in STM image (indicated by the red arrow in Fig. 5.34b and c). However, in contrast to Au(111) the complete anthracene is resolved and not only the lifted part. This provides evidence that the rotation angle

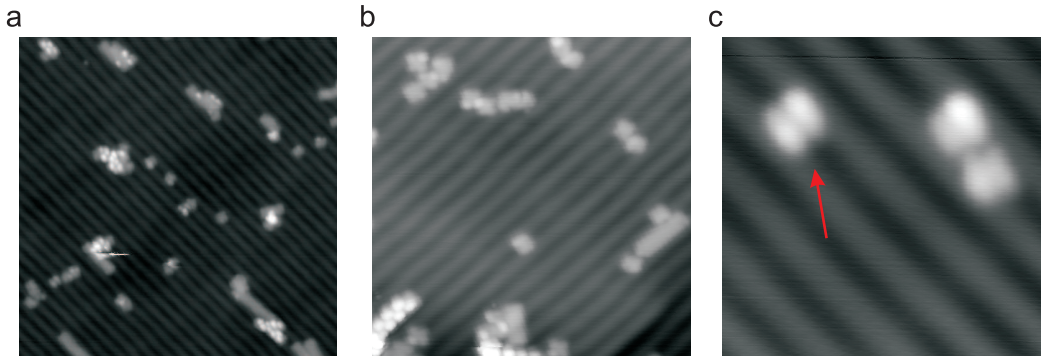

Figure 5.34: **a** 40x40 nm^2 and **b** 20x20 nm^2 STM overviews of DBDA on Au(100) after heating the sample to 590 K. **c**, 8x8 nm^2 STM image after heating the sample to 590 K.

between the anthracenes in DBDA is smaller than on Au(111). After heating the Au(111) sample to 670 K all DBDA molecules polymerize and cyclodehydrogenate to GNRs. On Au(100) the anthracene oligomers arranged along the step edges and are probably caused by the lower heating temperature of 590 K. Also on Au(111) anthracene oligomers appear at the step edges after heating the sample to 600 K. After heating the sample to 670 K all oligomers are transformed to GNRs. The efficiency of the polymerization on the Au(100) surface turns out to be lower than on the Au(111) surface. 84 % of the molecules are probably planarized anthracene dimers which did not covalently link. The few existing GNRs (in total 15 %) on Au(100) show defects or are not completely planarized.

On Au(788) and Au(111) the fabrication of GNRs is fruitful [142, 104], whereas the Au(100) surface proves to be unsuitable for the growth of GNRs. Theory predicts a larger binding energy for amine on Au(100) than for Au(111) (12.7 kcal/mol compared to 10.8 kcal/mol) [144]. This increases the diffusion barrier for the anthracenes and reduces the length of the chains. However, this does not explain the high amount of single planarized anthracene dimers. The corrugation of the Au(100) surface and the higher binding energy of the Au(100) surface probably reduce the angle between the anthracenes in the dimer. This rotation is essential for the polymerization as it lowers the steric repulsion between the precursor molecules. DBA does not covalently link to anthracene chains, whereas DBDA polymerizes (see chapter 5.3.2.1 and 5.3.2.2). In case of Au(100) the reduced angle between the anthracene units might stop the DBDA molecules from linking.

5.4 Summary

In this chapter two types of molecular building block were used to grow GNRs: trapezoid-shaped building blocks and anthracene-based building blocks.

The goal of this chapter was the bottom-up polymerization of graphene nanoribbons (GNRs) on the surface. The synthesis of the trapezoid-shaped building blocks was challenging for the organic chemists (S. Hecht an co-workers, from the Humboldt Universität zu Berlin). The synthesis of the trapezoid-shaped precursor molecules requires a planarization step during which the bond between the trapezoid and the bromine breaks and an non-reactive species is created. This species is a fully conjugated trapezoid-shaped graphene

flake without bromine atoms. As anticipated no polymerization on the surface was observed for these building blocks. The evaporation temperature of the trapezoid-shaped graphene flakes is very high (700 K), and the dehalogenation was expected to occur during the deposition. Therefore, the missing bromines were not recognized in STM images and steric hindrance was assumed as the reason for the quenched polymerization. To reduce the steric repulsion the chemists (S. Hecht an co-workers, from the Humboldt Universität zu Berlin) synthesized unplanarized molecules and unplanarized molecules equipped with two tert-butyl groups. As the precursor molecules were not planarized during the synthesis the bromines are still attached to them. The butyl groups reduce the adsorption temperature and heating the substrate to 670 K leads to an empty surface. The unplanarized trapezoids polymerized to a zipper-like structure. Regardless of the successful polymerization the sterical repulsion between the building blocks is too large as the molecular chains dissociate at an elevated temperature, which is necessary for the planarization of the chains.

The steric repulsion is a huge obstacle for the fabrication of GNRs. Although the successful polymerization for 10,10'-dibromo-9,9'-bianthryl (DBDA) has been reported on Au(111) [104] 9,10-dibromo-anthracene (DBA) does not polymerize on the same substrate. The chemical structure of a DBA oligomer as well as of a DBDA oligomer is identical as both precursor molecules polymerize to an anthracene oligomer. The difference lies in the polymerization of DBDA, which starts as an anthracene dimer, compared to the polymerization of DBA, which starts from a single anthracene, each equipped with two bromines. The anthracenes in the dimer precursor molecule are rotated by 81° (C. Joachim and F. Ample - Institute of Materials Research and Engineering, Singapore) with respect to each other. This rotation is essential for growing GNRs on Au(111) because it reduces the steric hindrance between the building blocks. The polymerization to anthracene chains (470 K) and the cyclodehydrogenation to fully conjugated GNRs (670 K) was successfully reproduced [104]. Beside single GNRs branches of GNRs emerge. These branches are a side effect of the cyclodehydrogenation. The ribbon edges are probably dehydrogenated, which leads to new active sites and uncontrolled bonds between the GNRs.

The efficiency of the dehydrogenation depends on the temperature. Decreasing the temperature to 600 K for the cyclodehydrogenation leads to partially dehydrogenated GNRs. The rotated phenyl rings, which are not fully dehydrogenated, appear as protrusions in STM images. However, also after heating the substrate to 600 K most of the GNRs are connected in an uncontrolled manner.

Using Au(100), instead of Au(111), blocks the fabrication of GNRs. After annealing the sample to 590 K anthracene oligomers and di-anthracene monomers still exist. The polymerization might be suppressed due to the higher adsorption energy of Au(100) [144] and the atomic corrugation of the Au(100) surface. The higher adsorption energy [144] causes a smaller rotation angle between the anthracenes in the precursor molecule. However, the rotation of the anthracenes is required to reduce the steric repulsion between the molecular building blocks (similar to DBA) so that the efficiency of the polymerization on Au(100) is reduced.

Chapter 6

Conductance, Electronic and Vibrational Structure of Graphene Nanoribbons

The previous chapter discussed the growth of GNRs for various precursor molecules. In this chapter the results of the GNRs fabrication with DBDA were used for analyzing their electronic properties. To understand the conductance of a single GNR the electronic structure of the ribbon has to be studied first. To measure the conductance of a single GNR the molecule is connected with the tip and pulled from the surface [16]. The STM tip and the surface are used as the electrodes of the junction. While the tip is retracted from the surface the length of the free standing wire and, thereby, the effective transport path of the electrons increases. Recording the current during the withdrawal of the tip allows the length-dependent measurement of the conductance of a single and isolated molecule [16]. The effect of the molecular orbitals on the conductance was studied by varying the electron energy. In order to investigate the influence of defects on the conductance of GNRs not fully cyclodehydrogenated GNRs were chosen. The last section of this chapter discusses inelastic tunneling spectroscopy of a free standing molecule. The aim was to measure the vibrational states of the GNRs in pulling configuration.

The theoretical calculations presented in this chapter are performed by C. Joachim and F. Ample (Institute of Materials Research and Engineering (IMRE), Singapore).

6.1 Spectroscopy

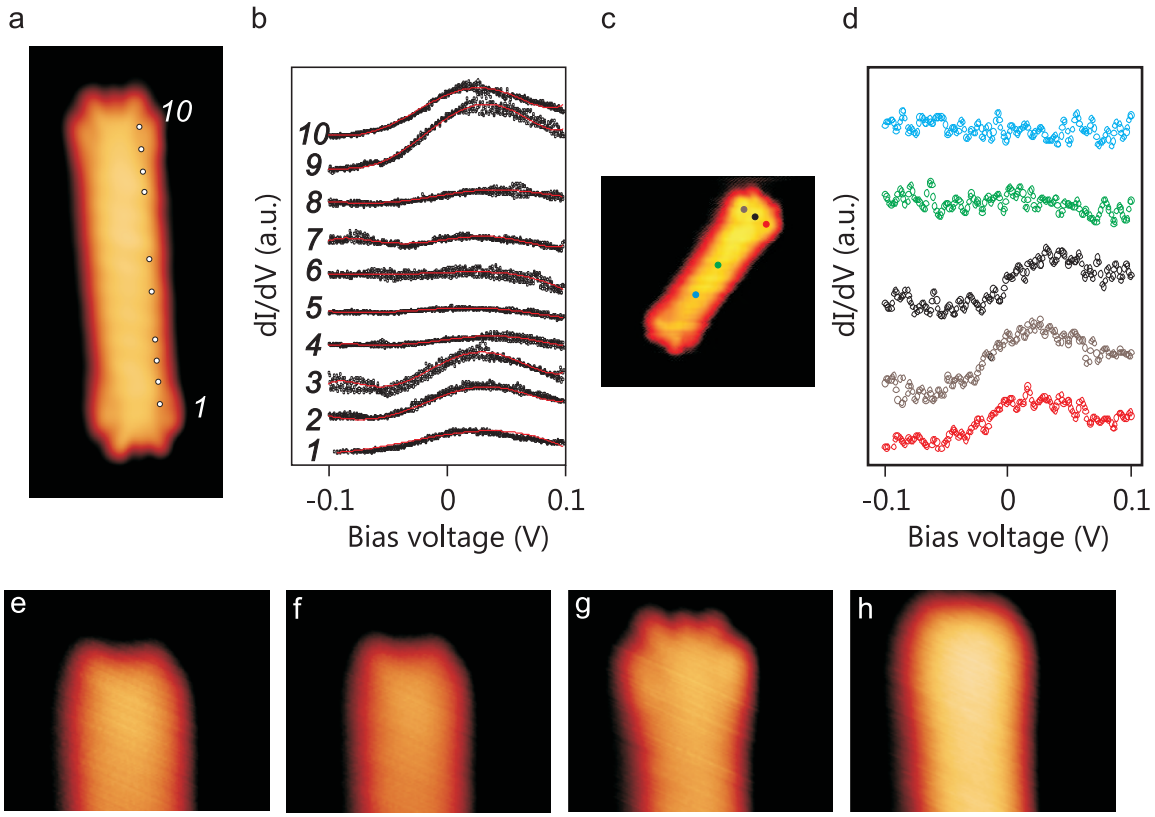

Figure 6.1: **a**, 3x7 nm^2 STM image and corresponding **b** dI/dV curves taken at different positions. **c**, 6.5x6.5 nm^2 STM image and corresponding **d** dI/dV curves taken at different positions. **e**,**f**,**g**,**h**, Bias series of the same GNR at **e** -1.55 V, **f** -0.95 V, **g** +0.05 V and **h** +1.05 V. (3x2.5 nm^2)

To measure the electronic states scanning tunneling spectroscopy (STS) was used. The bias voltage was modulated by a 610 Hz sinus signal with an amplitude of 20 mV. A Stanford lock-in amplifier measured the dI/dV signal from the current by extracting the first harmonic frequency. In case of a metallic tip with a flat LDOS, the dI/dV signal is proportional to the LDOS of the molecule and the surface (for more details see chapter 2.5). In general, before any dI/dV spectroscopy experiment was performed the metallic nature of the tip was confirmed by measuring the Au(111) surface state [21].

Spectra were taken at several points along the armchair edges and at the center of the GNR. To resolve electronic states close to the Fermi energy the bias voltage was ramped from -0.1 V to +0.1 V at each point. In the dI/dV spectra taken at the termini a peak appears at 0.03 V that completely vanishes at the center of the GNR (Figures 6.1a,b and c,d). The GNRs grown from DBDA building blocks show armchair edges sideways and zigzag structure at the short edges at the termini (see Fig. 6.2g). This peak appears only at the zigzag edges and is assigned to the Tamm state, which has been predicted by theory and observed experimentally recently [145, 97]. The Tamm state appears in the LDOS as a sharp peak at the Fermi energy and belongs to two flat bands with a wave vector k between $\frac{2}{3}\pi$ and π close to E$_F$ [12]. Armchair edges do not have this state [12].

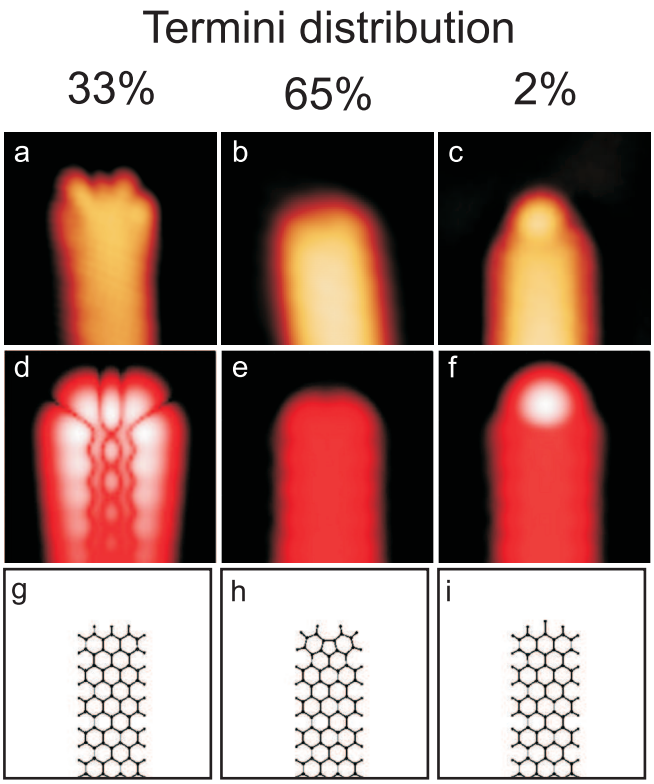

Figure 6.2: **a-c** 3x3 nm^2 STM images, **d-e** ESQC calculated conductance maps **g-h** and chemical structure of **a**,**d**,**g** of a defect-free terminus, **b**,**e**,**h**, of a defect at the terminus and **c**,**f**,**i** of a terminus before activation.

Observing electronic states with large $k_{||}$ values is unusual in STM because the decay rate of the current increases with the square of $k_{||}$, which is equivalent to less efficient tunneling of electrons with large $k_{||}$ [146]. In general, states with $k_{||} \approx 0$ dominate the tunneling current. Only if there exist no states with small wave vectors tunneling from states with larger $k_{||}$ can be observed [147]. This seems to be the case for the present experiments as the Tamm state is located close to the Fermi energy at a k-vector between $\frac{2}{3}\pi$ and π [12]. However, estimating k_{II} of the tunnel electrons was not possible as the effective mass of the electrons is unknown. The shape of the terminus differs at low bias voltages compared to larger bias voltages in STM imaging (Figures 6.1e-h). At high bias voltages (positive and negative) the ribbon end is featureless. In contrast, taking images between -0.2 V and +0.2 V has a high influence on the appearance of the terminus. Fig. 6.1g displays an STM image taken at -0.05 V that shows a fringed ribbon end. The small bias window and the Tamm state, which is located at 0.30 V in the dI/dV spectrum, point to an electronic and not a topographic effect (Fig. 6.1).

In appearance of the termini at low bias voltage two more species of GNRs exist. The first species is terminated by a bright lobe (Fig. 6.2c) which is extremely rare as only 2 % of the GNR have this feature. In comparison to calculations (Figures 6.2f), this lobe is assigned to a bromine atom (Fig. 6.2i). Despite the dehalogenation at 470 K not all termini are activated. This explains its small abundance. Around 65 % do not show any feature at the ribbon terminus neither at high bias voltages nor at low (Fig. 6.2b). Calculations explain the defect of the second species by a missing carbon atom at the zigzag edges (Figures 6.2e

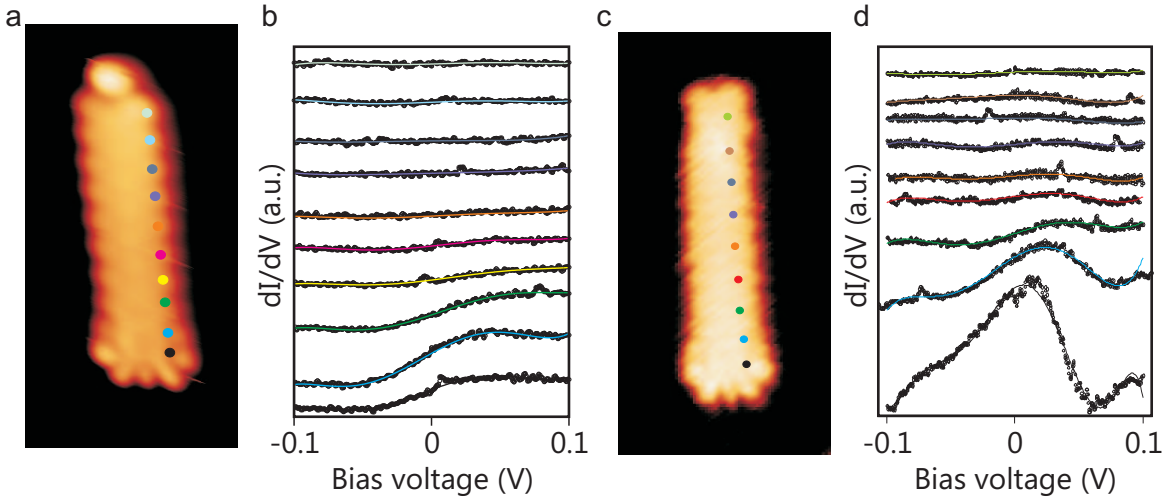

Figure 6.3: **a**, 3x6 nm^2 STM image of a bromine terminus and corresponding **b** dI/dV curves taken at different positions. **c**, 3.5x7 nm^2 STM image of a defected terminus and corresponding **d** dI/dV curves taken at different positions.

and h). The short edges are no longer in the zigzag conformation which is essential for the Tamm state. For both species the chemical structure is modified so that the Tamm state vanishes. Figures 6.3b and d show dI/dV spectra along the armchair edges of the two species. Both ribbons have a defect-free and a chemically modified terminus. At the defect-free ribbon terminus the localized Tamm state is clearly visible whereas both ribbons at the defected end lack an electronic state between -0.1 V and +0.1 V. Another explanation for the defected terminus can be found in the literature. Applying a voltage pulse turns the featureless terminus into the fringed-shape, an evidence for the existence of the Tamm state [145]. The calculations of Talirz et al. suggest that two hydrogens are bonded to the center carbon of the terminus and that they can be cleaved by a voltage pulses.

Fig. 6.4 shows a partially planarized GNR before a and after b pulling the molecule from the surface (see chapter 6.2.5 for more details). In Fig. 6.4a the upper terminus is defected and the characteristic shape of the Tamm states is not visible as it is for the other end. After the pulling attempt the appearance of the upper terminus changed to the defect-free shape. The bond between molecule and tip broke at a tip height of ∼2 nm and a bias of 0.05 V was applied. The fringed silhouette of the Tamm states appears in Fig. 6.4b where a small feature, which is indicated by the red arrow, turns up next to the upper terminus. Fig. 6.4c shows a detail of Fig. 6.4b with an different contrast. This feature could be an atom or a cluster which was bonded to the ribbon terminus. If this atom (cluster) was bonded to the terminus before the manipulation and caused the defected appearance (flat appearance) the proposed model of a defected terminus cannot be valid. Although the pulling was performed at the other end of the ribbon the interaction was strong enough to chemically change the opposite terminus. The explanation of a defected terminus is not valid as the missing carbon atom cannot be replaced by the pulling experiment. If an anthracene oligomer breaks into two parts during the heating steps two different types of defects might occur: a missing carbon atom as in Fig. 6.2h and an additional carbon atom at the activated site of the other part. The latter could be changed by a voltage pulse, whereas the former is unrepairable.

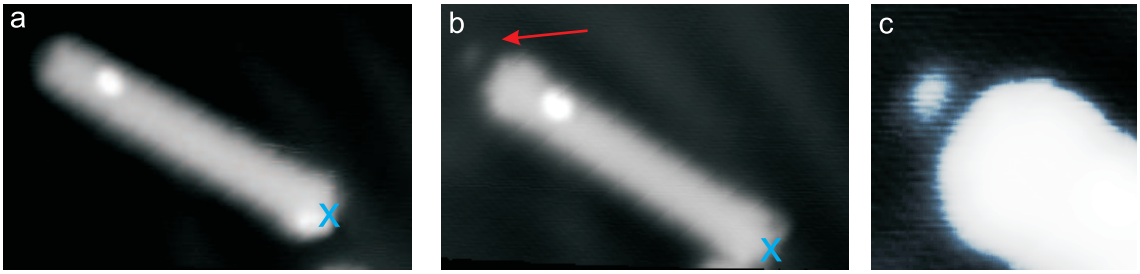

Figure 6.4: **a**,**b**, 10x6.5 nm^2 STM images **a** before and **b** after an unsuccessful attempt to pull up a GNR. The bias is +1.8 V during the pulling experiment and the position of the tip approach is marked by the cross. The red arrow indicates a new feature which appears after the pulling. **c**, 3x3 nm^2 detail of **b**.

So far only the Tamm state close to the Fermi energy was discussed. To detect the HOMO and the LUMO the bias window of the dI/dV spectrum is increased (Fig. 6.5a). At negative energies a peak appears at -0.9 V which is assigned to the HOMO. The LUMO is located at +1.7 V where the spectrum features a shoulder. So the N=7 wide armchair GNRs have a HOMO-LUMO gap of 2.8 eV which is in very good agreement with recent reports (E_g = 2.8±0.4 eV) [142]. dI/dV spectroscopy shows that the Tamm states are localized at the zigzag edges. This is confirmed by mapping of the electronic structure. Simultaneously with a constant-current image the dI/dV map is recorded. Similar to a dI/dV spectrum the bias voltage U_0 is modulated by a 610 Hz sinusoidal signal with an amplitude of 20 mV. The lock-in amplifier extracts the first derivative of the current. In contrast to the dI/dV spectrum, the bias voltage U_0 was maintained during a dI/dV map. Therefore, the LDOS is mapped at this energy. The dI/dV map recorded at a bias voltage of 0.05 V shows only at the terminus a feature close to the Fermi level (Fig. 6.5d). On the contrary, at -1.15 V (Fig. 6.5b) and at +1.6 V (Fig. 6.5e) a bright feature decorates the armchair edges of the ribbon. The bias energies of the dI/dV maps shown in figures 6.5b and e matches the position of the HOMO and the LUMO, respectively. Therefore, the HOMO and the LUMO are delocalized along the armchair edges of the GNR. The dI/dV map at a bias voltage at the gap shows no features (Fig. 6.5c).

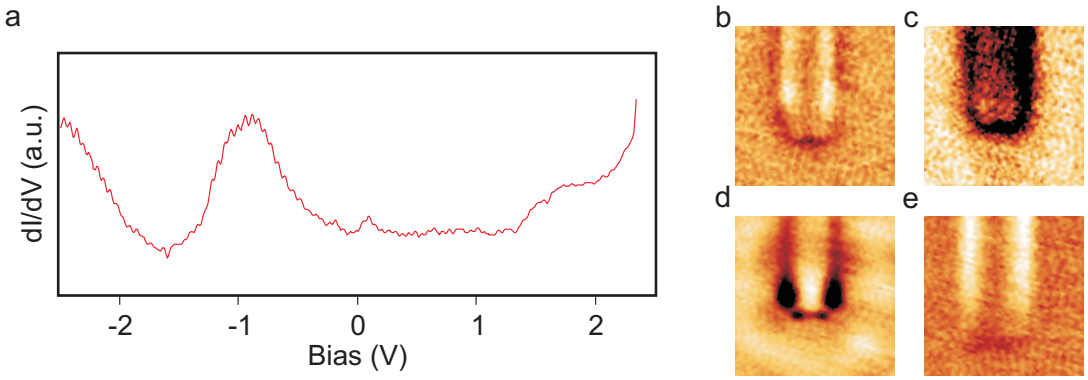

Figure 6.5: **a**, dI/dV spectra of a GNR. **b**,**c**,**d**,**e**, dI/dV maps at **b** -1.15 V, **c** -0.55 V, **d** 0.05 V and **e** +1.6 V (5x5 nm^2)

6.2 Conductance Measurements

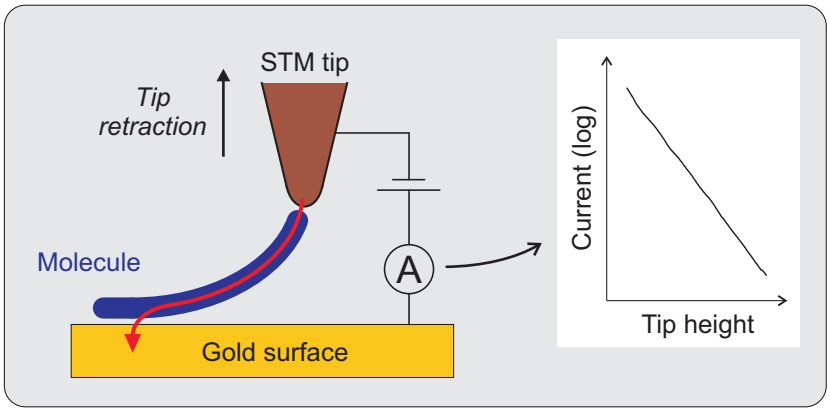

Figure 6.6: Sketch of a molecular wire pulled up by the STM tip. Reprinted by permission from Macmillan Publishers Ltd: Nature Nanotechnology [148], copyright 2013.

The vertical pulling technique has been used to record the conductance of a single polyfluorene chain (see Fig. 6.6) [16]. The gold surface is a much better conductor than the molecule. Therefore, the current only passes through the lifted part of the molecule which does not interact with the substrate whereas tip and surface act as electrodes. By pulling the molecular polyfluorene chain from the surface the effective length of the wire increases. Lafferentz et al. find characteristic oscillations of the conductance with a periodicity that matches the distance of the fluorene units [16]. Pulling a molecular chain from the surface requires a strong and stable bond between tip and molecule. The energy to break the tip-molecule bond must be higher than the energy necessary to lift the chain from the surface. The bond is created by approaching the tip vertically towards the end of a chain. A jump in the current indicates that a bond between tip and molecule is formed. Then the tip is retracted while the current is recorded. This technique was used to measure the conductance of a single GNR. Before each pulling experiment the GNR is characterized by conventional STM imaging.

6.2.1 Pulling

Figures 6.7a and b show images before and after a pulling experiment. Sometimes the bond between tip and molecule breaks, which happens at different tip heights. After the rupture of the junction between tip and molecule STM images of the same ribbon show the molecule which moved towards the tip (Fig. 6.7b). This provides evidence that the part of the GNR adsorbed on the surface moves to the tip position while it is lifted from the surface. Fig. 6.7c displays a characteristic pulling curve. The arrows in Fig. 6.7c show the vertical direction of the tip movement. The arrow pointing up signifies the approaching of the tip to the surface and the arrow pointing down means the tip was withdrawn. The current increases as the tip approaches the surface and finally saturates at the limit of the preamplifier. Fig. 6.7d shows the current curves of the same GNR which was pulled up with different preamplifier gains. Therefore, the current is also resolved for close tip-sample distances. The jump in the current resulting from the creation of the bond is visible in

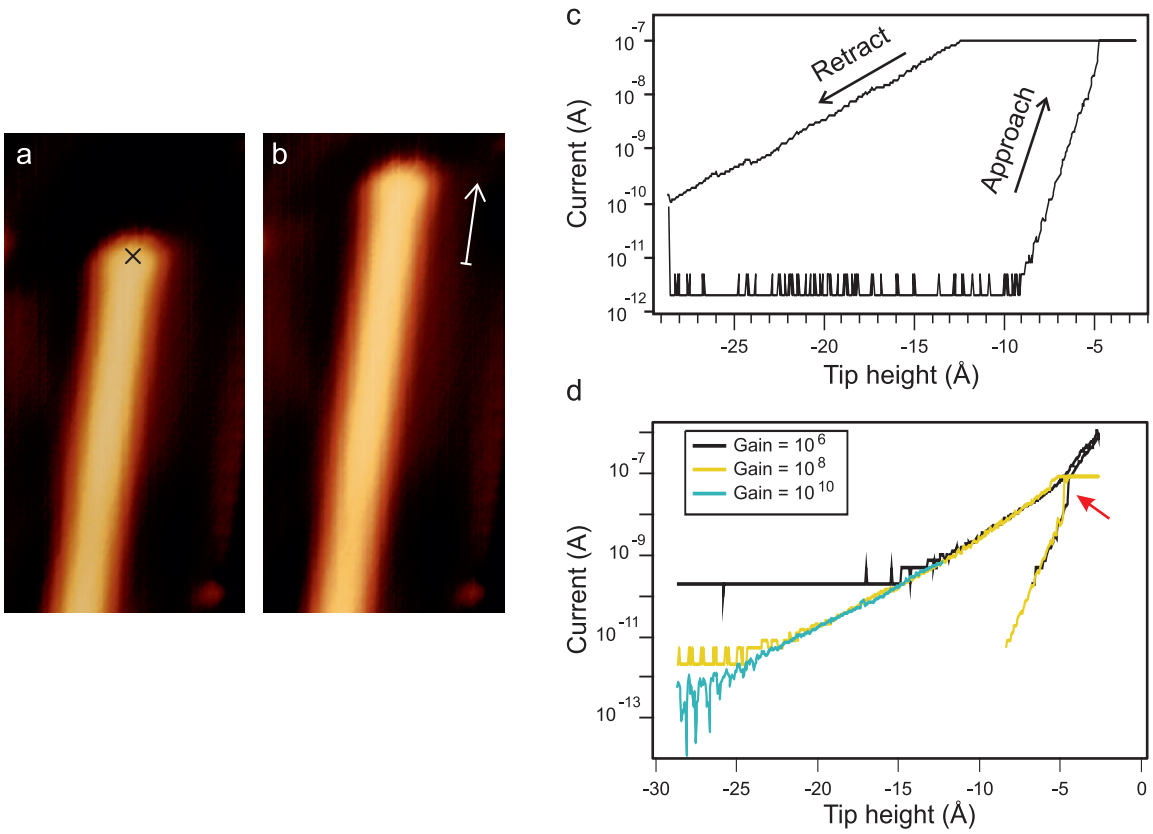

Figure 6.7: **a**,**b**, 7x14 nm^2 STM images **a** before and **b** after pulling a GNR. **c**, The measured current curve for a GNR with a bias voltage of -0.10 V. **d**, Three pulling curves of the same GNR at different preamplifier gains. The applied bias voltage is -0.05 V and the red arrow indicates the formation of the bond between tip and molecule.

Fig. 6.7d as indicated by a red arrow. In the following, the tip is retracted and the current decays. The slope of the current during the withdrawal is less steep than during the approach where no molecular chains are attached. While the tip is retracted the current is also larger than during the approach at the same tip-sample height. This indicates a successful pulling experiment. In both cases figures 6.7c and d a small bias of 0.10 V and -0.05 V was used, respectively. Both slopes fall off exponentially which points to direct tunneling as transport mechanism. For hopping or pseudo-ballistic transport no decay of the current with respect to the tip-sample distance is expected. In direct tunneling the conductance is described by:

$$G = G_0 e^{-\beta d} \tag{6.1}$$

G_0 is the contact conductance, β is the inverse decay length and d is the length of the free standing part of the molecule. β is fitted from the slope of the current for various pulling experiments and used as a benchmark to compare the transport for different electron energies. For low bias voltages β is 0.45±0.06 Å^{-1}. This inverse decay length describes the slope of the current for electrons with energies in the HOMO-LUMO gap. The electron energy was increased to study the role of the molecular orbitals on the electron transport. On that account the pulling experiments were repeated in a similar way with the exception

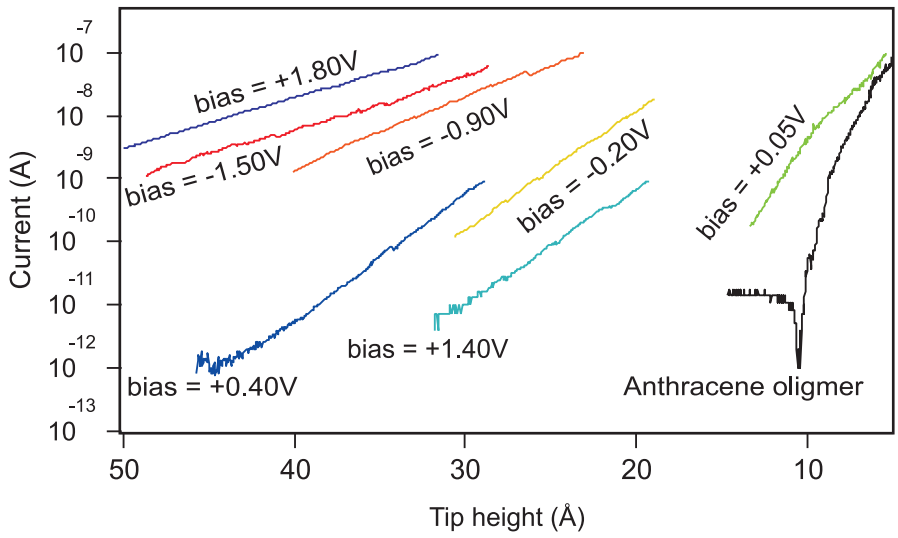

Figure 6.8: Pulling curves for different GNRs at different electron energies.

that two different bias voltages were used during the experiment. At small tip-sample-distances the voltage was kept low, typically between +0.1 V and -0.1 V, to prevent a high current which would damage the molecule. At ∼2 nm the bias voltage was set to the desired value and the tip was withdrawn further from the surface. Fig. 6.8 shows several pulling curves at different bias voltages. Two features are characteristic for all pulling spectra: the exponential decay and the G_0, which varies heavily between the pulling experiments. G_0 reflects the quality of the tip-molecule contact but also the position of the bond, e.g., if the molecule is connected to the last or the second to last atom of the tip [149]. The strength of the bond between tip and molecule could change the transmission probability and, thereby, G_0. The influence of the molecule-surface contact on G_0 is expected to be low as the molecule-surface contact changes during the pulling experiment with the movement of the molecule towards the tip. By all means, the inverse decay length is independent of G_0 and the slope stays the same while only the origin of the current at z=0 is shifted.

Another significant property of the current is how it falls off as a function of the tip height in a smooth and featureless manner. In case of polyfluorene periodic oscillations in the current occur which match the distance between the fluorene units [16]. The smooth shape of the current in Fig. 6.7 points to a continuous bending of the GNR which is in good agreement with calculations (F. Ample and C. Joachim, Institute of Materials Research and Engineering, Singapore) [148]. After a pulling experiment the shape of the GNRs did not change, even for GNRs longer than 20 nm (see figures 6.7a and b). This points to a high degree of stiffness of the GNRs which coincides with the properties of graphene [141].

All pulling curves decay exponentially independent of the bias voltage and the electron energy. In all cases the transport mechanism is direct tunneling and the inverse decay length can be fitted for each voltage. Fig. 6.8 also shows the pulling curve of the anthracene oligomer for comparison. The inverse decay length of the anthracene oligomer with 0.76±0.04 $Å^{-1}$ is much larger than for the GNRs. This is expected because of the low electron delocalization and the larger HOMO-LUMO gap of anthracene oligomers. According to theory (F. Ample and C. Joachim, Institute of Materials Research and Engineering, Singapore), the HOMO-LUMO gap is 1.42 eV for a GNR and 2.5 eV for an anthracene oligomer.

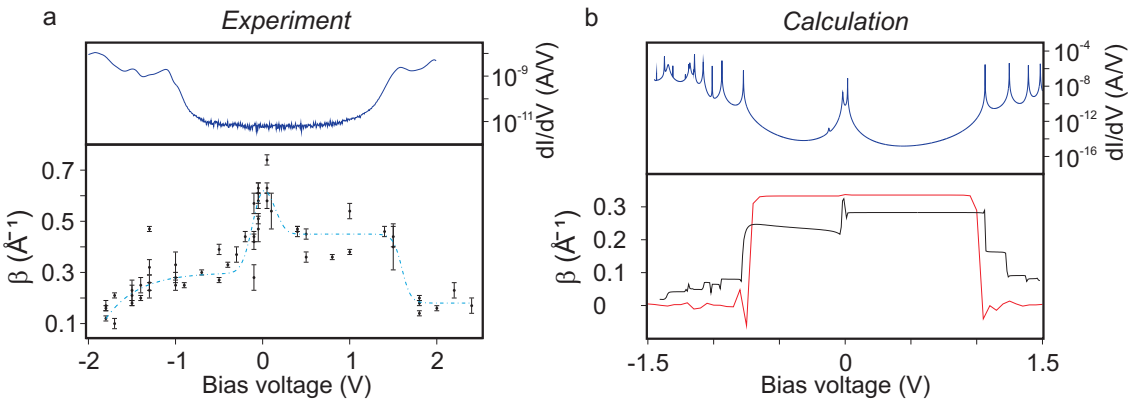

Figure 6.9: Experimental and calculated $\mathrm{d}I/\mathrm{d}V$ spectrum (in pulling geometry) and inverse decay length vs the electron energy. Black: A GNR in pulling geometry. Red: A planar GNR. Calculations done by C. Joachim and F. Ample (Institute of Materials Research and Engineering (IMRE), Singapore).

At the high bias voltages of +1.8 V and -1.5 V the current flattens. To study the transition between the different slopes as a function of the bias voltage pulling curves of different GNRs with various bias voltages were measured (see Fig. 6.9a). There is a sharp drop of β at +1.6 V and a smooth decrease starts for bias energies lower than -1.3 V. These energies coincidence with the position of HOMO and LUMO of the GNR. The STS spectrum shown in Fig. 6.9a was taken of a GNR in pulling conformation. HOMO and LUMO are slightly shifted compared to the STS spectrum of a planar GNR (see Fig. 6.10) but the similarity of both spectra is surprising. For a symmetric molecule in a junction a symmetric $\mathrm{d}I/\mathrm{d}V$ spectrum is expected [150]. This is not the case for the GNRs. The reason might be the unsymmetric junction: one terminus of the ribbon is connected to the tip while the other part is adsorbed planar on the surface. Additionally the geometry of the molecule is unsymmetric during the conduction experiment. In pulling geometry the HOMO is found at -1.1 V and the LUMO at +1.6 V. Theoretically the inverse decay length depends on the position of the HOMO (E_h) as well as the position of the LUMO (E_l), the effective electron mass m^* and the HOMO-LUMO gap [151]

$$\beta(E) = \sqrt{\frac{2m^*(E)}{\hbar^2}\frac{(E-E_l)(E-E_h)}{E_g}} \tag{6.2}$$

where E is the electron energy. In the experiment β decreases with the onset of the HOMO or LUMO in very good agreement with the calculations. The inverse decay length drops at positive bias energies (+1.8 V to +2.4 V) to 0.18±0.03 $\mathrm{Å}^{-1}$. In case of negative energy it decreases continuously to ∼0.1 $\mathrm{Å}^{-1}$. These small values provide evidence that the molecular orbitals participate in the electron transport. The asymmetry of the inverse decay length is related to the asymmetric distribution of the electronic states around the Fermi level. A symmetric distribution of the electronic states would also lead to a symmetric β-curve [148].

The Tamm states have no influence on the conductance which is surprising as they are located close to the Fermi level. The reason for their diminishing importance on the

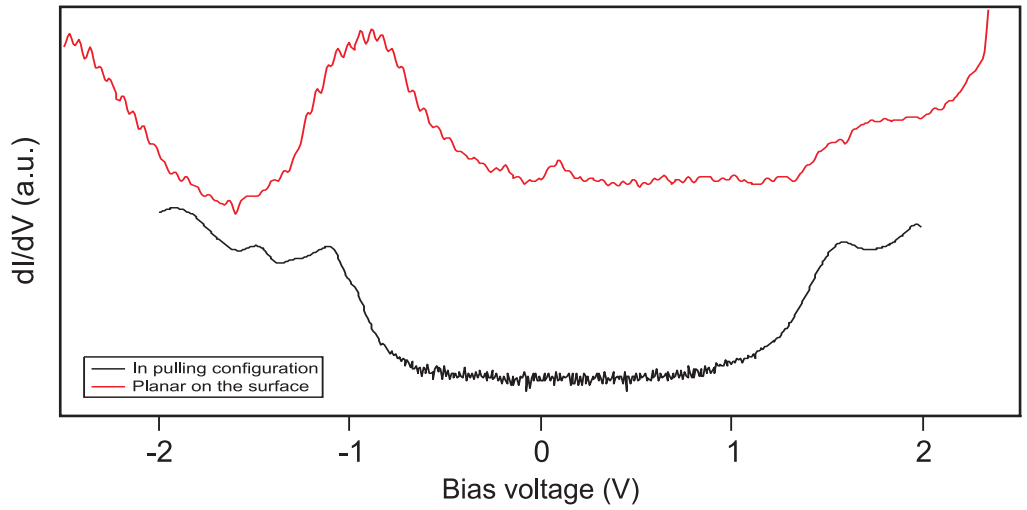

Figure 6.10: Experimental $\mathrm{d}I/\mathrm{d}V$ conductance curves for two different configurations of the GNRs. Red: The ribbon is adsorbed planar on the surface. Black: The ribbon is in pulling geometry between STM tip and surface. The red curve is shifted upwards for better visibility.

conductance is the missing overlap between them. Spectroscopy finds the Tamm states localized at the zigzag edges which are at opposite positions in the ribbon. As each of them has a calculated spatial extension of about ∼1.8 nm the Tamm states of the ribbon termini overlap only for short GNRs (less than 3 nm) for which the calculations predict pseudo-ballistic transport (see chapter 6.2.2). $\mathrm{d}I/\mathrm{d}V$ maps of the GNR show that the HOMO and the LUMO are delocalized along the armchair edges (see figures 6.5b and e). Hence for electron energies matching the molecular orbitals pseudo-ballistic transport is expected. If pseudo-ballistic transport would dominate the conductance the inverse decay length would become zero, which is not the case. This will be discussed in the following section.

The peak which appears in the inverse decay length close to the Fermi energy (Fig. 6.9a) is not related to the Tamm states as the peak occurs for defected termini as well as for defect-free termini (see chapter 6.2.4). It originates from the curvature of the ribbon in pulling geometry. Fig. 6.9b compares the calculated dependence of the inverse decay length on the electron energy for a planar ribbon (red) and for a ribbon in pulling geometry (black). The peak in β appears only in the latter curve of ribbons with the same geometry as in the experiments.

6.2.2 Comparison with Theory

Fig. 6.11 presents the calculated conductance of a planar GNR, whereby case I has the same chemical structure as the experimentally observed ribbon. As long as the opposite Tamm states overlap theory predicts no decay of the conductance for a ribbon with armchair edges (case I in Fig. 6.11a). If the ribbon length is too large for the Tamm states to interact the current decays exponentially. This behavior could not be observed experimentally since the fabrication of adequately short ribbons was impossible. Matching the bias voltage to the position of the HOMO level (Fig. 6.11b) leads to a pseudo-ballistic transport which is

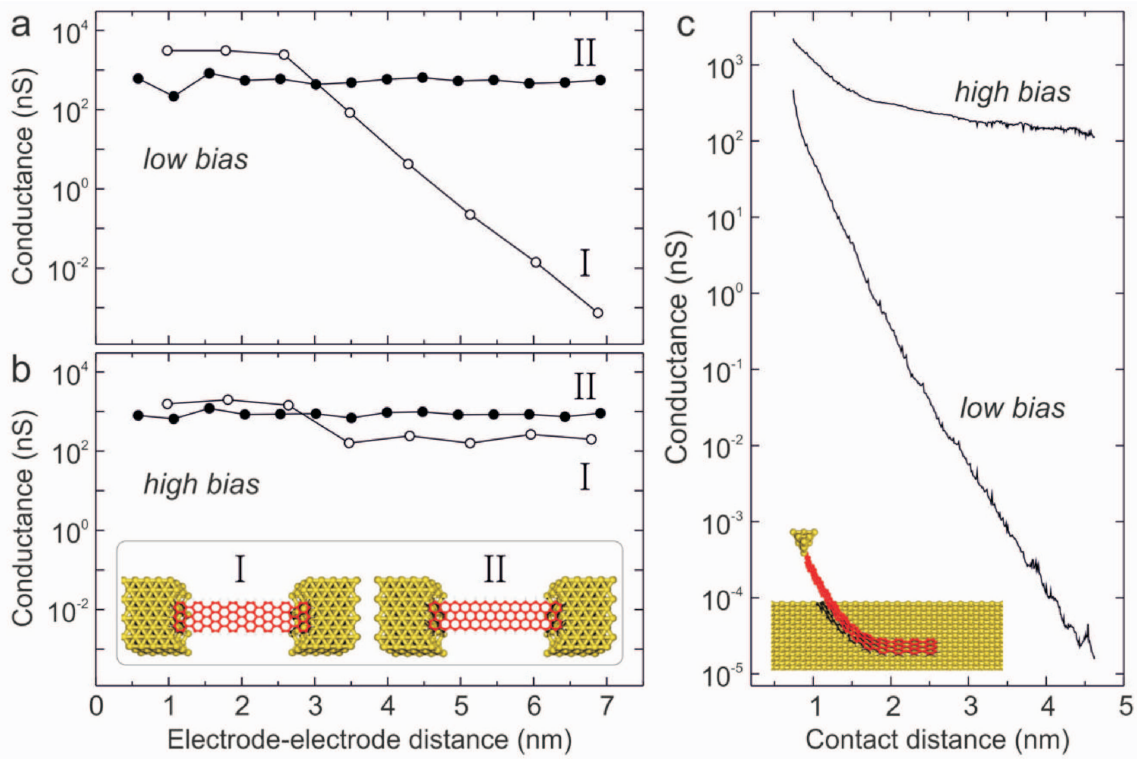

Figure 6.11: Calculated decay for a planar armchair (I) and zigzag (II) GNR at a) low bias and b) high bias where the electron energy matches the HOMO. Calculated decay for an armchair GNR in pulling geometry. Calculations done by C. Joachim and F. Ample (Institute of Materials Research and Engineering (IMRE), Singapore).

independent of the ribbon length. The conductance does not decay with the length of the molecules.

Case II describes a zigzag GNR, more precisely, a GNR with zigzag edges along the ribbon and armchair edges at the termini. Neither the ribbon length nor the electron energy plays a role for the slope of the conductance. In all of the case no exponential decay of the conductance is observed and the conductance is constant with respect to the ribbon length. The Tamm states, which are close to the Fermi level, are delocalized along the ribbon backbone and enable pseudo-ballistic transport even at low bias energies. If the desired transport should be direct tunneling GNRs with armchair edges are preferred and GNRs with zigzag edges for pseudo-ballistic transport. Fabricating GNRs with zigzag edges is challenging. Growing graphene by CVD on various metal surfaces leads to zigzag edges [152], whereas on SiC(0001) graphene with armchair edges is produced [153]. A drawback is the lack of control in regard to the width and the shape of the graphene flake. Many designs of molecular building blocks, which would polymerize to GNRs, face the problem that more than one possibility exists to link two precursor molecules. The chemical structure is, therefore, no longer completely defined by the design of the molecular building block.

However, in the experimentally obtained conductance curves, the current decays exponentially in the low as well as in the high bias regime. The difference between the calculated GNR and the experimentally observed GNRs lies in their geometry. In the calculations a

planar GNR is assumed whereas in experiment the GNR is attached to the tip and slightly bent. The calculated conductance for a GNR in pulling (i.e. curved) conformation in the high bias regime (see Fig. 6.11c) decays exponentially with the increase of the effective transport path of the electrons through the ribbon. See the inset in Fig. 6.11c for the calculated geometry of the molecule in pulling geometry. Bending the GNR modifies the electronic structure and the delocalization is disturbed. Fig. 6.9b shows the calculated inverse decay length for a planar (red) and a bent (black) GNR. In case of the planar geometry β reduces to zero with the onset of the molecular orbitals. In case of the GNR in pulling geometry β decreases it the electron energy matches the molecular orbitals but stays above zero.

6.2.3 Complete Pulling of a Graphene Nanoribbon

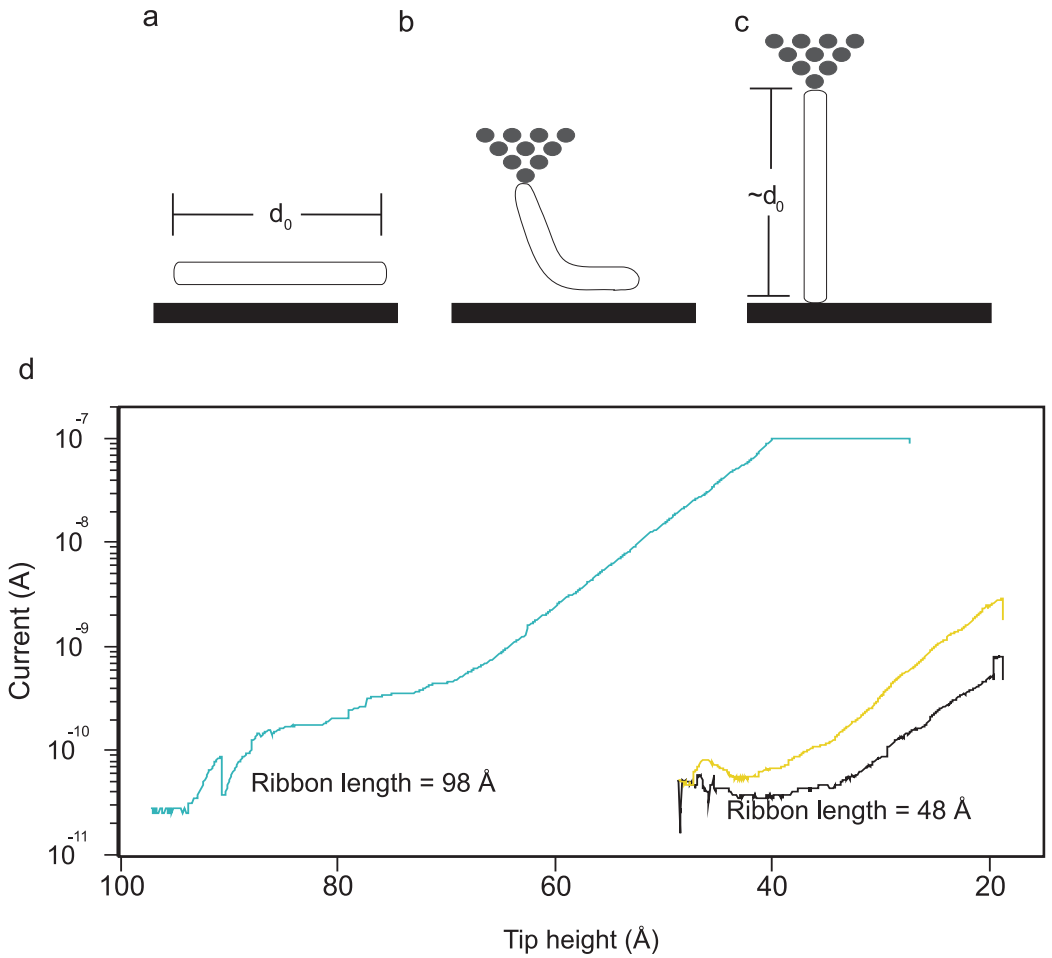

Figure 6.12: **a**,**b**,**c**, Sketched conformation of the ribbon in the junction **a** before pulling, **b** in pulling geometry and **c** at a tip height which equals the length of the ribbon. **d**, Three pulling curves of two different graphene nanoribbons. The length of the nanoribbons is 98 Å and 48 Å. In both cases a bias voltage of +1.8 V is applied.

In the previous section 6.2.2 the lack of pseudo-ballistic transport at high electron energies is explained by the geometry of the ribbon during the pulling experiment. The curvature of the molecule disturbs the electronic delocalization which is required for pseudo-ballistic

transport. If the ribbon is pulled completely from the surface the geometry of the ribbon should changes from a bent conformation to a straight conformation (see figures 6.12a-c). Fig. 6.12a shows the ribbon with a length d_0 which is bent during the pulling experiment (Fig. 6.12b). If the tip height is similar to the ribbon length the ribbon geometry of the ribbon should be straight and, according to theory, pseudo-ballistic transport should occur. Fig. 6.12d shows a pulling spectra of ribbons with a length of 48 Å and 98 Å, which were pulled completely of the surface. For both ribbons the inverse decay length at small tip heights equals ∼0.18 Å^{-1}, which coincides with the results from chapter 6.2.1. If the tip is withdrawn further the inverse decay length decreases almost to zero. The current stays constant as a function of the tip height which points to a different charge transport mechanism. This is in good agreement with the previously discussed calculations which found pseudo-ballistic transport only for a straight ribbon conformation.

6.2.4 Influence of the Ribbon Terminus and Length

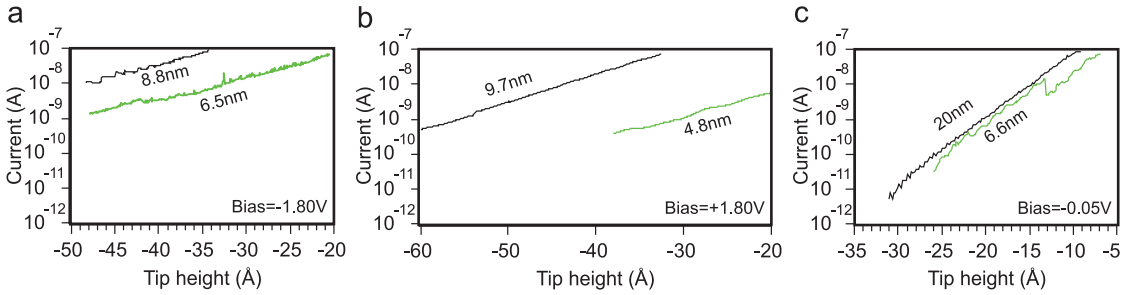

Figure 6.13: Current as a function of the tip height for GNRs with a different length and a bias voltage of **a** -1.80 V, **b** +1.8 V and **c** -0.05 V.

Many different GNRs were pulled up for Fig. 6.9. To exclude an effect of the ribbon length the measured conductance of a short and a long GNR was compared for the three bias regimes (see Fig. 6.13). For the negative voltage of -1.8 V the slope of the current decays very similar to the short and the long GNR (Fig. 6.13a), and the inverse decay length amounts to 0.16±0.01 Å^{-1} for the short and 0.17 ± 0.02 Å^{-1} for the long GNR. At the positive high bias regime β is 0.18±0.01 Å^{-1} for the 4.8 nm short and 0.20±0.01 Å^{-1} for the 9.7 nm long GNR (Fig. 6.13b). For the high positive and negative bias regime no influence of the ribbon length on the conductance was observed. The values are the same in the range of error. Two spectra were selected with a bias of -0.05 V for the low bias regime. The inverse decay length for the 6.6 nm short GNR is 0.44±0.04 Å^{-1} and for the 20 nm long GNR β 0.42±0.01 Å^{-1} (Fig. 6.13c). Also in this case the ribbon length does not affect the conductance. Only the effective length of the free standing part of the ribbon is important for the conductance.

Three different termini were found for the GNRs. To see if the conductance changes as a consequence of the missing Tamm state the inverse decay length was compared to ribbons with and without a Tamm state in Fig. 6.14. This is the same data as shown in Fig. 6.9 except for the color code. Green data points are ribbon ends with a Tamm state and the blue data points ribbon ends without a Tamm state. For ribbons larger than 4 nm, which is the shortest ribbon pulled up (see Fig. 5.32), neither the Tamm state nor the defected terminus play a role in the conductance measurements. This is in agreement with theory,

which predicts pseudo-ballistic transport only for armchair GNRs shorter than ~3 nm (see chapter 6.2.2).

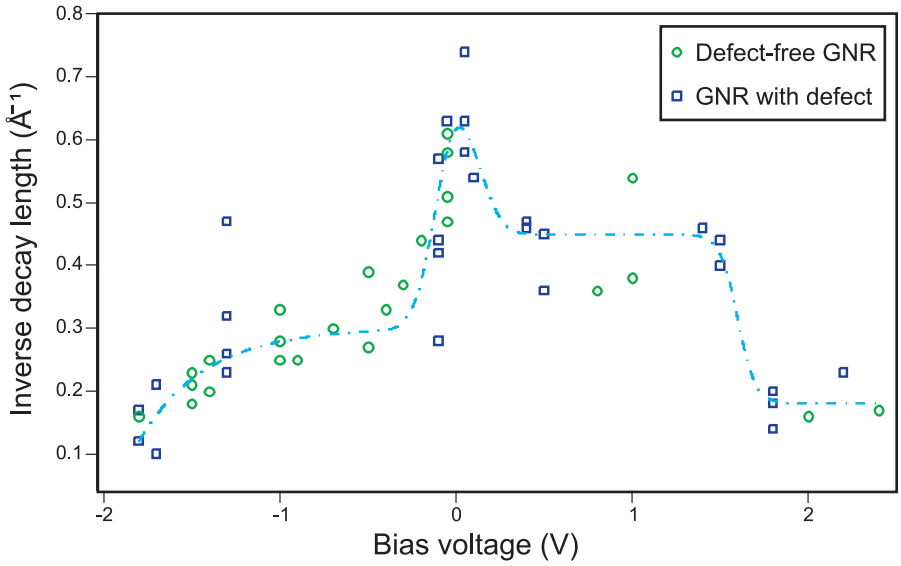

Figure 6.14: Experimental inverse decay length as a function of the electron energy for defected and defect-free termini. Green: GNR with a Tamm state Blue: GNR without a Tamm state.

6.2.5 Influence of Defects

To produce defects in a controlled manner, the Au(111) substrate has been heated to 600 K instead of 670 K. This leads to partially dehydrogenated GNRs as discussed before (Fig. 5.33) [139]. The protrusions in the GNRs are caused by phenyl rings which are not dehydrogenated and face away from the ribbon backbone.

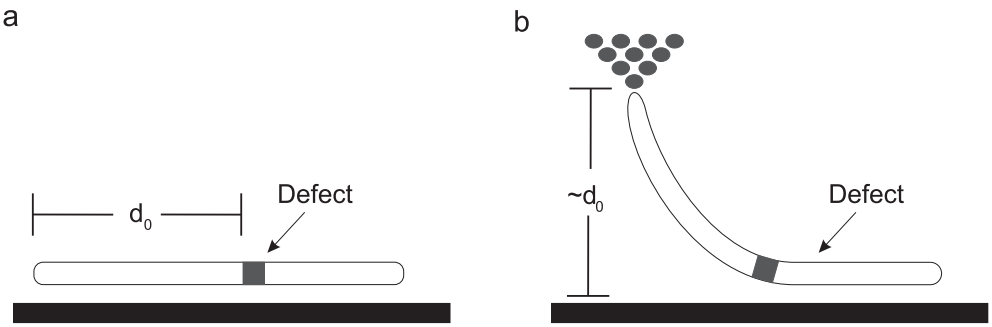

Figure 6.15: Sketch of a pulling experiment. A defected GNR is pulled up from the surface. d_0 describes the distance between the defect and the terminus connected by the tip. At a tip height of $\sim d_0$ the defect should be pulled from the surface.

To study the influence of these missing bonds on the conductance before each experiment the position of the phenyl rings is determined by STM imaging. Fig. 6.15 sketches a pulling experiment of a defected ribbon where d_0 is the distance between the defect and the terminus connected to the tip (Fig. 6.15a). If the tip height is similar to d_0 the defect is pulled from the surface (Fig. 6.15b).

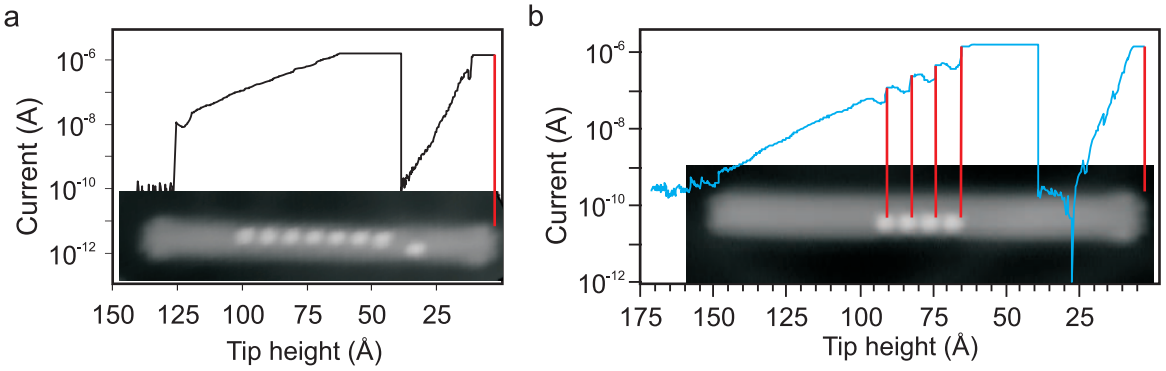

Figure 6.16: **a**, Pulling experiment of a GNR which is not fully cyclodehydrogenated. The applied bias voltage is -1.8 V. Inset shows the corresponding 15x3.5 nm^2 STM image. **b**, Pulling experiment of a GNR which is not fully cyclodehydrogenated. The applied bias voltage is -1.8 V. Inset shows the corresponding 16x4 nm^2 STM image.

Three different regimes exist for the electron energy: the low bias regime with energies in the HOMO-LUMO gap and the two high bias regimes with energies above the molecular orbitals depending on the polarity. In case of applying a negative bias up to -1.8 V no change in conductance is observed as compared to the defect-free ribbons and β is in average 0.10±0.02 Å^{-1}. This is in good agreement with the defect-free ribbons. Most of the spectra recorded at a bias energy of -1.8 V are either completely smooth (Fig. 6.16a) or have smaller jumps at a tip height which correspond to the position of the defects (see Fig. 6.16b). At a tip height which matches a defect, the defects is detached from the surface. This is illustrated by the STM image in the pulling curve. Both, the STM image and the pulling curve have the same scaling. Fig. 6.16b shows a beautiful pulling spectrum. The current in Fig. 6.16b is completely flat before and after the defects with the same inverse decay length of β=0.08 Å^{-1}. The tip height of the first dip in the current matches the position of the first defect of the ribbon, which is indicated by the red line in Fig. 6.16b. The defect probably leads to a stronger bending and disturbs the delocalization of the electronic states which causes a dip in the current (see chapter 6.2.2). The low bias regime is similar to the negative high bias regime as in Fig. 6.16a.

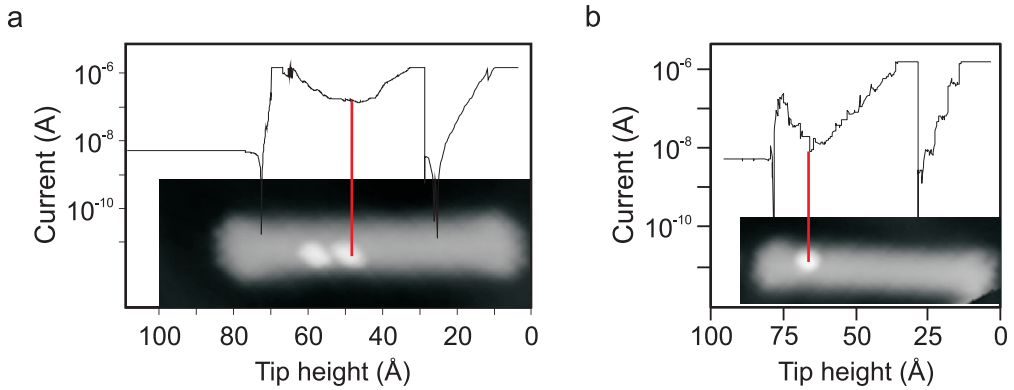

Figure 6.17: **a**, Pulling experiment of a GNR which is not fully cyclodehydrogenated. The applied bias voltage is +1.8 V. Inset shows the corresponding 10x3.5 nm^2 STM image. **b**, Pulling experiment of a GNR which is not fully cyclodehydrogenated. The applied bias voltage is +1.8 V. Inset shows the corresponding 9x3 nm^2 STM image.

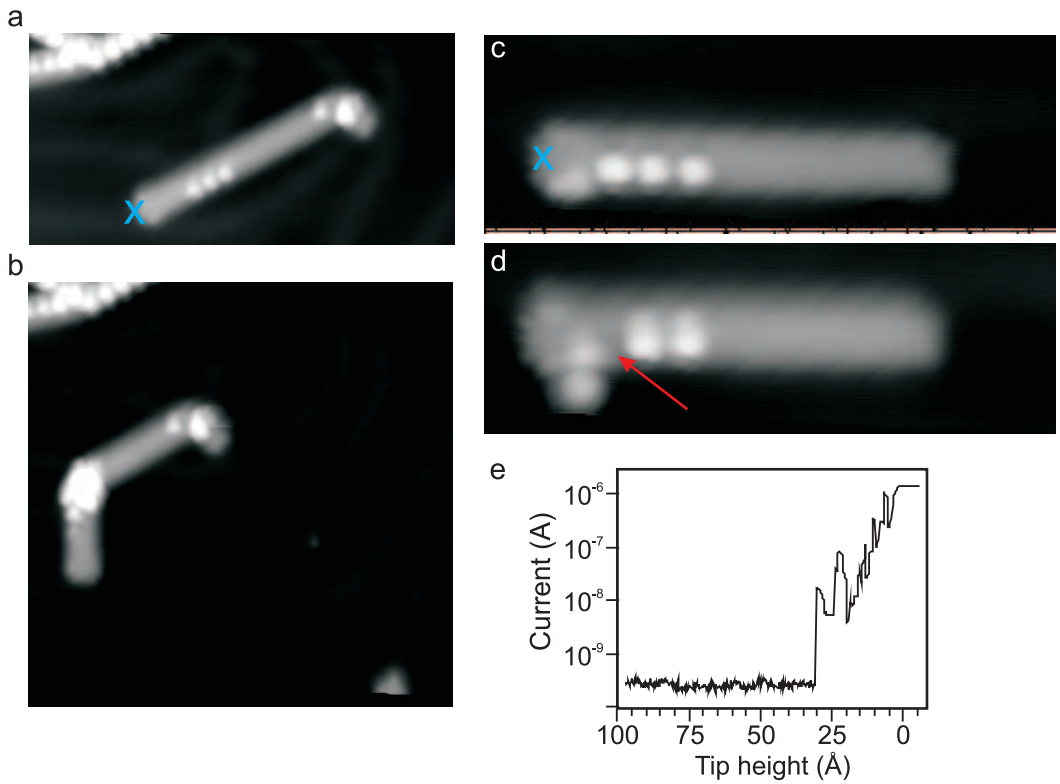

Figure 6.18: **a** 20x10 nm^2 STM image before and **b** 20x20 nm^2 STM image after pulling up a GNR. The bias is +1.8 V and the position of the tip approach is marked by the cross. **c**,**d**, 12x4 nm^2 STM images **c** before and **d** after pulling up a GNR. The bias is +0.5 V and the position of the tip approach is marked by the cross. **e**, Current spectrum of a successful pulling after taking the image **c**

The situation differs for the positive high bias regime. At +1.6 V and higher the slope of the current decays until the defect is lifted up as usual. Close to the tip height, which matches the position of the defect in the ribbon (indicated by the red lines in figures 6.17a and b), the current increases by up to one order of magnitude (at 70 Å in Fig. 6.17a and and at 75 Å in b). Then the contact is lost probably due to the large current flux, which damages the molecule. Afterwards, the molecule disappeared from the surface. Only in a few cases the molecule was found on the surface after a pulling experiment. Fig. 6.18a shows the molecule before and Fig. 6.18b after pulling. The bias energy was +1.8 V. At the position of the defects a bright pile is resolved, which gives evidence that the molecule was chemically changed. Additionally, the direction of the ribbons changes. Before the pulling experiment the ribbon was completely straight and after the experiment the ribbon is separated into two straight parts at the position of the defects. The appearance of these straight parts in STM images is similar to the ribbon ends before the pulling experiment. This proves again the high stiffness of GNRs [141].

At a tip height equal to the position of the defect in the GNR an increase of the current is observed only at high positive energies and never for negative energies. Therefore, the increase in the current cannot just be for a geometrical cause, e.g. the possibility for a planar ribbon geometry between tip and substrate which leads to pseudo-ballistic transport. This explanation would be independent of the polarity of the voltage; also for voltages below the HOMO the current should increase dramatically which is not the

case. A different explanation is a dehydrogenation and planarization of the isolated phenyl groups which appear for bias energies above the LUMO. The resulting increase of the conductance destroys the molecule. In case of the graphitic nanoribbons joule heating occurred above +1.6 V [103]. The rearrangement of the edges of graphitic nanoribbons can be triggered by applying a bias of +1.6 V and higher [103]. Zigzag edges are preferred because of their higher conductance which is related to the Tamm states located close to E_F. Most of the current flows along the zigzag edges and a contact between a zigzag edge and a non-zigzag edge or, in general, a point defect reduces the current flow and acts as a resistor [103].
Fig. 6.18c is recorded before the pulling experiment and Fig. 6.18d after. Although only a bias of +0.5 V was applied during the pulling the first defect vanishes. Instead, a dark line appeares similar to the voltage pulse experiments discussed before (indicated by the red arrow in Fig 6.18d) [139]. This might point to a planarizations of the defect.

6.3 Vibrations

During the conductance and the $\mathrm{d}I/\mathrm{d}V$ measurements of a single GNR the tip and the molecule form a stable bond which lasts for several minutes. To detect the vibrational states of the ribbon the second derivative of the current is recorded [32]. The interaction of the electron with the molecular dipoles causes an electronic or vibrational excitation $h\nu$ where the electron inelastic scatters and loses part of its energy. If the energy of the electrons is too small the inelastic channel is closed. If the electron energy is larger than $h\nu$ an additional transport channel opens and the slope of the current increases. This change in slope is equal to a step in the $\mathrm{d}I/\mathrm{d}V$ signal and a peak in the $\mathrm{d}^2I/\mathrm{d}V^2$ signal. As a result the vibrational spectrum should be symmetric with regard to the origin, and for each peak a dip appears at the corresponding inverted energy (see Fig. 2.6 in chapter 2.6). For these experiments a GNR is pulled up to a tip height of 1.85 nm where the ribbon stays in the junction for longer than 20 minutes and five spectra are recorded between -400 mV and +400 mV. The energy window of -400 mV to +400 mV was chosen as it covers the energy range of vibrational excitations (see table 6.1).

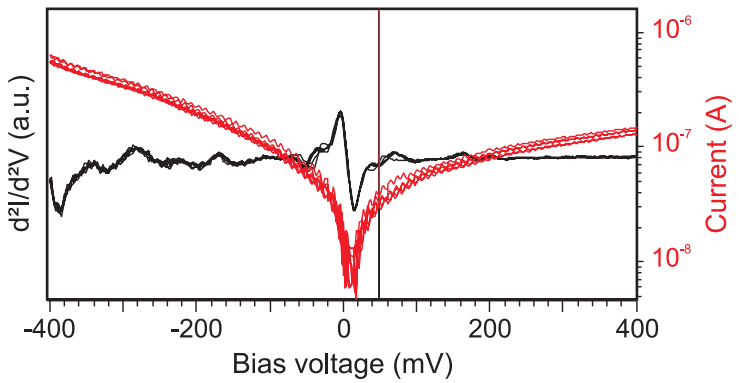

Figure 6.19: $\mathrm{d}^2I/\mathrm{d}V^2$ spectrum of a GNR in pulling geometry without averaging (Black: $\mathrm{d}^2I/\mathrm{d}V^2$, Red: Current). The absolute value of the current is shown in logarithmic scaling.

Energy	Mode	Method	Reference
49.09 mV	Radial breathing like mode	Raman Spectr.	[110]
49.09 mV	Radial breathing like mode	Raman Spectr.	[104]
50.08 mV	C-C torsion	HREELS	[140]
75.50 mV	Edge mode	HREELS	[140]
98.31 mV	C-H Bending mode	HREELS	[140]
118.15 mV		Raman Spectr.	[104]
119.02 mV	Third overtone of radial breathing like mode	Raman Spectr.	[110]
151.25 mV	Edge phonon mode	Raman Spectr.	[110]
151.25 mV		Raman Spectr.	[104]
156.21 mV		Raman Spectr.	[104]
156.21 mV	Edge phonon mode	Raman Spectr.	[110]
166.25 mV		Raman Spectr.	[104]
167.37 mV	D mode	Raman Spectr.	[110]
198.37 mV		Raman Spectr.	[104]
199.60 mV	G mode	Raman Spectr.	[110]
249.96 mV	C≡C of dehydrogenated edges	Raman Spectr.	[110]
322.72 mV	2D	Raman Spectr.	[110]

Table 6.1: Overview of the observed vibrations of a planar adsorbed armchair GNR on Au(111) from other techniques. Raman Spectr. stands for Raman spectroscopy

Similar to the pulling experiments of chapter 6.2.1 the tip is approached to the terminus of the GNR. If a junction is formed the STM tip is retracted. During the approach and the withdrawal a small bias of 50 mV is applied to the sample. This is necessary to prevent a high current at small tip heights which could damage the molecule. At a tip height of 1.85 nm the bias voltage is swept five times from -400 mV to +400 mV to collect more data and to prove the reproducibility as well as the stability of the junction.
Fig. 6.19 shows a representative $\mathrm{d}^2I/\mathrm{d}V^2$ spectrum of a GNR in pulling geometry. The bias voltage was ramped five times from -400 mV to +400 mV and to show its reproducibility the spectrum has not yet been averaged. The duration for one bias sweep is 2.5 min. In each sweep the shape of the $\mathrm{d}^2I/\mathrm{d}V^2$ signal is similar, independent of its direction, i.e., from -400 mV to +400 mV or from +400 mV to -400 mV. The intensity of the current and of the $\mathrm{d}^2I/\mathrm{d}V^2$ signal depends on the polarity of the bias voltage. The asymmetry in the current results from an asymmetric distribution of the electronic states around the Fermi level (see chapter 6.2.1) which might cause the weaker $\mathrm{d}^2I/\mathrm{d}V^2$ signal for positive bias voltage. Features above +200 mV are difficult to observe.

Table 6.1 summarizes the vibrational excitations known from literature. The large amount of the vibrations listed in the range of 75 and 250 mV complicates the analysis of the measured $\mathrm{d}^2I/\mathrm{d}V^2$ spectra. The positions of the Raman modes are characteristic for the quality and the thickness of the graphene flake. As discussed in the literature the G mode at ∼199 mV is a transversal and linear optical phonon mode [85, 104, 110]. The D mode at 167.37 V is related to the breathing of the phenyl rings [85, 104, 110]. With the shift of the 2D mode at 322.72 mV the number of graphene layer of the sample can be identified, and the intensity of the D mode increases with the amount of defects. Additionally, the D band scattering is forbidden in Raman spectroscopy for edges with zigzag structure. This can be used to distinguish zigzag edges from armchair edges. (see chapter 3.2 for details) [85].

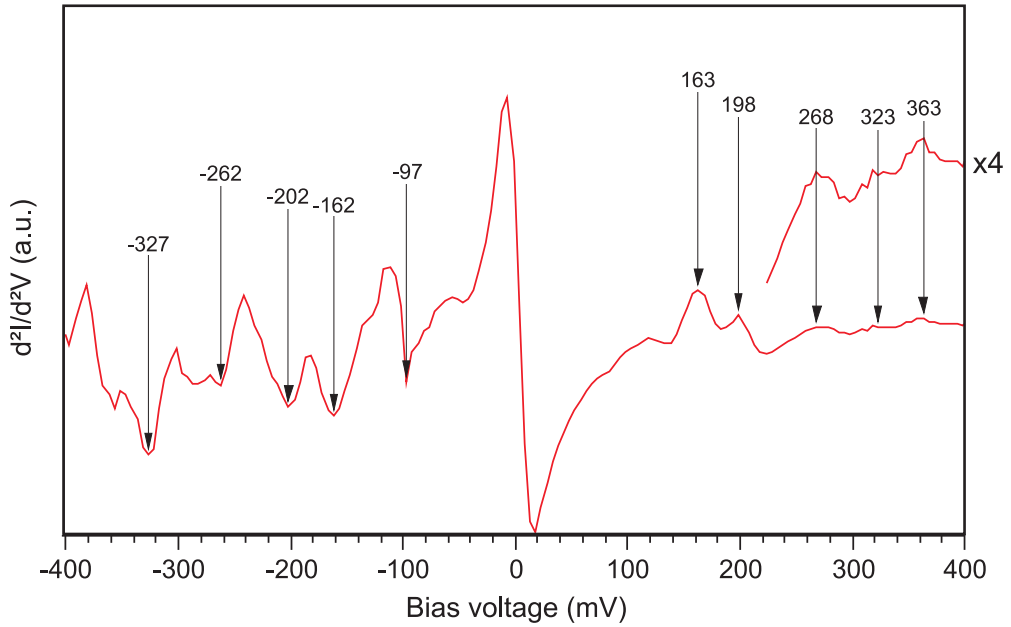

Figure 6.20: Averaged $\mathrm{d}^2I/\mathrm{d}V^2$ from 12 different GNRs which have been pulled up. The pulling spectrum of each GNR was averaged over five sweeps from -400 to +400 mV.

Fig. 6.20 shows the vibration spectrum averaged from 12 measured pulling experiments. The intensity for positive bias voltages is also weaker in this case as explained above. Strong features at the negative sides appear at -97 mV, -162 mV, -202 mV, -262 mV and -327 mV. Not every dip at negative energy has a clear peak at the corresponding positive energy. This might be caused by the asymmetric shape of the current and the resulting lower intensity of the $\mathrm{d}^2I/\mathrm{d}V^2$ at positive bias voltage. However, the dips at -162 mV and -202 mV belong to the peaks at +163 mV and +198 mV, respectively. The excitation at -162 mV is assigned to the D mode and the excitation at -202 mV to the G mode [110, 104]. In Raman spectroscopy the intensity of the D mode depends on the edge structure while its intensity is enhanced for armchair edges, which is the edge structure of the investigated GNRs [154]. The weak feature at -262 mV can be related to the C≡C vibration of the dehydrogenated edges [110]. This would support the interpretation of the existing branches, which appear due to the dehydrogenation of the edges. The shift, compared to the value known from the literature, might be explained by the pulling geometry of the ribbon and the missing surface interaction of the hydrogens; in the literature the vibrations were measured from planar adsorbed ribbons. The feature at -327 mV is assigned to the 2D mode, which is also slightly shifted compared to 322.72 mV as derived from the literature [110], and the C-H bending mode is observed at -97 mV [140]. To examine if the ribbon geometry causes the shift the $\mathrm{d}^2I/\mathrm{d}V^2$ signal is measured from a planar adsorbed ribbon and compared to the $\mathrm{d}^2I/\mathrm{d}V^2$ signal of the same ribbon in pulling geometry.

The second derivative of the current was measured on the clean Au(111) surface (gold), then on the terminus of the planar adsorbed GNR (blue) and finally in the pulling geometry (red). Fig. 6.21 shows two typical sets. The pulling geometry reduces the interaction of the GNR with the substrate, therefore, the excitation energy of the vibration might shift. In case of a CO molecule the mechanical coupling of the CO molecule to the substrate increases the CO vibration energy by ∼3.7 meV [155]. On the other hand, the interaction

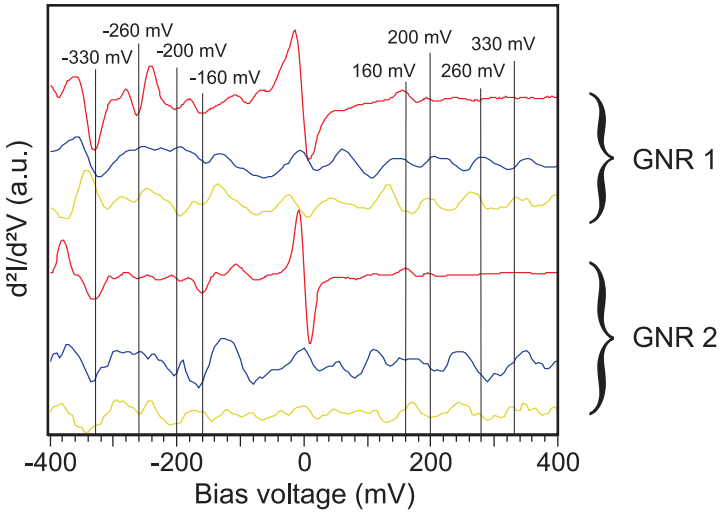

Figure 6.21: Set of $\mathrm{d}^2I/\mathrm{d}V^2$ spectra from two different GNRs. Red: In pulling geometry. Blue: At the center of a planar adsorbed GNR. Gold: On the clean Au(111) surface.

between the CO dipole and its image decreases the CO vibration energy by 3.1 to 6.2 meV [155]. The bending of the ribbon might also cause a shift in the excitation energy of the breathing modes of the phenyl rings. Comparing the vibrational spectrum of a planar adsorbed GNR and of the same GNR in pulling geometry does not provide an evidence that the energy of the vibrational excitation shifts because of the different geometry (see Fig 6.21). However, it might also be that the resolution of the $\mathrm{d}^2I/\mathrm{d}V^2$ signal is not sufficient. In particular, the features in the $\mathrm{d}^2I/\mathrm{d}V^2$ spectrum of the planar adsorbed GNR are broadened, and no clear shift of the vibration energy was observed due to the pulling geometry.

6.4 Summary

Scanning tunneling microscopy and scanning tunneling spectroscopy (STS) were used to characterize the electronic states of a defect-free N=7 wide armchair graphene nanoribbon (GNR). The HOMO, the LUMO and the Tamm state were studied by STS. The HOMO and the LUMO are located at -0.9 V and +1.7 V, respectively, which signifies a HOMO-LUMO gap of 2.8 eV. This is in good agreement with recent reports (E_g = 2.8±0.4 eV) [142]. The HOMO as well as the LUMO are delocalized along the armchair edges sideways of the ribbon. The Tamm state at 0.03 V, which is localized at the zigzag edges of the termini, is a fingerprint for a defect-free GNR. Small changes in the chemical structure of a zigzag terminus lead to the disappearance of the Tamm state and of the characteristic fringed shape of the ribbon end in STM images.

To measure the conductance of a single GNR vertical pulling manipulation with STM was used [16]. A single ribbon is lifted from the surface with the STM tip, whereby the effective transport path d of the electrons increases. The slope of the current as a function of the tip height is smooth and featureless which points to a continuous bending of the ribbon. A stepwise lifting of a molecular chain would lead to periodic oscillations in the current [16]. By varying the bias energy the role of the molecular orbitals on the conductance can be studied. However, the current decays exponentially independent of the bias voltage, and the current curves are fitted by

$$G = G_0 e^{-\beta d} \tag{6.3}$$

to compare the inverse decay length β depending on the electron energy. G_0 is the contact conductance. For bias voltages, which match the HOMO or the LUMO, the inverse decay length decreases from ∼0.45 Å^{-1} in the HOMO-LUMO gap to ∼0.10 Å^{-1}. Nevertheless, the conductance falls off exponentially and not linearly, while direct tunneling is the charge transport mechanism. This is surprising as pseudo-ballistic transport was expected for electron energies which coincide with the energy of the molecular orbitals. Calculations predict the pulling conformation of the ribbons, e.g., the bending, as the reason for the quenched pseudo-ballistic transport. The bending of the GNR disturbs the delocalization. This is in good agreement with the experimental observations, which find a decrease of the inverse decay length for a more planar ribbon geometry at large tip heights. Although the energy of the Tamm state is close to the Fermi energy the Tamm state does not participate in the conductance as it is localized at the ribbon terminus. Only for ribbons shorter than ∼3 nm theory predicts an overlap of the opposite Tamm states and an improved conductance. However, ribbons that short were not observed experimentally.

Reducing the temperature for cyclodehydrogenation to 600 K produces GNRs with phenyl rings which are partially not planarized. To study the role of these defects on the conductance the ribbons are characterized by STM imaging and afterwards pulled from the surface. The influence of the rotated phenyl rings on the conductance is small in regard to low and negative bias voltages. For these bias energies the inverse decay length is similar to the defect-free ribbons. At positive bias voltages higher than the LUMO lifting up a defect leads to an increase of the current by one order of magnitude. An explanation could be the dehydrogenation and planarization of the "defected" phenyl rings by Joule heating. It has been reported that a bias voltage of 1.6 V applied to a graphitic nanoribbon leads

to a rearrangement of the edge structure [103]. Zigzag edges are preferred because of their higher conductance. The current mainly flows along the zigzag edges and a contact between a zigzag edge and a non-zigzag edge or, in general, a point defect reduces the current flow and acts as a resistor [103]. Therefore, the carbon atoms at the edges vaporize, which leads to a reconstruction into a zigzag or an armchair structure [103].

The vibrational states of a single ribbon were measured by inelastic tunneling spectroscopy in pulling geometry. Features at -97 mV, -162 mV, -202 mV, -262 mV and -327 mV are resolved in the spectrum. Comparing these energies to vibrations known from the literature makes an identification of the vibrations possible. The weak feature at $\sim$-262 mV might be assigned to the C$\equiv$C vibration of the partially dehydrogenated edges [110]. The G mode and the D mode are attributed to the dips at $\sim$-202 mV and $\sim$-162 mV, respectively [110, 104]. The intensity of the D mode depends on the edge structure in Raman spectroscopy [154], and its intensity is enhanced for armchair edges, which is the edge structure of the investigated GNRs [154]. The 2D mode is attributed to the dip at $\sim$-327 mV [110], and the feature at -97 mV might be related to the C-H bending mode [140]. Finally, the vibrational spectra of the same ribbon is compared: first planar adsorbed on the surface and then in pulling geometry. However, no obvious change of the vibrational spectra is detected due to the geometry on the ribbon.

Chapter 7

Force Measurements of Polyfluorene Chains

This chapter is based on a collaboration between the group of E. Meyer (University of Basel) and L. Grill (Fritz-Haber-Institut der Max-Planck Gesellschaft, Berlin). The experiments were conducted by Shigeki Kawai and myself at a low temperature STM/AFM of the University of Basel. The STM was used to image and characterize the molecular wires. The actual experiment was to pull a molecule from the surface and to measure the required force with an AFM. In contrast to an STM, the AFM measures the frequency shift of the cantilever (frequency modulation was used) instead of the current. The frequency shift signal can be related to the vertical force acting on the cantilever, which is discussed in greater detail in section 7.1.

Single molecule force spectroscopy was used to study the elongation of polyazobenzene peptides chains [8]. Azobenzene exists in two conformations: either *trans* or *cis* [156, 157]. The change of the conformation, i.e., isomerization, may be optically excited. A *cis* to *trans* isomerization is achieved by illuminating the molecule with a laser at a wavelength of 436 nm. Due to the different electronic structure a *trans* to *cis* isomerization can be triggered by an optical excitation at 366 nm [158]. The polyazobenzene peptides wire was attached to the AFM tip and illuminated with a laser at a wavelength of 420 nm [8]. As the trans-isomer is slightly larger than the cis-isomer the length of the molecular wire was increased [8]. A force of 205 pN emerged after the chain was shortened by three 365 nm pulses causing the *trans* to *cis* isomerization [8].
Atomic force microscopy was also used to measure the unfolding of individual titin immunoglobulin domains where a maximum force of 150 to 300 pN was reported [159]. Single ubiquitin chains were stretched at a constant force of 120 pN, and an elongation in steps of 20 nm was observed [160]. However, all these experiments are not performed on a single molecular scale, and neither the molecule before the stretching experiment nor the contact or the geometry of the molecule in the junction are well-defined. On a single molecule level 3,4,9,10-perylene-tetracarboxylicacid-dianhydride was lifted by a AFM/STM tip from the surface [149]. While the molecule was pulled from the surface the frequency shift signal was recorded, and a force of 0.6 nN was necessary to remove the molecule from the surface [149]. The drawback of these molecules is their short length of 1.14 nm [161] and that, therefore, no periodic measurement signal is to be expected.

The idea of this section is to measure the frequency shift of long and uniform wires so that the features in the signal and hence active forces can be assigned to the molecular structure. A promising candidate for such experiments is DBTF, which polymerizes to polyfluorene chains after dehalogenation [16]. The advantages of these chains are their length larger than 100 nm [16] and their homogeneous chemical structure. Due to the periodic repetition of the fluorene units a periodic frequency shift signal is expected, and the required force to lift a molecule from the surface can be obtained. Length-dependent conductance measurements proved that single polyfluorene chains can be pulled off the surface with an STM tip. In the current signal oscillations were detected with a periodicity of ∼10 Å, which coincides with the length of a single fluorene unit [16]. Hence, each oscillation is related to a fluorene unit lifted from the surface. In this chapter AFM pulling experiments with the same molecules are discussed. Instead of measuring the current as in scanning tunneling microscopy experiments, the frequency shift is recorded while lifting up the chains with an AFM tip.

7.1 Atomic Force Microscopy

Atomic force microscopy and scanning tunneling microscopy are both scanning probe techniques and the experimental setup is similar. In case of scanning tunneling microscopy the tunneling current is measured between a conducting tip and a conducting sample, whereas the force acting between the tip and the sample is detected in atomic force microscopy. These forces are measured by the deflection cantilever which mounts the AFM tip. Therefore, in atomic force microscopy experiments a conducting sample is no longer necessary. In order to measure only the force perpendicular to the surface the cantilever is rigid in two directions and soft perpendicular to the surface. Furthermore, the cantilever is characterized by its spring constant k, its eigenfrequency f_0 and its quality factor Q. The quality factor Q describes the damping properties of the cantilever. A high quality factor indicates an under-damped oscillator as well as a low rate of energy loss relative to the stored energy. The spring constant of the cantilever lies between 0.001 N/m and 100 N/m [162]. The amplitude of the cantilever depends on the spring constant, and to reach small amplitudes in the range of a few Ångström spring constants in the order of several hundred N/m are necessary [163]. The experiments discussed in chapter 7.2 were performed on a commercial Omicron AFM/STM microscope equipped with a quartz tuning fork. Quartz tuning forks have a very high Q-factor in the order of 10^5 [164]. Cantilevers with large quality factors like that tend to have a high frequency stability and little energy consumption [163]. Both prongs oscillate opposite to each other if their eigenfrequencies match [163]. However, mounting the tip on one prong breaks this symmetry because of the additional mass and the interaction between tip and sample [163]. This problem was solved by attaching one of the two beams onto the cantilever holder.

Two different operation modes exist for atomic force microscopy: static atomic force microscopy and dynamic atomic force microscopy. In static atomic force microscopy the cantilever bends in response to the force F_{ts}, which acts between tip and sample. The force F_{ts} is used to measure the image. To guarantee a defect-free imaging the cantilever must be much softer than the bonds in tip and sample [163]. Additionally, its eigenfrequency should be higher then the desired detection bandwidth to prevent a resonant excitation of the cantilever. This might increase the oscillation amplitude of the tip and damage the

sample [163]. Obtaining images in static atomic force microscopy is extremely challenging experimentally. The attractive forces between tip and sample have to be canceled to prevent a jump-to-contact. This has been achieved by immersing the tip and the sample in a liquid or by applying electromagnetic forces to the cantilever [164]. An advantage, however, is the easy interpretation of the experimental data. A static AFM image is the map of the piezo height for a constant force F_{ts}.

In dynamic atomic force microscopy the cantilever is operated either in amplitude modulation or frequency modulation. In the case of amplitude modulation the amplitude and the frequency (which is set close to the eigenfrequency) is fixed. The measurement signals are the change in the amplitude and the change in the phase of the cantilever, both caused by the interaction of the tip with the sample [163]. The time scale of a change in the amplitude is proportional to the quality factor. For cantilevers with a high quality factor imaging in the amplitude modulation mode is very slow. This improves with the frequency modulation mode as a change in the eigenfrequency occurs in one oscillation cycle [163]. In case of the frequency modulation mode the cantilever is operated at its eigenfrequency and the amplitude is kept fixed. The change in the frequency Δf is recorded.

The tip-cantilever system can be treated as a harmonic oscillator with a point mass m^* [165]. If the tip is far away from the sample the resonance frequency is

$$\omega_0 = (k_0/m^*)^{\frac{1}{2}} \tag{7.1}$$

The force acting on the tip is a sum of the restoring force of the cantilever F_{can} and of the tip-sample interaction force F_{ts}. The cantilever force is similar to that of a Hookean spring:

$$F_{can} = -k_0(s - s_0) \tag{7.2}$$

s is the vertical displacement of the cantilever from the position s_0 where the force acting on the tip equals zero. The total force acting on the tip amounts to

$$F_{total} = F_{can} + F_{ts} \tag{7.3}$$

If the force gradient is constant during the oscillation cycles the total spring constant can be written as:

$$k = k_0 + \delta k = k_0 + \frac{dF_{ts}}{dz} \tag{7.4}$$

This leads to a frequency of

$$\omega = (\frac{k_0}{m^*} + \frac{1}{m^*}\frac{dF_{ts}}{dz})^{\frac{1}{2}} \approx \omega_0(1 - \frac{1}{2k_0}\frac{dF_{ts}}{dz}) \tag{7.5}$$

The Taylor approximation is valid if the gradient of the tip-sample interaction force is small compared to the spring constant of the cantilever. The frequency shift of the frequency

signal is the gradient of the tip-sample interaction force. If the force gradient is constant during the oscillation cycle the change in frequency can be considered proportional to the force gradient [163].

$$\Delta f = \frac{1}{2k_0}\frac{dF_{ts}}{dz} \tag{7.6}$$

For the experiments the STM was used for imaging the surface and the AFM mode was used only during the vertical pulling experiments.

7.2 Dibromoterfluorene

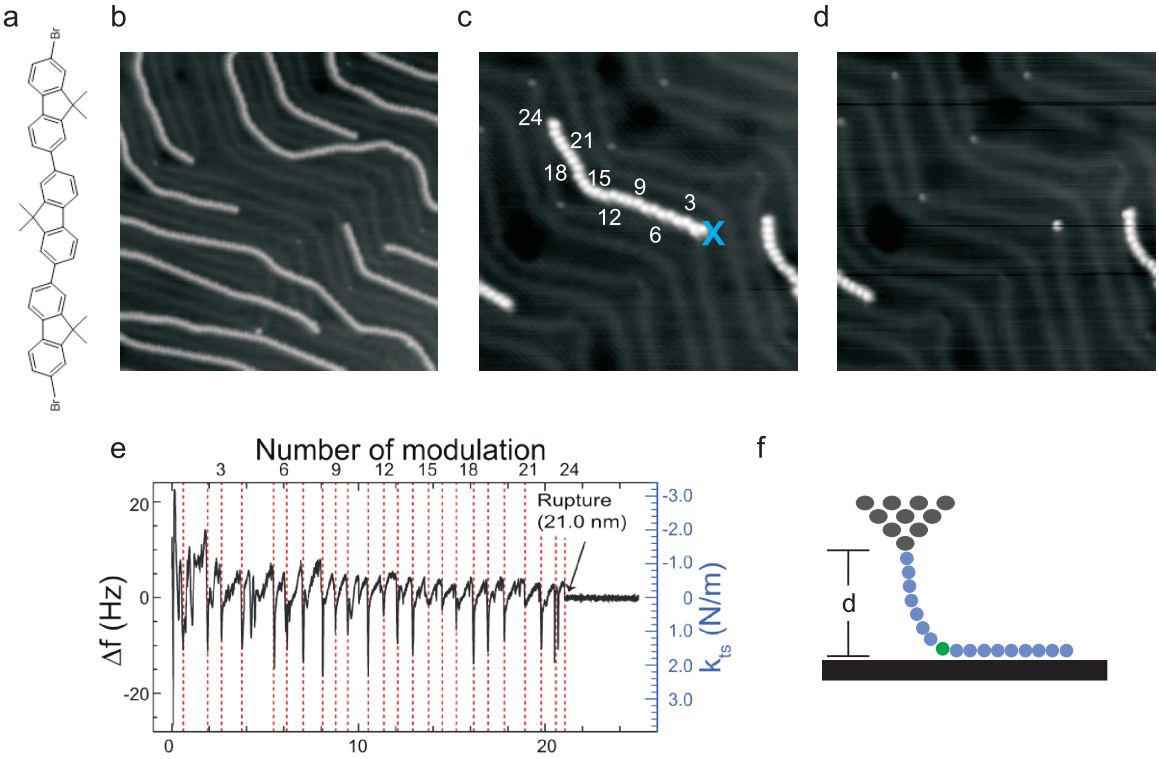

Figure 7.1: **a**, Chemical structure of DBTF. **b** 50x50 nm^2 STM image on Au(111) of DBTF after heating the sample to 490 K. **c**,**d**, 30x30 nm^2 STM images **c** before and **d** after pulling up a polyfluorene chain. The position of the tip approach is indicated by a blue cross. The numbers count the fluorene units in the chain. **e**, The corresponding frequency shift. **f**, Sketched pulling experiment of a polyfluorene chains. The fluorene unit which is lifted next is highlighted in green. Data obtained in collaboration with Shigeki Kawai.

The experiments were performed under ultra-high vacuum conditions with a commercial Omicron AFM/STM setup operating at 4.8 K. The DBTF molecules (Fig. 7.1a) were deposited onto the clean Au(111) sample. Immediately after the deposition the sample was heated to 490 K in order to activate and polymerize the molecules. The sample was then transferred into the STM/AFM. For imaging and characterizing the molecular chains the STM mode was used. Only for the pulling experiments the frequency shift is recorded. Fig. 7.1b shows an STM image of the polyfluorene chains which align along the herringbone reconstruction. This corresponds to previously reported experiments on the same molecule [16].

To measure the force signal the AFM tip is approached to the terminus of a polyfluorene chain so that a junction is formed between tip and molecule. A jump in the tunneling current is used as an indication for a successfully established connection between tip and molecule (see chapter 6.2.1). If a bond between tip and molecule is formed the tip position is kept fixed and the bias voltage is reduced to zero to eliminate disturbances of the AFM signal by the current signal. Then the tip is retracted from the surface and the frequency shift is recorded. An oscillation amplitude of 30 pm is used.

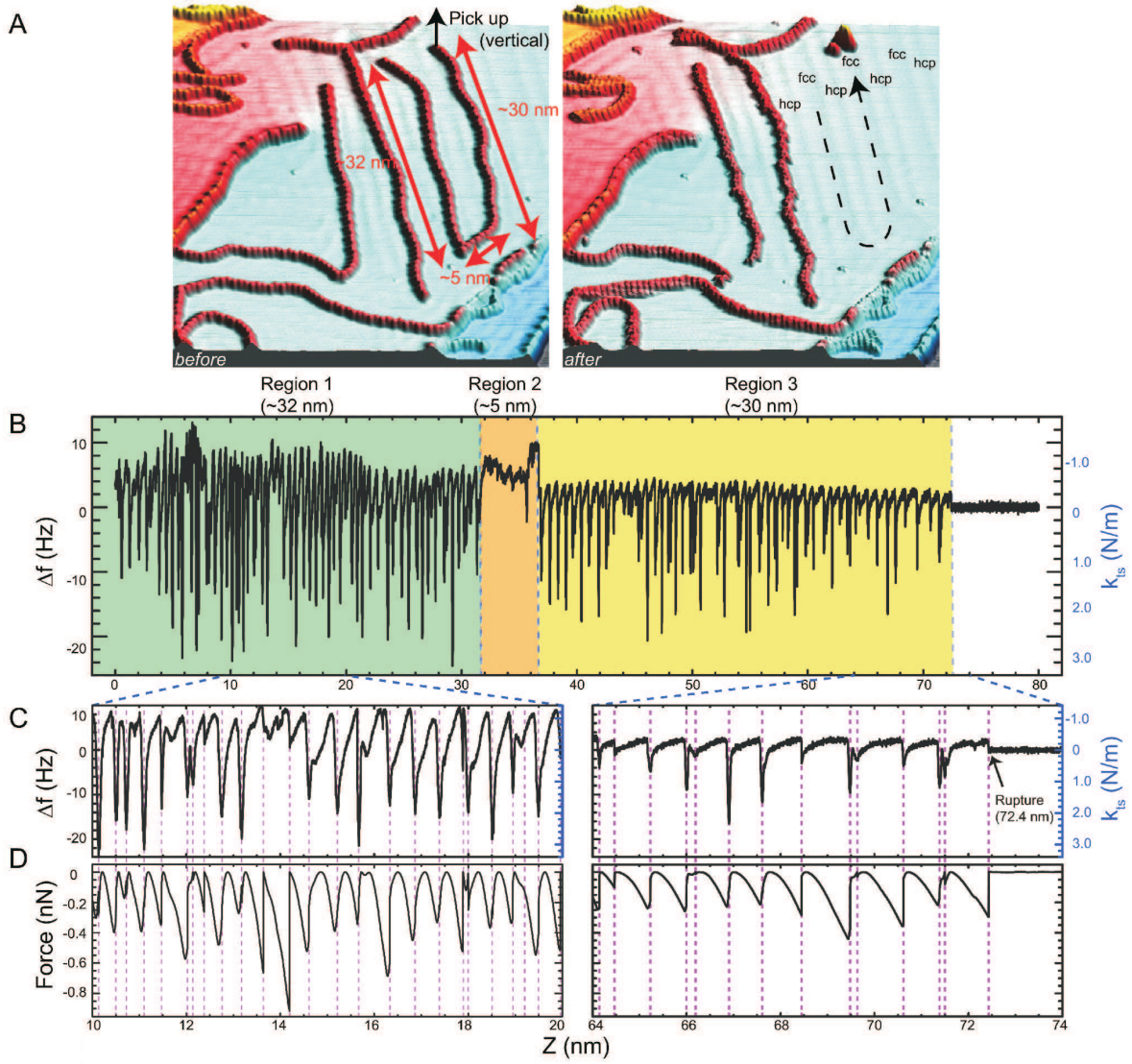

Figure 7.2: **a**, 50x50 nm^2 STM image on Au(111) of a polyfluorene chain before and after the pulling experiment. **b**, Measured frequency shift during the pulling experiment. **c**,**d** Magnified view of **c** the frequency shift and **d** the corresponding normal force. Data obtained in collaboration with Shigeki Kawai.

Fig. 7.1c shows a polyfluorene molecule which consists of 24 fluorene units. The blue cross indicates the position where the tip was approached. In the following the tip was retracted 25 nm from the surface while the frequency shift was recorded. Fig. 7.1e shows the corresponding frequency shift Δf obtained during the pulling experiment. The molecule has a length of about 20 nm as measured from the STM image, which coincides with the tip height of the last feature observed in the frequency spectrum. This points to a vertical geometry of the wire connected to the tip. Afterwards the chain disappeared from the surface and was not found in the STM image of the same area (Fig. 7.1c). This provides evidence that the molecular chain was completely removed from the surface. The recorded Δf signal (Fig. 7.1e) has a periodic pattern and each period is terminated by a large dip. In total 24 dips are detected in the frequency shift which is in agreement with the

number of fluorene units of the chain (Fig. 7.1c). Therefore, the periodic variation can be correlated to the number of fluorene units in the chain. This leads to the assumption that the wire is lifted unit by unit from the surface, and each unit gives rise to the same signal. Reported length-dependent conductance measurements on polyfluorene wires come to the same result [16]. In contrast to the conductance measurements, the frequency signal does not decay exponentially as a function of the tip height, and the magnitude of the Δf signal is independent of the tip height. This points to a low influence of the freestanding part but also of the adsorbed part of the chain on the frequency shift. If the adsorbed part of the chain dominates the Δf signal its strength would decrease as a function of the tip height due to the decreasing number of contributing fluorene units. For the freestanding part it is vice versa: The length increases with respect to the tip height and a stronger signal is expected. However, this is not the case as the magnitude of the frequency shift stays the same which provides evidence that the main contribution of the Δf signal results from the fluorene unit to be lifted up next. The pulling experiment is sketched in Fig. 7.1f. The highlighted fluorene unit is lifted next.

This becomes even more obvious for a polyfluorene wire consisting of 87 units (Fig. 7.2a). In a pulling curve the average distance between two dips is 0.91 nm, which is in agreement with the calculated length of a fluorene (0.83 nm) in gas phase as well as with previous reports [16]. The frequency shift is proportional to the effective stiffness of the tip-sample interaction [163]. However, the abrupt jumps to negative frequencies in the Δf signal make it impossible to correctly carry out force extraction. Therefore, the integration area is reduced to the period of each event, and the integration starts with zero attractive force and zero interaction energy for each period. The calculated force curves are shown in Fig. 7.2D. The maximum attractive force of a period is, on average, -0.5 nN and -0.3 nN, depending on the region of the spectrum. The magnitude of the observed force coincides with the required force to remove a 3,4,9,10-perylene-tetracarboxylicacid-dianhydride molecule from the surface [149]. Based on the maximum strength of the features the frequency shift spectrum can be divided into three regions as indicated by the color code (Fig. 7.2b). The z range of the three different regions matches the arrangement of the molecule on the surface (Fig. 7.2a). However, this behavior was observed only once and could not be reproduced.

7.3 Summary

The polymerization of dibromoterfluorene (DBTF) to polyfluorene on Au(111) was reproduced [16]. Similar to the previously reported conductance experiments [16] the frequency shift Δf of a single polyfluorene chain was recorded while the molecule was pulled from the surface (see chapter 6.2). In contrast to the conductance experiments [16], the frequency shift does not decay exponentially as a function of the tip height and allows measurements of very long polymers. In the Δf-signal an oscillating structure with a period of $\sim$0.91 nm was observed. The lifted and the adsorbed part of the polyfluorene chain do not contribute to the recorded frequency shift signal. The main contribution in the frequency shift results from the fluorene to be lifted up next as the magnitude and the shape of the frequency shift stay the same with respect to the tip height. The average maximum attractive force of one period equals -0.5 nN. Hence, a force of 0.5 nN has to be overcome to remove a fluorene unit from the surface.

Chapter 8

Summary and Outlook

In the present work the growth and characterization of molecular wires are investigated. Molecular wires are an essential component to connect different functional molecules in future molecular electronics. In this thesis the growth of graphene nanoribbons and porphyrin tapes is studied. For an industrial application a reliable fabrication of the wires must be guaranteed. Top-down techniques lack of the control over the edge-structure and the width of the molecular wire. In contrast, bottom-up techniques like on-surface polymerization automatically lead to a well-defined width and edge structure of the molecular wire. The studied molecular wires were fabricated using on-surface polymerization based on molecular building blocks equipped with halogen atoms of a lower bonding energy compared to the other bonds in the molecule. At an elevated sample temperature the halogen atoms dissociate, and a reactive site is created which enables other activated molecular building blocks to link covalently. By a careful choice of the molecular building block the structure of the resulting molecular network can be designed at a molecular scale. The different stages of the growth of molecular chains were characterized by low temperature scanning tunneling microscopy. For the polymerization process the surface is more than just a supporting template. Depending on the binding energy of the halogene-carbon bond and the catalytic activity of the surface the temperature for molecular activation differs. To steer the polymerization in a controlled manner the role of the surface on the synthesis has to be investigated. Therefore, the same molecules are deposited onto two different surfaces. The higher catalytic activity of the Cu(111) surface, in contrast to the Au(111) surface, reduces the dehalogenation temperature of 2,11-dibromohexabenzocoronene (diBr-HBC) to below room temperature. This might be important for the activation of molecules with a low dissociation or desorption temperature as no heating step is required. Apart from the activation temperature, also the resulting chains are different for Au(111) and Cu(111). On Cu(111) adatoms are available at room temperature, which mediate the linking of the HBC chains. Thus, on Cu(111) metal-ligand bonds are formed between the HBCs, whereas on Au(111) the chains are covalently linked. If the molecular building blocks polymerize to chemically different structures the surface might be utilized to favor one structure over the other. This has been studied by depositing 2,3-dibromoanthracene on Au(111) and Au(100). Two species emerge on Au(111): a narrow dimer and a larger trimer. The spacing of the atomic rows of the Au(100) reconstruction is smaller than the size of the trimer, which is, thereby, suppressed and only the narrow dimers are fabricated. Both discussed examples show the role of the surface on the polymerization process. Therefore, designing

the molecular building block is the first step in a polymerization experiment, while the second step is the choice of the surface with which the desired growth of the molecules can be obtained.

The steric repulsion between the molecular building blocks signifies a major challenge for on-surface polymerization. In particular, if a preceding dehydrogenation is necessary for the planarization of the oligomers. 10,10'-dibromo-9,9'-bianthryl (DBDA), an anthracene-based molecule, polymerizes to anthracene oligomers after heating the Au(111) substrate to 470 K. A second annealing step at 670 K is required for the cyclodehydrogenation. The fabrication of GNRs with DBDAs as molecular building blocks was successfully reproduced from recent studies in the literature. In this case the active sites of the molecular building blocks are surrounded by hydrogen atoms at either side. These hydrogens might lead to a repulsive Coulomb interaction between the molecules and, thereby, hinder the polymerization. This effect is probably observed for the porphyrin-based molecules. Before the dehydrogenation sets in, no polymerization takes place on Au(111), although the molecules are activated. A side effect of the dehydrogenation are further activated sites which facilitate the linking of the precursor molecules in an uncontrolled manner leading to a variety of different structures. In this thesis three approaches are conducted to reduce the repulsion between the molecular building blocks: depositing dimers, equipping the building blocks with tert-butyl groups and synthesizing a not fully planarized version of the molecule. The concept of all three approaches is to increase the flexibility of the molecules, which may result in a lower steric hindrance. The not completely planarized 1,4-Bis(4-bromophenyl)-2,3,6,11-tetraphenyltriphenylene (TPP) molecules successfully polymerize and then decompose into a zipper-structure during the heating step for the dehydrogenation. The tert-butyl groups do not reduce the steric repulsion for the studied molecules as no polymerization is observed, but they might lower the adsorption energy of the molecules. The trapezoid-shaped molecule and the porphyrin-based molecule, both equipped with tert-butyl groups, desorb during the second heating step. The first approach is based on the deposition of dimers in comparison to monomers. 9,10-dibromoanthracene (DBA) and 10,10'-dibromo-9,9'-bianthryl (DBDA) differ only in the number of anthracenes within the precursor molecule and are both expected to polymerize to anthracene oligomers. In contrast to DBDA, DBA does not polymerize on Au(111). DBDA is equipped with an additional anthracene unit which enables a tilted adsorption geometry. The rotation between the two anthracenes in the precursor molecule is, therefore, essential for the reduction of the steric hindrance between the molecules. This is also supported by the results of DBDA deposited on Au(100). The higher adsorption energy of Au(100) compared to Au(111) causes a more planar adsorption geometry of the two anthracenes in the dimer. This leads to a smaller angle between the anthracene units and to an increase of the steric repulsion, whereby the efficiency of the polymerization drops. The dimer and the unplanarized version of a molecule could increase the polymerization efficiency. However, for larger molecules, e.g., porphyrin dimers, no polymerization was observed as a rather planar adsorption geometry might be caused by a stronger molecule-substrate interaction.

The discussion of the conductance experiments requires a detailed insight of the electronic structure of the graphene nanoribbons fabricated by DBDA. The transport mechanism might depend on the molecular orbitals and, therefore, differ, depending on the electron energy. The HOMO and LUMO are found at -0.9 and 1.7 eV with respect to the Fermi level, respectively. This corresponds to a HOMO-LUMO gap of 2.8 eV, which is in very good agreement with values obtained by other methods. The HOMO as well as the LUMO

are delocalized along the armchair edges of the ribbon. The theoretically predicted Tamm state at 0.03 eV is localized at the short zigzag edges of the termini and vanishes if the chemical structure of the zigzag edges is slightly changed. The vertical pulling technique by STM was used to measure the length-dependent conductance of single ribbons. The tip is approached towards the terminus so that a strong bond between tip and molecule is formed. By lifting the ribbon from the surface the length of the freestanding part of the molecule and, thereby, the effective transport path of the electrons increases. Conductance curves for different bias voltages were recorded to study the influence of the molecular orbitals. The current in the length-dependent conductance spectra for bias voltages in the range of -2.4 V to +1.8 V decays smoothly and featureless. This points to a continuous bending of the ribbon because the stepwise lifting of a molecular chain would lead to periodic oscillations in the current as reported in the literature. Independent from the electron energy the exponential decay of the current provides an indication that direct tunneling is the charge transport mechanism. The inverse decay length β for electron energies in the HOMO-LUMO gap amounts to $\sim$0.45 Å^{-1} and drops to $\sim$0.1 Å^{-1} with the onset of the molecular orbitals. Contrary to expectations, pseudo-ballistic transport ($\beta = 0$) is not observed for electron energies which coincide with a molecular level. According to calculations (C. Joachim and F. Ample - Institute of Materials Research and Engineering, Singapore), the bending of the ribbon disturbs the electronic delocalization necessary for pseudo-ballistic transport. This is in agreement with the experiments: For large tip heights of the size of the ribbon the inverse decay length becomes zero. The ribbon geometry should become planar if the molecule is completely pulled off the surface. The Tamm states, which are close to the Fermi level, are localized at the zigzag edges and do not overlap for graphene nanoribbons longer than $\sim$3 nm. Therefore, the Tamm states do not participate in the electron transport.

By reducing the temperature of the second heating step the efficiency of the cyclodehydrogenation is lowered, which leads to partially dehydrogenated phenyl rings. These phenyl rings are rotated with respect to the ribbon and are used in this work for the fabrication of defected ribbons in a controlled manner. The influence of these defects on the charge transport was studied with conductance experiments. As long as the defected part of the ribbon is not lifted from the surface the slope of the current is similar to that of a defect-free ribbon. The decay of the current stays the same if a low or a high negative bias voltage is applied to the sample. For positive high bias voltages the current increases by one order of magnitude with lifting the defected part from the surface, which is possibly caused by a rearrangement of the ribbon edges due to Joule heating. To measure the vibrations of a molecular wire by inelastic tunneling spectroscopy the ribbon was pulled from the surface by the tip. At a fixed tip height the bias voltage was swept from -400 to +400 mV, and the second derivative of the current was recorded which contains features that correspond to the excitation of molecular vibrations of the same energy. Features are found at -97 mV, -162 mV, -202 mV, -262 mV and -327 mV in the spectrum, which could be assigned to the C-H bending mode, D mode, G mode, a C≡C vibration and the 2D mode, respectively, as compared to the literature. This is the first vibrational measurement of a single graphene nanoribbon in pulling conformation.

The last part of this thesis is based on a collaboration with the group of E. Meyer (University of Basel) with the aim to measure the force necessary to lift a single molecular wire from the surface: Polyfluorene chains were fabricated on Au(111) and pulled from the surface using an AFM. The thus caused frequency shift exhibits a characteristic periodicity

that is in agreement with the observed oscillation in the tunneling current and reflects the chemical structure of the poylmer. In contrast to conductance experiments, the frequency shift signal does not decay as a function of the tip height. Even for tip heights as large as 72 nm, with a single polyfluorene chain connected to the tip, the magnitude of the signal stays constant. The main contribution in the frequency shift is found to result from the fluorene unit lifted up next while a maximum attractive force between the molecule and the surface of -0.5 nN is observed.

Summing up, three different subjects were investigated in this present thesis: (1) the growth of molecular wires, the conductance, (2) the electronic and vibrational structure of graphene nanoribbons and (3) the force spectroscopy on polyfluorene chains. The vertical pulling technique is a versatile tool for the characterization of a single molecule. The bent geometry of the molecule becomes planar for large tip heights, this could be used to study the energy shift depending on the molecular geometry of the electronic excitation. In such a geometry, the different contact between tip-molecule and surface-molecule needs to be considered potentially causing assymmetry in the electronic spectrum. The growth experiments find steric repulsion between the molecular building block as a major challenge for the fabrication of molecular wires, in particular, if cyclodehydrogenation is required. The opposite hydrogens of two molecular building blocks might cause repulsion and, thereby, hinder the polymerization. Using dimers as precursor molecules enables its two units to tilt with respect to each other, which seems to reduce the steric repulsion to other dimers. The choice of the substrate is found to be crucial for the fabrication of molecular wires. The optimal substrate which leads to the desired growth is unlikely the same as the ideal substrate for the application of the molecular wire. For example, the stepwise growth of a tdBA dimer equipped with one bromine and one iodine, where each has a different activation temperature, could prevent the molecules from polymerizing into dimers on Au(100) and, thereby, lead to the successful fabrication of GNRs. Due to leakage current of the conducting Au(100) surface it might not be suitable for electronic applications, and a transfer of the molecular wires to another surface would be necessary. A printing mechanism for the transfer of molecular wires from one surface to the other would be of interest.

Bibliography

[1] G. Moore *Electron Devices Meeting, 1975 International*, p. 11, 1975.

[2] F. Schwierz, "Graphene transistors," *Nat. Nanotechnol.*, vol. 5, no. 7, p. 487, 2010.

[3] A. Aviram and M. A. Ratner, "Molecular rectifiers," *Chem. Phys. Lett.*, vol. 29, no. 2, p. 277, 1974.

[4] R. M. Metzger, B. Chen, U. Höpfner, M. V. Lakshmikantham, D. Vuillaume, T. Kawai, X. Wu, H. Tachibana, T. V. Hughes, H. Sakurai, J. W. Baldwin, C. Hosch, M. P. Cava, L. Brehmer, and G. J. Ashwell, "Unimolecular electrical rectification in hexadecylquinolinium tricyanoquinodimethanide," *J. Am. Chem. Soc.*, vol. 119, no. 43, p. 10455, 1997.

[5] R. Martel, T. Schmidt, H. R. Shea, T. Hertel, and P. Avouris, "Single- and multi-wall carbon nanotube field-effect transistors," *Appl. Phys. Lett.*, vol. 73, no. 17, p. 2447, 1998.

[6] Z. J. Donhauser, B. A. Mantooth, K. F. Kelly, L. A. Bumm, J. D. Monnell, J. J. Stapleton, D. W. Price, A. M. Rawlett, D. L. Allara, J. M. Tour, and P. S. Weiss, "Conductance switching in single molecules through conformational changes," *Science*, vol. 292, no. 5525, p. 2303, 2001.

[7] T. Rueckes, K. Kim, E. Joselevich, G. Y. Tseng, C.-L. Cheung, and C. M. Lieber, "Carbon nanotube-based nonvolatile random access memory for molecular computing," *Science*, vol. 289, no. 5476, p. 94, 2000.

[8] T. Hugel, N. B. Holland, A. Cattani, L. Moroder, M. Seitz, and H. E. Gaub, "Single-molecule optomechanical cycle," *Science*, vol. 296, no. 5570, p. 1103, 2002.

[9] M. J. Comstock, N. Levy, A. Kirakosian, J. Cho, F. Lauterwasser, J. H. Harvey, D. A. Strubbe, J. M. J. Fréchet, D. Trauner, S. G. Louie, and M. F. Crommie, "Reversible photomechanical switching of individual engineered molecules at a metallic surface," *Phys. Rev. Lett.*, vol. 99, p. 038301, 2007.

[10] S. Dutta and S. K. Pati, "Novel properties of graphene nanoribbons: a review," *J. Mater. Chem.*, vol. 20, p. 8207, 2010.

[11] M. Y. Han, B. Özyilmaz, Y. Zhang, and P. Kim, "Energy band-gap engineering of graphene nanoribbons," *Phys. Rev. Lett.*, vol. 98, p. 206805, 2007.

[12] K. Nakada, M. Fujita, G. Dresselhaus, and M. S. Dresselhaus, "Edge state in graphene ribbons: Nanometer size effect and edge shape dependence," *Phys. Rev. B*, vol. 54, p. 17954, 1996.

[13] X. Wang and H. Dai, "Etching and narrowing of graphene from the edges," *Nat. Chem.*, vol. 2, no. 8, p. 661, 2010.

[14] L. Grill, M. Dyer, L. Lafferentz, M. Persson, M. V. Peters, and S. Hecht, "Nano-architectures by covalent assembly of molecular building blocks," *Nat. Nanotechnol.*, vol. 2, no. 11, p. 687, 2007.

[15] M. Bieri, M.-T. Nguyen, O. Gröning, J. Cai, M. Treier, K. Ait-Mansour, P. Ruffieux, C. A. Pignedoli, D. Passerone, M. Kastler, K. Müllen, and R. Fasel, "Two-dimensional polymer formation on surfaces: Insight into the roles of precursor mobility and reactivity," *J. Am. Chem. Soc.*, vol. 132, no. 46, p. 16669, 2010.

[16] L. Lafferentz, F. Ample, H. Yu, S. Hecht, C. Joachim, and L. Grill, "Conductance of a single conjugated polymer as a continuous function of its length," *Science*, vol. 323, no. 5918, p. 1193, 2009.

[17] A. Tsuda and A. Osuka, "Fully conjugated porphyrin tapes with electronic absorption bands that reach into infrared," *Science*, vol. 293, no. 5527, p. 79, 2001.

[18] C. Boulas, J. V. Davidovits, F. Rondelez, and D. Vuillaume, "Suppression of charge carrier tunneling through organic self-assembled monolayers," *Phys. Rev. Lett.*, vol. 76, p. 4797, 1996.

[19] D. F. Perepichka and M. R. Bryce, "Molecules with exceptionally small HOMO–LUMO gaps," *Angew. Chem., Int. Ed.*, vol. 44, no. 34, p. 5370, 2005.

[20] S. Bengió, V. Navarro, M. A. González-Barrio, R. Cortés, I. Vobornik, E. G. Michel, and A. Mascaraque, "Electronic structure of reconstructed Au(100): Two-dimensional and one-dimensional surface states," *Phys. Rev. B*, vol. 86, p. 045426, 2012.

[21] W. Chen, V. Madhavan, T. Jamneala, and M. F. Crommie, "Scanning tunneling microscopy observation of an electronic superlattice at the surface of clean gold," *Phys. Rev. Lett.*, vol. 80, p. 1469, 1998.

[22] H. Lüth, *Solid surfaces, interfaces and thin films*, vol. 8431. Springer, 2010.

[23] X. F. Zhang, "A 200-kv STEM/SEM produces 1 Å SEM resolution," *Microsc. Today*, vol. 19, p. 26, 2011.

[24] G. Binnig, H. Rohrer, C. Gerber, and E. Weibel, "Surface studies by scanning tunneling microscopy," *Phys. Rev. Lett.*, vol. 49, no. 1, p. 57, 1982.

[25] G. Binnig, H. Rohrer, C. Gerber, and E. Weibel, "7 x 7 reconstruction on Si(111) resolved in real space," *Phys. Rev. Lett.*, vol. 50, p. 120, 1983.

[26] R. S. Becker, J. A. Golovchenko, D. R. Hamann, and B. S. Swartzentruber, "Real-space observation of surface states on Si(111) 7x7 with the tunneling microscope," *Phys. Rev. Lett.*, vol. 55, p. 2032, 1985.

[27] J. Repp, G. Meyer, S. M. Stojković, A. Gourdon, and C. Joachim, "Molecules on insulating films: Scanning-tunneling microscopy imaging of individual molecular orbitals," *Phys. Rev. Lett.*, vol. 94, p. 026803, 2005.

[28] L. Gross, N. Moll, F. Mohn, A. Curioni, G. Meyer, F. Hanke, and M. Persson, "High-resolution molecular orbital imaging using a p-wave STM tip," *Phys. Rev. Lett.*, vol. 107, p. 086101, 2011.

[29] D. M. Eigler and E. K. Schweizer, "Positioning single atoms with a scanning tunnelling microscope," *Nature*, vol. 344, no. 6266, p. 524, 1990.

[30] M. F. Crommie, C. P. Lutz, D. M. Eigler, *et al.*, "Confinement of electrons to quantum corrals on a metal surface," *Science*, vol. 262, no. 5131, p. 218, 1993.

[31] G. Meyer, F. Moresco, S. W. Hla, J. Repp, K. F. Braun, S. Folsch, and K. H. Rieder, "Manipulation of atoms and molecules with the low-temperature scanning tunneling microscope," *Jpn. J. Appl. Phys.*, vol. 40, no. part 1, p. 4409, 2001.

[32] B. C. Stipe, M. A. Rezaei, and W. Ho, "Localization of inelastic tunneling and the determination of atomic-scale structure with chemical specificity," *Phys. Rev. Lett.*, vol. 82, p. 1724, 1999.

[33] S. W. Hla, L. Bartels, G. Meyer, and K. H. Rieder, "Inducing all steps of a chemical reaction with the scanning tunneling microscope tip: Towards single molecule engineering," *Phys. Rev. Lett.*, vol. 85, p. 2777, 2000.

[34] Y. Jiang, Q. Huan, L. Fabris, G. C. Bazan, and W. Ho, "Submolecular control, spectroscopy and imaging of bond-selective chemistry in single functionalized molecules," *Nature Chem.*, vol. 5, no. 1, p. 36, 2012.

[35] J. V. Barth, H. Brune, G. Ertl, and R. J. Behm, "Scanning tunneling microscopy observations on the reconstructed Au(111) surface: Atomic structure, long-range superstructure, rotational domains, and surface defects," *Phys. Rev. B*, vol. 42, p. 9307, 1990.

[36] G. Binnig, H. Rohrer, C. Gerber, and E. Weibel, "Tunneling through a controllable vacuum gap," *Appl. Phys. Lett.*, vol. 40, no. 2, p. 178, 1982.

[37] D. BONNELL, *Scanning probe microscopy and spectroscopy: theory, techniques, and applications*. Wiley-vch, 2001.

[38] J. Bardeen, "Tunnelling from a many-particle point of view," *Phys. Rev. Lett.*, vol. 6, p. 57, 1961.

[39] J. Tersoff and D. R. Hamann, "Theory and application for the scanning tunneling microscope," *Phys. Rev. Lett.*, vol. 50, p. 1998, 1983.

[40] C. J. Chen, "Tunneling matrix elements in three-dimensional space: The derivative rule and the sum rule," *Phys. Rev. B*, vol. 42, p. 8841, 1990.

[41] A. D. Gottlieb and L. Wesoloski, "Bardeen's tunnelling theory as applied to scanning tunnelling microscopy: a technical guide to the traditional interpretation," *Nanotechnology*, vol. 17, no. 8, p. R57, 2006.

[42] C. J. Chen, *Introduction to scanning tunneling microscopy*, vol. 227. Oxford University Press New York, 1993.

[43] W. Ho, "Single-molecule chemistry," *J. Chem. Phys.*, vol. 117, no. 24, p. 11033, 2002.

[44] P. K. Hansma, *Tunneling spectroscopy: capabilities, applications, and new techniques*, vol. 9. Plenum Press New York, 1982.

[45] L. Bartels, G. Meyer, and K. H. Rieder, "Basic steps of lateral manipulation of single atoms and diatomic clusters with a scanning tunneling microscope tip," *Phys. Rev. Lett.*, vol. 79, p. 697, 1997.

[46] X. Wang, Q. Li, J. Xie, Z. Jin, J. Wang, Y. Li, K. Jiang, and S. Fan, "Fabrication of ultralong and electrically uniform single-walled carbon nanotubes on clean substrates," *Nano Lett.*, vol. 9, no. 9, p. 3137, 2009.

[47] J. C. Cuevas and E. Scheer, *Molecular electronics: an introduction to theory and experiment*, vol. 1. World Scientific Publishing Company, 2010.

[48] W. Wang, T. Lee, and M. A. Reed, "Mechanism of electron conduction in self-assembled alkanethiol monolayer devices," *Phys. Rev. B*, vol. 68, p. 035416, 2003.

[49] J. G. Simmons, "Generalized formula for the electric tunnel effect between similar electrodes separated by a thin insulating film," *J. Appl. Phys.*, vol. 34, no. 6, p. 1793, 1963.

[50] J. He, F. Chen, J. Li, O. F. Sankey, Y. Terazono, C. Herrero, D. Gust, T. A. Moore, A. L. Moore, and S. M. Lindsay, "Electronic decay constant of carotenoid polyenes from single-molecule measurements," *J. Am. Chem. Soc.*, vol. 127, no. 5, p. 1384, 2005.

[51] X. Li, J. He, J. Hihath, B. Xu, S. M. Lindsay, and N. Tao, "Conductance of single alkanedithiols: Conduction mechanism and effect of molecule-electrode contacts," *J. Am. Chem. Soc.*, vol. 128, no. 6, p. 2135, 2006.

[52] A. Nitzan, "Electron transmission through molecules and molecular interfaces," *Annu. Rev. Phys. Chem.*, vol. 52, no. 1, p. 681, 2001.

[53] B. Q. Xu, X. L. Li, X. Y. Xiao, H. Sakaguchi, and N. J. Tao, "Electromechanical and conductance switching properties of single oligothiophene molecules," *Nano Lett.*, vol. 5, no. 7, p. 1491, 2005.

[54] T. Hines, I. Diez-Perez, J. Hihath, H. Liu, Z.-S. Wang, J. Zhao, G. Zhou, K. Müllen, and N. Tao, "Transition from tunneling to hopping in single molecular junctions by measuring length and temperature dependence," *J. Am. Chem. Soc.*, vol. 132, no. 33, p. 11658, 2010.

[55] S. Ho Choi, B. Kim, and C. D. Frisbie, "Electrical resistance of long conjugated molecular wires," *Science*, vol. 320, no. 5882, p. 1482, 2008.

[56] S. H. Choi, C. Risko, M. C. R. Delgado, B. Kim, J. L. Bredas, and C. D. Frisbie, "Transition from tunneling to hopping transport in long, conjugated oligo-imine wires connected to metals," *J. Am. Chem. Soc.*, vol. 132, no. 12, p. 4358, 2010.

[57] L. Venkataraman, J. E. Klare, C. Nuckolls, M. S. Hybertsen, and M. L. Steigerwald, "Dependence of single-molecule junction conductance on molecular conformation," *Nature*, vol. 442, no. 7105, p. 904, 2006.

[58] I. Diez-Perez, J. Hihath, T. Hines, Z. S. Wang, G. Zhou, K. Müllen, and N. Tao, "Controlling single-molecule conductance through lateral coupling of [pi] orbitals," *Nat. Nanotechnol.*, vol. 6, no. 4, p. 226, 2011.

[59] S. Datta, *Quantum transport: atom to transistor*. Cambridge University Press, 2005.

[60] R. Landauer, "Spatial variation of currents and fields due to localized scatterers in metallic conduction," *IBM J. Res. Dev.*, vol. 1, no. 3, p. 223, 1957.

[61] J. I. Pascual, J. Méndez, J. Gómez-Herrero, A. M. Baró, N. García, and V. T. Binh, "Quantum contact in gold nanostructures by scanning tunneling microscopy," *Phys. Rev. Lett.*, vol. 71, p. 1852, 1993.

[62] J. Krans, J. Van Ruitenbeek, V. Fisun, I. Yanson, and L. De Jongh, "The signature of conductance quantization in metallic point contacts," *Nature*, vol. 375, no. 6534, p. 767, 1995.

[63] E. Scheer, N. Agraït, J. C. Cuevas, A. L. Yeyati, B. Ludoph, A. Martín-Rodero, G. R. Bollinger, J. M. van Ruitenbeek, and C. Urbina, "The signature of chemical valence in the electrical conduction through a single-atom contact," *Nature*, vol. 394, no. 6689, p. 154, 1998.

[64] G. Cuniberti, G. Fagas, and K. Richter, *Introducing molecular electronics: A brief overview*. Springer, 2005.

[65] L. A. Bumm, J. J. Arnold, M. T. Cygan, T. D. Dunbar, T. P. Burgin, L. Jones, D. L. Allara, J. M. Tour, and P. S. Weiss, "Are single molecular wires conducting?," *Science*, vol. 271, no. 5256, p. 1705, 1996.

[66] C. Joachim, J. K. Gimzewski, R. R. Schlittler, and C. Chavy, "Electronic transparence of a single c_{60} molecule," *Phys. Rev. Lett.*, vol. 74, p. 2102, 1995.

[67] M. A. Reed, C. Zhou, C. J. Muller, T. P. Burgin, and J. M. Tour, "Conductance of a molecular junction," *Science*, vol. 278, no. 5336, p. 252, 1997.

[68] Y. S. Park, A. C. Whalley, M. Kamenetska, M. L. Steigerwald, M. S. Hybertsen, C. Nuckolls, and L. Venkataraman, "Contact chemistry and single-molecule conductance: A comparison of phosphines, methyl sulfides, and amines," *J. Am. Chem. Soc.*, vol. 129, no. 51, p. 15768, 2007.

[69] B. Xu and N. J. Tao, "Measurement of single-molecule resistance by repeated formation of molecular junctions," *Science*, vol. 301, no. 5637, p. 1221, 2003.

[70] A. Landau, L. Kronik, and A. Nitzan, "Cooperative effects in molecular conduction," *J. Comput. Theor. Nanosci.*, vol. 5, no. 4, p. 535, 2008.

[71] P. Varotsos, N. Sarlis, and M. Lazaridou, "Interconnection of defect parameters and stress-induced electric signals in ionic crystals," *Phys. Rev. B*, vol. 59, p. 24, 1999.

[72] H. Vazquez, R. Skouta, S. Schneebeli, M. Kamenetska, R. Breslow, L. Venkataraman, and M. S. Hybertsen, "Probing the conductance superposition law in single-molecule circuits with parallel paths," *Nat. Nanotechnol.*, vol. 7, no. 10, p. 663, 2012.

[73] R. Temirov, A. Lassise, F. B. Anders, and F. S. Tautz, "Kondo effect by controlled cleavage of a single-molecule contact," *Nanotechnology*, vol. 19, no. 6, p. 065401, 2008.

[74] K. S. Novoselov, A. K. Geim, S. V. Morozov, D. Jiang, Y. Zhang, S. V. Dubonos, I. V. Grigorieva, and A. A. Firsov, "Electric field effect in atomically thin carbon films," *Science*, vol. 306, no. 5696, p. 666, 2004.

[75] D. Wei and Y. Liu, "Controllable synthesis of graphene and its applications," *Adv. Mater.*, vol. 22, no. 30, p. 3225, 2010.

[76] A. K. Geim, "Graphene: status and prospects," *Science*, vol. 324, no. 5934, p. 1530, 2009.

[77] A. K. Geim and K. S. Novoselov, "The rise of graphene," *Nat. Mater.*, vol. 6, no. 3, p. 183, 2007.

[78] K. S. Novoselov, D. Jiang, F. Schedin, T. J. Booth, V. V. Khotkevich, S. V. Morozov, and A. K. Geim, "Two-dimensional atomic crystals," *Proc. Natl. Acad. Sci. U. S. A.*, vol. 102, no. 30, p. 10451, 2005.

[79] J. Coraux, A. T. N'Diaye, C. Busse, and T. Michely, "Structural coherency of graphene on Ir(111)," *Nano Lett.*, vol. 8, no. 2, p. 565, 2008.

[80] S. Marchini, S. Günther, and J. Wintterlin, "Scanning tunneling microscopy of graphene on ru(0001)," *Phys. Rev. B*, vol. 76, p. 075429, 2007.

[81] A. L. Vázquez de Parga, F. Calleja, B. Borca, M. C. G. Passeggi, J. J. Hinarejos, F. Guinea, and R. Miranda, "Periodically rippled graphene: Growth and spatially resolved electronic structure," *Phys. Rev. Lett.*, vol. 100, p. 056807, 2008.

[82] Y. Gamo, A. Nagashima, M. Wakabayashi, M. Terai, and C. Oshima, "Atomic structure of monolayer graphite formed on Ni(111)," *Surf. Sci.*, vol. 374, no. 1-3, p. 61, 1997.

[83] K. S. Kim, Y. Zhao, H. Jang, S. Y. Lee, J. M. Kim, K. S. Kim, J. H. Ahn, P. Kim, J. Y. Choi, and B. H. Hong, "Large-scale pattern growth of graphene films for stretchable transparent electrodes," *Nature*, vol. 457, no. 7230, p. 706, 2009.

[84] S. Bae, H. Kim, Y. Lee, X. Xu, J. S. Park, Y. Zheng, J. Balakrishnan, T. Lei, H. R. Kim, Y. I. Song, *et al.*, "Roll-to-roll production of 30-inch graphene films for transparent electrodes," *Nat. Nanotechnol.*, vol. 5, no. 8, p. 574, 2010.

[85] A. Jorio, "Raman spectroscopy in graphene-based systems: Prototypes for nanoscience and nanometrology," *ISRN Nanotechnology*, vol. 2012, 2012.

[86] A. C. Ferrari, J. C. Meyer, V. Scardaci, C. Casiraghi, M. Lazzeri, F. Mauri, S. Piscanec, D. Jiang, K. S. Novoselov, S. Roth, and A. K. Geim, "Raman spectrum of graphene and graphene layers," *Phys. Rev. Lett.*, vol. 97, p. 187401, 2006.

[87] A. F. Young and P. Kim, "Quantum interference and klein tunnelling in graphene heterojunctions," *Nat. Phys.*, vol. 5, no. 3, p. 222, 2009.

[88] K. Novoselov, A. K. Geim, S. Morozov, D. Jiang, M. K. I. Grigorieva, S. Dubonos, and A. Firsov, "Two-dimensional gas of massless dirac fermions in graphene," *Nature*, vol. 438, no. 7065, p. 197, 2005.

[89] K. S. Novoselov, Z. Jiang, Y. Zhang, S. V. Morozov, H. L. Stormer, U. Zeitler, J. C. Maan, G. S. Boebinger, P. Kim, and A. K. Geim, "Room-temperature quantum hall effect in graphene," *Science*, vol. 315, no. 5817, p. 1379, 2007.

[90] K. Novoselov, V. Fal, L. Colombo, P. Gellert, M. Schwab, K. Kim, *et al.*, "A roadmap for graphene," *Nature*, vol. 490, no. 7419, p. 192, 2012.

[91] K. Tielrooij, J. Song, S. Jensen, A. Centeno, A. Pesquera, A. Z. Elorza, M. Bonn, L. Levitov, and F. Koppens, "Photoexcitation cascade and multiple hot-carrier generation in graphene," *Nat. Phys.*, 2013.

[92] F. Schedin, A. Geim, S. Morozov, E. Hill, P. Blake, M. Katsnelson, and K. Novoselov, "Detection of individual gas molecules adsorbed on graphene," *Nat. Mater.*, vol. 6, no. 9, p. 652, 2007.

[93] Y. M. Lin, C. Dimitrakopoulos, K. A. Jenkins, D. B. Farmer, H. Y. Chiu, A. Grill, and P. Avouris, "100-GHz transistors from wafer-scale epitaxial graphene," *Science*, vol. 327, no. 5966, p. 662, 2010.

[94] L. Liao, Y. C. Lin, M. Bao, R. Cheng, J. Bai, Y. Liu, Y. Qu, K. L. Wang, Y. Huang, and X. Duan, "High-speed graphene transistors with a self-aligned nanowire gate," *Nature*, vol. 467, no. 7313, p. 305, 2010.

[95] Y. Wu, Y. M. Lin, A. A. Bol, K. A. Jenkins, F. Xia, D. B. Farmer, Y. Zhu, and P. Avouris, "High-frequency, scaled graphene transistors on diamond-like carbon," *Nature*, vol. 472, no. 7341, p. 74, 2011.

[96] F. Schwierz, "Electronics: Industry-compatible graphene transistors," *Nature*, vol. 472, no. 7341, p. 41, 2011.

[97] C. Tao, L. Jiao, O. V. Yazyev, Y. C. Chen, J. Feng, X. Zhang, R. B. Capaz, J. M. Tour, A. Zettl, S. G. Louie, *et al.*, "Spatially resolving edge states of chiral graphene nanoribbons," *Nat. Phys.*, vol. 7, no. 8, p. 616, 2011.

[98] L. Yang, C. H. Park, Y. W. Son, M. L. Cohen, and S. G. Louie, "Quasiparticle energies and band gaps in graphene nanoribbons," *Phys. Rev. Lett.*, vol. 99, p. 186801, 2007.

[99] M. Baldoni, A. Sgamellotti, and F. Mercuri, "Electronic properties and stability of graphene nanoribbons: An interpretation based on clar sextet theory," *Chem. Phys. Lett.*, vol. 464, no. 4-6, p. 202, 2008.

[100] L. Tapasztó, G. Dobrik, P. Lambin, and L. P. Biro, "Tailoring the atomic structure of graphene nanoribbons by scanning tunnelling microscope lithography," *Nat. Nanotechnol.*, vol. 3, no. 7, p. 397, 2008.

[101] A. Fasoli, A. Colli, A. Lombardo, and A. Ferrari, "Fabrication of graphene nanoribbons via nanowire lithography," *Phys. Status Solidi B*, vol. 246, no. 11-12, p. 2514, 2009.

[102] L. Jiao, L. Zhang, X. Wang, G. Diankov, and H. Dai, "Narrow graphene nanoribbons from carbon nanotubes," *Nature*, vol. 458, no. 7240, p. 877, 2009.

[103] X. Jia, M. Hofmann, V. Meunier, B. G. Sumpter, J. Campos-Delgado, J. M. Romo-Herrera, H. Son, Y.-P. Hsieh, A. Reina, J. Kong, M. Terrones, and M. S. Dresselhaus, "Controlled formation of sharp zigzag and armchair edges in graphitic nanoribbons," *Science*, vol. 323, no. 5922, p. 1701, 2009.

[104] J. Cai, P. Ruffieux, R. Jaafar, M. Bieri, T. Braun, S. Blankenburg, M. Muoth, A. P. Seitsonen, M. Saleh, X. Feng, *et al.*, "Atomically precise bottom-up fabrication of graphene nanoribbons," *Nature*, vol. 466, no. 7305, p. 470, 2010.

[105] M. Moreno-Moreno, A. Castellanos-Gomez, G. Rubio-Bollinger, J. Gomez-Herrero, and N. Agraït, "Ultralong natural graphene nanoribbons and their electrical conductivity," *Small*, vol. 5, no. 8, p. 924, 2009.

[106] D. Cram, J. Hendrickson, and G. Hammond, *Organic Chemistry: 3d Ed.* Mcgraw-hill series in undergraduate chemistry, McGraw-Hill, 1970.

[107] S. Krasnikov, C. Doyle, N. Sergeeva, A. Preobrajenski, N. Vinogradov, Y. Sergeeva, A. Zakharov, M. Senge, and A. Cafolla, "Formation of extended covalently bonded ni porphyrin networks on the Au(111) surface," *Nano Research*, vol. 4, no. 4, p. 376, 2011.

[108] L. Lafferentz, V. Eberhardt, C. Dri, C. Africh, G. Comelli, F. Esch, S. Hecht, and L. Grill, "Controlling on-surface polymerization by hierarchical and substrate-directed growth," *Nature Chem.*, vol. 4, no. 3, p. 215, 2012.

[109] C. J. Villagómez, T. Sasaki, J. M. Tour, and L. Grill, "Bottom-up assembly of molecular wagons on a surface," *J. Am. Chem. Soc.*, vol. 132, no. 47, p. 16848, 2010.

[110] H. Huang, D. Wei, J. Sun, S. L. Wong, Y. P. Feng, A. C. Neto, and A. T. S. Wee, "Spatially resolved electronic structures of atomically precise armchair graphene nanoribbons," *Sci. Rep.*, vol. 2, 2012.

[111] K. Besocke, "An easily operable scanning tunneling microscope," *Surf. Sci.*, vol. 181, no. 1-2, p. 145, 1987.

[112] G. Meyer, "A simple low-temperature ultrahigh-vacuum scanning tunneling microscope capable of atomic manipulation," *Rev. Sci. Instrum.*, vol. 67, no. 8, p. 2960, 1996.

[113] S. Zöphel, "Der aufbau eines tieftemperatur-rastertunnelmikroskops und strukturuntersuchungen auf vicinalen kupferoberflächen," *Promotionsarbeit FU Berlin*, 2000.

[114] P. Stoltze, "Simulation of surface defects," *J. Phys.: Condens. Matter*, vol. 6, no. 45, p. 9495, 1994.

[115] N. Lin, S. Stepanow, M. Ruben, and J. Barth, "Surface-confined supramolecular coordination chemistry," in *Templates in Chemistry III* (P. Broekmann, K.-H. Dötz, and C. Schalley, eds.), vol. 287 of *Top. Curr. Chem.*, p. 1, Springer Berlin Heidelberg, 2009.

[116] B. Hammer and J. Norskov, "Why gold is the noblest of all the metals," *Nature*, vol. 376, no. 6537, p. 238, 1995.

[117] K. Kopitzki and P. Herzog, *Einführung in die Festkörperphysik*. Springer DE, 2007.

[118] P. Havu, V. Blum, V. Havu, P. Rinke, and M. Scheffler, "Large-scale surface reconstruction energetics of Pt(100) and Au(100) by all-electron density functional theory," *Phys. Rev. B*, vol. 82, p. 161418, 2010.

[119] C. Wöll, S. Chiang, R. J. Wilson, and P. H. Lippel, "Determination of atom positions at stacking-fault dislocations on Au(111) by scanning tunneling microscopy," *Phys. Rev. B*, vol. 39, p. 7988, 1989.

[120] F. Reinert and G. Nicolay, "Influence of the herringbone reconstruction on the surface electronic structure of au (111)," *Appl. Phys. A*, vol. 78, no. 6, p. 817, 2004.

[121] M. Crommie, C. Lutz, and D. Eigler, "Imaging standing waves in a two-dimensional electron gas," *Nature*, vol. 363, no. 6429, p. 524, 1993.

[122] Y. W. Son, M. L. Cohen, and S. G. Louie, "Half-metallic graphene nanoribbons," *Nature*, vol. 444, no. 7117, p. 347, 2006.

[123] R. Gutzler, H. Walch, G. Eder, S. Kloft, W. M. Heckl, and M. Lackinger, "Surface mediated synthesis of 2D covalent organic frameworks: 1,3,5-tris(4-bromophenyl)benzene on graphite(001), cu(111), and ag(110)," *Chem. Commun.*, vol. 0, p. 4456, 2009.

[124] G. Sedghi, V. M. García-Suárez, L. J. Esdaile, H. L. Anderson, C. J. Lambert, S. Martín, D. Bethell, S. J. Higgins, M. Elliott, N. Bennett, *et al.*, "Long-range electron tunnelling in oligo-porphyrin molecular wires," *Nat. Nanotechnol.*, vol. 6, no. 8, p. 517, 2011.

[125] S. Haq, F. Hanke, M. S. Dyer, M. Persson, P. Iavicoli, D. B. Amabilino, and R. Raval, "Clean coupling of unfunctionalized porphyrins at surfaces to give highly oriented organometallic oligomers," *J. Am. Chem. Soc.*, vol. 133, no. 31, p. 12031, 2011.

[126] W. H. Soe, H. S. Wong, C. Manzano, M. Grisolia, M. Hliwa, X. Feng, K. Müllen, and C. Joachim, "Mapping the excited states of single hexa-peri-benzocoronene oligomers," *ACS Nano*, vol. 6, no. 4, p. 3230, 2012.

[127] A. Kirakosian, M. J. Comstock, J. Cho, and M. F. Crommie, "Molecular commensurability with a surface reconstruction: Stm study of azobenzene on Au(111)," *Phys. Rev. B*, vol. 71, p. 113409, 2005.

[128] J. Mendez, M. F. Lopez, and J. A. Martin-Gago, "On-surface synthesis of cyclic organic molecules," *Chem. Soc. Rev.*, vol. 40, p. 4578, 2011.

[129] G. Rothenberg, *Catalysis*. Wiley Online Library, 2008.

[130] T. Zambelli, J. Wintterlin, J. Trost, and G. Ertl, "Identification of the "active sites" of a surface-catalyzed reaction," *Science*, vol. 273, no. 5282, p. 1688, 1996.

[131] L. Gross, F. Moresco, P. Ruffieux, A. Gourdon, C. Joachim, and K. H. Rieder, "Tailoring molecular self-organization by chemical synthesis: Hexaphenylbenzene, hexa-*peri*-hexabenzocoronene, and derivatives on Cu(111)," *Phys. Rev. B*, vol. 71, p. 165428, 2005.

[132] P. Ruffieux, O. Gröning, M. Bielmann, C. Simpson, K. Müllen, L. Schlapbach, and P. Gröning, "Supramolecular columns of hexabenzocoronenes on copper and gold (111) surfaces," *Phys. Rev. B*, vol. 66, p. 073409, 2002.

[133] C. Wagner, D. Kasemann, C. Golnik, R. Forker, M. Esslinger, K. Müllen, and T. Fritz, "Repulsion between molecules on a metal: Monolayers and submonolayers of hexa-*peri*-hexabenzocoronene on Au(111)," *Phys. Rev. B*, vol. 81, p. 035423, 2010.

[134] M. Kadodwala, A. Davis, G. Scragg, B. Cowie, M. Kerkar, D. Woodruff, and R. G. Jones, "Structural determination of the Cu(111)($\sqrt{3}\times\sqrt{3}$) r30°clbr surface using the normal incidence x-ray standing wave method," *Surf. Sci.*, vol. 324, no. 2-3, p. 122, 1995.

[135] W. Wang, X. Shi, S. Wang, M. A. Van Hove, and N. Lin, "Single-molecule resolution of an organometallic intermediate in a surface-supported ullmann coupling reaction," *J. Am. Chem. Soc.*, vol. 133, no. 34, p. 13264, 2011.

[136] C. Dean, A. Young, I. Meric, C. Lee, L. Wang, S. Sorgenfrei, K. Watanabe, T. Taniguchi, P. Kim, K. Shepard, *et al.*, "Boron nitride substrates for high-quality graphene electronics," *Nat. Nanotechnol.*, vol. 5, no. 10, p. 722, 2010.

[137] X. Wang, Y. Ouyang, L. Jiao, H. Wang, L. Xie, J. Wu, J. Guo, and H. Dai, "Graphene nanoribbons with smooth edges behave as quantum wires," *Nat. Nanotechnol.*, vol. 6, no. 9, p. 563, 2011.

[138] D. Käfer, A. Bashir, X. Dou, G. Witte, K. Müllen, and C. Wöll, "Evidence for band-like transport in graphene-based organic monolayers," *Adv. Mater.*, vol. 22, no. 3, p. 384, 2010.

[139] S. Blankenburg, J. Cai, P. Ruffieux, R. Jaafar, D. Passerone, X. Feng, K. Mu"ullen, R. Fasel, and C. A. Pignedoli, "Intraribbon heterojunction formation in ultranarrow graphene nanoribbons," *ACS Nano*, vol. 6, no. 3, p. 2020, 2012.

[140] C. Bronner, F. Leyssner, S. Stremlau, M. Utecht, P. Saalfrank, T. Klamroth, and P. Tegeder, "Electronic structure of a subnanometer wide bottom-up fabricated graphene nanoribbon: End states, band gap, and dispersion," *Phys. Rev. B*, vol. 86, p. 085444, 2012.

[141] C. Lee, X. Wei, J. W. Kysar, and J. Hone, "Measurement of the elastic properties and intrinsic strength of monolayer graphene," *Science*, vol. 321, no. 5887, p. 385, 2008.

[142] S. Linden, D. Zhong, A. Timmer, N. Aghdassi, J. H. Franke, H. Zhang, X. Feng, K. Müllen, H. Fuchs, L. Chi, and H. Zacharias, "Electronic structure of spatially aligned graphene nanoribbons on Au(788)," *Phys. Rev. Lett.*, vol. 108, p. 216801, 2012.

[143] P. Ruffieux, J. Cai, N. C. Plumb, L. Patthey, D. Prezzi, A. Ferretti, E. Molinari, X. Feng, K. Müllen, C. A. Pignedoli, and R. Fasel, "Electronic structure of atomically precise graphene nanoribbons," *ACS Nano*, vol. 6, no. 8, p. 6930, 2012.

[144] B.-K. Pong, J.-Y. Lee, and B. L. Trout, "First principles computational study for understanding the interactions between ssDNA and gold nanoparticles: Adsorption of methylamine on gold nanoparticulate surfaces," *Langmuir*, vol. 21, no. 25, p. 11599, 2005.

[145] L. Talirz, H. Söde, J. Cai, P. Ruffieux, S. Blankenburg, R. Jafaar, R. Berger, X. Feng, K. Müllen, D. Passerone, R. Fasel, and C. A. Pignedoli, "Termini of bottom-up fabricated graphene nanoribbons," *J. Am. Chem. Soc.*, vol. 135, no. 6, p. 2060, 2013.

[146] R. Wiesendanger, *Scanning probe microscopy and spectroscopy: methods and applications*. Cambridge University Press, 1994.

[147] R. Feenstra, J. A. Stroscio, and A. Fein, "Tunneling spectroscopy of the Si(111)2x1 surface," *Surf. Sci.*, vol. 181, no. 1-2, p. 295, 1987.

[148] M. Koch, F. Ample, C. Joachim, and L. Grill, "Voltage-dependent conductance of a single graphene nanoribbon," *Nat. Nanotechnol.*, vol. 7, no. 11, p. 713, 2012.

[149] N. Fournier, C. Wagner, C. Weiss, R. Temirov, and F. S. Tautz, "Force-controlled lifting of molecular wires," *Phys. Rev. B*, vol. 84, p. 035435, 2011.

[150] M. Mayor, H. B. Weber, J. Reichert, M. Elbing, C. von Hänisch, D. Beckmann, and M. Fischer, "Electric current through a molecular rod-relevance of the position of the anchor groups," *Angew. Chem., Int. Ed.*, vol. 42, no. 47, p. 5834, 2003.

[151] C. Joachim and M. Magoga, "The effective mass of an electron when tunneling through a molecular wire," *Chem. Phys.*, vol. 281, no. 2-3, p. 347, 2002.

[152] J. Tian, H. Cao, W. Wu, Q. Yu, and Y. P. Chen, "Direct imaging of graphene edges: Atomic structure and electronic scattering," *Nano Lett.*, vol. 11, no. 9, p. 3663, 2011.

[153] G. M. Rutter, N. P. Guisinger, J. N. Crain, P. N. First, and J. A. Stroscio, "Edge structure of epitaxial graphene islands," *Phys. Rev. B*, vol. 81, p. 245408, 2010.

[154] L. G. Cançado, M. A. Pimenta, B. R. A. Neves, M. S. S. Dantas, and A. Jorio, "Influence of the atomic structure on the raman spectra of graphite edges," *Phys. Rev. Lett.*, vol. 93, p. 247401, 2004.

[155] J. W. Niemantsverdriet, *Spectroscopy in catalysis*. Wiley-VCH, 2007.

[156] G. Zimmerman, L.-Y. Chow, and U.-J. Paik, "The photochemical isomerization of azobenzene," *J. Am. Chem. Soc.*, vol. 80, no. 14, p. 3528, 1958.

[157] A. Cembran, F. Bernardi, M. Garavelli, L. Gagliardi, and G. Orlandi, "On the mechanism of the cis-trans isomerization in the lowest electronic states of azobenzene: S0, S1, and T1," *J. Am. Chem. Soc.*, vol. 126, no. 10, p. 3234, 2004.

[158] H. Rau and E. Lueddecke, "On the rotation-inversion controversy on photoisomerization of azobenzenes. experimental proof of inversion," *J. Am. Chem. Soc.*, vol. 104, no. 6, p. 1616, 1982.

[159] M. Rief, M. Gautel, F. Oesterhelt, J. M. Fernandez, and H. E. Gaub, "Reversible unfolding of individual titin immunoglobulin domains by AFM," *Science*, vol. 276, no. 5315, p. 1109, 1997.

[160] M. Schlierf, H. Li, and J. M. Fernandez, "The unfolding kinetics of ubiquitin captured with single-molecule force-clamp techniques," *Proc. Natl. Acad. Sci. U. S. A.*, vol. 101, no. 19, p. 7299, 2004.

[161] F. Tautz, "Structure and bonding of large aromatic molecules on noble metal surfaces: The example of PTCDA," *Prog. Surf. Sci.*, vol. 82, no. 9-12, p. 479, 2007.

[162] E. Meyer, "Atomic force microscopy," *Prog. Surf. Sci.*, vol. 41, no. 1, p. 3, 1992.

[163] F. J. Giessibl, "Advances in atomic force microscopy," *Rev. Mod. Phys.*, vol. 75, p. 949, 2003.

[164] F. Giessibl, "Principles and applications of the qplus sensor," in *Noncontact Atomic Force Microscopy* (S. Morita, F. J. Giessibl, and R. Wiesendanger, eds.), NanoScience and Technology, p. 121, Springer Berlin Heidelberg, 2009.

[165] G. Haugstad, *Atomic Force Microscopy: Understanding Basic Modes and Advanced Applications*. Wiley, 2012.

List of publications

Publications within this thesis

M. Koch, F. Ample, C. Joachim and L. Grill, "Voltage-dependent conductance of a single graphene nanoribbon", Nat. Nanotechnol, vol. 7, no. 11, p. 713, 2012

M. Koch, F. Ample, C. Joachim and L. Grill, "Electronic Structure and Properties of Graphen Nanoribbons: Zigzag and armchair edges", Springer, in print

Publications concerning other topics

M. Piantek, G. Schulze, M. Koch, K. J. Franke, F. Leyssner, A. Krüger, C. Navio, J. Miguel, M. Bernien, M. Wolf, W. Kuch, P. Tegeder, and J. I. Pascual, "Reversing the Thermal Stability of a Molecular Switch on a Gold Surface: Ring-Opening Reaction of Nitrospiropyran", J. Am. Chem. Soc, vol. 131, no. 35, p. 12729, 2009

F. Leyssner, M. Koch, St. Meyer, Y. Luo, R. Haag, and P. Tegeder, "Invited presentation of research: Coverage and temperature dependent isomerization of tetra-tert-butyl-imine on Au(111)", Bunsen-Magazin, 13. Jahrgang, 5 (2011) 148.

J. Mielke, F. Leyssner, M. Koch, S. Meyer, Y. Luo, S. Selvanathan, R. Haag, P. Tegeder, and L. Gril, "Imine derivatives on Au (111): Evidence for inverted thermal isomerization", ACS nano, vol 5, no. 3, p. 2090, 2011

C. Gahl, D. Brete, F. Leyssner, M. Koch, E. R. McNellis, J. Mielke, R. Carley, L. Grill, K. Reuter, P. Tegeder, and M. Weinelt, "Coverage- and Temperature-Controlled Isomerization of an Imine Derivative on Au(111)", vol. 135, no. 11, p. 4273, 2013

Acknowledgments

In the first place I would like to thank all the people of the physical chemistry department and, in particular, the AG Grill for a good atmosphere and the funny discussions.

I want to express my gratidude to Leonhard Grill, the supervisor of this thesis, for his advice, support and guidance during this research. Even in stressful periods he took the time for fruitful discussion and helped me with my projects.

I would especially like to thank Martin Wolf for making this thesis possible and for the great environment of the Fritz-Haber-Insitut.

Thanks also to Katharina Franke for being the second supervisor of my dissertation and the opportunity to present my work in her group.

I would like to thank Stefan Hecht, David Bleger, Marie Gille and Andreas Viertel for the synthesis of the molecules, which made the measurements of this work possible.

Christian Joachim and Francesco Ample I would like to thank for the theoretical insight and the discussions we had.

Many thanks to Karsten Horn for his constructive comments as well as his support and encouragement during the work on the LT-STM.

I want to express my gratitude to Ernst Meyer und Shigeki Kawai for the collaboration and the interesting experiments.

Also thanks to all the members of the elab who helped me to quickly repair our electronic equippment.

Last but not least I would like to thank my parents and my friends for their patience during this time, and my wife Mirijam also for her proofreading skills.

Selbstständigkeitserklärung

Ich erkläre, dass ich die vorliegende Arbeit selbstständig und nur unter Verwendung der angegebenen Literatur und Hilfsmittel angefertigt habe.

Berlin, den 14. Juni 2013 Matthias Koch